

Statistical properties of deformed Samarium isotopes and constraining the nucleosynthesis of ^{180}Ta

Kgashane Leroy Malatji



Dissertation presented for the
degree of Doctor of Philosophy in the Faculty of Sciences at
Stellenbosch University.

Supervisor: Prof. M. Wiedeking (iThemba LABS)

Co-supervisors: Prof. S. Siem (University of Oslo)

Prof. P. Papka (Stellenbosch University)

December, 2019

Declaration

By submitting this thesis electronically, I declare that the entirety of the work contained therein is my own, original work, that I am the authorship owner thereof (unless to the extent explicitly otherwise stated) and that I have not previously in its entirety or in part submitted it for obtaining any qualification.

Date: December, 2019

Abstract

This thesis focuses on two areas of research, i) statistical properties of well-deformed samarium isotopes and ii) constraining the nucleosynthesis of ^{180}Ta .

The rare-earth isotopic chain of samarium provides an excellent opportunity to systematically investigate the evolution of nuclear structure effects from the near spherical ^{144}Sm isotope to the well-deformed ^{154}Sm . As the nuclear shape changes, statistical properties such as the nuclear level density (NLD) and γ -strength function (γSF) are expected to be affected. In particular resonance modes in the rare-earth region may reveal interesting features when their evolution is investigated across several nuclei in an isotopic chain. An experiment was performed at the Oslo Cyclotron Laboratory (OCL) to measure particle- γ coincidences from which the NLDs and γSF s were extracted using the Oslo Method. A deuteron beam was used to populate excited states in $^{154,155}\text{Sm}$. Results from this work indicate a pronounced $M1$ scissors resonance at ≈ 3 MeV in ^{155}Sm . Surprisingly, the γSF of ^{154}Sm appears to be more featureless. The measured integrated strength in both $^{154,155}\text{Sm}$ shows nonetheless a reasonable agreement with previous measurements of other deformed samarium isotopes. Overall, the results provide complementary information to the $(^3\text{He},\alpha\gamma)^{148}\text{Sm}$, $(^3\text{He},^3\text{He}'\gamma)^{149}\text{Sm}$, $(\text{d},\text{d}'\gamma)^{152}\text{Sm}$, $(\text{d},\text{p}\gamma)^{153}\text{Sm}$, $(\text{p},\text{d}\gamma)^{147,149,151,153}\text{Sm}$, $(\text{p},\text{p}')^{154}\text{Sm}$ and $(\alpha,\alpha'\gamma)^{154}\text{Sm}$ data previously measured.

A small number of naturally occurring neutron-deficient nuclides with $Z > 33$, referred to as p -nuclei, cannot be produced by (n,γ) processes in the cosmos. Instead, these stable nuclides are thought to be produced by the photodisintegration (p -process) of both slow-neutron capture (s -process) and rapid-neutron capture (r -process) seed nuclei. However, for ^{180}Ta , the p -process is not sufficient to explain the observed solar abundances and therefore additional processes are invoked. The ^{180}Ta production mechanism causes controversy since calculations show that several processes, sometimes exclusively, can reproduce its observed abundance, making it a particularly interesting case to study. Since the astrophysical sites for the nucleosynthesis of ^{180}Ta remain unknown, a combination of several processes is undeniably possible. However, the significance of individual processes cannot be clearly determined, as a result of the uncertainties on the reaction rates for ^{180}Ta due to the unavailability of experimental data. The $^{180,181,182}\text{Ta}$ NLDs and γSF s were recently measured at the OCL. From these results, the (n,γ) cross sections are calculated using the nuclear reaction code TALYS and compared to previous results. Furthermore, the reaction rates are calculated and used in s -process calculations in low-mass AGB stars and

p-process simulations in Type-II supernovae to investigate the nucleosynthesis of ^{180}Ta . From this work the newly constrained reaction rates of the *s*-process show that in low-mass AGB stars the contribution to the production of ^{180}Ta is negligible and only partially contributes to the production of ^{181}Ta . The *p*-process nucleosynthesis of nature's rarest stable isotope ^{180}Ta in Type-II supernovae using newly constrained data is significant and therefore suggests the *p*-process to be the fundamental production mechanism of ^{180}Ta in the universe.

Boikgopolelo

Kakanyo-thero ye e lebišitše go karolo tše pedi tša nyakišišo, i) mekgwa ya dipalopalo ya di-isotope tša samarium tšeo di golofetšego, le ii) go tšweletšo ya ^{180}Ta .

Selokaloke sa isotope ya samarium se beela tšhono ye botse yago nyakišiša ka tlhagelelo ya ditlamorago tša tlhamego ya nuclear go tšwa go ^{144}Sm isotope ya nkgokolo go ya go ^{154}Sm yeo e golofetšego. Ge sebopego sa nuclear se fetoga, mekgwa ya dipalopalo bjalo ka tekanyo ya boima bja nuclear (NLD) le morero wa maatla (γSF), di lebeletšwe go ka amega. Kudukudu mekgwa ya go galagala e ka tšwetša kgakala dibopego ge tlhagelelo ya tšona e nyakišišwa mo go nuclei tše mmalwa mo di-isotopong. Go dirilwe boitekelo Oslo Cyclotron Laboratory (OCL) go lekola diNLD le di γSF , go šomišwa mokgwa wa Oslo. Go dirišitšwe deuteron beam go hlola seemo sa tlhalalo ka gare ga $^{154,155}\text{Sm}$. Dipelo go tšwa mošomong wo, di laetša kwagatšo ya maatla a $M1$ gola ≈ 3 MeV kago ^{155}Sm . Eupja, ^{154}Sm γSF e lebelelega e hloka sebopego. Le ge golebjalo, kelo ya maatla a kopantšwego a $^{154,155}\text{Sm}$, e laetša tumelelano yago kwagala le boitekelo bjo bo fetilego, ya di-isotope tše dingwe tša samarium tšago golofala. Ka kakaretšo, dipelo di fa tshedimošo yago tlaleletšana go mešomo yago feta ya $(^3\text{He},\alpha\gamma)^{148}\text{Sm}$, $(^3\text{He},^3\text{He}'\gamma)^{149}\text{Sm}$, $(d,d'\gamma)^{152}\text{Sm}$, $(d,p\gamma)^{153}\text{Sm}$, $(p,d\gamma)^{147,149,151,153}\text{Sm}$, $(p,p')^{154}\text{Sm}$ le $(\alpha,\alpha'\gamma)^{154}\text{Sm}$.

Palo ye nnyane ya di-nuclide tšago tšwelela ka tlhago tša go bale tlhaelo ya dineutron tša $Z > 33$, e bitšwago p -nuclei, ga di kgone go ka tšweletšwa ka ditshepidišo tša (n,γ) tlhagong. Bakeng seo, di-nuclides tšeo go šišinywa gore di tšweletšwa ke peu ya nuclei ka photodisintegration (p -process) ya slow- le rapid-neutron capture process (s - le r -process). Efela, ge ele ^{180}Ta , p -process ga se ya lekanela go hlaloša boati bja yona mo tlhagong, ka fao go hlokega ditshepidišo tša go tlaleletša. Mekgwa ya go tšweletša ^{180}Ta e hlola ngangišano ka ge dipalo di laetša gore ditshepidišo tše mmalwa, ka nnoši nako ye nngwe, di ka tšweletša gape temošo ya boati. Ka ge mafelo a tlhago a tlholego ya ^{180}Ta a sa tsebje go fihla ga bjale, go na le kgonagalo mo go kase ganetšwego ya tlhakantšho ya ditshepidišo tše mmalwa. Fela ge, bohlokwa bja tshepidišo ya go ikema ga bo hlatsesege, ka lebaka la dipelaelo lebelong la diphetogo tša ^{180}Ta bakeng sa tlhokego ya dipalopalo tša boitekelo. Malobanyana $^{180,181,182}\text{Ta}$ NLD le γSF di ile tša elwa OCL. Go tšwa dipoelong tšeo, karolo tšeo di farologanyego tša (n,γ) di balwa go šomišwa sebalwa sa diphetogo tša nuclear sa TALYS gomme tša bapetšwa le dipelo tša morago. Go feta fao, lebelo la diphetogo le šomišwa ka dipalopalo tša s -process ka gare ga dinaledi tša low-mass AGB le tutuetšo ya p -process go naledi ya go thuthupa ya Type-II go nyakišiša tšweletšo ya ^{180}Ta . Go

tšwa mošomong wo, mabelo a diphetogo ao a goretšwego a maswa a *s*-process, a laetša gore go dinaledi tša low-mass AGB, seabe sa tšweletšo ya ^{180}Ta ga se bohlokwa gomme se kgatha tema ka boripanyana go tšweletšeng ga ^{181}Ta . Tšweletšo ya *p*-process ya ^{180}Ta ka go naledi ya go thuthupa ya Type-II go šomišwa dipalopalo tše diswa e bohlokwa gomme e šišinya gore *p*-process ke motheo wa tshepedišo ya tšweletšo ya ^{180}Ta tlhagong.

Uittreksel

Hierdie tesis het twee navorsings fokus areas naamlik, i) die statistiese eienskappe van goed-ervormde samarium isotope, en ii) die inperking van nukleosintetiese reaksies van ^{180}Ta .

Die isotoop ketting van die seldsame aardelement samarium bied 'n uitstekende geleentheid om sistematies die verandering van kernstruktuur effekte vanaf die byna sferiese ^{144}Sm isotoop tot die heel-ervormde ^{154}Sm te bestudeer. Met die vervorming van die kern, word verwag dat statistiese eienskappe van die kern soos die vlak-digtheid (KVD) en die γ -sterke funksie (γSF) sal verander. In besonder word verwag dat die opwekking van resonansies in hierdie massa gebied moontlik interessante kenmerke sal oopenbaar met 'n ondersoek oor verskeie isotope van dieselfde element. Uit data wat by die Oslo Siklotron Fasiliteit (OSF) opgeneem is, is KVDe en γSF s ge-ekstraer met gebruik van die Oslo metode. 'n Deuteron bundel is gebruik om opgewekte toestande in $^{154,155}\text{Sm}$ te vul. Die data toon aan dat daar 'n opmerklike $M1$ skêr-resonansie by 'n opwekking van ≈ 3 MeV in ^{155}Sm voorkom terwyl die γSF van ^{154}Sm vormloos is. Nieteenstaande is die gemete geïntegreerde sterkte van beide $^{154,155}\text{Sm}$ goed vergelykbaar met vorige gemete waardes van ander vervormde samarium isotope. Hierdie resultate voorsien komplimentere informasie tot die reeds gepubliseerde gemete stelle ($^3\text{He}, \alpha\gamma$) ^{148}Sm , ($^3\text{He}, ^3\text{He}'\gamma$) ^{149}Sm , ($d, d'\gamma$) ^{152}Sm , ($d, p\gamma$) ^{153}Sm , ($p, d\gamma$) $^{147,149,151,153}\text{Sm}$, (p, p') ^{154}Sm en ($\alpha, \alpha'\gamma$) ^{154}Sm data.

'n Kleiner getal neutron-arm nukliedes wat natuurlik voorkom, met $Z > 33$, en as p -nukliedes bekend staan, kan nie met die (n, γ) reaksie in die heelal geproduseer word nie. Daar word verwag dat hierdie nukliedes deur die fotodisintegrasie (p -proses) van kerne gevorm word deur beide stadige-neutron vangs (s -proses) en vinnige-neutron vangs (r -proses) van stabiele kerne. Vir ^{180}Ta kan nie net die p -proses die waargenome natuurlike voorkoms van die isotoop verklaar nie. Teoreties is daar verskeie produksie reaksies wat die korrekte natuurlike voorkoms van ^{180}Ta voorspel en waarvan sommige sterk genoeg is om selfs alleenlik die natuurlike voorkoms te kan verklaar. Dit is wat ^{180}Ta so interessant maak om te bestudeer. Waar ^{180}Ta geproduseer word is nie bekend nie sodat dit heel waarskynlik is dat meer as een proses tot die produksie bydra. Weens 'n gebrek aan eksperimentele data was dit nie moontlik om uitsluitel te gee oor die moontlike reaksies nie, nog minder hul sterktes, wat bydra tot die produksie van ^{180}Ta . Vanuit die KVDe en γSF s van $^{180,181,182}\text{Ta}$ wat ook by OSF gemeet is, is die (n, γ) kansvlakke bereken met gebruik van die kode TALYS en vergelyk met vorige resultate. Daaruit is reaksie obrengse bereken wat as invoer data vir die s -proses produksie van ^{180}Ta in lae-massa AGB

sterre gedien het sowel as vir die p -proses produksie in Tipe-II supernovas. Die kleiner limiete van die reaksie sterktes bereken in hierdie tesis wys daarop dat in lae massa AGB sterre die bydrae van die s -proses, tot die produksie van ^{180}Ta , weglaatbaar klein is en net gedeeltelik die produksie van ^{181}Ta verklaar. Daarbenewens is uit die data nuwe limiete vasgestel wat daarop dui dat die p -proses in Tipe-II supernovas, die oorwegende produksie meganisme van ^{180}Ta is, die skaarste stabiele isotoop in die heelal.

Acknowledgements

First and foremost, I would like to acknowledge my supportive supervisors Mathis Wiedeking, Sunniva Siem and Paul Papka. Thank you for granting me the opportunity to work with you over the years and for believing in me even when I doubted myself. This accomplishment would have not been possible without your consistent support, encouragements and guidance throughout my academic and personal life. Mathis and Sunniva, words can not express my heartfelt gratitude towards your humaneness, I am forever grateful for having crossed paths with you.

To the funding body, the National Research Foundation (NRF) of South Africa under grant No: 100465, 92600, and 92789, thank you for your invaluable and reliable financial support. In particular, the Professional Development Program (PDP) scholarship for emerging researchers in S. Africa came in handy. I am thankful to the International Atomic Energy Agency (IAEA) grant under research contract No: 20454.

I am grateful to the Norwegian Research Council for partly supporting my international trips financially, through the International Partnerships for Excellent Education and Research (INTPART) grant, to the University of Oslo for student-exchange program, experiments, research meetings and workshops. In addition, for sponsoring complementary intensive summer school courses and training that I have attended in S. Africa and Oslo.

Special salutation to Stephane Goriely for your invaluable input into this work. You are always ready to dive into theory and patiently explain to me over and over again. Thank you for words of encouragements and understanding.

Special thanks to the nuclear physics and cyclotron laboratory group at the University of Oslo for being kind and creating such a welcoming environment for one to learn. Thank you all for being involved in my project, inviting me into your homes for some refreshments and good company. You kept my research visits homely. Ann-Cecilie it is amazing how quickly you respond to your emails and messenger, and yet give detailed and well thought input.

To a friend and collaborator Kristine, I have enjoyed your good company, both at the office and outdoors. Thank you for your kindness and making sure I keep fit while in Oslo. Thank you for

reading my dissertation.

I am grateful to the iThemba LABS physics group, the management team (finance, information technology, administration, security, etc.), and the soccer team for your support and encouragements. It is because of you that iThemba LABS feels like home away from home. Kealeboga!!

To my lovely wife Katlego and to our beautiful daughter Amogelang, I could not have made it this far without your support and care. Over the years you have managed to help me become a better version of myself. Thank you for your patience and understanding during my studies. Lerato ke leo mchana!!

Last but not least, to my mother and brothers who went through so much to help me achieve my goals: *Ga ke selo ntle le lena*. Thato, Malemela le Buti Mpho, kealeboga bana ba Mologadi for dilo ka moka.

Dedication

This work is dedicated to my mother Joyce Mmabodimo Malatji...

ke a leboga Mologadi morwedi 'a Matlala.

Contents

Declaration	ii
Abstract	iv
Boikgopolelo	vi
Uittreksel	viii
Acknowledgements	x
Dedication	xi
Table of Contents	xi
List of Figures	xiii
List of Tables	xxii
Abbreviation	xxiv
1 Introduction	1
1.1 Physics motivation and objectives for $^{154,155}\text{Sm}$	4
1.2 Physics motivation and objectives for ^{180}Ta	5
2 Nuclear Structure and Nuclear Astrophysics theory	8
2.1 Nuclear Level Density	8
2.1.1 The Fermi-Gas Model	8
2.1.2 Constant Temperature Model	10

2.1.3	Constant Temperature Model + Fermi-Gas Model	10
2.1.4	Hartree-Fock-Bogoliubov plus Combinatorial Model	11
2.2	γ -ray Strength Function	15
2.2.1	Resonances in the γ -ray strength function	16
2.2.2	E1 pygmy resonance	17
2.2.3	M1 scissors resonance	18
2.2.3.1	Reduced transition strengths	23
2.2.4	Low-Energy Enhancement	26
2.3	Radiative neutron capture cross-section and reaction-rate calculations	27
3	Experimental details	30
3.1	Oslo Cyclotron Laboratory	30
3.1.1	Target	31
3.1.2	Particle detection	32
3.1.3	γ -ray detection	33
3.2	Coincidence technique	35
4	Data analysis and the Oslo Method	38
4.1	Energy calibration and particle identification	38
4.1.1	Particle energy calibration and identification	38
4.1.2	γ -ray energy calibration and identification of γ -ray transitions	44
4.1.3	Particle- γ coincidences	47
4.2	The Oslo Method	49
4.2.1	Unfolding continuum γ -ray spectra	49
4.2.2	The folding iteration technique	50
4.2.3	The Compton subtraction method	52
4.2.4	Extracting the first-generation γ -ray spectra	54

4.2.5	Extracting the nuclear level density and the γ -ray strength function . . .	58
4.2.5.1	Normalization	60
4.2.5.2	Nuclear Level density	60
4.2.5.3	The γ -ray strength function	64
4.2.6	Challenges and possible systematic errors in the normalization procedure	67
4.3	Resonances and photo-absorption data	69
4.4	The scissors resonance	72
5	Discussion of results	74
5.1	NLDs and γ SFs of $^{154,155}\text{Sm}$ and the scissors resonance	74
5.2	$^{180,181,182}\text{Ta}$ NLDs and γ SFs and $^{180}\text{Ta}^m$ nucleosynthesis	83
5.3	Nucleosynthesis applications	88
5.3.1	S-process nucleosynthesis of $^{180}\text{Ta}^m$ and ^{181}Ta	88
5.3.2	P-process nucleosynthesis of ^{180}Ta	90
6	Summary and Conclusion	94
6.1	The scissors resonance in $^{154,155}\text{Sm}$	94
6.2	$^{180}\text{Ta}^m$ nucleosynthesis	96
	Bibliography	114
	Appendix A	115

List of Figures

1.1	A simplistic overview of the nucleosynthesis processes responsible for the production of light to heavy elements found in nature today. Figure taken from Ref. [2].	2
1.2	The solar abundances as a function of mass number A of heavy elements synthesized in nature by the s - (solid line), r - (solid circles) and p -process (open squares). Figure taken from Ref. [15].	3
1.3	A schematic plot showing the several nucleosynthesis processes proposed to reproduce ^{180}Ta in nature.	5
1.4	A schematic level scheme of ^{180}Ta showing the ground state decays to ^{180}Hf and ^{180}W by EC and β^- emission, respectively.	6
2.1	Comparison of the cumulative number of known levels (black staircase) with the HFB + combinatorial calculations (red curve) as a function of E_x , for light to heavy mass, spherical and deformed nuclei [53].	12
2.2	Ratio of HFB + combinatorial (D_{th}) with the experimental (D_{exp}) s - and p -wave neutron resonance spacings [53]. Globally, the ratio D_{exp}/D_{th} are predicted within a factor of 2.	13
2.3	Comparison of the cumulative number of known levels with the HFB + combinatorial calculations, ρ_{HFB} , as a function of E_x for ^{90}Y with and without the normalization (left panel). The $^{89}\text{Y}(n,\gamma)^{90}\text{Y}$ cross-sections obtained with and without the normalized NLD as compared to the experimental data (right panel). Figure from Ref. [53].	14
2.4	The γ -decay and photo-absorption processes.	15
2.5	Resonances observed in the total γ -ray strength function.	17

2.6	Comparison of OCL experimental data to the other experimental data showing an enhancement at around S_n in the γ SF of $^{116-119,121,122}\text{Sn}$ isotopes. The different colored lines show the total predicted γ SF and respective resonances. Figure taken from [79].	18
2.7	A schematic representation of the $M1$ scissors resonance. The macroscopic (a) description showing the orbital (neutrons against proton clouds) and spin scissors (spin-up nucleons against spin-down nucleons) mode [24]. The microscopic (b) description illustrates the transitions for high- j orbitals Ω and the effect of deformation ε [22].	19
2.8	A schematic representation of the $M1$ strength distribution in heavy deformed even-even nuclei [88].	20
2.9	The very first experimental evidence of the low-lying magnetic dipole resonance from the work of Richter <i>et al.</i> [88] on ^{156}Gd (a) and Guttormsen <i>et al.</i> [89] on ^{161}Dy (b).	21
2.10	The total low-lying $M1$ and $E2$ strengths deduced from experiments for ^{134}Ba , $^{144-150}\text{Nd}$, $^{148-154}\text{Sm}$, $^{156-160}\text{Gd}$, $^{160-164}\text{Dy}$, $^{164-170}\text{Er}$, $^{172-176}\text{Yb}$, $^{178-180}\text{Hf}$, $^{182-186}\text{W}$, $^{190-192}\text{Os}$ and ^{196}Pt isotopes [91].	22
2.11	The extracted $M1$ scissors resonance using the Oslo method for $^{231-133}\text{Th}$ and $^{237-239}\text{U}$ [23]. Contributions from all other resonances have been subtracted to reveal the features of the scissor resonance. Various excitation energy regions of the data are utilized.	23
2.12	The systematics for $^{154,155,156,157,158,160}\text{Gd}$ (a) showing the ground-state decay width distributions which are directly related to the reduced transition strength (as shown in Eq. 2.17) extracted from NRF measurements [61, 104]. The reduced $M1$ scissor resonance strength for the even- and odd- A $^{153,155,156,157,158,159}\text{Gd}$, ^{160}Tb and $^{160,161,162,163,164}\text{Dy}$ (b) extracted from different experimental techniques [106].	25
2.13	Nuclear chart detailing where the LEE has been observed experimentally using the Oslo Method, as indicated by yellow stars. The red circles indicate isotopes studied but no LEE has been observed, whereas the blue diamonds point out to isotopes in which is unclear yet whether or not the LEE is present. Figure taken from Ref. [123]	26

3.1	The Oslo Cyclotron Laboratory showing the experimental hall and cyclotron hall separated by a concrete wall, with the respective target stations and beam lines [130].	31
3.2	The 8 trapezium shaped Si particle detectors distributed on a ring including cables to read out the signals and in each trapezoid, the strip covers an angle of $\Delta\theta = 2^\circ$ [132].	33
3.3	Experimental setup at the OCL, showing the γ -ray array with 24 NaI(Tl) + 6 LaBr ₃ :Ce detectors.	34
3.4	A schematic diagram of the NaI(Tl) γ -ray scintillator detector (upper panel) [134], showing the principle of scintillator based γ -ray detector such as the NaI(Tl) or the LaBr ₃ :Ce (lower panel) [135]. The incident high energy photon produces light (or relatively low energy photons) when interacting with the scintillator material. The low energy photons interact with the semi-transparent photo-cathode which converts them into low-energy electrons. At this point, the produced electron charge is too small to serve as an electrical signal since a typical pulse requires several hundreds of photo-electrons. Therefore, the electrons are directed and multiplied by series of dynodes, giving rise to $\approx 10^7 - 10^{10}$ electrons [136]. The output pulse is collected at the anode.	35
3.5	A schematic diagram of the electronics setup, located in the data room at the OCL. Each individual NaI(Tl), ΔE and E signal is processed by a separate spectroscopic amplifier, TFA, LED, and ADC. Additionally, each NaI(Tl) time signal is allocated its own TDC channel. Figure adopted from Ref. [36].	36
4.1	The uncalibrated $\Delta E - E$ matrix showing all the detectors for the $^{154}\text{Sm}(d,X)$ reaction, used to identify the ejectile particles in a nuclear reaction.	39
4.2	The calibrated $\Delta E - E$ plot for the $^{154}\text{Sm}(d,X)$ reaction, showing different reactions channels opened during the reaction (upper panel). The range spectrum for the $\Delta E - E$ detectors showing peaks representing different particles (lower panel). The dashed lines show the gate used to select only (d,p γ) reactions. . . .	40
4.3	The calibrated $\Delta E - E$ plot for the $^{154}\text{Sm}(d,X)$ (upper panel) and $^{28}\text{Si}(d,X)$ (lower panel) reaction, in comparison to calculated values from the SiRi kinematic calculator for SiRi strip at $132\pm 1^\circ$ of the $\Delta E - E$ detector.	41
4.4	The calibrated $\Delta E - E$ plot for the $^{154}\text{Sm}(d,p\gamma)$ (upper panel) and $^{28}\text{Si}(d,p\gamma)$ (lower panel) reactions, both gated on the ejected protons.	42

4.5	Excitation energy spectrum without a γ -ray coincidence requirement extracted from the $^{154}\text{Sm}(d,d'\gamma)$ (a), $^{154}\text{Sm}(d,p\gamma)$ (b) and $^{28}\text{Si}(d,p\gamma)$ (c). The solid vertical black lines indicates the location of neutron separation energy S_n	43
4.6	The calibrated γ -ray energy spectrum of ^{29}Si with identified energies retrieved from NNDC [143]. The spectra is obtained with a gate set on the $E_x = 4934$ keV state in the excitation energy spectra shown in Fig. 4.5 (lower panel) for one NaI(Tl) detector.	44
4.7	The $^{154}\text{Sm}(d,p\gamma)$ energy-time matrix for all NaI(Tl) detectors before "walk"-effect correction.	45
4.8	The energy-time matrix from the ^{154}Sm reaction after "walk" correction for the CACTUS array (upper panel). The projection of Fig. 4.8 (a) on the time-axis after signals were time calibrated from CACTUS (lower panel). The dashed lines (t_1, t_2) and (t_3, t_4) are gates on the prompt and random events, respectively, with the same width.	46
4.9	Excitation energy spectrum with a γ -ray coincidence requirement extracted from the $^{154}\text{Sm}(d,d'\gamma)$ (upper panel) and $^{154}\text{Sm}(d,p\gamma)$ (lower panel). Dashed lines indicates the location of the neutron separation energy S_n	47
4.10	An illustration of energy deposition by photons through photoelectric absorption, Compton scattering, and pair production in the detector material, resulting in full and/or partial recovery of initial γ -ray energy. Figure taken from Ref. [136].	50
4.11	Illustration of the interpolation of the Compton part from measured response functions c_1 and c_2 [137]. The scattering angle θ increases as the energy transferred to the electron increases.	52
4.12	The raw γ -ray spectra (a), unfolded γ -ray spectra (b) and first generation (primary) γ -ray (discussed in sec. 4.2.4) spectra of $^{154,155}\text{Sm}$ from this work. . . .	54
4.13	A demonstration of the procedure for extracting first-generation γ -rays. Figure from Ref. [145].	55
4.14	The first-generation γ -ray matrix for ^{155}Sm . The arrows point at vertical valleys of low counts in the initial matrix (left panel) that have been compensated in (right panel) (most easily visible at $E_\gamma \approx 0.9$ and 1.2 MeV).	57
4.15	The raw, unfolded and first generation (primary) γ -ray matrix of $^{154,155}\text{Sm}$ and ^{181}Ta from this work. The dashed lines indicate the energy region in which the nuclear level density and γ -ray strength function were extracted.	57

4.16	The experimental first generation γ -ray spectra (data points with error bars) from $(d,d'\gamma)^{154}\text{Sm}$ (upper panel) and $(d,p\gamma)^{155}\text{Sm}$ (bottom panel) reaction at 15 and 13 MeV beam, respectively, from selected initial excitation energies E_x (indicated in the figure) compared to the product $\rho(E_x - E_\gamma) \times \mathcal{T}(E_\gamma)$ (solid curve) following the global iterative χ^2 minimization of Ref. [29].	59
4.17	The normalized experimental NLDs for $^{154,155}\text{Sm}$. The set of vertical arrows indicate the location at which the χ^2 minimization was performed.	61
4.18	The normalized experimental NLDs for ^{155}Sm using different spin distribution models. The set of vertical arrows indicate the location in which χ^2 minimum was performed.	62
4.19	The normalized spin distribution at low-excitation energies for $^{154,155}\text{Sm}$	63
4.20	The spin cut-off parameter as a function of excitation energy for ^{155}Sm . The CT model assumes a linear dependence of the spin cut-off on excitation energy. Represented in the right panel, are similar spin cut-off parameters models following Eq. 2.7, where a fit is made to reliable spins at known discrete lower-lying levels tabulated in NNDC [143].	63
4.21	The spin distribution at $E_x^{spin}=1.987$ MeV, with $\sigma(E_x^{spin})=4.881$ determined using the spin cut-off of Eq. 2.5, for ^{155}Sm . The red line indicates the highest spin populated $J=15/2$ and the colored blue area shows possible spin population by the $(d,p\gamma)$ or (d,p) reaction, corresponding to 73.4% of the totals levels being populated.	64
4.22	The extrapolated γ -ray transmission coefficient of ^{155}Sm . The set of arrows at low and high γ -ray energies E_γ indicate the region where the exponential function has been fitted.	65
4.23	The experimental γ SF of $^{154,155}\text{Sm}$ (upper panel). The green data represent the γ SF of ^{155}Sm with spin population correction and the red data points, the γ SF without the spin population correction (lower panel).	66
4.24	The experimental $l=0$ neutron resonance spacing D_0 and the average radiative width $\langle\Gamma_\gamma(S_n)\rangle$ plotted against the neutron number N of even-even $^{144-148,152}\text{Nd}$, $^{148-152}\text{Sm}$ and $^{154-158}\text{Gd}$ isotopes.	68
4.25	The normalized experimental NLDs for $^{154,155}\text{Sm}$. A sudden drop in the ^{154}Sm NLD at high E_x is as a result of low statistics for extracting the primary γ -rays at around E_x^{max} limit shown in Fig 4.15 (a) for ^{154}Sm	68

4.26	The newly extracted experimental γ SFs of $^{154,155}\text{Sm}$ compared to photo-nuclear reaction measurements. The observed resonances in the γ SF are fitted with the SLO and EGLO.	70
4.27	The experimental γ SF of ^{182}Ta from the $^{181}\text{Ta}(d,p\gamma)$ reaction in comparison to the $(n,\gamma)^{182}\text{Ta}$ $E1+M1$ ARC data experiments [64], $^{181}\text{Ta}(\gamma,\gamma)$ NRF data [158], $^{181}\text{Ta}(\gamma,n)$ [159] and $^{181}\text{Ta}(\gamma, xn)$ [33] photo-nuclear reaction data. The solid line denote the $E1+M1$ total fit whereas the dotted line are the separate $E1$ and $M1$ fits.	71
4.28	The extracted scissors resonance experimental of $^{154,155}\text{Sm}$, fitted with the SLO. The errors here follow directly from the extraction and may not represent the actual errors.	73
5.1	The normalized experimental NLDs of $^{154,155}\text{Sm}$ from the present experiment compared to those of $^{152,153}\text{Sm}$ [26], $^{151,153}\text{Sm}$ [27] and $^{147,149}\text{Sm}$ [28]. The solid lines denote the known discrete levels and the dashed lines represent the CT model interpolation between the experimental data (solid squares) and $\rho(S_n)$ (open squares).	75
5.2	The microscopic NLDs from Goriely's (ldmodel=4) and Hilaire's combinatorial (ldmodel=5) tables [40, 55] for the even-odd $^{153,155}\text{Sm}$ isotopes. The normalized data represented by the dotted line is corrected for the slope and absolute value but completely independent of the present experimental data and that of ^{153}Sm [26]. Figures from Ref. [163]	76
5.3	The present experimental NLDs of the even-even and even-odd samarium isotopes compared to the $^{151,153}\text{Sm}$ [27], $^{147,149}\text{Sm}$ [28] and $^{152,153}\text{Sm}$ [26].	77
5.4	The normalized experimental γ SF of even-even $^{152,154}\text{Sm}$ (left panel) and of even-odd $^{147,149,151,153,155}\text{Sm}$ (right panel) isotopes.	78
5.5	The ^{149}Sm [25] and $^{151,153}\text{Sm}$ [27] experimental γ SF compared to the theoretical models, the simple modified Lorentzian (SMLO) (blue lines) and the mean-field-plus-quasiparticle random-phase approximation including the LEE (D1M+QRPA+0lim) (red lines) models [164, 165]. Figure from Ref. [166]	78
5.6	The experimental low-lying $M1$ strength, $B_{SR}(M1)$ plotted against the mass number A . The present measurements (red solid triangle) are compared to $^{149,151,153}\text{Sm}$ data from Ref. [27, 28], $^{152,153}\text{Sm}$ of Ref. [26], and $^{150,152,154}\text{Sm}$ from Ref. [93]	79

5.7	The $^{154,155}\text{Sm}$ γSF extracted at several excitation energy regions.	81
5.8	The ^{181}Ta NLD populated with the $^{181}\text{Ta}(d,d')$, $^{181}\text{Ta}(d,d')$ and $^{181}\text{Ta}(^3\text{He},^3\text{He}')$ reactions at reaction at 12.5, 15 and 34 MeV beam energies, respectively. The level density deduced from known discrete levels is represented by the solid line and an interpolation between the experimental data and $\rho(S_n)$ (dashed line) is achieved with CT model [42]. Figure taken from Ref. [38].	83
5.9	The newly extracted experimental NLDs of $^{180,181,182}\text{Ta}$ normalized using the BSFG, CT+FG (1&2) and HFB+comb models. The solid black line denotes the level density of known discrete levels. Figure taken from Ref. [38].	84
5.10	The newly extracted experimental γSFs of $^{180,181,182}\text{Ta}$ compared to $^{181}\text{Ta}(\gamma, n)$ [159], $^{181}\text{Ta}(\gamma, xn)$ [33] photo-nuclear data and $^{181}\text{Ta}(\gamma, \gamma')$ NRF measurements [158].	85
5.11	The $^{179,180,181}\text{Ta}(n, \gamma)$ cross-sections (bands) extracted from the experimental NLDs and γSFs in panel (c), (b) and (a) respectively. The $^{181}\text{Ta}(n, \gamma)^{182}\text{Ta}$ cross-sections determined using the BSFG, CT+FG (1&2) and HFB+comb models and their normalizations are compared to previous TOF [172, 173] and activation [171] measurements (a), and the $^{180}\text{Ta}^m(n, \gamma)$ cross-section to TOF measurements [174] (b). Figure taken from Ref. [177].	87
5.12	Surface overabundances $[X/\text{Fe}] = \log_{10}[X/X_{\odot}] - \log_{10}[\text{Fe}/\text{Fe}_{\odot}]$ as a function of the atomic mass A for all nuclei (open squares) and s -only nuclei (solid squares) at the end of the AGB phase, <i>i.e.</i> , after the 29th thermal pulse, of the $2 M_{\odot}$ $[\text{Fe}/\text{H}] = -0.5$ model star. Highlighted are the $^{180}\text{Ta}^m$ (red triangles) and ^{181}Ta (blue triangles) overabundances and their uncertainties associated with the reaction rates studied in the present work as well as those affecting the $^{179}\text{Hf}(\beta^-)^{179}\text{Ta}$ decay rate (see text for more details). The y-axis is given in logarithmic scale. Figure taken from Ref. [177].	90
5.13	Upper (solid line) and lower limits (dashed line) of the $^{180}\text{Ta}^m$ (red lines) and ^{181}Ta (blue lines) overabundances $[X/\text{Fe}]$ inside the star, just below the convective envelope, as a function of the mass coordinate M_r after the 26th thermal pulse of our $2 M_{\odot}$ $[\text{Fe}/\text{H}] = -0.5$ model star. The upper and lower limits are associated with the reaction rates uncertainties from the present work as well as those affecting the $^{179}\text{Hf}(\beta^-)^{179}\text{Ta}$ decay rate (see text for more details). The convective envelope extends above $M_r = 0.665 M_{\odot}$. Figure taken from Ref. [177].	91

- 5.14 P -nuclide overproduction factors $[X/X_{\odot}]$ obtained for the $Z = Z_{\odot}$ $25 M_{\odot}$ model star with TALYS rates for nuclei other than tantalum and the new tantalum production and destruction rates. The ^{180}Ta value corresponds to the total ground state plus isomeric overabundances. The shaded region delineates a factor of 3 around a mean value. For more details see [13, 30]. Figure taken from Ref. [177]. 92
- 6.1 The raw γ -ray spectra (a), unfolded γ -ray spectra (b) and first generation (primary) γ -ray (discussed in sec. 4.2.4) spectra of ^{154}Sm extracted from the data collected with the $\text{LaBr}_3:\text{Ce}$ detectors from this work. 115
- 6.2 The experimental first generation γ -ray spectra (data points with error bars) from $(d,t\gamma)^{180}\text{Ta}$ (upper panel) and $(d,d'\gamma)^{181}\text{Ta}$ (bottom panel) reaction at 15 MeV beam, respectively, from selected initial excitation energies E_x (indicated in the figure) compared to the product $\rho(E_x - E_{\gamma}) \times \mathcal{T}(E_{\gamma})$ (solid curve) following the global iterative χ^2 minimization of Ref. [29]. 115
- 6.3 The normalized experimental NLDs for $^{180,181,182}\text{Ta}$ isotopes. The set of vertical arrows indicate the location at which the χ^2 minimization was performed. The individual plots have been presented in Refs. [36, 37, 38, 133] but in this thesis, the most recent and final normalization version of the data set is presented. . . . 116
- 6.4 The experimental γ SFs of $^{180,181,182}\text{Ta}$. The individual plots have been presented in Refs. [36, 37, 38, 133] but in this thesis, the most recent and final normalization version of the data set is presented. 117

List of Tables

3.1	List of available beams at OCL.	30
3.2	The mass, thickness and enrichment of the targets, the beam current and energy, and reactions studied in the experiments presented in this work. The ^{154}Sm experiment was performed with 24 NaI(Tl) + 6 LaBr ₃ :Ce detectors and a total of 26 NaI(Tl) for the $^{180,181,182}\text{Ta}$ experiments discussed in Refs [37, 133]. The ^{28}Si data were used for calibration purposes.	32
4.1	New and improved measurements of intensities and FWHMs deduced for the NaI(Tl) response functions. To obtain best possible results of the unfolding, the resolution of the response function is currently set to 10% of the experimental resolution [103], and not 50% as cited in Ref. [137]. Parameters p represent the probabilities that an event will belong to at-least one of the five components of the spectrum (<i>i.e.</i> full energy (f), the single- (s) and double-escape (d), and the annihilation (a) peaks). ε_{tot} is the total γ -ray efficiency.	51
4.2	The regions where the global χ^2 minimization was applied to $^{180,181,182}\text{Ta}$ and for $^{154,155}\text{Sm}$ matrices.	60
4.3	Parameters used for extraction and normalization of $\rho(E_x)$ and $\mathcal{T}(E_\gamma)$ in $^{154-155}\text{Sm}$ and $^{180-182}\text{Ta}$	62
4.4	Resonance parameters used for fitting to experimental γSF of both $^{154,155}\text{Sm}$, where ω , σ and Γ are the energy centroid, cross-section and width of the resonance.	71
4.5	Resonance parameters used for fitting to scissors resonance, where $B(M1)_{SR}$ is the integrated resonance strength.	72
5.1	The experimental $B_{SR}(M1)$ for samarium isotopes extracted at given energy ranges. The deformation parameter β_2 is taken from the RIPL-3 database [58] and E_{sc} is the centroid of the scissors resonance.	80

5.2	The Maxwellian-averaged (n, γ) cross-sections of $^{179,180,181}\text{Ta}$	88
-----	---	----

Abbreviations

NLD Nuclear level density

γ SF γ -ray strength function

PDR Pygmy Dipole Resonance

SR Scissors Resonance

LEE Low-Energy Enhancement

GEDR Giant Electric Dipole Resonances

HFB Hartree-Fock-Bogoliubov

TRM two-rotor model

IBM-2 Interacting Boson Model-2

CN Compound nuclear

AGB Asymptotic Giant Branch

TOF Time of flight technique

KADoNiS Karlsruhe Astrophysical Database of Nucleosynthesis in Stars

MACS Maxwellian-Averaged (n, γ) Cross-Section

HF Hauser-Feshbach model

NRF Nuclear Resonance Fluorescence

ARC Average Resonance Capture

TSC Two-Step Cascade

QPRA Quasi-Particle Random Phase Approximation

Chapter 1

Introduction

"Aristotle said a bunch of stuff that was wrong. Galileo and Newton fixed things up. Then Einstein broke everything again. Now, we've basically got it all worked out, except for small stuff, big stuff, hot stuff, cold stuff, fast stuff, heavy stuff, dark stuff, turbulence, and the concept of time."

— **Zach Weinersmith**, *Science: Abridged Beyond the Point of Usefulness* (2017), 1 Physics 1.1 History

Our current understanding of the universe, *i.e.*, matter, space and time requires us to push beyond boundaries of what we already know in order to resolve the mysteries of nature. A decade ago, the National Research Council [1] identified eleven key scientific open questions for the new millennia, including the origin of heavier elements from iron to uranium. These have been the key priorities and have to be addressed by future scientific projects. The origin of heavier elements has remained a puzzle for nuclear scientists over the years. The main source of information on the chemical composition of the universe or elemental abundances is obtained mainly from the solar-system abundances and meteorites from outer space. To explain the origin of the different elements and their isotopes observed in nature, nuclear physics and nuclear astrophysics play an crucial role in identifying the possible nucleosynthesis processes, mechanisms and sites in which these elements are synthesized. A number of processes responsible for the production of light elements up to iron and beyond, is shown in Fig. 1.1. Of interest to this dissertation is the production of elements beyond iron which involves mainly the slow and rapid neutron-capture processes. The slow neutron-capture process (*s*-process) produces half of the heavier elements above germanium in asymptotic giant branch stars and during He-burning stages in massive stars [3, 4]. The rapid neutron-capture process (*r*-process) produces elements from tellurium to uranium, which takes place in neutron star mergers [5, 6, 7, 8], and for now high-neutron density environments such as supernovae explosions [9, 10, 11] cannot be ruled out as a possible site as well.

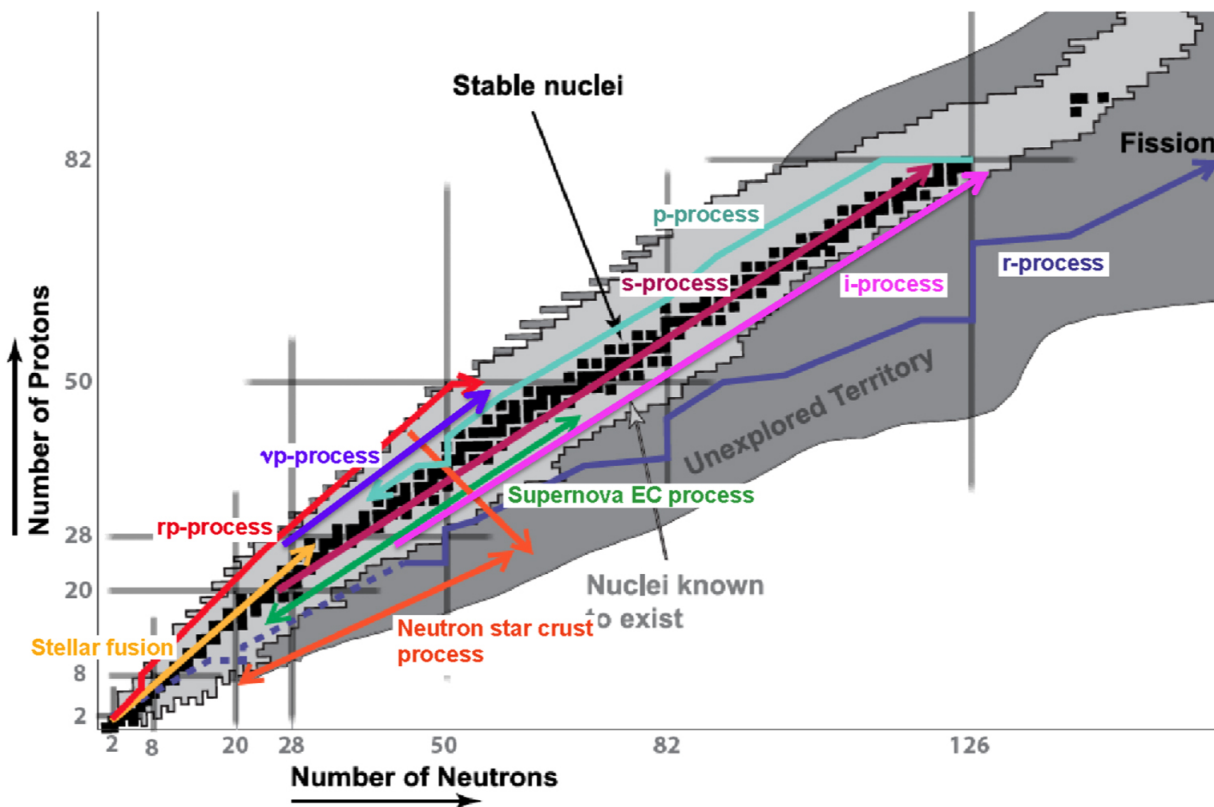


Figure 1.1. A simplistic overview of the nucleosynthesis processes responsible for the production of light to heavy elements found in nature today. Figure taken from Ref. [2].

A recent review of the experimental techniques to constrain the neutron-capture reaction rates relevant for the r -process is given in Ref. [12]. The nucleosynthesis of most naturally occurring neutron-deficient nuclides known as p -nuclei with $Z \geq 34$ is not completely understood yet and depends on the current understanding of the s -process and r -process. These stable p -nuclei cannot be produced by the neutron-capture processes [13, 14] but are thought to be produced in high-density, high-temperature environments by the photodisintegration (p -process) of s - and r -process seed nuclei [13, 14]. The p -process proceeds by means of γ -ray capture by nuclei, produced during the s - and r -process, which subsequently decay by emitting a particle *e.g.*, (γ, n) , (γ, p) , (γ, α) etc. Fig. 1.2 shows the calculated solar abundances of heavier elements than iron produced during the s -, r - and p -process nucleosynthesis. Some features are prominent in Fig. 1.2 which can be explained by the structures of nuclei, in particular by the enhanced stability of nuclei due to the specific configuration of neutrons and protons in nuclei. However, to make reliable astrophysical model predictions, uncertainties in nuclear physics and structure inputs such as neutron-capture cross-sections, deformation parameters, optical model potentials, nuclear level densities (NLD), γ -ray strength functions (γ SF) etc., need to be constrained from accurate measurements.

Nuclear structure properties are different for each nucleus as described by the shell model [16] of the nucleus. Nuclei with enhanced stability are known to possess a special number of protons and neutrons, called magic numbers ($N = 8, 20, 28, 50, 82, 126$ for neutrons and $Z = 8, 20, 28, 50, 82$

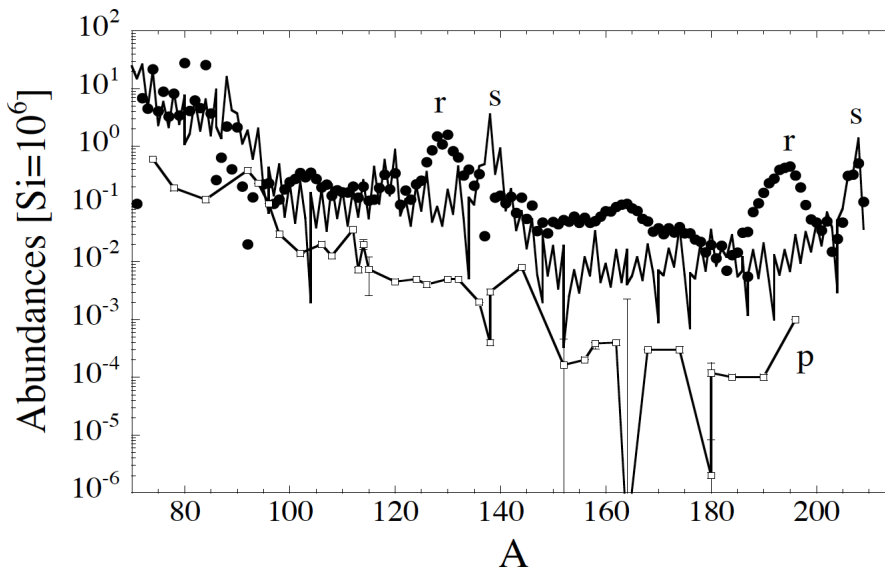


Figure 1.2. The solar abundances as a function of mass number A of heavy elements synthesized in nature by the s - (solid line), r - (solid circles) and p -process (open squares). Figure taken from Ref. [15].

for protons), and have spherical symmetry in the ground state. As more nucleons are added to these spherical stable nuclei, the motion of excess nucleons can polarize the spherical core leading to a collective motion of nucleons and asymmetric or deformed mass distribution [16, 17]. The measure of deformation, denoted as β_2 , is related to the eccentricity of a deformed shape. The deformation parameter β_2 ranges from 0 to $\approx \pm 0.4$ for spherical to a well-deformed system. As the nucleus transitions from the spherical symmetry to the deformed shape and its excitation energy increases, the number of nuclear energy levels increases tremendously and eventually their wave functions overlap. At such high-excitation energies, the γ -decay properties are best described as average statistical nuclear properties *i.e.* the NLD and γ SF. The γ SF describe the average γ -ray transition probabilities for an electromagnetic de-excitation of the nucleus, whereas the NLD gives the average number of levels as a function of excitation energy.

Some enhancements in the γ SF, seen as resonances, are observed for deformed isotopes due to collective, correlated movements, which are not observed for the spherical nuclei. Of interest to this dissertation, are resonances observed below the neutron threshold S_n such as the Pygmy Dipole (PDR) and in particular the scissors resonance (SR). The strength of the SR has been shown to be correlated to nuclear deformation and the presence of SR on the γ SF has the potential to enhance the reaction rates which again enters into the nucleosynthesis calculations using astrophysical models.

NLDs and γ SFs are powerful tools for investigate structural properties of nuclei while at the same time providing input parameters into models to obtain capture cross section information relevant to nucleosynthesis. In this dissertation the versatility of the the NLD and γ SF is

highlighted by utilizing them to investigate the nucleosynthesis of ^{180}Ta and the SR of $^{154,155}\text{Sm}$. In sections 1.1 and 1.2 below the motivations and objectives for both cases is presented.

1.1 Physics motivation and objectives for $^{154,155}\text{Sm}$

The rare-earth isotopic chain of samarium provides an excellent opportunity for systematically investigating the evolution of nuclear-structure effects from the semi-magic and near spherical ($\beta_2=0.00$) ^{144}Sm isotope to the well-deformed system ^{154}Sm ($\beta_2=0.27$). The samarium isotopic chain is one of the few chains with several stable isotopes and therefore it is experimentally accessible at stable-beam facilities. As the nuclear shape changes, statistical properties such as the NLD and γSF may be affected. In particular, resonance modes, such as the $E1$ PDR, $M1$ SR and the recently confirmed Low-Energy Enhancement (LEE) may reveal interesting features when their evolution is investigated across several nuclei in an isotopic chain.

In recent years there has been a surge in experimental studies of the PDR states lying on the low-energy tail of the isovector giant dipole resonance. The PDR has been interpreted as an exotic mode of excitation due to the motion of a weakly bound neutron excess against an almost inert proton-neutron core [18]. The photo-absorption cross section of ^{154}Sm , deduced from inelastic proton scattering shows the surprising presence of two bumps with centroids at 5.9 MeV and 7.8 MeV [19, 20]. This resonance-like structure was assigned to the PDR in the deformed nucleus ^{154}Sm . Since this PDR shows the same energy ratio as the two peaks observed in the Giant Electric Dipole Resonance (GEDR), a tentative interpretation of this splitting could be connected to the splitting of the resonance structure with respect to their K quantum number. This interpretation would lead to a macroscopic picture of a deformed proton-neutron saturated core, oscillating against a neutron skin along two different axes. An experiment was performed at iThemba LABS and used the inelastic scattering of alpha particles to excite the PDR in ^{154}Sm and subsequently detect its γ -ray decay [21]. The most reliable knowledge can be obtained when results from several different experiments are compared. Additional measurements of the ^{154}Sm γSF at low energies are desirable, and will provide complementary information to the (p,p') and (α,α') data on resonance features that lie on the low-energy tail of the GEDR.

Since the initial discovery of the SR three decades ago many of its mysteries have been solved. The strength of this mode is proportional to the square of the ground-state deformation; hence even-even nuclei were initially considered to be the best candidates to exhibit well developed SR modes. However, it soon became apparent that this mode is also present in even-odd and odd-odd systems, although its intensity may be fragmented significantly enough to elude detection [22]. Recent work in the actinide region has uncovered that the SR exhibits a double bump structure, independent on the evenness or oddness of nucleonic numbers [23]. It is interesting to speculate that one of these structures might be due to the isovector spin scissors

mode which was only recently proposed [24]. However, such a splitting has not been reported for any of the rare-earth nuclei. The γ SF of the isotopes $^{148,149}\text{Sm}$ have already been measured and a weak structure was identified to be due to the SR [25]. With data already available on these weakly deformed $^{148,149}\text{Sm}$ isotopes, together with the recent measurements of $^{152,153}\text{Sm}$ [26] and $^{147,149,151,153}\text{Sm}$ [27, 28], it will be very beneficial to investigate the most deformed systems also. The study of ^{154}Sm and ^{155}Sm provide a near-complete picture on the evolution of the SR as the isotopic chain transitions from near spherical to very deformed. The main objectives are;

- (i) to perform an experiment where the silicon particle detectors and NaI(Tl) γ -ray array are utilized to measure particle- γ coincidence events from which the NLDs and γ SFs of $^{154,155}\text{Sm}$ are extracted below S_n using the Oslo Method [29].
- (ii) Investigate the resonances in the $^{154,155}\text{Sm}$ γ SFs and extract the integrated scissors resonance strength $B_{SR}(M1)$.

Furthermore, the $^{154,155}\text{Sm}$ NLDs and γ SFs are compared to those of neighboring samarium isotopes measured from different experiments and facilities.

1.2 Physics motivation and objectives for ^{180}Ta

As already mentioned above, most naturally occurring neutron-deficient nuclides are thought to be produced by the p -process. However, for ^{138}La and ^{180}Ta , for instance, the p -process is not sufficient to explain their observed solar abundances and additional processes are invoked, as shown in Fig. 1.3 in the case of ^{180}Ta . While the situation for ^{180}Ta is not clear, it was shown

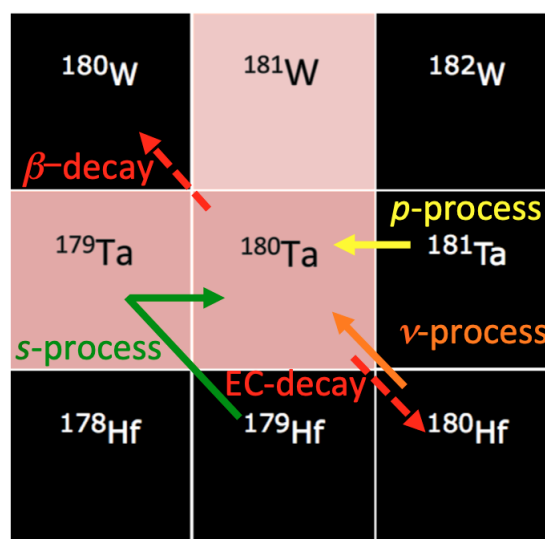


Figure 1.3. A schematic plot showing the several nucleosynthesis processes proposed to reproduce ^{180}Ta in nature.

by iThemba LABS researchers that for ^{138}La the p -process is not efficient enough, but that

neutrino (ν) captures during the p -process in Type-II supernovae may be responsible for its galactic enrichment [13, 30, 31]. A peculiar feature of ^{180}Ta in the solar system is that it is the rarest stable isotope in nature, with an isotopic abundance of only 0.012% and its abundance is based in a $J^\pi = 9^-$ isomeric state at an excitation energy $E_x = 77.2$ keV with a half-life of $\approx 10^{15}$ years. This odd-odd isotope is unstable in its ground state with a half-life of ≈ 8.15 hours and it decays by electron capture (EC) to ^{180}Hf or β^- emission to ^{180}W as illustrated in Fig. 1.4. The extreme long half-life of the $J^\pi = 9^-$ isomeric state is due to the intrinsic

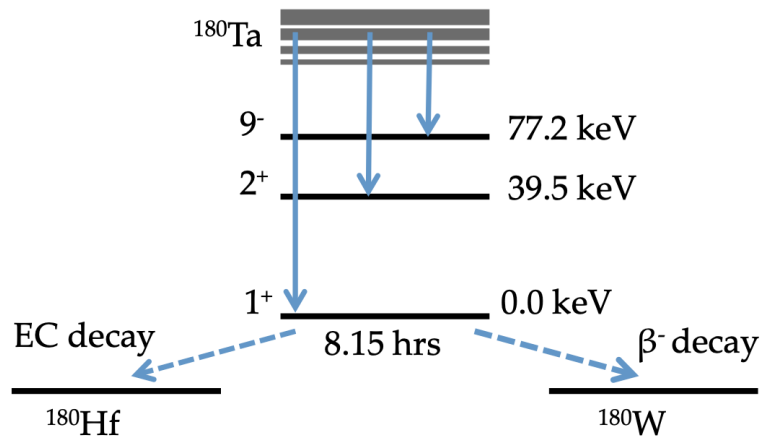


Figure 1.4. A schematic level scheme of ^{180}Ta showing the ground state decays to ^{180}Hf and ^{180}W by EC and β^- emission, respectively.

structure of the state [10] as a result of the alignment of the odd neutron in the $9/2[624]$ Nilsson orbital and the odd proton in the $9/2[514]$ orbital. Therefore, the decays from this state are hindered in addition to the K selection rules.

The production mechanism of ^{180}Ta in nature brings about controversy since calculations show that several processes, sometimes exclusively, can reproduce the observed ^{180}Ta abundance [10], making it a particularly interesting case to study. The s -, r - and p -processes in high-density, high-temperature environments, have all been proposed to explain the synthesis of ^{180}Ta . It has been theoretically shown that ^{180}Ta galactic enrichment could be exclusively explained by the p -process [30, 32, 33]. In explosive environments, neutrino captures and scattering reactions, which include $^{180}\text{Hf}(\nu_e, e)^{180}\text{Ta}$ and $^{181}\text{Ta}(\nu, \nu'n)^{180}\text{Ta}$, have also been proposed to significantly contribute to its synthesis [9, 10, 11, 30, 34]. Additionally, the s -process has been proposed to explain the production of ^{180}Ta , mostly via branching in ^{179}Hf through the reaction $^{179}\text{Hf}(\beta^-)^{179}\text{Ta}(n, \gamma)^{180}\text{Ta}$ and/or $^{179}\text{Hf}(n, \gamma)^{180}\text{Hf}^m(\beta^-)^{180}\text{Ta}$ [3, 4, 35].

Since the astrophysical sites for the nucleosynthesis of ^{180}Ta remain unknown, a combination of the above processes is undeniably possible. However, the significance of individual processes cannot be clearly determined, as a result of the uncertainties on the reaction rates for ^{180}Ta due to the unavailability of experimental data, *e.g.*, the radiative neutron capture rates of ^{179}Ta or other nuclear ingredients needed to constrain these rates, such as the NLD and γSF [13]. No

measurements of the NLD and γ SF data existed below the neutron separation energy (S_n) for ^{180}Ta and below $E_x < 5.8$ MeV for ^{181}Ta , until very recently when comprehensive measurements were performed for $^{180,181,182}\text{Ta}$ [36, 37, 38] led by iThemba LABS. In the absence of direct (n,γ) cross section measurements, both properties are critical for constraining the radiative neutron capture cross section within the Hauser-Feshbach formalism [39] which is implemented in the nuclear reaction code TALYS [40]. The objectives of the nucleosynthesis work are;

- (i) to investigate the NLDs and γ SFs of $^{180,181}\text{Ta}$ populated in inelastic scattering and neutron pick-up reactions, in addition to the $^{180,181,182}\text{Ta}$ work reported in Refs. [36, 37]. These data sets are normalized and constrained using various phenomenological and microscopic NLD models.
- (ii) The $^{180,181,182}\text{Ta}$ NLDs and γ SFs will be used as input to determine the $^{179,180,181}\text{Ta}(n,\gamma)$ cross sections using the nuclear reaction code TALYS [40].
- (iii) From the latter, the Maxwellian-averaged cross sections (MACS) and radiative neutron capture rates will be obtained, and used in stellar evolution calculations to investigate the role of the s -process nucleosynthesis of $^{180,181}\text{Ta}$ in low-mass AGB stars and the p -process nucleosynthesis of ^{180}Ta in Type-II supernova (SNII) model.

Chapter 2

Nuclear Structure and Nuclear Astrophysics theory

"I am going to give what I will call an elementary demonstration. But elementary does not mean easy to understand. Elementary means that very little is required to know ahead of time in order to understand it, except to have an infinite amount of intelligence."

— **Richard Feynman**, *Feynman's lost lecture*

In this chapter a short review of the nuclear structure models and nuclear astrophysics theory that form the basis for this dissertation is given. Especially the NLD and γ SF models and the neutron capture cross-section will be covered.

2.1 Nuclear Level Density

In the following subsections, the phenomenological models such as the Fermi-Gas and Constant Temperature models which give an analytic expression of the NLD are described. In addition, the global microscopic model, the Hartree-Fock-Bogoliubov plus combinatorial model, which allows for prediction of the properties of all nuclei and for more reliable and accurate extrapolations away from valley of stability to the drip lines is discussed.

2.1.1 The Fermi-Gas Model

The Fermi-gas model (FG) initially proposed by H. Bethe in 1936 [41] describes the nucleus as a gas of free non-interacting fermions distributed independently in single particle orbits with equal energy spacings. The initial level density formula of Bethe [41], $\rho(E) \sim \exp(2\sqrt{aE})$, could not fit simultaneously the known discrete lower-lying levels and the neutron (or proton) resonances

at higher-excitation energy. Therefore, the original formulation has been modified several times to describe the nuclear level density, for a given angular momentum number J and for both parities, as a function of the intrinsic excitation energy U , as follows [42]:

$$\rho(U, J) = \frac{\sqrt{\pi} \exp[2\sqrt{aU}] (2J + 1) \exp[-(J + 1/2)^2/2\sigma^2]}{12 \frac{1}{a^{1/4}} U^{5/4} 2\sqrt{2\pi}\sigma^3} [MeV^{-1}]. \quad (2.1)$$

The observable nuclear level density for all spins and parities is given by:

$$\rho(U) = \frac{\sqrt{\pi} \exp[2\sqrt{aU}]}{12 \frac{1}{a^{1/4}} U^{5/4} \sqrt{2\pi}\sigma}, \quad (2.2)$$

where a is the level density parameter which is adjustable to allow for fitting to available experimental data. The intrinsic excitation energy $U = E_x - \Delta$, where the pairing energy $\Delta = n \frac{12}{\sqrt{A}} + \delta$ with $n = -1, 0, 1$ for odd-odd, even-odd and even-even nuclei, respectively. Δ is closely correlated to the neutron and proton pairing energies in order to account for even-odd effects in nuclei.

For the odd-odd nuclei the pairing energy is negative and therefore the correction parameter δ is used to account for this effect by fitting to available experimental data for each nucleus [43]. Eq. 2.2 reproduces well the available experimental data. A variation of Eq. 2.2, termed the Back-Shifted Fermi-Gas (BSFG) model exist, in which the intrinsic excitation energy $U = E_x - E_1$. In the case where the shift Δ becomes too large, it is "back-shifted" by subtracting the free parameter E_1 . With limited theoretical and experimental [44, 45, 46] information available, the spin-dependence parameter, σ , usually known as the spin cut-off parameter is given by [42]:

$$\sigma^2 = 0.0888 \sqrt{a(E_x - E_1)} A^{2/3}, \quad (2.3)$$

where E_1 is the free adjustable parameter and A is the mass number. For many nuclei, the free parameter E_1 is determined by fitting to experimental data. More recent and generally preferred energy- and mass-dependent spin cut-off parameter formulations have been proposed and given by von Egidy and Bucurescu [47, 48]:

$$\sigma^2 = 0.391 A^{0.675} (E_x - 0.5Pa')^{0.312}, \quad (2.4)$$

and assuming the rigid moment of inertia¹:

$$\sigma^2 = \Theta_{rigid} T = 0.0146 A^{5/3} \frac{1 + \sqrt{1 + 4a(E_x - E_1)}}{2a}, \quad (2.5)$$

where Pa' is the deuteron pairing energy. In order to determine the total level density at the neutron separation energy $\rho(S_n)$, knowledge of the spin or angular momentum distribution of the level density at S_n is crucial. With the assumption that both parities are distributed equally,

¹Here it is assumed that the rigid moment of inertia Θ is directly related to the excitation energy E_x , following the procedure described in [49] and initially proposed by Ericson [50].

the spin distribution at S_n can be defined as [42, 50]:

$$g(E_x = S_n, J) \simeq \frac{2J + 1}{2\sigma^2(E_x)} \exp \left[-\frac{(J + 1/2)^2}{2\sigma^2(E_x)} \right], \quad (2.6)$$

where J is the spin of the ground state of the target nucleus and $g(E_x, J)$ is normalized to unity. The main source of uncertainties in estimating the total NLD comes from σ assuming the spin distribution of Eq. 2.6. In addition by following the approach of [49, 51], the energy-dependent spin cut-off parameter can be determined by a fit which goes through only two anchor points σ_{disc}^2 and $\sigma_{S_n}^2$, as follows:

$$\sigma^2(E_x) = \sigma_{disc}^2 + \frac{E_x - E_{disc}}{S_n - E_{disc}} [\sigma_{S_n}^2 - \sigma_{disc}^2], \quad \text{for } E_{disc} \leq E \leq S_n, \quad (2.7)$$

where σ_{disc}^2 is the first point determined by fitting Eq. 2.6 to reliable spins at the known discrete lower-lying levels at excitation energy $E_x = E_{disc}$, and E_{disc} is the average excitation energy at the discrete states. At high excitation energy, $\sigma_{S_n}^2$ is estimated from the rigid moment of inertia, see Eq. 2.5.

2.1.2 Constant Temperature Model

In 1965, Gilbert and Cameron [42] noticed that the level density below the neutron threshold, particularly in the energy region $2\Delta_0 \lesssim E_x \lesssim 10$ MeV can be described by the Constant Temperature model (CT), initially proposed by Ericson in 1959 [50],

$$\rho(E_x) = \frac{1}{T_{CT}} \exp \frac{E_x - E_0}{T_{CT}}, \quad (2.8)$$

where the free parameter T_{CT} is the constant nuclear temperature related to the slope of $\rho(E_x)$ and E_0 is the constant temperature shift parameter. The pair-gap parameter Δ_0 represents the excitation energy at which the first nucleon pair breaking occurs² [43]. As outlined in Ref. [42], these parameters can systematically be determined from their dependence on the nuclear properties such as the nuclear mass A , even-odd shell effects, shell structure and deformation effects.

2.1.3 Constant Temperature Model + Fermi-Gas Model

Since the Constant Temperature model [50] gives a good fit to the experimental data below ≈ 10 MeV and at higher energies the Fermi-Gas model [42] fits well the proton/neutron resonance

²The pair-gap parameter $\Delta_0 = 12A^{-1/2}$ in units of MeV is the first-order pairing phase transition.

data, the total nuclear level density can be described as follows [51]:

$$\begin{aligned}\rho^{tot}(E_x) &= \rho_{CT}^{tot}(E_x), & \text{if } E_x \leq E_M, \\ &= \rho_{FG}^{tot}(E_x), & \text{if } E_x \geq E_M,\end{aligned}\tag{2.9}$$

where E_M is the matching excitation energy between the two models. The spin distribution of the Fermi-gas model in Eq. 2.6 is also applied in the constant temperature region.

2.1.4 Hartree-Fock-Bogoliubov plus Combinatorial Model

The global microscopic description of the level density, the Hartree-Fock-Bogoliubov plus combinatorial Model (HFB+comb), describes the spin-, parity- and energy-dependent description of the NLD [52, 53]. This combinatorial approach compete with phenomenological models in the reproduction of the experimental data not only by describing the statistical NLD at high excitation energies but also could explain the non-statistical (discrete) behavior of the excited states at very low excitation energy. The incoherent intrinsic particle-hole $p - h$ state densities, $\rho_{ph}(E_x, M, \pi)$, are constructed using the single-particle level scheme extracted from the HFB model, where M is the spin projection on the intrinsic symmetry axis of the nucleus. The collective rotational and vibrational excitations are accounted for once the incoherent particle-hole $p - h$ state densities have been determined, in addition to the shell effects, pairing correlations and deformation effects for the prediction of the ground state properties [53].

The nuclear level density, $\rho(E_x)$, is estimated from known basic nuclear structure properties such as: single-particle levels scheme energies ε_i^k , pairing strength δ_i^k of each level, quadrupole deformation β_2 , and deformation energy E_{def} [53, 54]. These parameters are derived consistently from the HFB calculations based on the effective nucleon-nucleon interaction of the deformed Skyrme-HFB framework [53]. This framework is characterized by pairing interactions taking into account not only the nuclear binding energy but also the even-odd mass effects. The above interaction is of primary importance and must be properly considered, for more reliable and accurate prediction of the $\rho(E_x)$. The microscopic approach is known to give a reasonable agreement with the experimental data, specifically with data extracted from charged particle reactions, at known discrete states (cumulative number of low-lying energy levels) at low excitation energies and accurately predicts the experimental s - and p -wave neutron resonance spacings D_{exp} at S_n [54] as shown in Figs. 2.1 and 2.2. The microscopical level densities ρ_{HFB} shown in Fig. 2.1 must be re-normalized to available experimental data through a scaling function as follows [53]:

$$\rho(E_x) = \exp(C_{\text{HFB}}\sqrt{E_x - \delta_{\text{HFB}}}) \times \rho_{\text{HFB}}(E_x - \delta_{\text{HFB}}, J, \pi),\tag{2.10}$$

where the pairing shift δ_{HFB} gives the level density from the tables at a different excitation energy

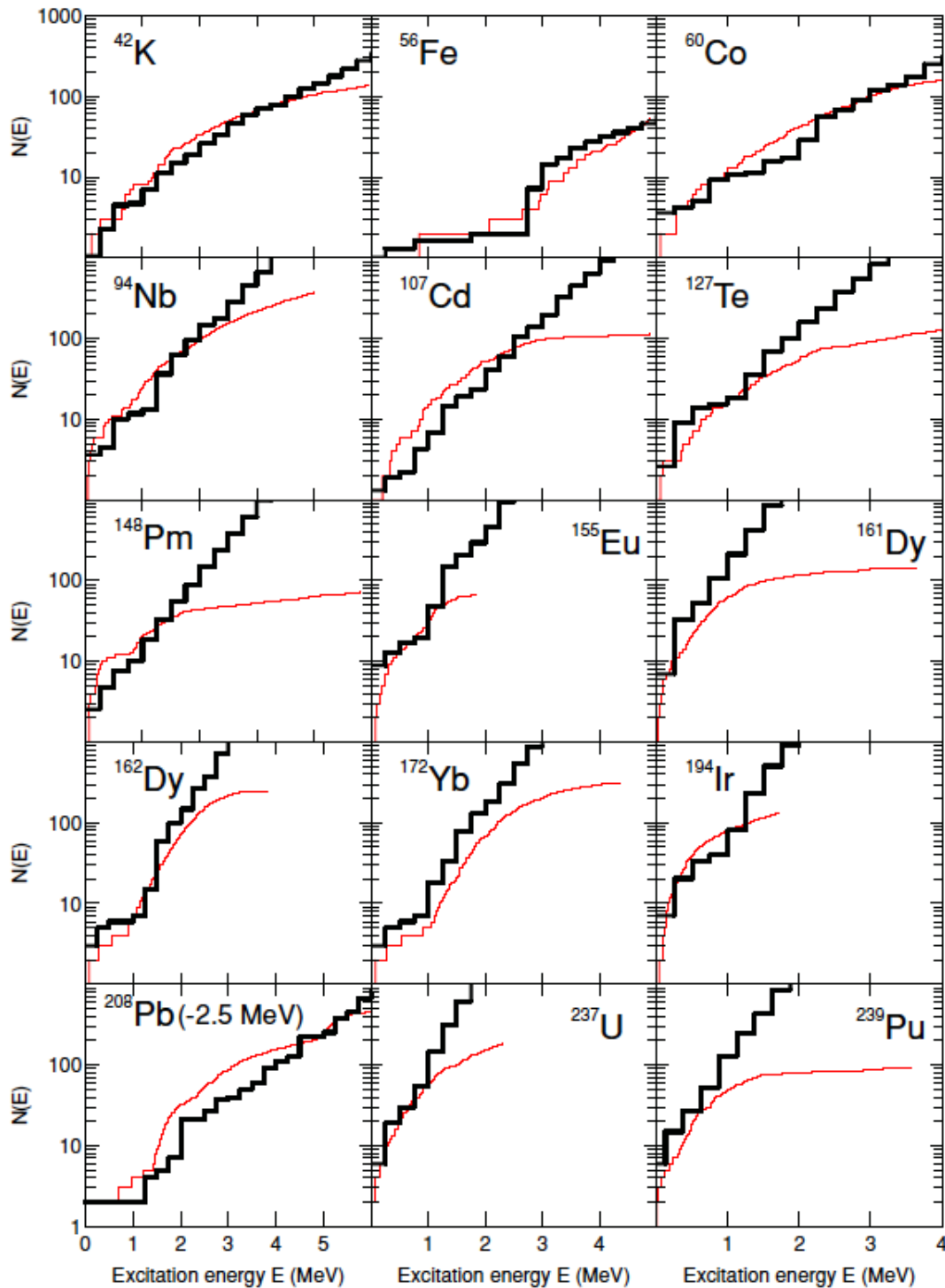


Figure 2.1. Comparison of the cumulative number of known levels (black staircase) with the HFB + combinatorial calculations (red curve) as a function of E_x , for light to heavy mass, spherical and deformed nuclei [53].

and the constant parameter C_{HFB} plays a similar role to that of the level density parameter α discussed³ in sec. 2.1.1. In the case where both the experimental s -wave neutron spacing D_0 and the discrete levels exist, Eq. 2.10 has been used to fit 289 nuclides [53] and the corresponding δ_{HFB} and C_{HFB} values for these nuclei are tabulated in Ref. [53]. The level densities for more

³The unaltered ρ_{HFB} values from the tables have default values $\delta_{\text{HFB}}=0$ and $C_{\text{HFB}}=0$.

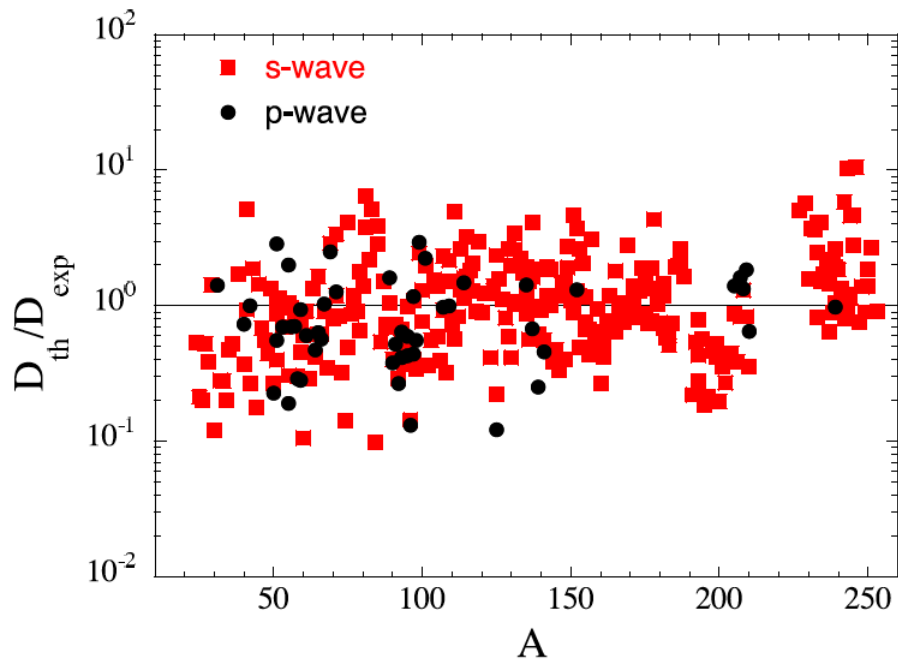


Figure 2.2. Ratio of HFB + combinatorial (D_{th}) with the experimental (D_{exp}) s - and p -wave neutron resonance spacings [53]. Globally, the ratio D_{exp}/D_{th} are predicted within a factor of 2.

than 8500 nuclei calculated for excitation energies up to $E_x \approx 200$ MeV and spin values up to $J = 49$, are made available in tabular form in the TALYS [40, 55] software package. In this work, the HFB + combinatorial NLD is used to calculate the neutron capture cross-sections within the Hauser-Feshbach statistical framework [39] as implemented in the TALYS reaction code [40, 55]. In Fig. 2.3, the procedure is shown for the $^{89}\text{Y}(n,\gamma)^{90}\text{Y}$ case. An improvement on the cross-section can be seen when the re-normalization procedure is applied to the cumulative number of known levels [53].

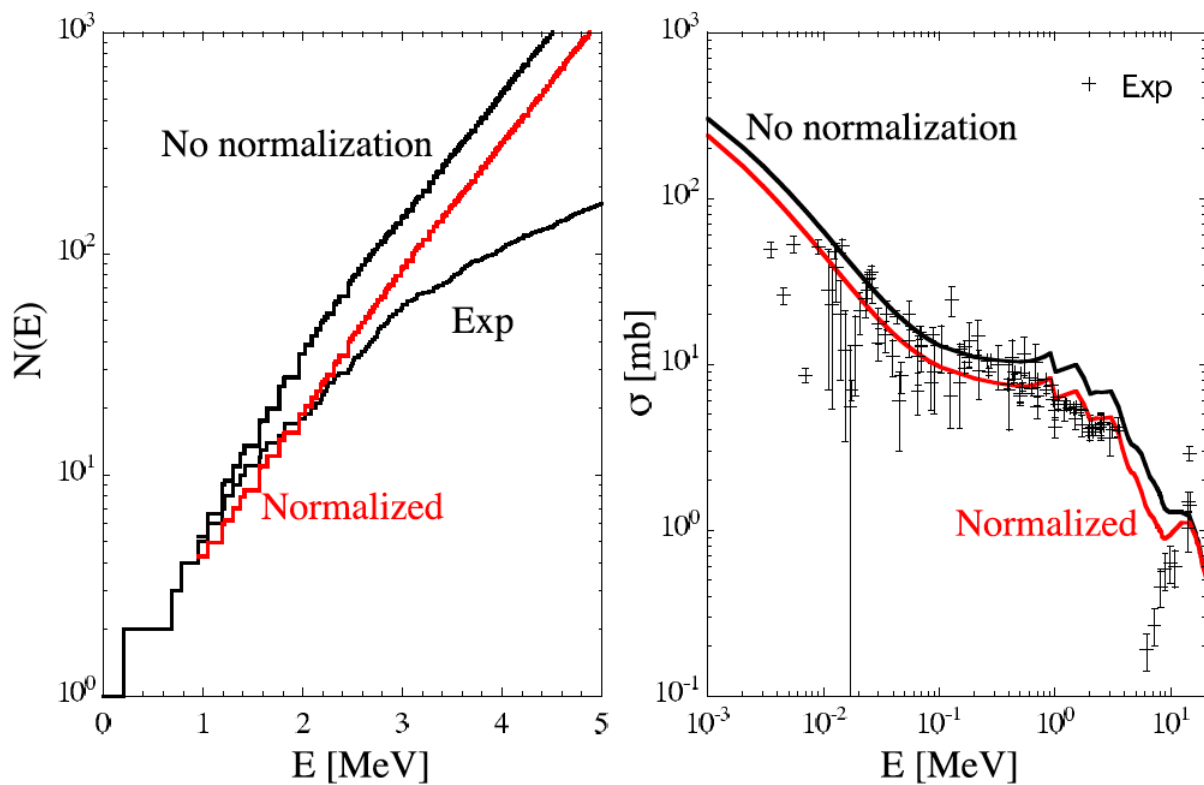


Figure 2.3. Comparison of the cumulative number of known levels with the HFB + combinatorial calculations, ρ_{HFB} , as a function of E_x for ^{90}Y with and without the normalization (left panel). The $^{89}\text{Y}(n,\gamma)^{90}\text{Y}$ cross-sections obtained with and without the normalized NLD as compared to the experimental data (right panel). Figure from Ref. [53].

2.2 γ -ray Strength Function

The γ -ray strength function, $f_{XL}(E_\gamma)$, is a measure of the average electromagnetic property of excited nuclei. At high excitation energy, the distribution of the average reduced radiative width, as a function of γ -ray energy, for transitions with multipolarity XL can be described by the γ -ray strength function (γ SF). The original description of a model-independent γ SF, following Eq. 1.1 and 2.2 in Bartholomew *et al.* [56], is given by:

$$f_{XL}(E_\gamma) = \frac{\langle \Gamma_\gamma^{XL}(E_i, E_\gamma, J^\pi) \rangle}{D(E_i, E_\gamma, \pi) E_\gamma^{(2L+1)}} = \frac{\langle \Gamma_\gamma^{XL}(E_i, E_\gamma, J^\pi) \rangle}{E_\gamma^{(2L+1)}} \rho(E_i, E_\gamma, \pi), \quad (2.11)$$

where the average level spacing $D(E_i, E_\gamma, \pi)$ of the initial states J^π in bin E_i is related to $\rho(E_i, E_\gamma, \pi) = 1/D(E_i, E_\gamma, \pi)$. The parameter $\langle \Gamma_\gamma^{XL}(E_i, E_\gamma, J^\pi) \rangle$ is the average partial radiative width of a distribution of states J^π within an excitation energy bin E_i for a given γ -ray transition energy E_γ . X denotes the electromagnetic character of the emitted γ -radiation (X is either electric, E , or magnetic, M), and L represents the given angular momentum ($L=1,2,3,\dots$ characterizing dipole, quadrupole, octupole, etc). The electromagnetic decays follow strict angular momentum and parity selection rules (see Ref. [57] for details).

The γ SF describes both the 1) γ -decay from the initial higher-lying excited states to a range of final lower-energy states, as the downward strength $\overrightarrow{f}_{if}^J{}_{XL}(E_\gamma)$, as given in Eq. 2.11, and 2) the photo-excitation from the initial low-energy or ground state to a range of higher-lying final levels, as the upward strength $\overleftarrow{f}_{if}^J{}_{XL}(E_\gamma)$, given by [58]:

$$\overleftarrow{f}_{if}^J{}_{XL}(E_\gamma) = \frac{1}{(2L+1)(\pi hc)^2} \frac{\langle \sigma_{XL}(E_\gamma) \rangle}{E_\gamma^{2L-1}}, \quad (2.12)$$

where $\langle \sigma_{XL}(E_\gamma) \rangle$ represents the average photo-absorption cross-section which is summed over all accessible spins of the final states. The above processes are illustrated in Fig. 2.4. It should

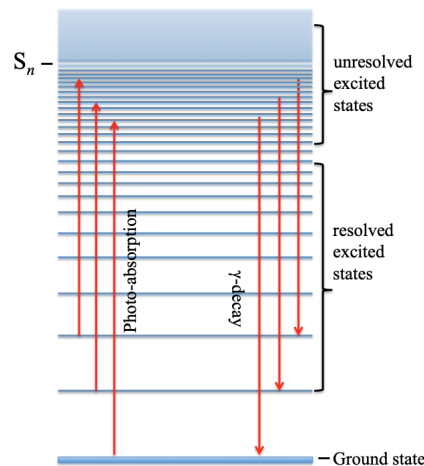


Figure 2.4. The γ -decay and photo-absorption processes.

be noted that both γ -decay and photo-absorption processes are correlated with each other assuming that the Fermi's golden rule [59] and the principle of detailed balance holds [60] and that states are equally populated irrespective of the population mechanism *i.e.* from below or above. The downward γ SF, $\vec{f}_{ifXL}^J(E_\gamma)$, is also related to the γ -ray transmission coefficient $T_{\gamma XL}(\gamma)$ as follows:

$$T_{\gamma XL}(E_\gamma) = 2\pi E_\gamma^{2L+1} \vec{f}_{ifXL}^J(E_\gamma), \quad (2.13)$$

which plays an important role in Hauser-Feshbach [39] calculations for radiative neutron capture reaction rates. The total γ -ray transmission coefficient (discussed in the coming sections) for capture reactions is dominated by $E1$ [13] and so far most information on the γ SF is from the photo-absorption measurements [58] at higher energies to around S_n . In addition to the photo-absorption measurements, the γ SF has been extracted below and around S_n from several experimental techniques including the Nuclear Resonance Fluorescence (NRF) [61], the Two-Step Cascade (TSC) [62], the Ratio method [63], the Average Resonance Capture (ARC) [64] and the Oslo method [29]. The Oslo method extracts the γ SF and NLD simultaneously from the charged particle- γ coincidence events below the S_n . More details on different techniques and calculation of the γ SF are given in Refs. [58, 65].

It has proven quite challenging, if not impossible, to measure directly and/or indirectly the γ SF for very neutron- and/or proton-rich nuclei due to unavailability of targets. Information on the γ SF on nuclei far away from stability is crucial for nucleon-capture processes of astrophysical importance, in particular the r -process [12]. Therefore, in order to describe the γ SF, phenomenological models such as the standard [66, 67] and generalized [68, 69] Lorentzian models have been developed. In addition, microscopic descriptions [18] such as the shell-model calculation [70, 71, 72] and Quasi-Particle Random Phase Approximation (QPRA) [73, 74] have been introduced, for more reliable extrapolations of the γ SF throughout the nuclear chart. The above theoretical models have shed light on the origin of observed $E1$ and/or $M1$ resonances in the γ SF. In the next subsection, we explore these resonances.

2.2.1 Resonances in the γ -ray strength function

The γ SF is dominated by resonances such as the Low-Energy Enhancement (LEE) sometimes called the "up-bend", the Pygmy Dipole Resonance (PDR), Scissors Resonance (SR) and at higher γ -ray energies the well-known Giant Electric Dipole Resonances (GEDR), as illustrated in Fig. 2.5. The LEE, PDR and GEDR are briefly explained but only the SR which is of relevance to this work is explained in more details. The GEDR is located at typical excitation energies of about $\approx 8 - 22$ MeV with a typical width of $\approx 2 - 7$ MeV depending on nuclear mass A and has been observed in the γ SF of all nuclei studied [58, 75, 76] throughout the nuclear chart. The GEDR arises from the isovector, $\Delta T = 1$, collective vibration mode in which protons

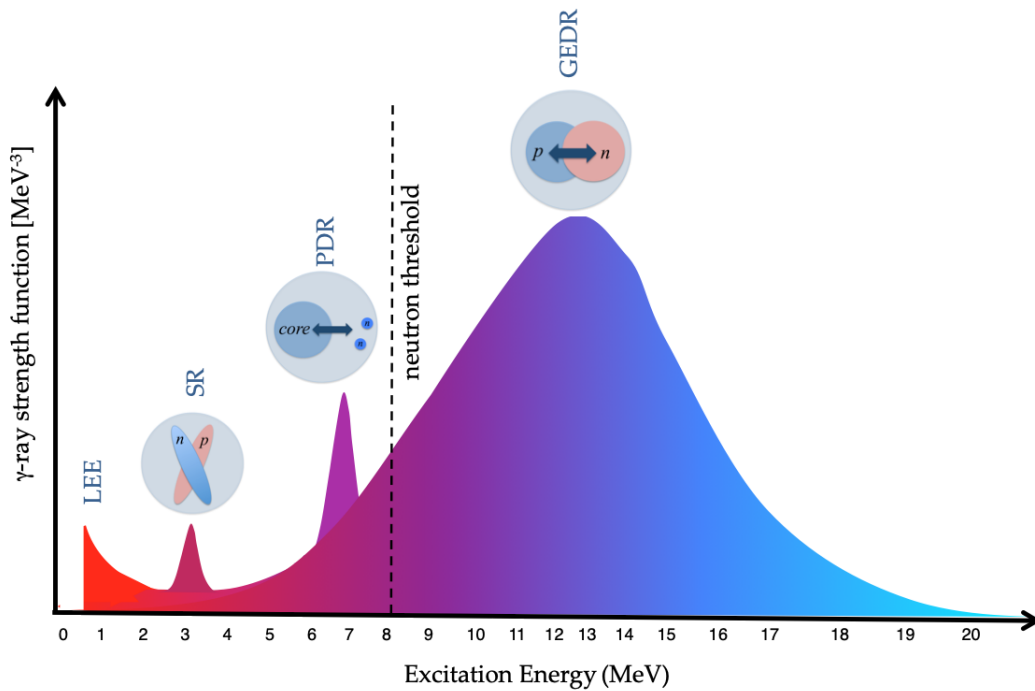


Figure 2.5. Resonances observed in the total γ -ray strength function.

oscillate off-phase against neutrons inside the nucleus. Other giant resonances, namely the giant magnetic dipole resonance has been experimentally observed and is due to the spin flip collective excitations between $\ell = 1/2$ subshells [77].

2.2.2 E1 pygmy resonance

Apart from the GEDR, there are several experimentally observed resonance-like structures located energetically below the GEDR and are lower in magnitude. In nuclei with an excess number of neutrons, an "anomaly" as pointed out in Bartholomew *et al.* [56] (and references therein.) and now called the pygmy dipole resonance has been observed at energies around S_n . Macroscopically the PDR is described as the collective vibration mode of excess neutrons against an ($T = 0$) isospin symmetric neutron-proton core (see Fig. 2.5 for illustrated). A recent full review on the experimental evidence and theoretical description of the PDR is given in Refs. [18] and [78], respectively. Fig. 2.6 shows the enhancement in the γ SFs of stable Sn isotopes extracted from transfer reaction/ion scattering experiments, which is explained as the PDR at energies around S_n . In addition to the Oslo-type experimental measurements, the PDR can be experimentally studied from proton and alpha scattering experiments using high-resolution magnetic spectrometer such as the K600 at iThemba LABS [80] or Grand Raiden at RCNP [81]. Microscopically, the PDR is believed to be caused by single- or collective-particle $E1$ transitions around S_n . The PDR is located in the proximity of energies which are important in the calculations of astrophysical reaction rates [82] and in general the electric dipole ($E1$)

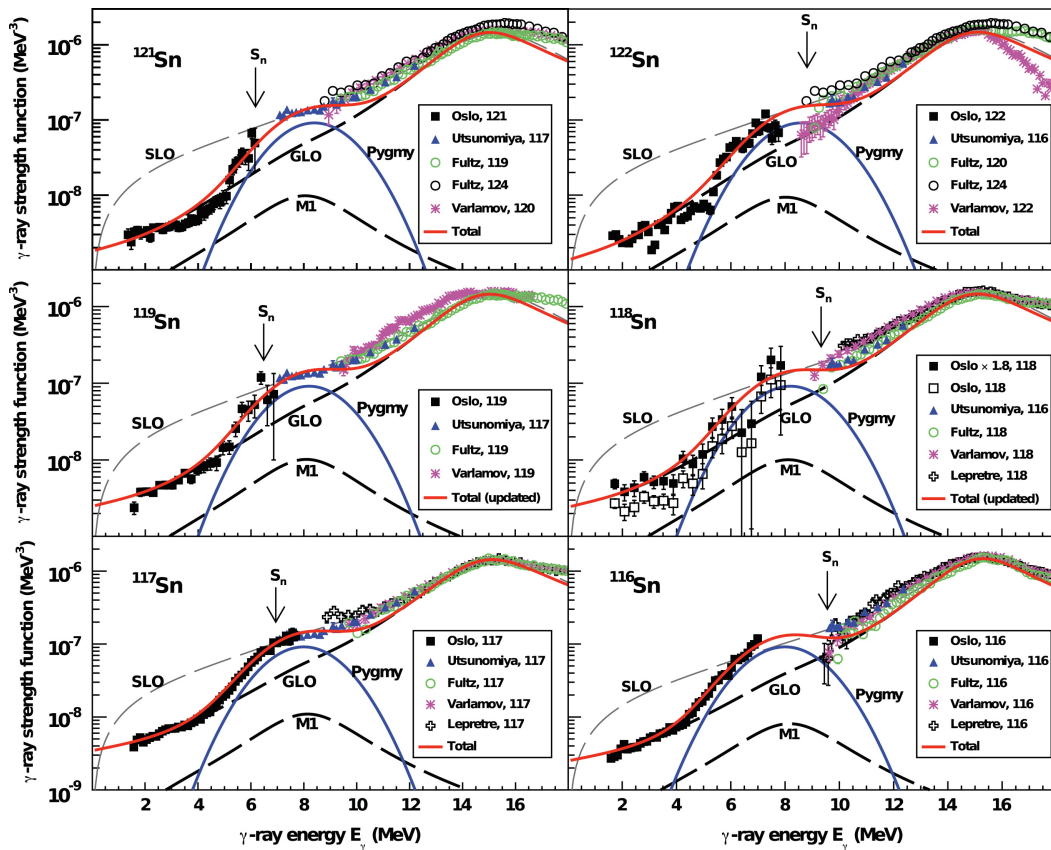


Figure 2.6. Comparison of OCL experimental data to the other experimental data showing an enhancement at around S_n in the γ SF of $^{116-119,121,122}\text{Sn}$ isotopes. The different colored lines show the total predicted γ SF and respective resonances. Figure taken from [79].

nature of the PDR has been pointed out to be connected to the neutron-skin thickness, hence is directly related to the isovector parameter which enters the nuclear matter equation of state [18].

2.2.3 M1 scissors resonance

The low-energy collective mode was first predicted in 1978 by Lo Iudice and Palumbo [83] before it was observed experimentally in 1984 [84]. On a macroscopic level, the collective magnetic dipole ($M1$) mode is described by the two-rotor model (TRM) [83] as a collective excitation mode in which the neutron and proton deformed density distributions can oscillate against each other out of phase (isovector) like the blade of a scissor or in phase (isoscalar). In Fig. 2.7 (a) the macroscopic description of the SR is illustrated. In order to estimate the excitation energies and the resonance strength $B(M1)$, the geometrical TRM considered the symmetry energy, from the liquid drop mass formula [85], which is related to non-symmetrical motion of nucleons. The formulation for these excitation energies (which include the mass parameter, a restoring force strength and pairing correlations of protons and neutrons participating in scissors motion) was adjusted to the observed experimental low-lying $B(E2)$ values and estimated higher but

reasonable values of $B(M1)$.

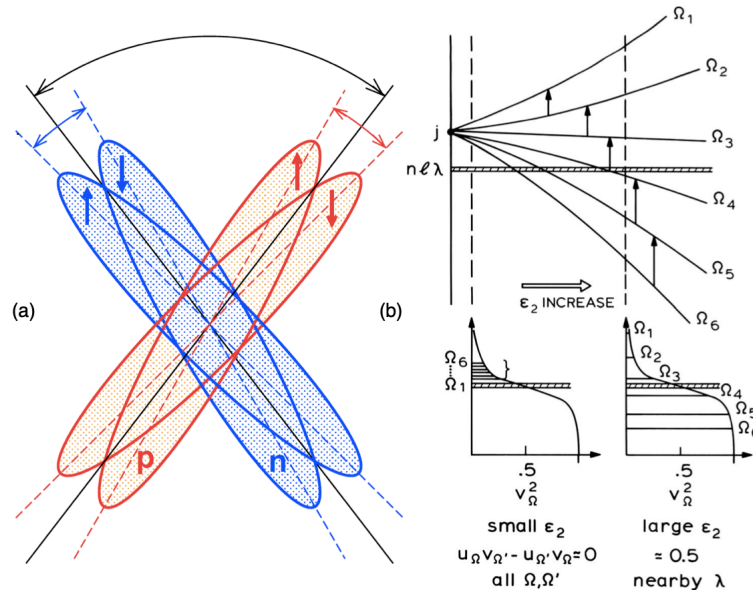


Figure 2.7. A schematic representation of the $M1$ scissors resonance. The macroscopic (a) description showing the orbital (neutrons against proton clouds) and spin scissors (spin-up nucleons against spin-down nucleons) mode [24]. The microscopic (b) description illustrates the transitions for high- j orbitals Ω and the effect of deformation ε [22].

A different approach, the Interacting Boson Model-2 (IBM-2), was introduced by Iachello [86], in which the interacting fermion nuclear system is treated algebraically, where two-neutrons and two-protons pairs are regarded as bosons. Within the IBM-2 the magnetic dipole operator for the fermion system m^F and boson system m^B are given as [22]:

$$m^F(M1) = \sqrt{\frac{3}{4\pi}} \sum_i [g_\ell(i)\hat{\ell}_i + g_s(i)\hat{s}_i] \mu_N, \quad (2.14)$$

and

$$m^B(M1) = \sqrt{\frac{3}{4\pi}} \sum_i (g_\pi \hat{L}_\pi + g_\nu \hat{L}_\nu) \mu_N, \quad (2.15)$$

where g_ℓ and g_s are the fermion orbital and spin g factors, and g_π and g_ν are the respective proton and neutron g factors. The quantities $\hat{\ell}$ and \hat{s} are the fermion orbital angular momentum and spin operators, while \hat{L}_π and \hat{L}_ν are the respective orbital angular momentum operators of the proton and neutron boson system. The parameter $\mu_N = e\hbar/2m_p c$ is the nuclear magneton. It is clear from Eq. 2.14 that for the fermion system, the $M1$ operator is a function of the spin and orbital component, whereas for the boson system in 2.15 neutrons and protons act as two separate, rotating, density distributions.

On the microscopic approach, Chen and Leander [87] expanded the idea of the two-particle rotor model which leads to strong $M1$ transitions within the high- j orbitals in deformed nuclei.

The single particle states in a spherical nucleus are given by the multiplicity $(2j+1)$, where $j = \ell + s$ is the total angular momentum, with s and ℓ being the spin and orbital angular momentum number. For the deformed system, the nuclear energy levels can be explained by the four quantum numbers $[N, j, \ell, \Omega]$, where Ω is projection of the single-particle angular momentum j along the nuclear symmetry axis as demonstrated in Fig. 2.7 (b). Due to reflection symmetry, $\Omega+$ and $\Omega-$ will have the same energy leading to a level degeneracy of $2(2j+1)$. The principal quantum number N of the major shell defines the number of oscillator quanta ($1\hbar\omega, 2\hbar\omega, \dots$) and also denotes the parity of the shell. The strong $M1$ transitions within the high- j orbitals in deformed nuclei have transition energies which corresponds to twice the pairing energy $2\Delta \approx 2-3$ MeV. These transitions may contribute to the observed enhancement in the γ SF at $\approx 2-3$ MeV γ -ray energies, known as the SR. The orbital component of Eq. 2.14 has been shown to be related to collective nuclear properties [88]. As shown in Fig. 2.7 (b), the increase in deformation leads to the splitting of j therefore giving rise to the orbital part of the $M1$ transitions. The spin component of Eq. 2.14 arise from single particle nuclear excitations as a result of transitions between separated j shells of type $j = \ell + \frac{1}{2} \rightarrow j = \ell - \frac{1}{2}$ due to the spin-orbit interaction. And therefore gives an enhancement in the γ SF termed the giant $M1$ or spin-flip resonance, which is located at excitation energies of $\approx 6-8$ MeV. A schematic representation of the magnetic dipole strength discussed above is shown in Fig. 2.8 for heavy deformed nuclei and detailed discussion of the $M1$ excitation in nuclei are given in Ref. [22].

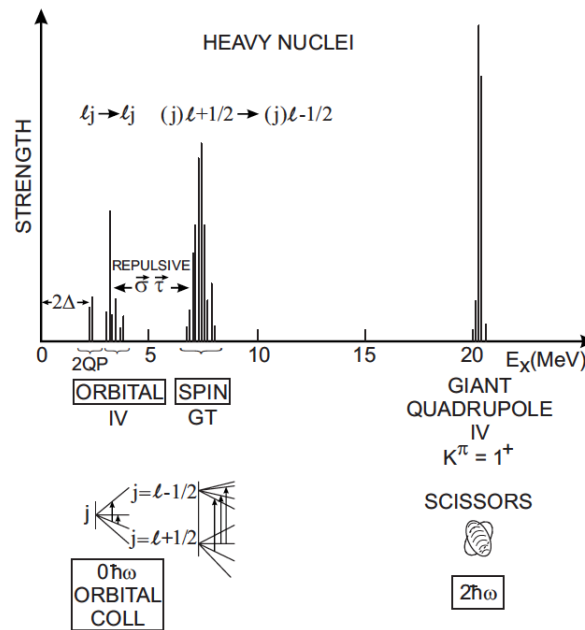


Figure 2.8. A schematic representation of the $M1$ strength distribution in heavy deformed even-even nuclei [88].

In 1984 for the very first time, the experimental evidence from high-resolution inelastic electron scattering measurements on deformed rare-earth nuclei [84] and from charged-particle reactions

[89] has shown that there exist a lower-lying dipole resonance just below the E1 pygmy resonance with a centroid around ≈ 3 MeV. Since then, many heavy deformed even-even and odd-mass nuclei in the rare-earth region have systematically been investigated. Up to present, the SR mode has been experimentally observed in vibrational and rotational nuclei, as well as in γ -soft nuclei and furthermore the SR has been verified in the actinide mass region [84, 88]. A range of different experimental techniques including inelastic electron scattering [61], nuclear resonance fluorescence [61], resonance neutron capture [90], and the Oslo Method [29] which extracts information from ion scattering or transfer reactions, have been used to investigate the low-energy magnetic dipole resonance. In Fig. 2.9 (a), a comparison of different experimental probes for ^{156}Gd is shown, where the presence of excited $J^\pi = 1^+$ states in $^{156}\text{Gd}(e,e')$ and $^{156}\text{Gd}(\gamma,\gamma')$ reactions further hinted that the SR mode is populated through the orbital part of the $M1$ operator as given in Eq. 2.14. Although the Oslo method [29] analytical technique can not reveal fine structures in the γ -spectra, a pronounced peak is observed at $E_\gamma \approx 2 \pm 0.2$ MeV in Fig. 2.9 (b) and is believed to be due to $M1$ transitions between high- j orbitals [89].

Following the groundbreaking measurements above, several systematic studies have been performed for even-even rare-earth nuclei from NRF experiments [91]. The $M1$ SR has been pointed out to be stronger in deformed even-even rare-earth region than odd-mass nuclei [92], and as already established by Ziegler *et al.* [93] this is correlated to nuclear deformation through the

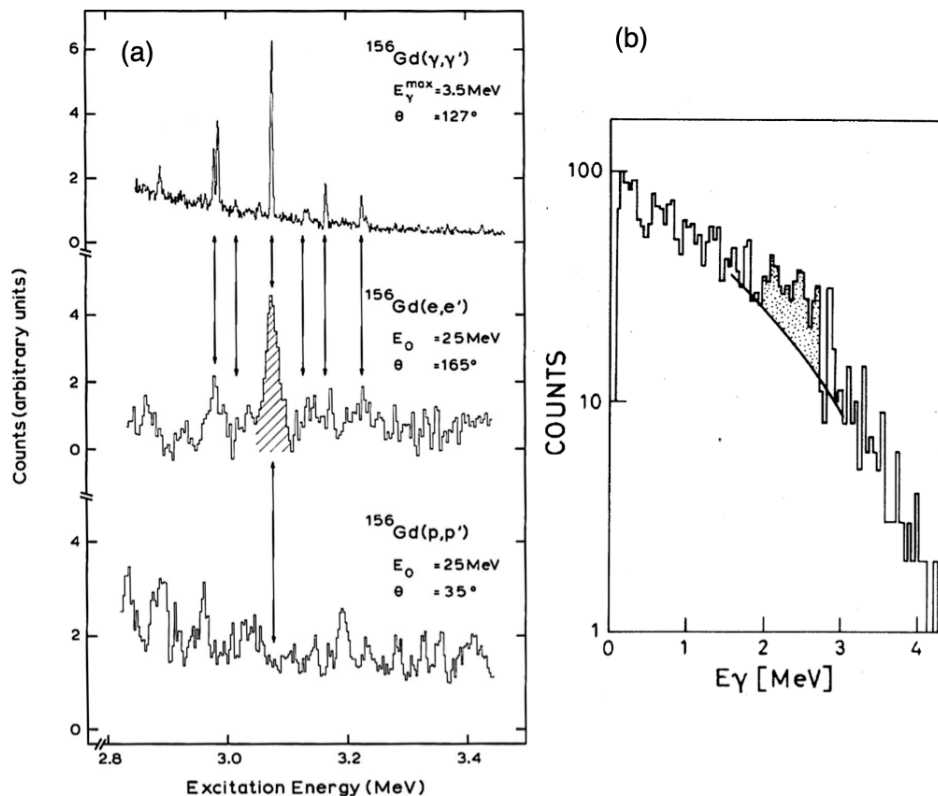


Figure 2.9. The very first experimental evidence of the low-lying magnetic dipole resonance from the work of Richter *et al.* [88] on ^{156}Gd (a) and Guttormsen *et al.* [89] on ^{161}Dy (b).

so-called " δ^2 law". According to " δ^2 law", the measured orbital $M1$ strength increases linearly with deformation parameter squared, thus [22]:

$$\sum_f B_{exp}(M1) \uparrow \sim B(E2; 0_1^+ \rightarrow 2_1^+) \sim \delta^2, \quad (2.16)$$

where $\delta \approx \epsilon_2 \approx 3/4 \cdot \sqrt{5/\pi} \cdot \beta_2$ is the quadrupole deformation of the nuclear ground state, approximated to first order. The axial deformation parameter β_2 is taken from Raman *et al.* [94] as compiled in Ref. [58]. Fig. 2.10 shows the total $M1$ strength, known as the reduced transition strength $\sum B(M1)_{exp}$ and $B(E2; 0_1^+ \rightarrow 2_1^+)$, plotted against mass number A from NRF measurements. The strength of orbital $M1$ scissors mode for the measurements in Fig.

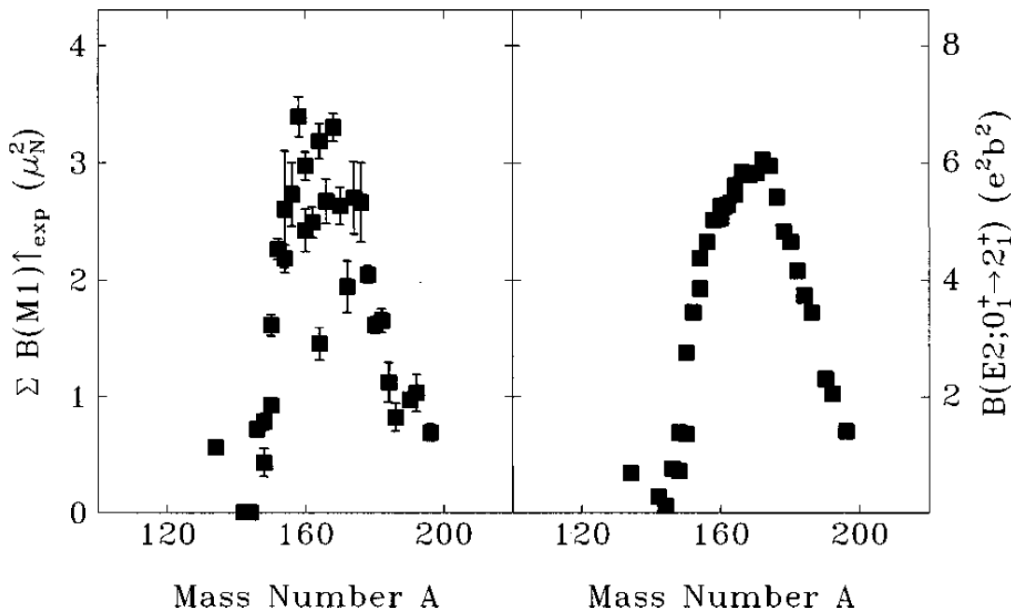


Figure 2.10. The total low-lying $M1$ and $E2$ strengths deduced from experiments for ^{134}Ba , $^{144-150}\text{Nd}$, $^{148-154}\text{Sm}$, $^{156-160}\text{Gd}$, $^{160-164}\text{Dy}$, $^{164-170}\text{Er}$, $^{172-176}\text{Yb}$, $^{178-180}\text{Hf}$, $^{182-186}\text{W}$, $^{190-192}\text{Os}$ and ^{196}Pt isotopes [91].

2.10 is localized at mean excitation energies of about $E_x = 66 \cdot \delta \cdot A^{-1/3} \approx 2 - 3$ MeV for most rare-earth nuclei [95]. Furthermore, more results extracted using the Oslo method [29] from transfer reactions or/and ion scattering experiments on the deformed rare-earth nuclei, show an enhancement in the γSF which increases with deformation at energies around 3 MeV [25, 27, 96, 97, 98, 99]. Very recently, a splitting of the $M1$ SR has been observed in the actinides [23, 100, 101] and their strength were measured to be twice as strong compared to those of rare earth isotopes. Fig. 2.11 shows the extracted low-lying $M1$ SR for some actinides studied with the Oslo method. The splitting of the SR in the actinides has been suggested to be due to an isovector spin scissors mode for the lower peak, and the higher peak corresponds to the isovector orbital scissor mode [24].

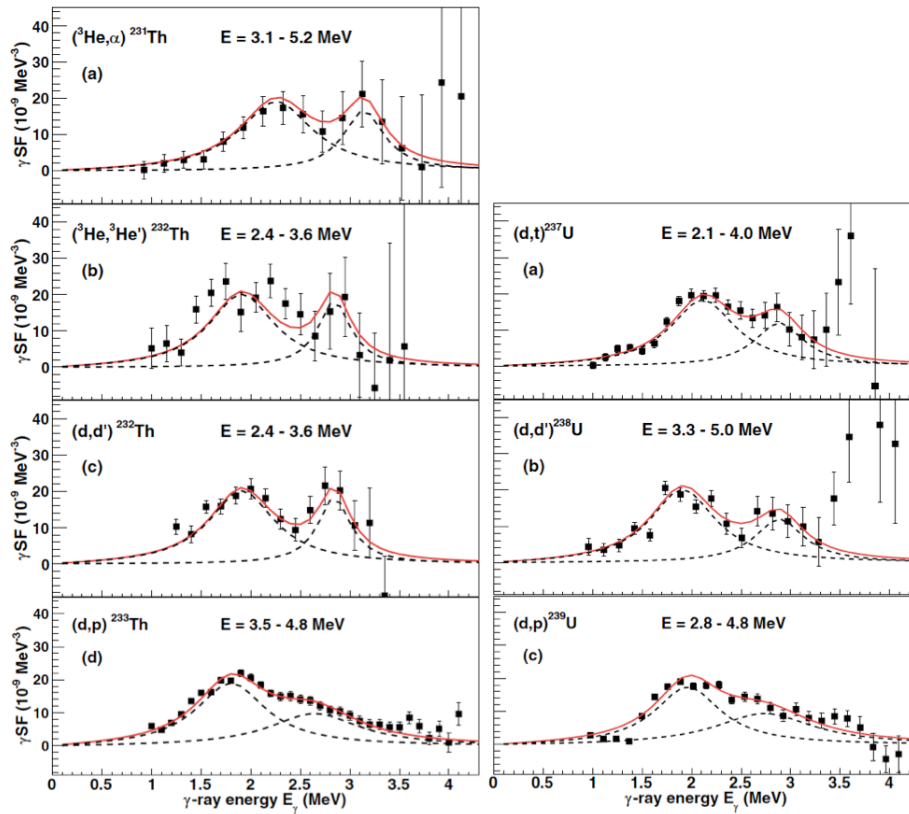


Figure 2.11. The extracted $M1$ scissors resonance using the Oslo method for $^{231-133}\text{Th}$ and $^{237-239}\text{U}$ [23]. Contributions from all other resonances have been subtracted to reveal the features of the scissor resonance. Various excitation energy regions of the data are utilized.

2.2.3.1 Reduced transition strengths

The $M1$ SR strength from different independent experiments is measured and sometimes described differently. A vast amount of information on reduced transitions strength for the SR comes from the NRF measurements [22]. In NRF experiments, the reduced transition strength for magnetic dipole transitions in even-even nuclei is calculated according to [61]:

$$B_{SR}(M1) \uparrow = 0.2598 \cdot \frac{\Gamma_0}{E_\gamma^3} [\mu_N^2] \quad (2.17)$$

where E_γ is the γ -ray energy and Γ_0 is the ground-state transition width which is calculated from the total energy-integrated photo-absorption cross-sections. The NRF technique is well suited to study dipole transitions from the ground state, and allows for determination of the spin or orbital character of the transitions as well as the γ -ray transition multipolarities [61]. As a result, transitions which belong to the SR can be identified and different transitions strength summed over. From NRF measurements the SR is build on the ground state as compared to the Oslo-type experiments in which the SR is build on excited states from γ -decay of the quasi-continuum.

In Oslo type of experiments the SR is observed in the γSF extracted from ion scattering or

transfer reactions. From the γ SF the $B_{SR}(M1)$ is extracted by determining the shape of the resonance using the Standard Lorentzian Function (SLO) of Brink [66] and Axel [67] and integrating over the distribution. The SLO is given as:

$$f_{E1}^{SLO}(E_\gamma) = \frac{1}{3\pi^2\hbar^2c^2} \frac{\sigma_{SLO}E_\gamma\Gamma_{SLO}^2}{(E_\gamma^2 - \omega_{SLO}^2)^2 + E_\gamma^2\Gamma_{SLO}^2} [MeV^{-3}], \quad (2.18)$$

where σ_{SLO} (in mb), Γ_{SLO} (in MeV) and ω_{SLO} (in MeV) are the peak cross-section, width of the resonance, and the resonance centroid. Although the SLO was originally used for $E1$ strength, it could still be applied to $M1$ and $E2$ resonances depending on the nuclear mass and the reproduction of experimental data [58]. The summed $B_{SR}(M1)$ is determined by numerically integrating Eq. 2.18 over the energy range relevant to the SR, as follows:

$$B_{SR} = \int \frac{dB_{SR}}{dE_\gamma} dE_\gamma = \frac{27(\hbar c)^3}{16\pi} \int f_{SR}(E_\gamma) dE_\gamma, \quad (2.19)$$

where the factor $27(\hbar c)^3/16\pi = 2.5980 \times 10^8 \mu_N^2 \text{MeV}^2$ [102]. The $B_{SR}(M1)$ can also be analytical estimated as follows [103]:

$$B_{SR} = \frac{9\hbar c}{32\pi^2} \left(\frac{\sigma_{SR}\Gamma_{SR}}{\omega_{SR}} \right), \quad (2.20)$$

which gives $\approx 10\%$ higher strength than that estimated from Eq. 2.19. The parameters σ_{SR} , Γ_{SR} and ω_{SR} represent the cross-section, width and centroid of the SR and are obtain by fit to normalized experimental γ SF.

The most striking features of the scissors resonance observed from various experimental setups and techniques is that 1) the $M1$ SR is located at energies approximated as $E_x = 66 \cdot \delta \cdot A^{-1/3}$, which corresponds to $E_x \approx 2\text{-}3$ MeV for deformed rare-earth nuclei [95]. Furthermore, 2) measurements from high-resolution inelastic proton-scattering showed that the SR is dominated and excited through the orbital-part rather than the spin-part of the magnetic dipole operator [22] as given in Eq. 2.14. However, the total transition strength, $B_{exp}(M1)$, has showed large deviations between different experiments. For example, the calculated $B_{exp}(M1)$ from Oslo type experiments has been observed to be twice as high compared to the values calculated from NRF measurements. Recently, Renstrøm *et al.* [102] showed that by extracting the integrated scissors strength using Eq. 2.19 over the same energy region, data from (γ, γ') and Oslo type experiments yield similar strength.

Several measurements of dipole scissors resonance strength in photon scattering experiments on the heavy rare earth deformed even-odd isotopes has in many cases pointed out to be hidden in the background of the experimental spectra [104, 105]. The low-lying dipole strength of the even-odd isotopes in the rare-earth and most probably in the actinide region, is fragmented and reduced significantly compared to the one in neighboring even-even isotopes [22]. However, these may change significantly from isotope to isotope depending on the respective level densities, the

ability to detect all the energy-escapes in the photon scattering experiments and finally be able to extract the $M1$ SR strength from the unresolved transitions [22]. Figure 2.12 (a) shows the systematics of $M1$ SR strength extracted for the even-even and even-odd deformed Gd isotopes.

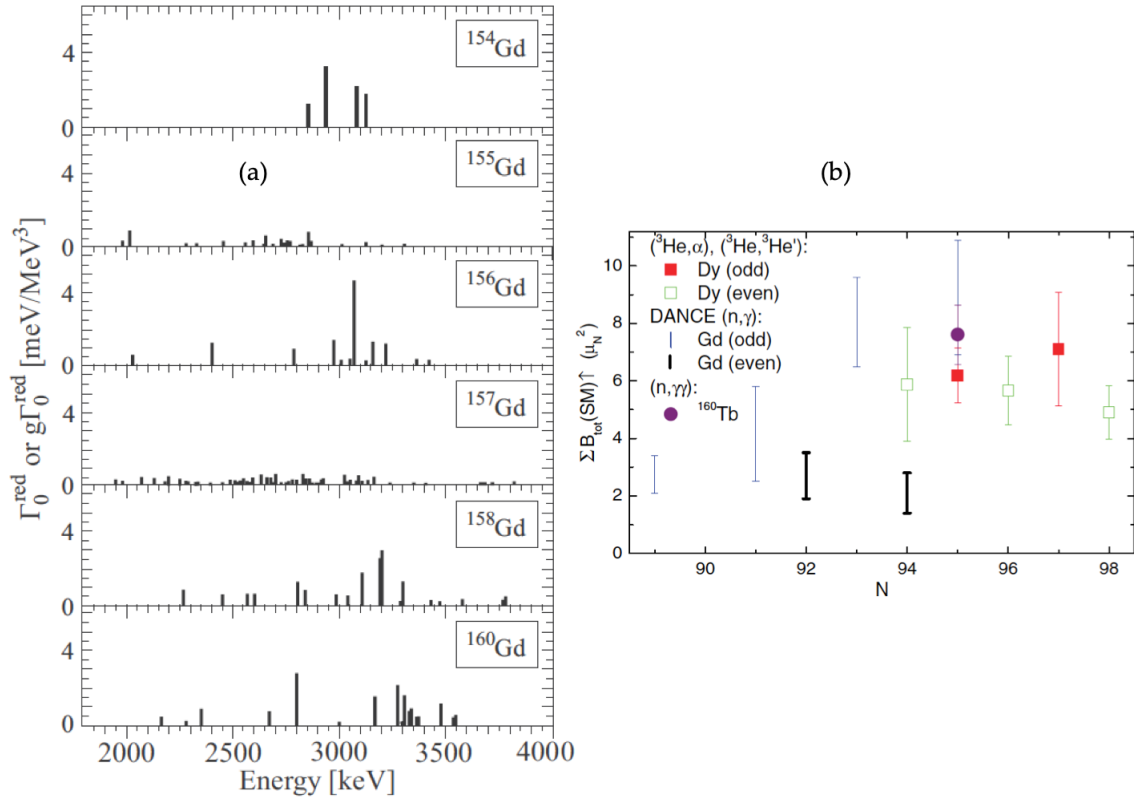


Figure 2.12. The systematics for $^{154,155,156,157,158,160}\text{Gd}$ (a) showing the ground-state decay width distributions which are directly related to the reduced transition strength (as shown in Eq. 2.17) extracted from NRF measurements [61, 104]. The reduced $M1$ scissor resonance strength for the even- and odd-A $^{153,155,156,157,158,159}\text{Gd}$, ^{160}Tb and $^{160,161,162,163,164}\text{Dy}$ (b) extracted from different experimental techniques [106].

Inconsistent to the reduced SR strength on even-odd compared to even-even measurements shown in Fig. 2.12 (a), a more recent experiment on Gd isotopes shown in Fig. 2.12 (b) reveal a significant $M1$ SR strength for the even-odd as compared to previously measured even-even isotopes, in addition to the observed even-odd staggering effect [106]. The observed even-odd staggering is not anticipated by any theory and is clearly not present in the charged particle induced reactions. From the observations in Fig. 2.12, it is clear that more measurements need to be performed in order to improve our knowledge of the underlying resonances properties across the nuclear chart, as well as to test established theories on resonances observed in the γSF . The current study will investigate the statistical nuclear properties of the deformed rare-earth even-even ^{154}Sm and even-odd ^{155}Sm isotopes and compare to existing measurements of the samarium chain.

2.2.4 Low-Energy Enhancement

In addition to the previously mentioned resonances that are observed in the γ SF, an unexpected enhancement in the γ SF at low energies $E_\gamma \leq 3$ MeV was discovered and recently confirmed in iron (Fe) isotopes, using the Oslo Method. This enhancement, today known as the low-energy enhancement (LEE), was observed experimentally for the first time from the $^{57}\text{Fe}(^3\text{He},\alpha\gamma)^{56}\text{Fe}$ reaction in 2004, and also confirmed with the TSC technique for ^{57}Fe [107]. Unlike the $M1$ scissors resonance, the LEE was not predicted theoretically before it was observed experimentally. Soon afterwards, the LEE was experimentally explored and observed in many light-to-medium mass nuclei such as $^{43-45}\text{Sc}$ [108, 109], $^{44-46}\text{Ti}$ [110, 111, 112], $^{50,51}\text{V}$ [113], $^{59,60,64,65,70}\text{Ni}$ [114, 115, 116, 117, 118], $^{73,74,76}\text{Ge}$ [119, 120], $^{93-98}\text{Mo}$ [121], $^{105,106}\text{Cd}$ [122] and also confirmed independently in ^{95}Mo [63] using a different setup and data extracted using the Ratio method. The LEE was observed in rare-earth $^{138,139}\text{La}$ [31] and $^{147,149,151,153}\text{Sm}$ [27, 28] isotopes as well. Fig. 2.13 points to regions in the nuclear chart where Oslo-type experiments were performed and the LEE was observed.

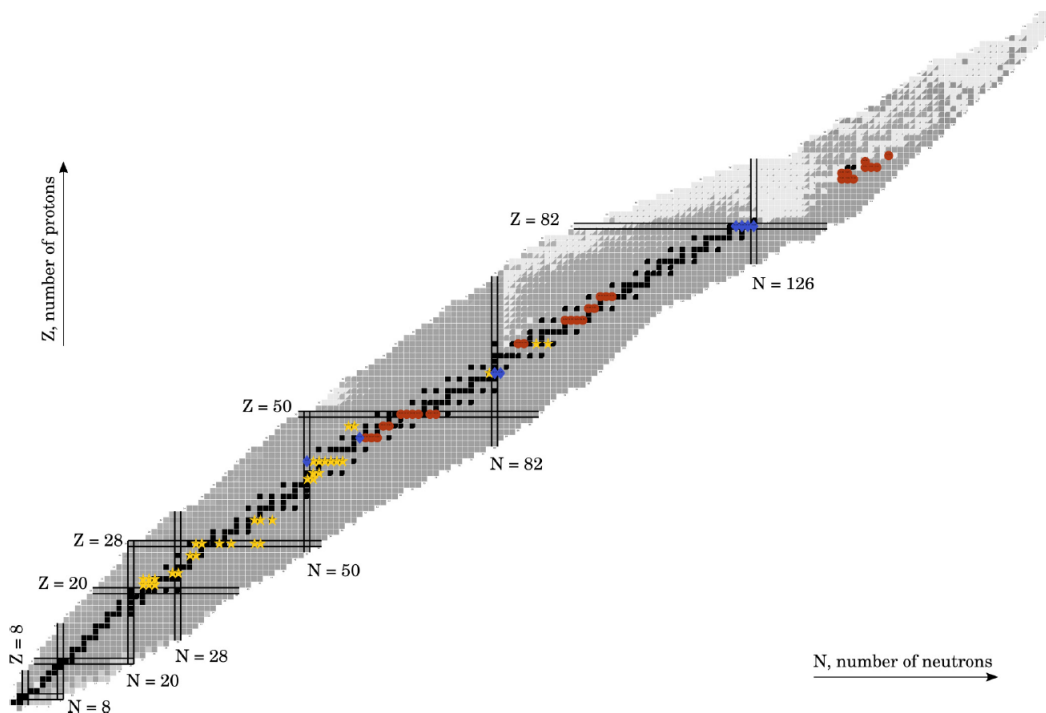


Figure 2.13. Nuclear chart detailing where the LEE has been observed experimentally using the Oslo Method, as indicated by yellow stars. The red circles indicate isotopes studied but no LEE has been observed, whereas the blue diamonds point out to isotopes in which it is unclear yet whether or not the LEE is present. Figure taken from Ref. [123]

Although the electromagnetic character of the transitions for the LEE is not experimentally clear yet, it was shown that decays are dominated by dipoles [124, 125]. However, so far recent measurements indicate a mixing of both components with a small bias towards magnetic character [126] at $E_\gamma \leq 2.9$ MeV exist. Two theoretical descriptions have been put forward to

explain the physical origin of this enhancement. The LEE has been suggested to be due to $E1$ transitions as a result of single-quasiparticle excitations in the continuum [127]. However, shell-model calculation from Refs. [70, 71] shows strong $M1$ transitions at low energies due to re-coupling of high- j orbitals for protons and neutrons. Furthermore, the LEE has proved to potentially enhance the r -process (n,γ) reaction rates by at least ≈ 2 orders of magnitude [128] for the very neutron-rich nuclei.

2.3 Radiative neutron capture cross-section and reaction-rate calculations

The particle-induced reaction cross-section, in particular the neutron capture or (n,γ) cross-section, are calculated on the basis of the Hauser-Feshbach (HF) statistical emission model [39]. The HF theory formulates that a capture reaction, $I + n \rightarrow C^\mu \rightarrow B^\mu + b$, can occur, at energies up to several MeV, through either a direct reaction or the formation and decay of a compound nuclear (CN) system C^μ which attain a statistical equilibrium before it decays. The residual nucleus B^μ can be left in an excited state, if the energy of the incident nucleon n is high enough, to further decay to its ground state through β - or γ -decay *i.e.* $I + n \rightarrow C + \gamma$. Therefore, the average neutron capture reaction cross-section in the center-of-mass energy E^μ are calculated as follows [60]:

$$\sigma_{n,\gamma}^\mu(E_n^\mu) \approx \frac{\pi\chi_n^2}{(2J_I^\mu + 1)(2J_n + 1)} \sum_{J^\pi} (2J + 1) \frac{T_n^\mu(E, J^\pi) T_\gamma^\mu(E, J^\pi)}{T_{tot}^\mu(E, J^\pi)}, \quad (2.21)$$

where J_n and J_I are the projectile and target spins, and $\pi\chi^2 = 0.6566/[m \cdot E^\mu(\text{MeV})]$ is the relative wave number in units of barn, m is the reduced mass of the projectile-target ($I^\mu + n$) system. The neutron transmission coefficient, T_n , gives the probability that the neutron will interact with the target nucleus I , leading to the formation of a CN state with spin-parity J^π and excitation energy E . In a similar way, T_γ gives the probability that γ -emission will take place upon formation of the CN state with spin-parity J^π and energy E . The total transmission coefficient, $T_{tot} = T_n + T_\gamma$, corresponds to the decay of the CN state with spin-parity J^π and energy E decaying into any possible combination of bound and unbound states in all energetically accessible exit and entrance channel combinations. In order for Eq. 2.21 to hold, two main assumptions must apply. Firstly, the formation of a projectile-target system which lives for about $\approx 10^{-18} - 10^{-16}$ s is assumed to reach a statistical equilibrium prior to nucleon- or γ -emission, depending on the reaction Q -value and decay channel. Secondly, the CN system is assumed to be independent of its formation, in other words it does not remember how it was formed, and the subsequent γ -emission are guided mainly by the statistical decays [43]. If the latter does not hold, a width fluctuation correction [129] is applied to Eq. 2.21 to account for entrance and exit channel correlations.

Above S_n , it can be seen from Eq. 2.21 that the neutron transmission coefficient, T_n , is notably larger than the γ -ray transmission coefficient, T_γ , and $T_n \approx T_{tot}$ and therefore $\sigma_{n,\gamma}^\mu(E_n^\mu) \approx T_\gamma$. The γ -ray transmission coefficient, T_γ , for a γ -emission from the compound nuclear state with J^π into any combination of final accessible states μ is given by:

$$T_\gamma^\mu(E, J^\pi) = \sum_{\mu=0, XL} T_{\gamma, XL}^\mu(E, J^\pi) + \int \sum_{XL} T_{\gamma, XL}(E, J^\pi) \times \rho(E - E_\gamma, J^\pi) \cdot dE_\gamma, \quad (2.22)$$

where the sum $\sum_{\mu=0, XL}$ runs over all experimentally known low-lying discrete states μ with multipolarity XL . The integral runs over the product of the nuclear level density $\rho(E_x - E_\gamma)$ in the continuum and the γ -ray transmission coefficient $T_{\gamma, XL}$, which is directly related to the downward γ -ray strength function $\vec{f}_{XL}(E_\gamma)$ (see sec. 2.2). The uncertainties associated in any HF cross-section calculations are not directly related to the model itself (other than through the width fluctuation corrections), but instead to the evaluation of the nuclear properties involved in the calculations of the transmission coefficients [13].

The radiative nucleon captures in high-density, high-temperature astrophysical environments involves medium-to-heavy targets. To estimate the radiative neutron capture and the reverse photo-neutron emission reaction rates, the target is considered not only to exist in its ground state but also to live in a distribution of thermally excited states μ . Assuming that thermodynamic equilibrium holds in addition to the calculated nuclear reaction cross-sections, $\sigma_{n,\gamma}^\mu$, which are built on the statistical emission model [39], the relative thermal velocities and energies of the projectile and target nuclei obey Maxwell-Boltzmann distributions. Therefore, the thermonuclear reaction-rate $N_A \langle \sigma v \rangle_{n,\gamma}^*(T)$ for neutron induced reactions at temperature T is obtained by integrating Eq. 2.21 over a Maxwell-Boltzmann distribution of energies E as follows [13]:

$$N_A \langle \sigma v \rangle_{n,\gamma}^*(T) = \left(\frac{8}{\pi m} \right)^{1/2} \frac{N_A}{(kT)^{3/2} G(T)} \times \int_0^\infty \sum_\mu \frac{(2J_I^\mu + 1)}{(2J_I^0 + 1)} \sigma_{n,\gamma}^\mu(E_n) E_n \exp\left(-\frac{E_n + E_x^\mu}{kT}\right) dE, \quad (2.23)$$

where N_A and k are the Avogadro's number and the Boltzmann's constant, and the reaction rate is given in units of $cm^3 mol^{-1} s^{-1}$. The normalized temperature-dependent partition function $G(T) = \sum_\mu (2J_I^\mu + 1) / (2J_I^0 + 1) \exp(-E_x^\mu / kT)$ can completely specify the state distribution of the target. When the target is in its ground state, $\mu = 0$, Eq. 2.23 gives the laboratory reaction-rates. The reverse photo-neutron emission reaction rates are obtained, based on the assumption that the principle of detailed balance⁴ (or reciprocity theorem) [60] is valid. For neutron-induced reactions, the astrophysical Maxwellian-averaged (n, γ) cross-section (MACS) are calculated from Eq. 2.23 as $N_A \langle \sigma v \rangle / \nu_T$ where $\nu_T = \sqrt{2k_B T / \mu}$ represent the maximum velocity distribution or is the thermal velocity on projectile and targets. Temperature T is usually given in units of

⁴The postulate that when the system is in statistical equilibrium, any forward process occurs at the same rate as the reverse process [60].

Giga-Kelvin (10^9K) and the Boltzmann constant $k_B = 8.6173 \times 10^{-5}\text{eV/K}$.

Chapter 3

Experimental details

"The principle of science, the definition, almost, is the following: The test of all knowledge is experiment. Experiment is the sole judge of scientific "truth"."

— **Feynman, Leighton and Sands**, *The Feynman Lectures on Physics (1963)*, p. 1-1

3.1 Oslo Cyclotron Laboratory

In this work, the γ -ray strength functions (γ SFs) and the nuclear level densities (NLDs) were measured from particle- γ coincidence experiments performed at the Oslo Cyclotron Laboratory (OCL) in October 2014 and September 2016. OCL is located in the basement of the physics department at the University of Oslo in Norway and houses an MC-35 Scanditronix cyclotron which delivers pulsed light-ion beams such as protons, deuterons, helium-3 and helium-4. The list of available beams at OCL are shown in Table 3.1, with a specified range of charge states, beam energies and intensities. An outline of the experimental setup which includes the beam

Table 3.1. List of available beams at OCL.

Ionized beams Particle type	Charge state	Energy range (MeV)	Intensity (μA)
Proton (p)	$^1\text{H}^+$	2-35	100
Deuteron (d)	$^2\text{H}^+$	4-18	100
helium-3 (^3He)	$^3\text{He}^{++}$	6-47	50
helium-4 (^4He)	$^4\text{He}^{++}$	8-35	50

lines and target stations is shown in Fig. 3.1. An external ion source (*i.e.*, bottle of hydrogen, deuterium, helium-3 or helium-4 gas) sends ions of interest to the cyclotron. The beam is

extracted from the cyclotron and is collimated and focused using slit D1 and the quadrupole magnet Q1. The beam can either be delivered to other target stations such as the radio-isotopes station using the switching magnet or it can be deflected 90° by the analyzing magnet and then delivered to the nuclear physics target station enclosed by the multi-detector NaI(Tl) array (CACTUS) [131] at the end of the beam line. After passing slit D4, the beam spot on target has a typical diameter of $\approx 1\text{-}2$ mm. Inside the target chamber which is under vacuum, a stable self-supporting target in the present experiments is positioned at the center of the target chamber and is surrounded by the Silicon Ring particle telescopes array (SiRi) [132]. A Faraday cup is located after the CACTUS array to measure the beam intensity.

3.1.1 Target

Table 3.2 lists the reactions studied for this work, beam energies, target properties and Q-values of nuclear reactions. At the start and end of each experiment, 1-2 hour runs are taken for calibration of the CACTUS multi-detector γ -ray array and silicon particle array SiRi, where

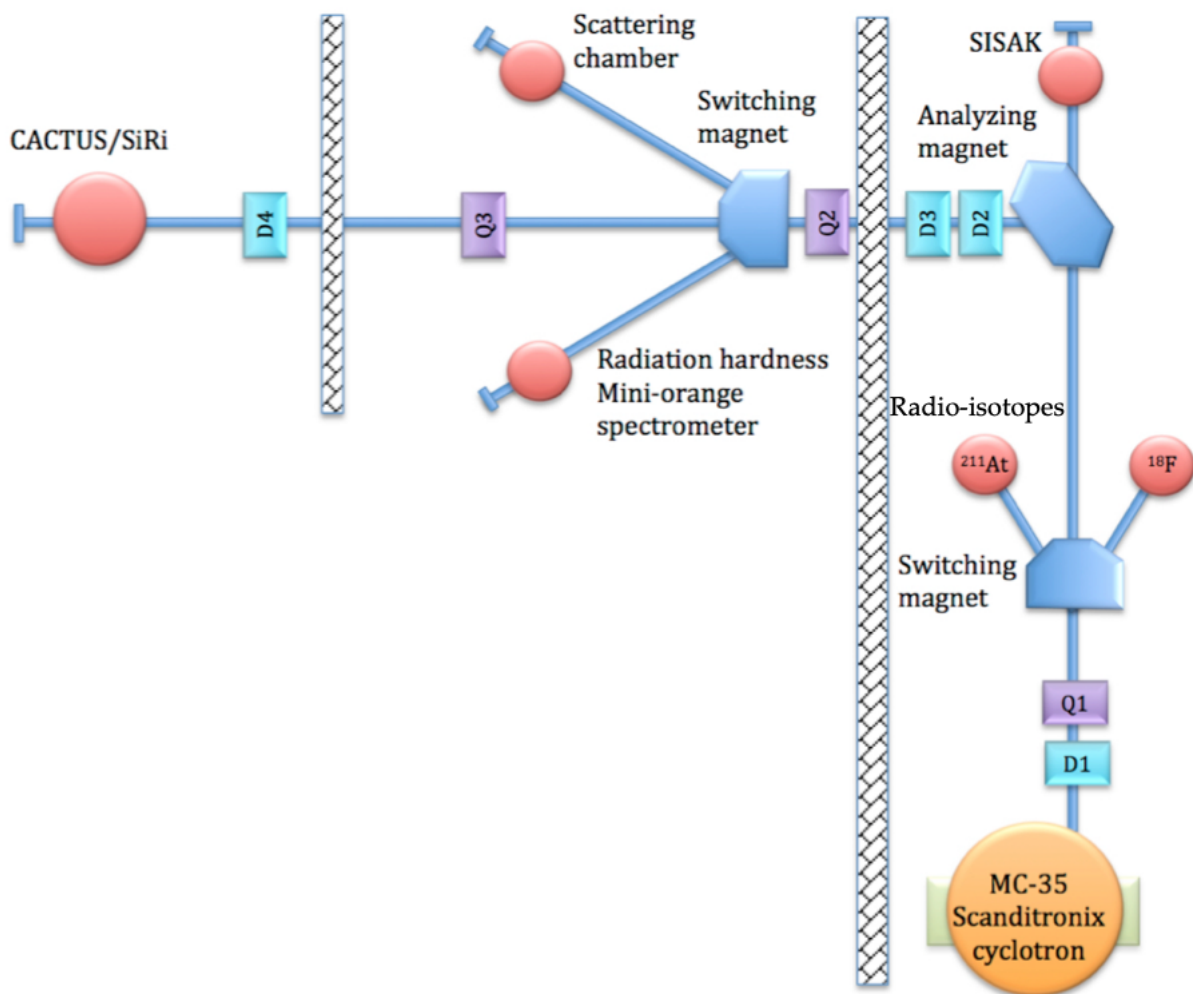


Figure 3.1. The Oslo Cyclotron Laboratory showing the experimental hall and cyclotron hall separated by a concrete wall, with the respective target stations and beam lines [130].

a deuteron beam impinged on a self-supporting ^{28}Si target. These stable targets provided by

Table 3.2. The mass, thickness and enrichment of the targets, the beam current and energy, and reactions studied in the experiments presented in this work. The ^{154}Sm experiment was performed with 24 NaI(Tl) + 6 LaBr₃:Ce detectors and a total of 26 NaI(Tl) for the $^{180,181,182}\text{Ta}$ experiments discussed in Refs [37, 133]. The ^{28}Si data were used for calibration purposes.

Target	Enrichment %	Thickness (mg/cm ²)	Current (pA)	Reaction	Beam energy (MeV)	Q-Value (MeV)
^{181}Ta	99.99	0.80	~ 2.00	$(^3\text{He}, ^3\text{He}'\gamma)^{181}\text{Ta}$	34.00	
				$(^3\text{He}, \alpha\gamma)^{180}\text{Ta}$		13.00
				$(\text{d}, \text{p}\gamma)^{182}\text{Ta}$	12.50	3.84
				$(\text{d}, \text{t}\gamma)^{180}\text{Ta}$	15.00	-1.32
				$(\text{d}, \text{d}'\gamma)^{181}\text{Ta}$	12.50 & 15.00	
^{154}Sm	98.69	3.20	~ 2.00	$(\text{d}, \text{d}'\gamma)^{154}\text{Sm}$	13.00 & 15.00	
				$(\text{d}, \text{p}\gamma)^{155}\text{Sm}$		3.58
^{28}Si	92.22	3.50	$\sim 0.80\text{-}2.00$	$(\text{d}, \text{d}'\gamma)^{28}\text{Si}$	12.50 & 13.00 & 15.00	
				$(\text{d}, \text{p}\gamma)^{29}\text{Si}$		6.25

iThemba LABS were transported in a glass container. However for the ^{154}Sm case, the glass container was filled with argon gas to avoid contact with air and therefore reducing target oxidization. On arrival at the OCL facility, the ^{154}Sm targets were stored in a chamber under vacuum.

3.1.2 Particle detection

The Silicon Ring particle detector (SiRi) is used to detect and measure the energy of the emitted charged particles from nuclear reactions. The charged ejectiles such as p, d, t, ^3He , and ^4He are identified by their deposited energy. SiRi consists of thick back E detectors and thin front ΔE detectors. The ΔE detectors are segmented into 8 strips, which makes SiRi in total to have 64 $\Delta E - E$ particle detectors. The trapezoidal shaped $\Delta E - E$ array is shown in Fig. 3.2 (a). Each trapezoid $\Delta E - E$ is inclined at 45° allowing the ejected particles to impinge on the detectors with an angle closest to the normal. The front ΔE detector has a thickness of $130 \mu\text{m}$ and that of the back E detector is $1550 \mu\text{m}$. A $10.5 \mu\text{m}$ thick aluminium foil is placed in front of each ΔE detector as shown in Fig. 3.2 (b), to shield them from low-energy δ -electrons that are emitted from target atoms when bombarded by the beam particles. In both experimental setups, the beam current was limited to $\sim 2 \text{ pA}$ to prevent pile-up events in the particle detectors. Also the beam energy was selected to be as high as possible but allowing the outgoing charged particles to be stopped completely in the E detector to avoid punch-through and thus depositing their full energy inside the detector. The $\Delta E - E$ array was placed at

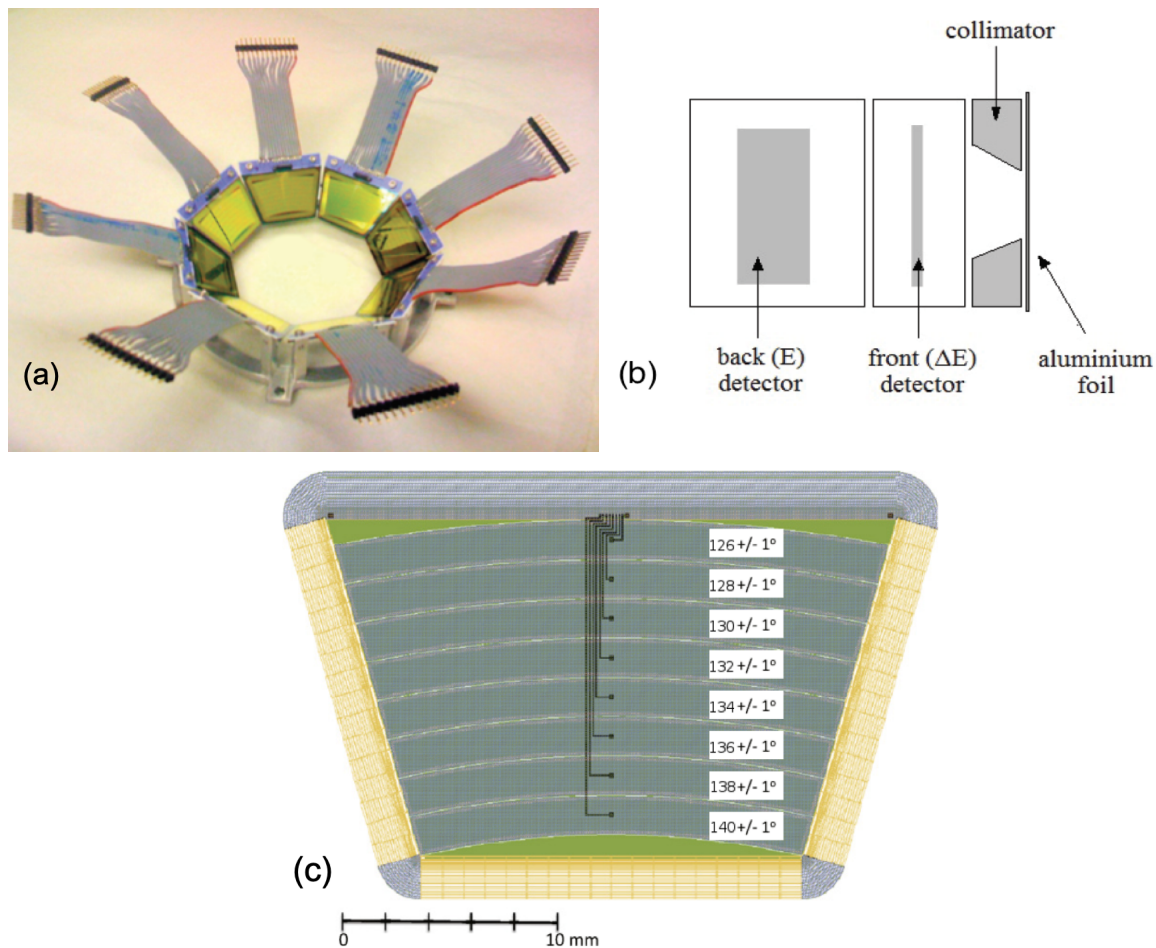


Figure 3.2. The 8 trapezium shaped Si particle detectors distributed on a ring including cables to read out the signals and in each trapezoid, the strip covers an angle of $\Delta\theta = 2^\circ$ [132].

backwards angles covering a polar angular range $\theta \approx 126^\circ$ to 140° , with respect to the beam axis, and each strip covers an angle of $\Delta\theta = 2^\circ$ as shown in Fig. 3.2 (c). The particle detector array was located ≈ 5 cm away from the target. The detectors were placed at backwards angles to decrease the detection of light ion beam elastically scattered off the heavy target compared to the emitted charged particles from the reaction of interest. The front (ΔE) detectors were collimated to ensure a narrow spread of the particle energies and to reduce the uncertainties in the outgoing reaction scattering angles $\Delta\theta$, by reducing the occurrences of incomplete detection of reaction ejectiles' energies on the edge of the detector's active area. The average energy resolution¹ of the SiRi array is 350 keV for ^3He and 130 keV for deuterons.

3.1.3 γ -ray detection

The target chamber is enclosed by the multi-detector scintillator γ -ray array (CACTUS) [137]. The γ -detection array is named after its resemblance with that of a cactus plant. Two different

¹The energy resolution of the particle detector is determined by measuring the full width half maximum (FWHM) of the ^3He / deuteron beam elastically scattered off the ^{181}Ta / ^{154}Sm target, respectively.

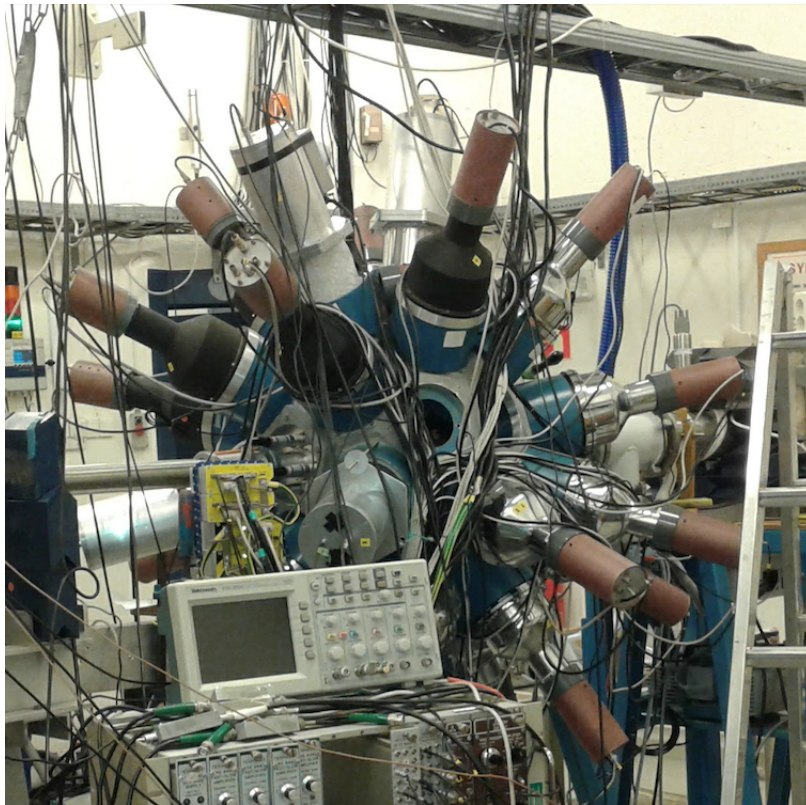


Figure 3.3. Experimental setup at the OCL, showing the γ -ray array with 24 NaI(Tl) + 6 LaBr₃:Ce detectors.

scintillator detector setups were used in this work, as the old CACTUS setup was in the process of being dismantled to give room to the new detector array OSCAR [138] (Oslo SCintillator ARray, consisting of lanthanum bromide "LaBr₃:Ce" detectors) in 2016. The first experiment in 2014 used a total of 26 NaI(Tl) detectors and in the second experiment in 2016, 24 NaI(Tl) + 6 LaBr₃:Ce (3.5"×8") detectors were used, making a total of 30 detectors in the array. The 2016 experimental setup is shown in Fig. 3.3. Both the experimental campaigns took about two weeks of beam time each. The two different detectors are not placed at a specific angle on a polyhedron shaped frame around the target chamber. In both setups, the NaI(Tl) scintillators were lead shielded to reduce "cross-talk" (*i.e.*, reduce Compton-scattered γ -rays escaping out of the individual NaI(Tl) and/or LaBr₃:Ce crystals to adjacent detectors) and therefore improve the peak-to-total ratio. The NaI(Tl) detectors are located 22 cm away from the target. Each NaI(Tl) crystal has dimensions of 12.7×12.7 cm² and a plastic ring is used to hold the crystal in place as shown Fig. 3.4. The front surface of each NaI(Tl) detector is collimated by a 10 cm thick lead of 7 cm diameter, in addition to the 2 mm thick copper absorber which is used to reduce background from X-rays. The CACTUS array covers a total solid angle of $\Omega = \frac{NA}{4\pi R^2} = 16.4\%$ of 4π sr, where $N = 26$ is the number of NaI(Tl) detectors in CACTUS, $R = 22$ cm is the distance between CACTUS detectors and the target. The collimated front area of each NaI(Tl) crystal is given by $A = \pi r^2$ with a radius $r = 3.5$ cm. The total efficiency (of 26 NaI(Tl)) for a 1332 keV γ -ray transition in ⁶⁰Co was measured to be $\approx 14.1(2)\%$, with a

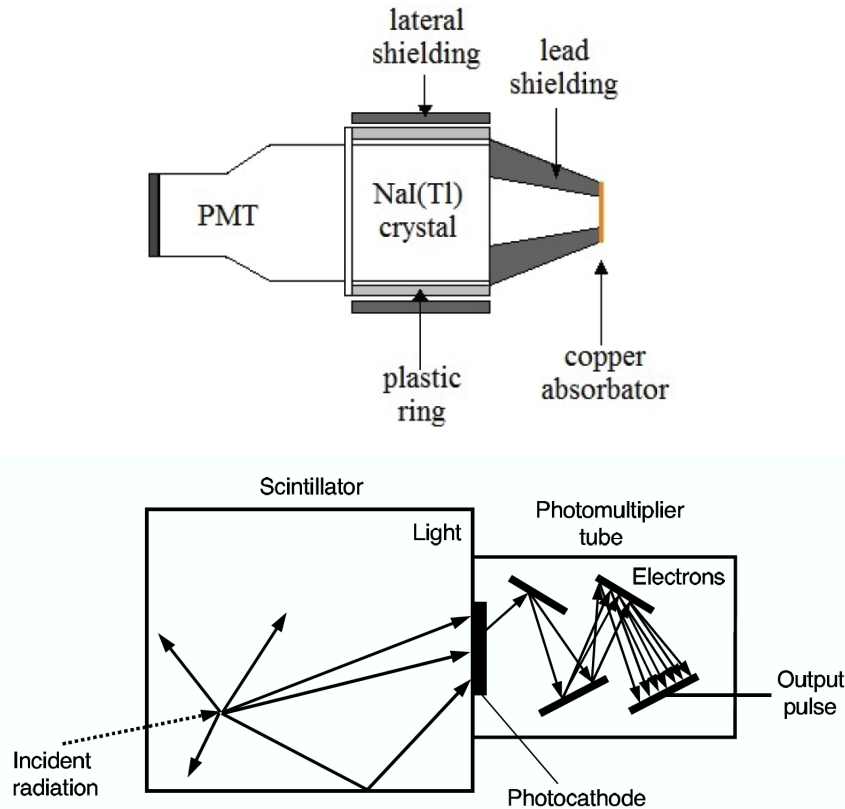


Figure 3.4. A schematic diagram of the NaI(Tl) γ -ray scintillator detector (upper panel) [134], showing the principle of scintillator based γ -ray detector such as the NaI(Tl) or the LaBr₃:Ce (lower panel) [135]. The incident high energy photon produces light (or relatively low energy photons) when interacting with the scintillator material. The low energy photons interact with the semi-transparent photo-cathode which converts them into low-energy electrons. At this point, the produced electron charge is too small to serve as an electrical signal since a typical pulse requires several hundreds of photo-electrons. Therefore, the electrons are directed and multiplied by series of dynodes, giving rise to $\approx 10^7 - 10^{10}$ electrons [136]. The output pulse is collected at the anode.

relative energy resolution of $\approx 6\%$ at FWHM.

3.2 Coincidence technique

In this work, we study the particle- γ coincidences from inelastic scattering reaction ($^3\text{He}, ^3\text{He}'\gamma$) and ($d, d'\gamma$), the neutron pick-up reactions ($^3\text{He}, \alpha\gamma$) and ($d, t\gamma$), and transfer reactions ($d, p\gamma$). The analog electronic system [139] was used in the experimental setups, and the results will be reported in the next chapter. The conditions and requirements which allows us to measure valid particle- γ coincidences are discussed in details in Ref. [131, 132, 140]. To be able to extract particle- γ coincidences,

- (i) the time between the detection of a γ -ray and the ejected particle should be measured,

- (ii) one must be able to differentiate between the ejected particles from the nuclear reaction, and
- (iii) finally distinguish the detected γ -ray in coincidence with the ejected light-ions of interest, from the rest of the detected γ -rays.

The SiRi discussed in sec. 3.1.2 is biased up to 30 V for ΔE and 350 V for E detectors, provided by the Mesytec MHV-4 modules. As pointed out, SiRi consists of 64 $\Delta E - E$ detectors which detected particle energies and transmit this energy signals directly to Mesytec MPR-16 preamplifiers. Energy signal cables from the 64 front ΔE detectors, grouped in 4 sets of 16 channels, are sent to four preamplifiers and an additional preamplifier is used for the remaining eight channels from the back E detector. The five preamplifiers are placed as close as possible to the target chamber to reduce effects of electronic noise and interference. From the Mesytec MPR-16 preamplifiers, the signals are transmitted to Mesytec MPR-18 modules, which houses the high-quality multichannel spectroscopic amplifiers, Timing-Filter Amplifiers (TFA) with integrated Leading Edge Discriminators (LED), as shown in Fig. 3.5. The energy information

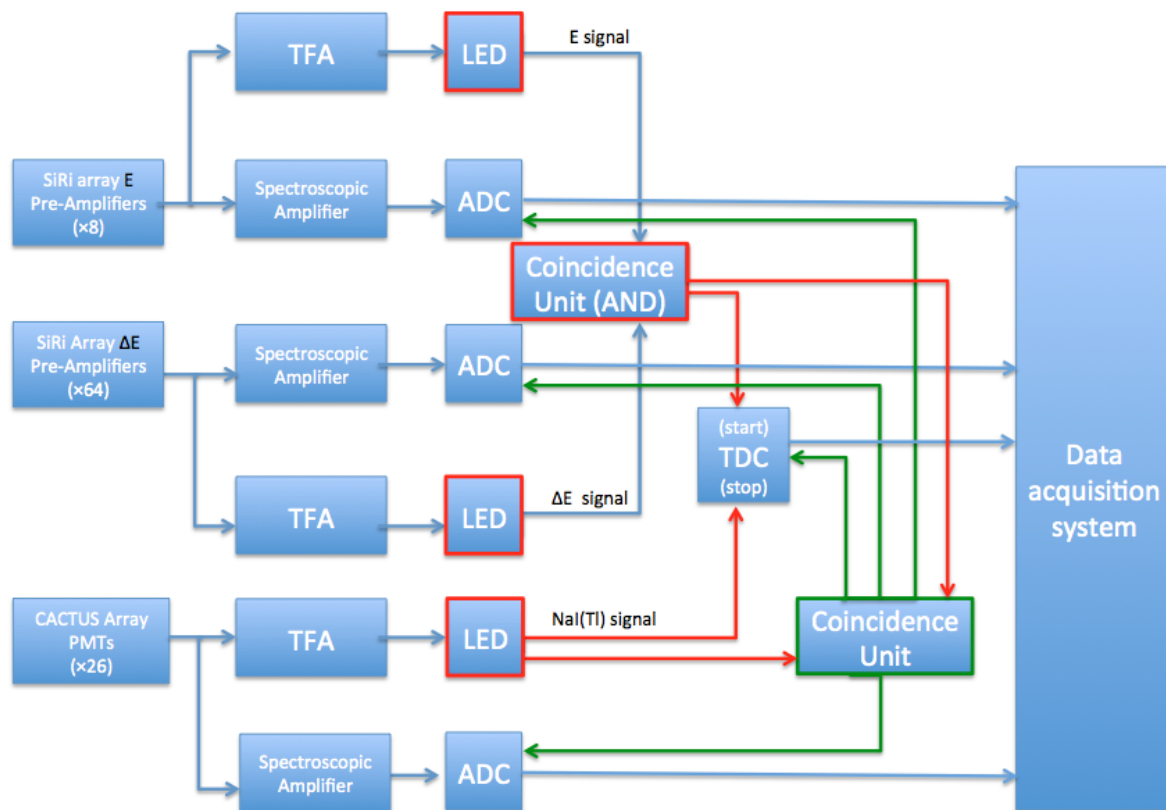


Figure 3.5. A schematic diagram of the electronics setup, located in the data room at the OCL. Each individual NaI(Tl), ΔE and E signal is processed by a separate spectroscopic amplifier, TFA, LED, and ADC. Additionally, each NaI(Tl) time signal is allocated its own TDC channel. Figure adopted from Ref. [36].

from the spectroscopy amplifier is further read out and digitized by the Analog-to-Digital

Converters (ADC) manufactured by Mesytec (MADC-32) or CAEN (mod. 785). Similarly, the multi-detector γ -ray array CACTUS (see sec. 3.1.3) provides energy signals which are delivered to a set of spectroscopic amplifiers, TFAs, LEDs and ADCs as shown in 3.5. A high voltage of about ≈ 700 to 800 V is applied to each NaI(Tl) photomultiplier tube. When a particle hits one, and only one $\Delta E - E$ detector, a start signal is sent to the time-to-digital converters (TDC) manufactured by CAEN (mod. 775) and opens a master gate for $\approx 1.2 \mu\text{s}$. The TDC master gate closes when a stop signal is registered from CACTUS array upon detection of at least one γ -ray. In order to create a small time interval where measurements are accepted, the NaI(Tl) stop signal is delayed by ≈ 200 ns, since in principle both the emitted particle and a γ -ray originating from the same nuclear reaction will reach SiRi and CACTUS almost simultaneously. The particle- γ coincidence event is accepted when a signal from the $\Delta E - E$ and the NaI(Tl) detectors are recorded within a TDC time window of ≈ 200 ns. At this point, a signal from the logic coincidence unit triggers the ADCs and TDCs to send out energy and timing information, respectively, to the data acquisition system. A schematic representation of the analog electronic setup is shown in Fig. 3.5.

Chapter 4

Data analysis and the Oslo Method

“Negative results are just what I want. They’re just as valuable to me as positive results. I can never find the thing that does the job best until I find the ones that don’t.”

— **Thomas A. Edison**

4.1 Energy calibration and particle identification

In this chapter, information on the detector energy calibration, time calibration and particle- γ coincidences is discussed for the $^{154}\text{Sm}(\text{d},\text{X})$ experiment. For the $^{181}\text{Ta}(\text{d},\text{X})$ and $^{181}\text{Ta}(\text{}^3\text{He},\text{X})$ cases, the calibration and particle- γ coincidences follow a similar procedure and are reported elsewhere [36, 37].

4.1.1 Particle energy calibration and identification

From the nuclear reactions, charged ejectiles of interest such as p, d, t, ^3He , and ^4He are discriminated by their different energies deposited in the thin front ΔE and thick back E particle detectors. The energy loss per unit length of charged ejectiles in the particle detectors depends on both the charge state z and the mass of the penetrating particle M . The magnitude of the energy loss per unit length of charged ejectiles into a material is given by the Bethe-Bloch formula¹[41, 141]:

$$-\left\langle \frac{dE}{dx} \right\rangle = Kz^2 \frac{Z}{A} \frac{1}{\beta^2} \left[\frac{1}{2} \ln \frac{2m_e c^2 \beta^2 \gamma^2 T_{max}}{I^2} - \beta^2 - \frac{\delta(\beta\gamma)}{2} \right], \quad (4.1)$$

¹Here it is assumed the particles interact with the target only through electromagnetic forces, and any energy loss to nuclear reactions between the particle and the target nuclei are ignored. Therefore, only the energy loss by the high velocity particle to the atomic electrons, which are bound to infinitely heavy nuclei, is considered.

where $\beta = v/c$, A , and Z are the relative particle velocity, atomic mass of absorber material, and atomic number of absorber material, T_{max} is the maximum kinetic energy transferred in a single collision, I is the mean excitation potential of the material. $\delta(\beta\gamma)$ is the density effect correction to ionization energy loss and K is a constant².

The parameters m_e , z and c are the electron mass, atomic number of the incident particle and speed of light, respectively. Therefore, any two particles with equal charges and different masses, *e.g.*, deuteron, and triton and particles having equal charge-to-mass (q/m) ratio, *e.g.*, d and α 's, can easily be distinguished by plotting the energy deposited in the ΔE detector versus the energy deposited in the E detector as shown in Fig. 4.1 (a), where the range³ of each particle in

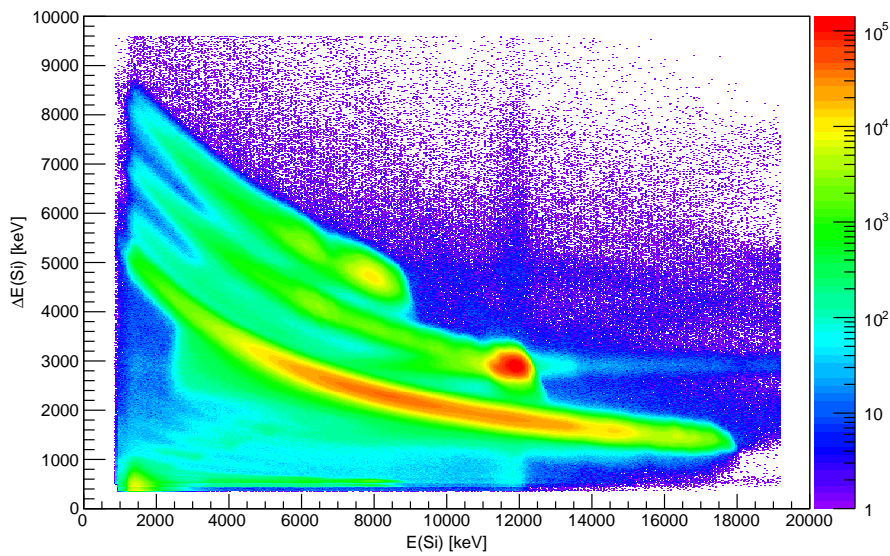


Figure 4.1. The uncalibrated $\Delta E - E$ matrix showing all the detectors for the $^{154}\text{Sm}(d,X)$ reaction, used to identify the ejectile particles in a nuclear reaction.

the $\Delta E - E$ is determined by the type of particle, type of absorber material and energy of the particle. The measured particle and γ -ray energies E are correlated to the observed spectrum channel number ch through a linear calibration as:

$$E = a_0 + a_1 \times ch, \quad (4.2)$$

where a_0 and a_1 are the calibration coefficients, commonly known as the detector energy offset and gain, respectively. The known states, usually the ground state, in each particle type, are used as calibration points to calibrate the particle spectra obtained from the front ΔE and back E detectors. The particle detectors are now aligned in order to obtain good energy and time resolution in the total spectra. The calibrated individual particle detectors are shown in Fig. 4.2

²The constant $K=4\pi N_A r_e^2 m_e c^2=0.307 \text{ MeV g}^{-1} \text{ cm}^2$ for $A=1 \text{ g mol}^{-1}$ and $T_{max}=2m_e c^2 \beta^2 \gamma^2 / (1 + 2\gamma m_e / M + (m_e / M)^2)$ where the Lorentz factor $\gamma = (1 - \beta^2)^{-2}$. The parameters N_A and r_e are the Avogadro's constant and classical electron radius.

³The range of the particle is the distance a charged particle travels in a detector, interacting simultaneously with the detector material (basically electrons) and thus continuously and gradually loses energy along its path.

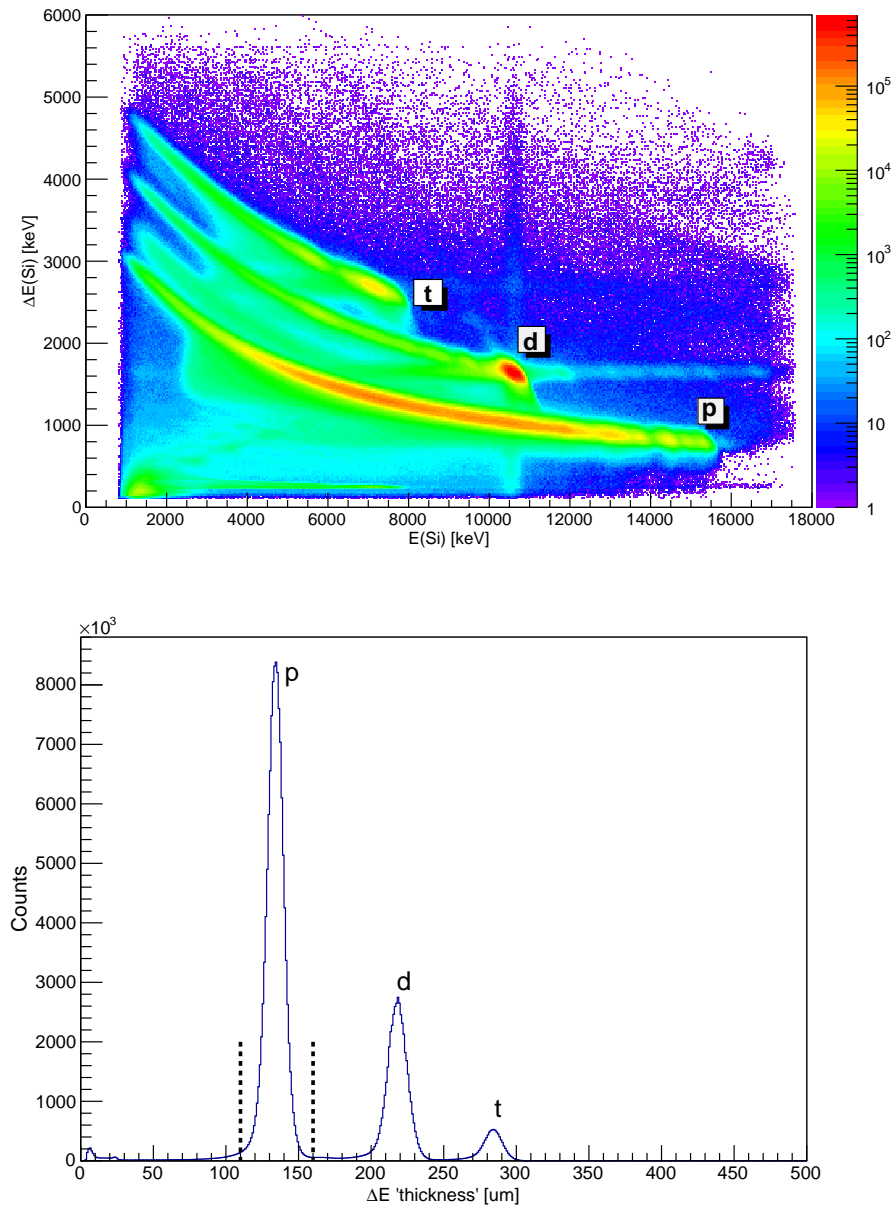


Figure 4.2. The calibrated $\Delta E - E$ plot for the $^{154}\text{Sm}(d,X)$ reaction, showing different reactions channels opened during the reaction (upper panel). The range spectrum for the $\Delta E - E$ detectors showing peaks representing different particles (lower panel). The dashed lines show the gate used to select only (d,p γ) reactions.

(upper panel) and the different detected charged particles, (*i.e.*, p,d and t) are well separated.

The expected charged-particle energy deposited in the detector at different scattering angles can be computed using the SiRi kinematic calculator [142] which is based on the Bethe-Bloch formula [41]. Calculations with SiRi accounts for the energy loss of charged particles when passing through the aluminium foil placed in front of the detector. The beam energy has been chosen to be as high as possible while at the same time estimated in such way that the particle will lose all their energies inside the detectors to avoid punch through. To check the quality of our calibration, the particle energies deposited in the $\Delta E - E$ are compared to the

expected values estimated from the SiRi kinematics calculator as shown in Fig. 4.3. These were

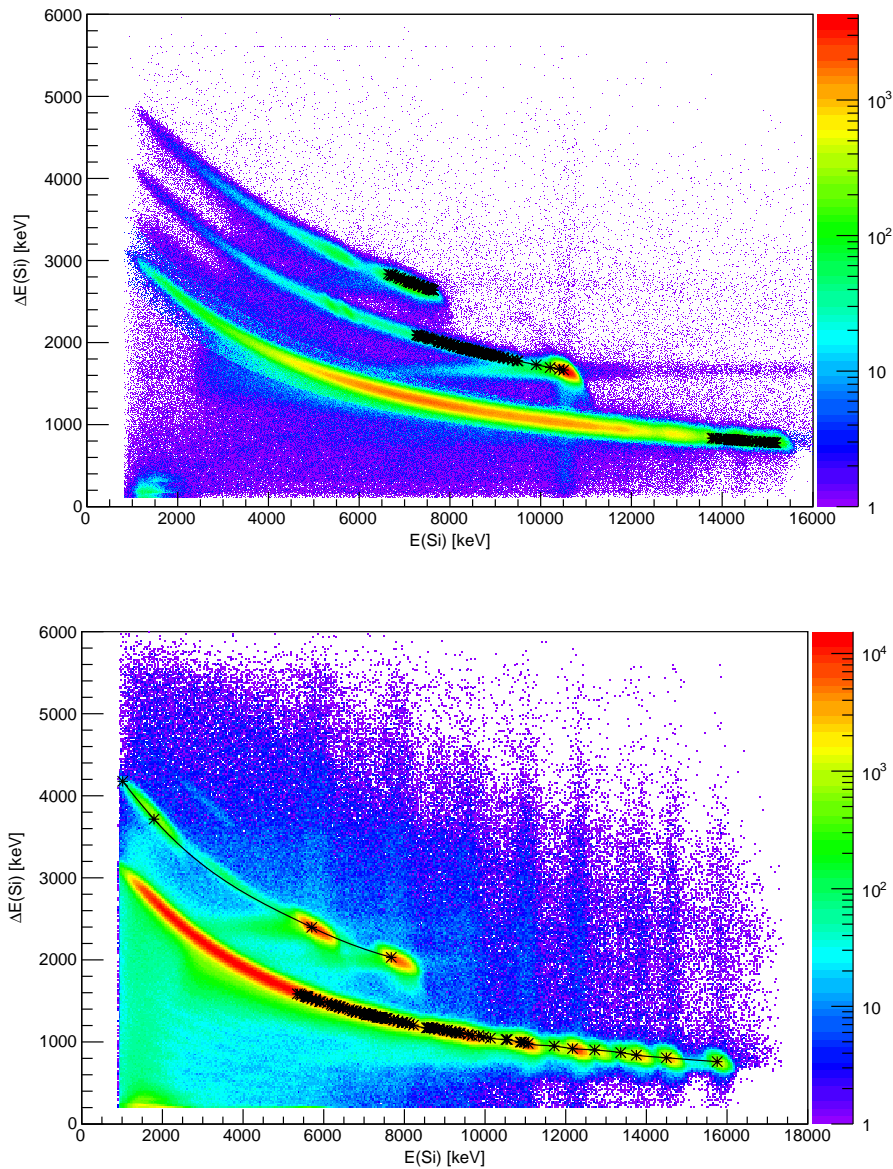


Figure 4.3. The calibrated $\Delta E - E$ plot for the $^{154}\text{Sm}(d,X)$ (upper panel) and $^{28}\text{Si}(d,X)$ (lower panel) reaction, in comparison to calculated values from the SiRi kinematic calculator for SiRi strip at $132 \pm 1^\circ$ of the $\Delta E - E$ detector.

calculated at the scattering angle $\theta = 132 \pm 1^\circ$ for known discrete states of the residual nucleus $^{154}\text{Sm}(d,X)^{153-155}\text{Sm}$ (upper panel) and $^{28}\text{Si}(d,X)^{28-29}\text{Si}$ (lower panel). From the $\Delta E - E$ plot, it is now possible to set a gate on an apparent thickness for a specific particle type using its unique energy range curve. To do so, we define the thickness as the range of a particle energy deposited in the $\Delta E + E$ and subtract the range for particle energy deposited in the E . Such a spectrum showing different particle thickness is shown in Fig. 4.2 (lower panel). By putting a gate on one of the particles, the particle- γ events for a specific reaction channel can be obtained. The proton gated $\Delta E - E$ matrix from $^{154}\text{Sm}(d,p\gamma)^{155}\text{Sm}$ and $^{28}\text{Si}(d,p\gamma)^{29}\text{Si}$ reactions are shown in Fig. 4.4.

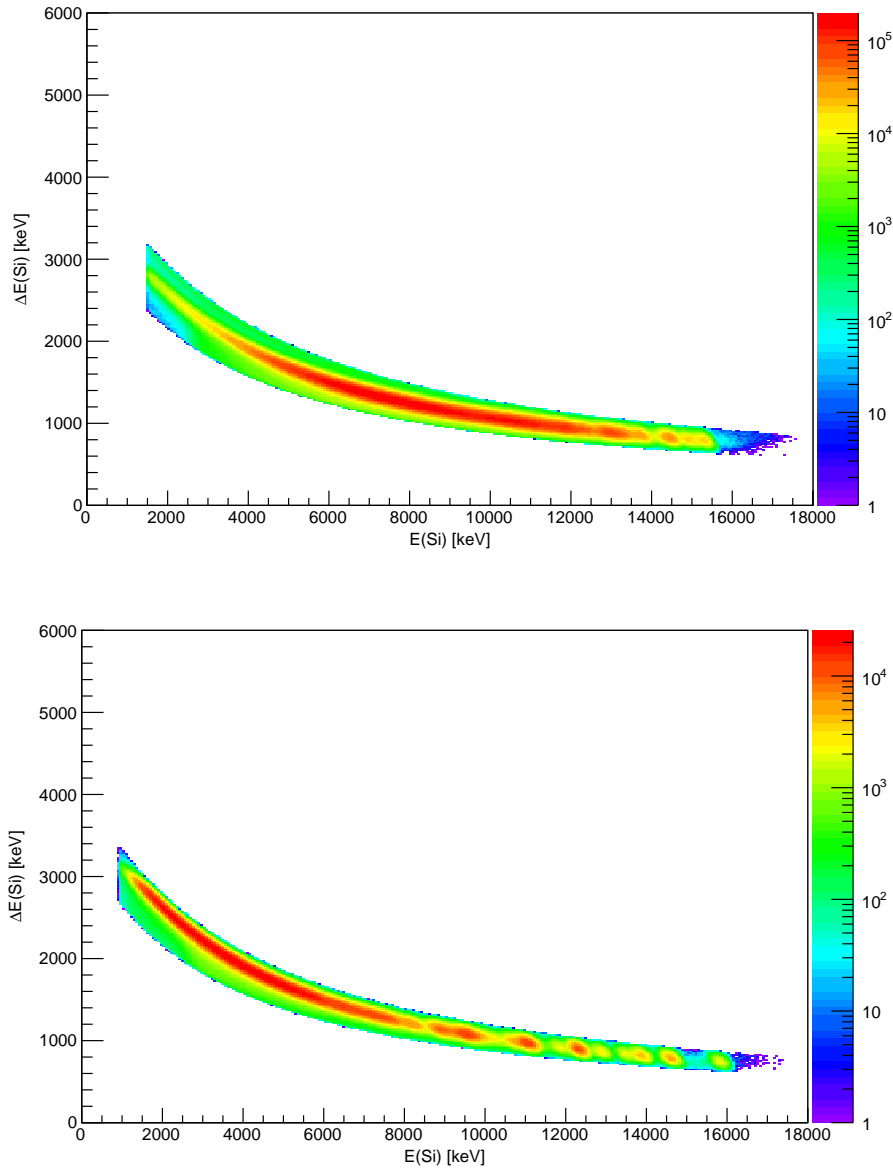


Figure 4.4. The calibrated $\Delta E - E$ plot for the $^{154}\text{Sm}(d,p\gamma)$ (upper panel) and $^{28}\text{Si}(d,p\gamma)$ (lower panel) reactions, both gated on the ejected protons.

The initial excitation energy E_x of the residual nucleus can be extracted from the measured ejectile energies $KE_{ejectile}$, the reaction kinematics and various Q -values, following the equation below:

$$E_x = KE_{beam} - KE_{ejectile} - KE_{recoil} - E_{loss} + Q_{value}, \quad (4.3)$$

where KE_{beam} and E_{loss} are the total kinetic energy of the beam and the energy lost by the particle through the target and the aluminium foil, respectively, Q_{value} is the Q -value of the nuclear reaction. The target nucleus' recoil energy KE_{recoil} is negligible, since the target nuclei in this work are significantly heavier than the projectile. The excitation spectra for residual nuclei $^{154,155}\text{Sm}$ and ^{29}Si are shown in Fig. 4.5. The high background and broad peak at around ≈ 4700 keV in Fig. 4.5 (a) is due to the elastic deuteron beam scattering off ^{16}O and populating

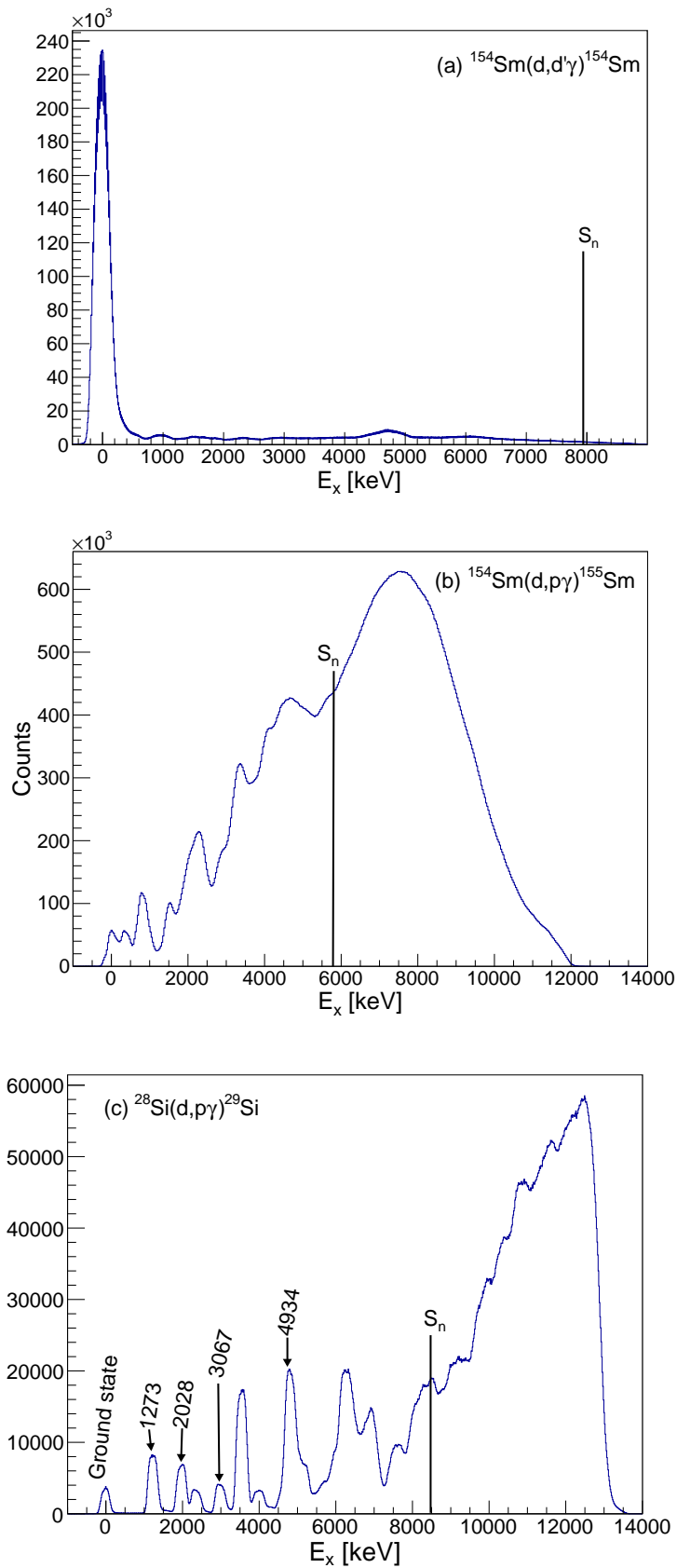


Figure 4.5. Excitation energy spectrum without a γ -ray coincidence requirement extracted from the $^{154}\text{Sm}(d,d'\gamma)$ (a), $^{154}\text{Sm}(d,p\gamma)$ (b) and $^{28}\text{Si}(d,p\gamma)$ (c). The solid vertical black lines indicates the location of neutron separation energy S_n .

its ground state. The ^{16}O contaminant is due to the samarium target which slowly oxidizes when exposed to air. By gating on a certain reaction, some background events and unwanted reactions were greatly reduced. The quality of the calibration is confirmed when we compare our experimental spectrum to known γ -ray transitions tabulated in the National Nuclear Data Center (NNDC) database [143]. In the next section, we discuss how the γ -ray detectors are calibrated.

4.1.2 γ -ray energy calibration and identification of γ -ray transitions

The excitation energy spectrum from the $^{28}\text{Si}(d,p\gamma)$ reaction (see Fig. 4.5 (c)) is gated on the states of interest, *e.g.*, $E_x=4934$ keV state, and the corresponding γ -ray spectra are extracted separately for all 24 NaI(Tl) and 6 LaBr₃:Ce detector set. Similar to the particle detector calibration, the NaI(Tl) detectors are calibrated assuming a linear calibration between expected energy deposit and the corresponding recorded spectrum channel number. Two well known γ -ray transitions, the 1273 keV $M1+E2$ transition with $J_{initial}^{\pi} = 3/2^+ \rightarrow J_{final}^{\pi} = 1/2^+$ and 4934 keV $E1$ transition with $J_{initial}^{\pi} = 3/2^- \rightarrow J_{final}^{\pi} = 1/2^+$, are chosen as reference points⁴ and the spectra from all the γ -detectors are subsequently aligned. The calibrated γ -ray spectrum for $^{28}\text{Si}(d,p\gamma)$ is shown in Fig. 4.6 for one NaI(Tl) detector. The observed energies were verified by comparing the extracted spectra to transitions tabulated in the NNDC database [143].

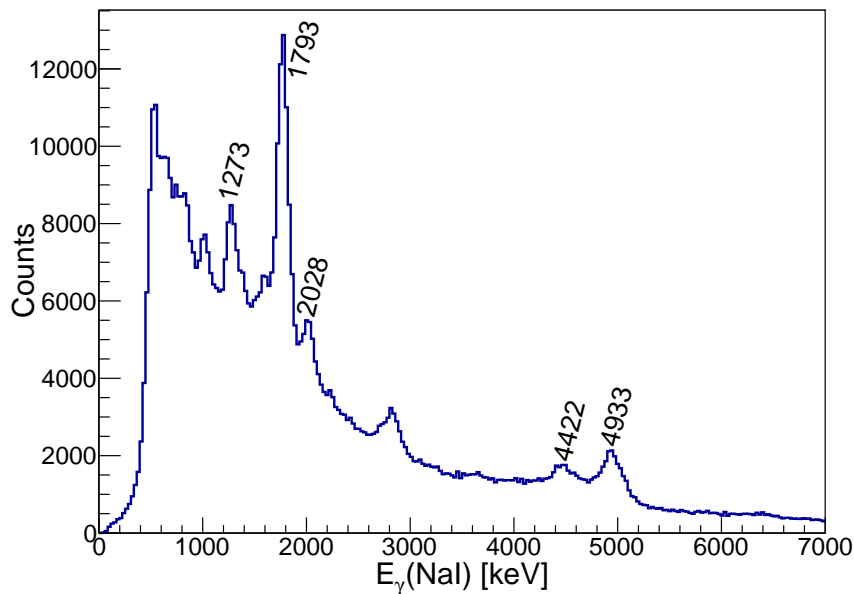


Figure 4.6. The calibrated γ -ray energy spectrum of ^{29}Si with identified energies retrieved from NNDC [143]. The spectra is obtained with a gate set on the $E_x=4934$ keV state in the excitation energy spectra shown in Fig. 4.5 (lower panel) for one NaI(Tl) detector.

⁴A choice for variety of γ -ray distribution is needed for calibration of the detectors over a broad range of deposited energies.

As discussed previously in sec. 3.2, the particle- γ events in coincidence are recorded with the time-to-digital converters (TDC). The ΔE -E provides the start signal for the TDC and the NaI(Tl) provides the TDC stop signal. In order to create sufficient time for the good events to be recorded efficiently the stop signal is delayed by 200 ns, which is longer than the pulse of the cyclotron. In addition, different signals cross the Leading Edge Discriminator (LED) threshold at different times. High-energy events have faster signal rise times and therefore cross the LED threshold first, similarly the low-energy events cross last. This phenomenon leads to the "walk"-effect, which is the timing difference that depends on the amplitude of the signal, with the implication that high- and low-energy events with identical time of occurrence will be effectively detected at different times. The "walk"-effect makes it difficult to obtain accurate timing information.

Fig. 4.7 shows the NaI(Tl) energy-time matrix for the $^{154}\text{Sm}(d,p\gamma)$ reaction. A curvature is

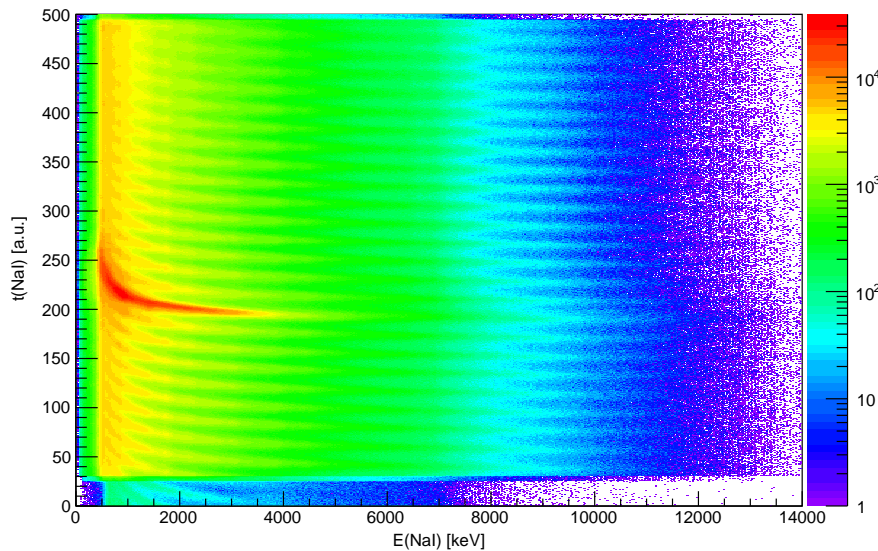


Figure 4.7. The $^{154}\text{Sm}(d,p\gamma)$ energy-time matrix for all NaI(Tl) detectors before "walk"-effect correction.

observed which increases for lower energies as the time of detection decrease. To compensate for this effect, a function of the form [132]:

$$t(E_\gamma) = a + \frac{b}{E_\gamma + c} + dx + 200, \quad (4.4)$$

is fitted to the energy-time matrix, where $t(E_\gamma)$ represent the detected time signal in arbitrary units (channels) and E_γ is the γ -ray energy. The coefficients a , b , c and d are determined in such a way that the time of detection for both the low- and high-energy events is independent of the signal amplitude and therefore $t(E_\gamma)$ becomes a constant function. Fig. 4.8 (upper panel) shows the "walk" corrected energy-time matrix in which all the 24 NaI(Tl) detectors are arbitrarily aligned at channel ≈ 200 which is represented by the offset of Eq. 4.4. The projected

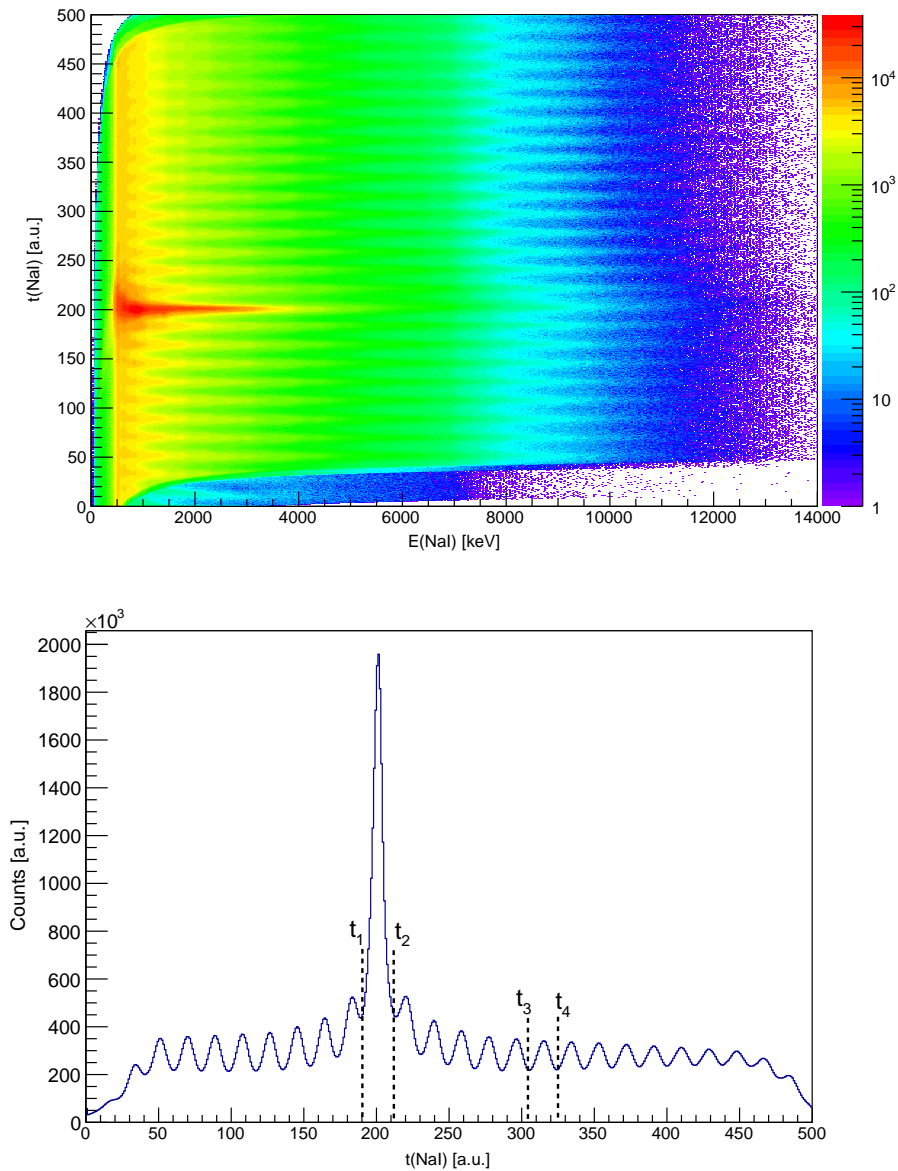


Figure 4.8. The energy-time matrix from the ^{154}Sm reaction after "walk" correction for the CACTUS array (upper panel). The projection of Fig. 4.8 (a) on the time-axis after signals were time calibrated from CACTUS (lower panel). The dashed lines (t_1, t_2) and (t_3, t_4) are gates on the prompt and random events, respectively, with the same width.

energy-time matrix on the y -axis is shown in Fig. 4.8 (lower panel), where the true events are detected with a narrow time window $t_2 - t_1 \approx 20$ ns. The random background events in the range (t_3, t_4) are subtracted from the prompt events (t_3, t_4) in order to obtain a true coincidence spectra. The same procedure has been performed for the $\text{LaBr}_3:\text{Ce}$ detectors and the particle detectors.

4.1.3 Particle- γ coincidences

By gating on the particle of interest, *e.g.*, protons from $^{154}\text{Sm}(d,p\gamma)$ reactions, the excitation energy E_x of the residual nucleus is extracted. Furthermore, setting a time gate on the prompt peak, the γ -rays detected in coincidence with particles of interest were identified. Now, one can construct a p- γ matrix in which the E_x of the residual nucleus is plotted against the γ -ray energy E_γ detected in coincidence with the particle corresponding to such E_x . Such a plot is shown in Fig. 4.9 and several characteristic features such as the $E_x=E_\gamma$ diagonal, which

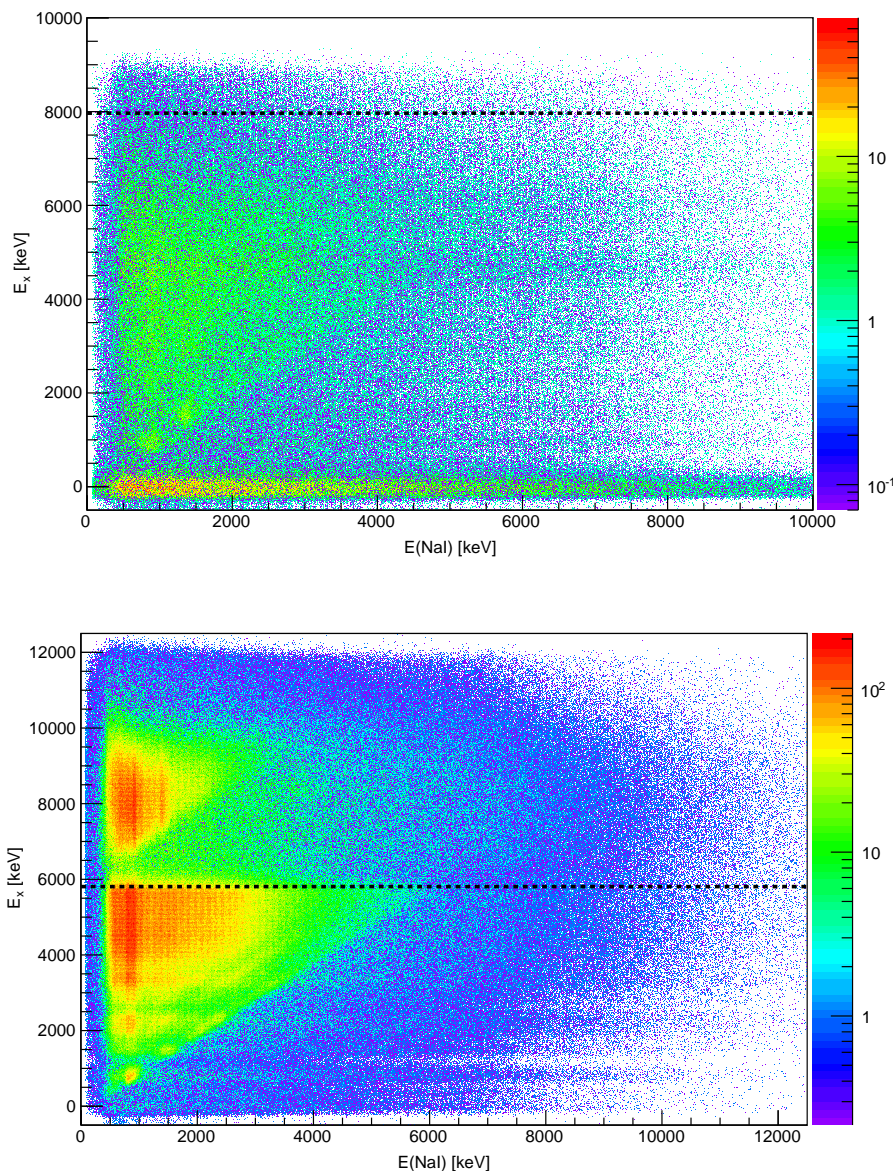


Figure 4.9. Excitation energy spectrum with a γ -ray coincidence requirement extracted from the $^{154}\text{Sm}(d,d'\gamma)$ (upper panel) and $^{154}\text{Sm}(d,p\gamma)$ (lower panel). Dashed lines indicates the location of the neutron separation energy S_n .

represents all the direct decays to the ground state, and a drop in coincidences events at $E_x \approx S_n$. Two triangular matrices are observed in Fig. 4.9 (lower panel) and are separated by the

dotted line representing S_n . Around S_n the nucleus has more probability of emitting a particle than a γ -ray, populating $A-1$ nucleus when assuming n or p emission.

4.2 The Oslo Method

The particle- γ coincidence matrices display a distribution of different γ -rays stemming from photoelectric absorption, Compton scattering, pair production and annihilation processes. An analytical technique, called the Oslo method, is employed to extract the nuclear level density (NLD) and the γ -ray strength function (γ SF) from the full energy γ -rays spectra. The Oslo method is divided into four major steps namely:

- (i) unfolding the continuum γ -ray spectra,
- (ii) extraction of first generation γ -rays from the unfolded continuum γ -ray spectra,
- (iii) simultaneous extraction of the NLD and the γ -ray transmission coefficient from the distribution of first-generation γ -rays, and
- (iv) finally normalization of the NLD and the γ SF using external experimental data.

Details of the Oslo method are discussed in this chapter.

4.2.1 Unfolding continuum γ -ray spectra

Radiation emitted from nuclear reactions interact with matter mainly through the following interactions: photoelectric absorption, Compton scattering, and pair production. These processes may deposit part or all of their energies to the atomic electrons as illustrated in Fig. 4.10. These broad distribution of energies is displayed in the continuum γ -ray spectra without distinct full energy γ -ray peaks, due to different reaction energy dependencies. To untangle the full energy γ -ray peaks from the background events, the folding iterative procedure [137] is applied to the continuum γ -ray spectrum and therefore removing contributions from the Compton scattered photons, single and double escape peaks, and one or both annihilation photons. Knowledge of how a photon detector used, *i.e.*, NaI(Tl) and LaBr₃:Ce detectors, respond to γ -rays over a broad energy range is essential. The relation between the total energy E measured by the detector and the incident γ -ray energy E_γ is referred to as the response function $R(E, E_\gamma)$ of the detector. The new and improved response functions of the NaI(Tl) detectors have been measured at OCL during in-beams measurements for several γ lines, populated with various inelastic scattering and transfer reactions, in ¹³C, ^{16,17}O, ²⁸Si, and ^{56,57}Fe [103] and allows for a more reliable determination of the detector's relative efficiency as a function of the γ -ray energy. In order to obtain the response function $R(E, E_\gamma)$ of the CACTUS array for all intermediate full-energy γ -ray peaks, an interpolation is made between the measured well known discrete γ -ray energies, as described in Ref. [103, 137]. This interpolation is performed for peak structures, such as the full energy (f), the single escape (s) and double escape (d), and the annihilation (a)

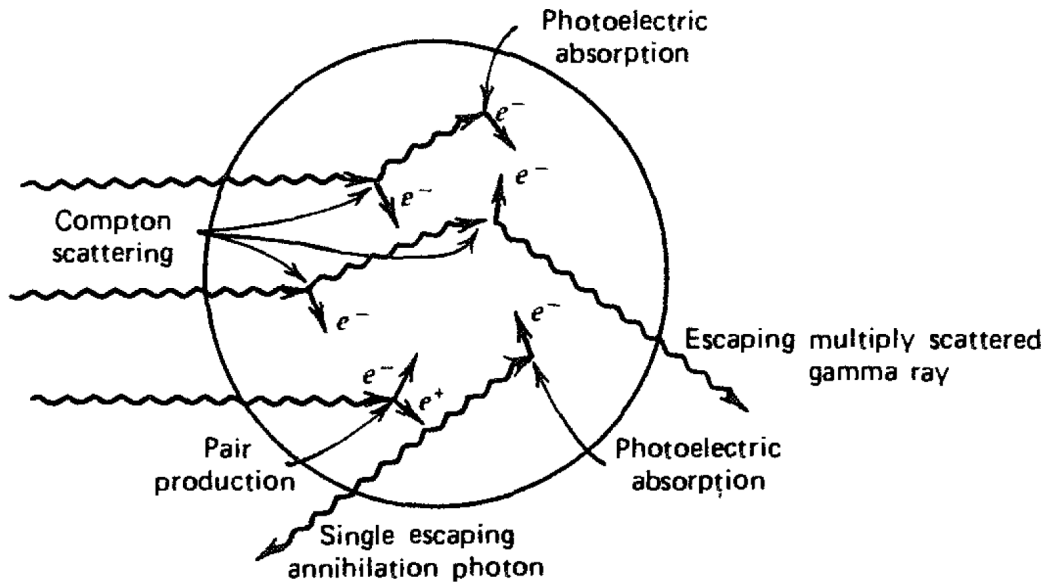


Figure 4.10. An illustration of energy deposition by photons through photoelectric absorption, Compton scattering, and pair production in the detector material, resulting in full and/or partial recovery of initial γ -ray energy. Figure taken from Ref. [136].

peaks, and a Gaussian distribution is now added at the interpolated peak positions, with proper intensities and energy resolutions. However, the interpolation of the Compton (c) background continuum, which is now the remaining part of the observed $R(E, E_\gamma)$ is made separately. Note that while the unfolding procedure follows the procedure described in Ref. [137], Table 1 of Ref. [137] should be overlooked and replaced with the recently measured [103] total γ -ray efficiencies and Full Width Half Maximum (FWHMs) deduced for the NaI(Tl) response functions, given in Tab. 4.1.

In Compton scattering, the incoming γ -ray that is scattered through an angle θ , with respect to its original position, transfers a portion of its energy E_γ to the electron as given by

$$E_e = E_\gamma - \frac{E_\gamma}{1 + \frac{E_\gamma}{m_e c^2} (1 - \cos \theta)}, \quad (4.5)$$

where $m_e c^2$ is the rest-mass of the electron (0.511 MeV). The interpolation is now performed between channels having the same γ -ray scattering angle θ , as illustration in Fig. 4.11.

4.2.2 The folding iteration technique

The response R_{ij} in channel i , when some energy is deposited in the detector by a γ -ray corresponding to channel j , is normalized such that $\sum_i R_{ij} = 1$. The normalization is performed for each incident γ -ray channel j . The folding iterative procedure is then applied to the unfolded

Table 4.1. New and improved measurements of intensities and FWHMs deduced for the NaI(Tl) response functions. To obtain best possible results of the unfolding, the resolution of the response function is currently set to 10% of the experimental resolution [103], and not 50% as cited in Ref. [137]. Parameters p represent the probabilities that an event will belong to at-least one of the five components of the spectrum (*i.e.* full energy (f), the single- (s) and double-escape (d), and the annihilation (a) peaks). ε_{tot} is the total γ -ray efficiency.

E_γ (keV)	FWHM[keV] ^a	ε_{tot}^b	P _f	P _c	P _s	P _d	P _a
800.0	72.8	0.923	0.5778	0.4222	0.0000	0.0000	0.0000
1600.0	103.1	1.003	0.3968	0.5896	0.0097	0.0000	0.0039
2400.0	135.7	1.023	0.3135	0.6537	0.0180	0.0000	0.0148
3200.0	163.9	1.037	0.2443	0.6918	0.0340	0.0071	0.0227
4000.0	188.2	1.045	0.1970	0.7059	0.0444	0.0086	0.0441
4800.0	207.3	1.053	0.1599	0.7256	0.0525	0.0092	0.0529
5600.0	222.7	1.059	0.1435	0.7489	0.0577	0.0084	0.0415
6400.0	238.6	1.066	0.1296	0.7671	0.0590	0.0081	0.0362
7200.0	263.5	1.071	0.1200	0.7760	0.0524	0.0089	0.0427
8000.0	287.4	1.073	0.1102	0.7850	0.0458	0.0096	0.0493
8800.0	310.2	1.076	0.0999	0.7953	0.0389	0.0104	0.0556
9600.0	331.9	1.079	0.0897	0.8054	0.0321	0.0111	0.0619
10400.0	351.9	1.081	0.0830	0.8126	0.0307	0.0113	0.0623

^aNormalized to 79.9 keV (6%) at 1.33 MeV.

^bNormalized to 1 at 1.33 MeV.

spectrum u as follows:

$$f = \mathbf{R}u, \quad (4.6)$$

where f is the folded γ -ray spectrum. The folding iterative procedure is performed in four steps as follows:

1. The observed raw γ -ray spectrum r is used as a trial function for the unfolded γ -ray spectrum u_0 , that is $u_0 = r$.
2. The first folded spectrum is calculated, as $f_0 = \mathbf{R}u_0$.
3. For the next trial function, the difference $r - f_0$ is added to the original trial function u_0 , as $u_1 = u_0 + (r - f_0)$.
4. The trial function u_1 is folded again to obtain f_1 , which is used again to determine the next trial function u_2 , $u_2 = u_1 + (r - f_1)$.

The above steps are repeated until f_n reproduces r within the experimental errors, where the number of iteration is typically $n \approx 10 - 30$.

The best unfolded γ -ray spectra, $u_n = u$, are obtained when the resolution of the response

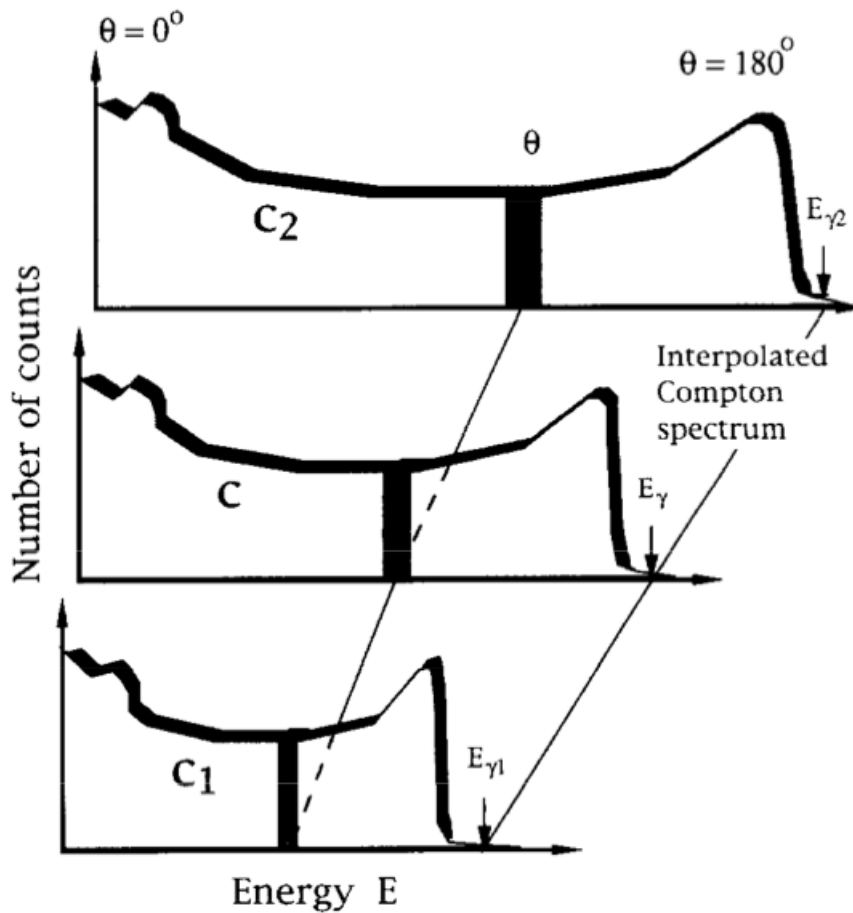


Figure 4.11. Illustration of the interpolation of the Compton part from measured response functions c_1 and c_2 [137]. The scattering angle θ increases as the energy transferred to the electron increases.

matrix FWHM^{resp} is 10% that of the observed experimental⁵ resolution FWHM^{exp} , (*i.e.*, $\text{FWHM}^{resp} = 0.1 \text{FWHM}^{exp}$). At this point, the so-called Compton subtraction technique is employed to the unfolded γ -ray spectrum u to reduce fluctuations on the spectra.

4.2.3 The Compton subtraction method

In order to smooth and subtract contributions of the Compton background events and preserve further fluctuations in the experimental spectra, the Compton subtraction technique [137] is applied. The unfolded γ -ray spectra $u_n = u$, which is now denoted u_0 , obtained from the folding iterative technique is used as input. A new spectra is defined which contains all the contributions without the Compton contribution as follows:

$$v(i) = p_f(i)u_0(i) + w(i), \quad (4.7)$$

⁵The 10% is applied in the current analysis to account for "tails" with negative counts on the sides of the full-energy peaks.

where $p_f u_0$ represents the full-energy contribution. The second term $w(i)$ contains contributions to the spectra as a result of single escape u_s , double escape u_d , and annihilation u_a peaks, is defined as follows:

$$\begin{aligned} w(i) &= u_s(i - i_{511}) + u_d(i - i_{1022}) + u_a(i_{511}) \\ &= p_s(i)u_0(i) + p_d(i)u_0(i) + \sum_i p_a(i)u_0(i). \end{aligned} \quad (4.8)$$

The i_{511} and i_{1022} represent channels corresponding to γ -ray energies 511 and 1022 keV, respectively. The probabilities $p_f(i)$, $p_s(i)$, $p_d(i)$, and $p_a(i)$, corresponding to an event in channel i , refer to the photo peak, single- and double-escape, and annihilation peak, are taken from Tab. 4.1 and were estimated from mono-energetic γ -ray transitions. The u_a spectrum is smoothed with the measured experimental resolution of 1.0 FWHM, in order to attain the energy resolution of the observed spectrum. The energy resolutions of the u_f , u_s and u_d spectra are determined by examining the observed spectrum (1.0 FWHM) and the response matrix (0.1 FWHM), giving the resolution of $\sqrt{1.0^2 - 0.1^2}$ FWHM = $\sqrt{1.01}$ FWHM \approx 1.0 FWHM. Once the spectra are smoothed, the Compton background $c(i)$ is extracted from the observed spectrum $r(i)$ by subtracting contributions $v(i) = u_f + u_s + u_d + u_a$, as follows:

$$c(i) = r(i) - v(i). \quad (4.9)$$

If we assume that the Compton background spectrum, $c(i)$, varies slowly as a function of the energy, the spectrum can be further smoothed to obtain the observed experimental resolution of 1.0 FWHM. The now smoothed Compton background spectrum, $c_{smoothed}(i)$ and the peak structures $w(i)$ are subtracted from the observed spectrum, $r(i)$, to obtain the unfolded γ -ray spectrum, $u_{unf}(i) = r(i) - [c_{smoothed}(i) + w(i)]$. The true γ -ray energy distribution, U_{true} , is obtained by correcting for the full energy probability $p_f(i)$ and the total experimental set-up γ -ray detection efficiency $\varepsilon_{tot}(i)$ (taken from Tab. 4.1) as follows:

$$U_{true}(i) = \frac{r(i) - [c_{smoothed}(i) + w(i)]}{p_f(i)\varepsilon_{tot}(i)}. \quad (4.10)$$

Fig. 4.12 shows the raw γ -ray spectra, r , the unfolded γ -ray spectra, u_{unf} , and the first generation γ -ray (discussed in sec. 4.2.4) spectra for the $^{154,155}\text{Sm}$ data. Similar data for ^{154}Sm data particle- γ coincidences collected using SiRi + 6 LaBr₃:Ce detectors is shown in Fig. 6.1 in Appendix A. The similarity between the folded and the raw γ -ray spectra can clearly be seen and shows the quality of the procedure. From the true γ -ray energy distribution spectrum $U_{true}(i)$, a matrix of excitation energy, E_x , versus unfolded first generation γ -rays can be constructed.

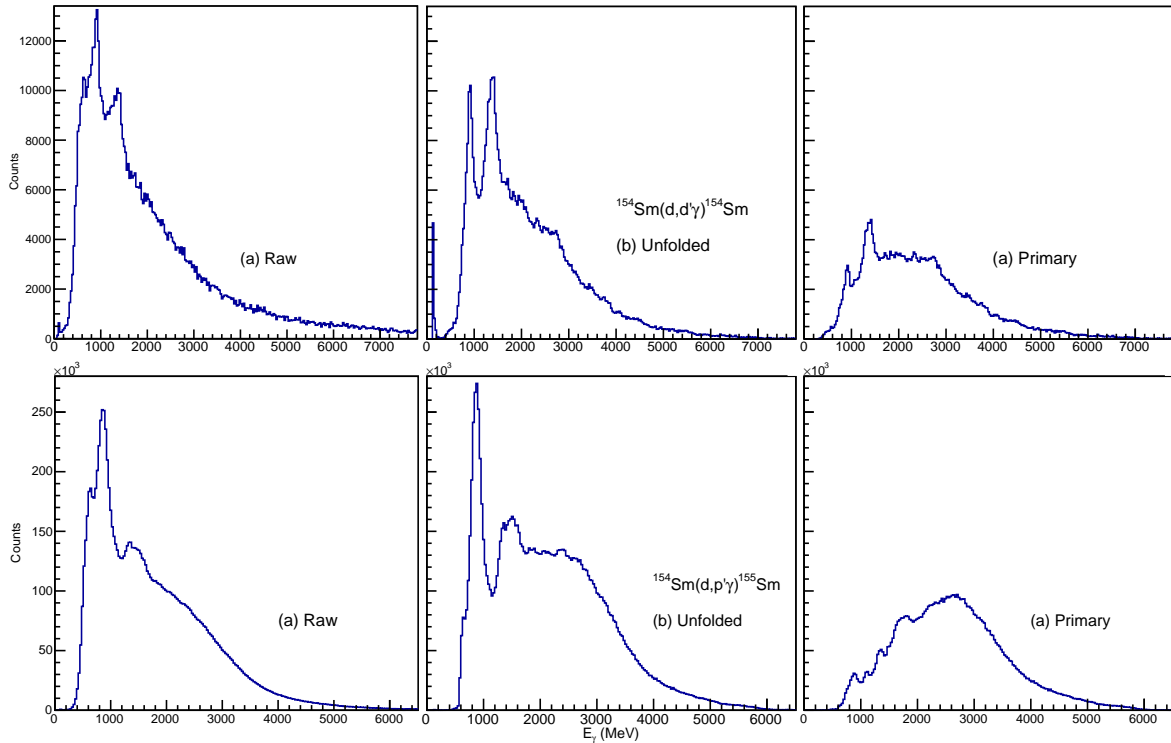


Figure 4.12. The raw γ -ray spectra (a), unfolded γ -ray spectra (b) and first generation (primary) γ -ray (discussed in sec. 4.2.4) spectra of $^{154,155}\text{Sm}$ from this work.

4.2.4 Extracting the first-generation γ -ray spectra

The unfolded γ -ray spectra contains all the full energy γ -rays from different highly-excited states at certain initial excitation energy E_x . The first emitted γ -rays from each decay cascade are called the first-generation (primary) γ -rays. An iterative procedure was developed by the OCL group to single out the first generation γ -rays in the unfolded total γ -ray spectra from decays that are emitted later in the cascade. The *first-generation method* is applicable under the assumption that the γ -decay pattern from any initial excited states is independent of how the nucleus was excited to this bin⁶. That is, the states populated by decays of higher-lying states have the same decay properties as the states populated directly by nuclear reactions at a specific excitation energy. The method is discussed in detail in Ref. [144], and only its main features are outlined below.

The spectrum h_i representing only the first generation γ -rays in each excitation energy bin i (with a typically width of 120 - 240 keV), could be isolated by subtracting the spectra from bins of lower energies, as follows:

$$h_i = f_i - g_i \quad \text{where} \quad g_i = \sum_{j < i} n_{ij} w_{ij} f_j. \quad (4.11)$$

⁶This assumption holds at high-excitation energies or higher level densities in which the target-projectile system attain a compound-like state prior to γ -emission.

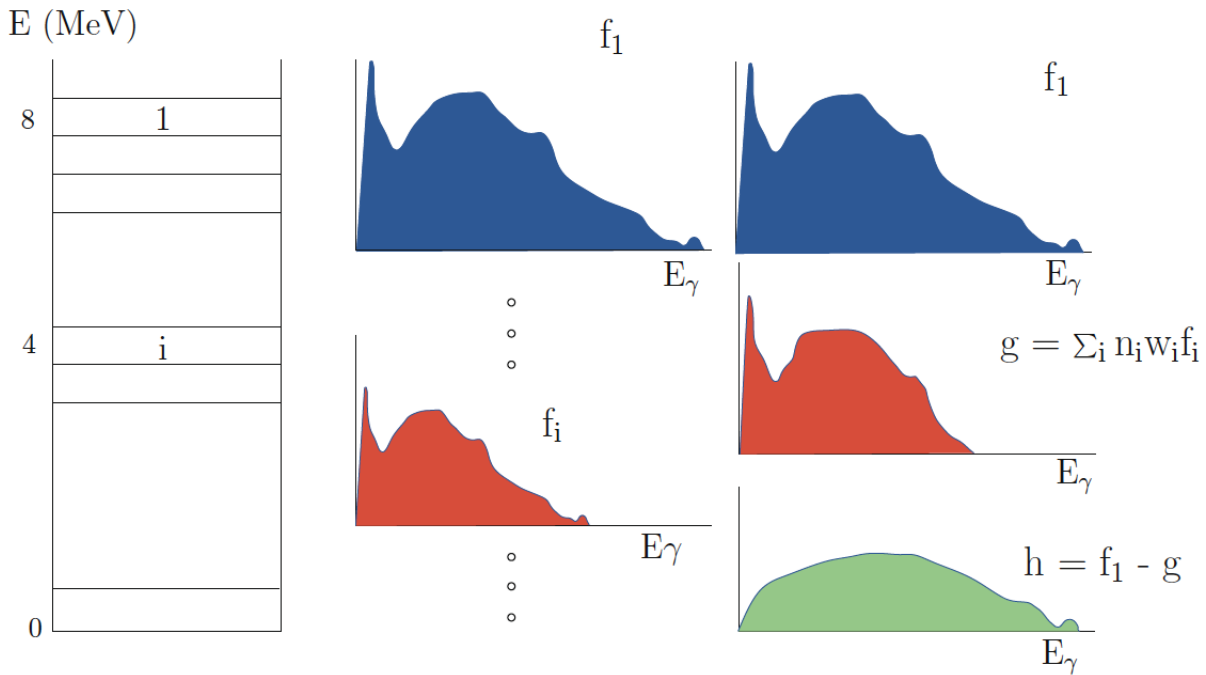


Figure 4.13. A demonstration of the procedure for extracting first-generation γ -rays. Figure from Ref. [145].

The parameter f_i denotes the unfolded total γ -ray spectrum of excitation energy bin i (initially denoted U_{true})⁷ and g_i is the weighted sum of all lower excitation energy spectra of the excitation bins $j < i$. This subtraction technique is illustrated in Fig. 4.13. The weighting function w_{ij} is initially unknown and represents the decay probability from bin i to bin j with $\sum_j w_{ij} = 1$. The w_{ij} corresponds directly to the first generation γ -ray spectrum and gives the branching ratios as a function of excitation energy. The former relation allows for the determination of w_{ij} and h_i through a fast converging iterative procedure [144]. Since the population cross-sections varies between different states, the normalization (or correction) factors n_{ij} for populating states in bin i and lower-lying levels in bin j are determined such that the total number of counts (or area) under each spectrum multiplied by n_{ij} , gives the same number of cascades. The correction factors n_{ij} can be determined using two separate methods depending on the experimental setup, thus the singles or the multiplicity method.

1. **Single normalization** : The singles particle spectrum which corresponds to the reactions listed in Tab. 3.2, without the requirement for coincidences, is proportional to the number of states populated, (*i.e.*, reaction yield) and therefore the number of cascades. The normalization coefficient is therefore given by the ratio of cross-sections for populating the initial state i and

⁷The notation is modified to reflect the parameters from the principal reference for the method [144].

for populating state j in a single spectra, as follows:

$$n_{ij} = \frac{S_i}{S_j}, \quad (4.12)$$

where S_i represents the singles cross-section which is proportional to the area of the spectrum $A(f_i)$ divided by the multiplicity M_i for bin i , thus $S_i = A(f_i)/M_i$.

2. Multiplicity normalization : The average γ -ray multiplicity M characterizes the average number of γ -rays in a cascade and is given by $\langle M_i \rangle = E_i / \langle E_\gamma \rangle$. E_γ and E_i represent the average energy of the γ -rays in the cascade decaying from energy level E_i in the populated bin E_i (This is the total energy carried by γ -rays when decaying from bin i). Using Eq. 4.12 the normalization coefficient, n_{ij} , can be calculated as follows:

$$n_{ij} = \frac{A(f_i) / \langle M_i \rangle}{A(f_j) / \langle M_j \rangle} = \frac{\langle M_j \rangle A(f_i)}{\langle M_i \rangle A(f_j)}, \quad (4.13)$$

where $A(f_i)$ is the area (or total number of cascades) of spectrum f_i .

Both normalization methods have been thoroughly tested and they are found to give similar results within the experimental uncertainties [146]. In the presence of isomeric states which have lifetimes greater than the TDC gate, the multiplicity method must be used to obtain accurate results⁸ and is used in this analysis. An area consistency check can be applied to Eq. (4.11) (see details in Ref. [144]), to verify that the area of the first generation γ -ray matrix $A(h_i)$ is equal to the area of the observed spectrum $A(f_i)$ minus the area of the sum spectra $A(g_i)$. Now, combining the results for each excitation energy bin i , we obtain the first generation matrix as shown in Fig. 4.14 (left panel) for the present experiment. In Fig. 4.14 (left panel), two valleys of less counts are observed around $E_\gamma \lesssim 0.9$ and 1.2 MeV and these are due to strong transitions to lower-lying states. In addition, as pointed out in Ref. [146] the direct reaction cross-section strongly depends on the intrinsic wave functions of low-lying states and as such these states may be populated very strongly by direct reactions, *e.g.*, (d,p) and be rather weakly/moderately populated by decays from higher-lying states. The procedure discussed above would lead to some higher-order γ -rays not being correctly subtracted in the first generation method and giving a vertical valley of low counts in the first generation γ -ray spectrum. The first generation matrix shown in Fig. 4.14 (left panel) exhibits such valleys at $E_\gamma \approx 0.9$ MeV and $E_\gamma \approx 1.2$ MeV and to compensate for this, the low-lying states have been excluded by artificially setting their weighting function w_{ij} to 0. The corrected first generation matrix is shown in 4.14 (right panel). In Fig. 4.15, the unfolded matrices obtained using the unfolding procedure and the first-generation γ -ray matrices obtained using the first-generation

⁸The photons from isomeric states are not detected in coincidence with the particle spectra and therefore these counts in the singles spectra do not account for the γ -ray transitions from these states.

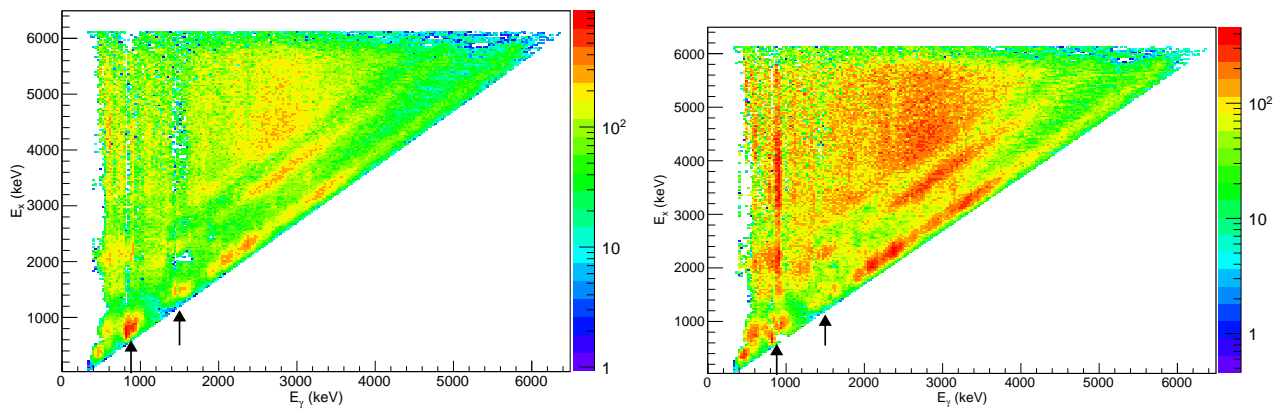


Figure 4.14. The first-generation γ -ray matrix for ^{155}Sm . The arrows point at vertical valleys of low counts in the initial matrix (left panel) that have been compensated in (right panel) (most easily visible at $E_\gamma \approx 0.9$ and 1.2 MeV).

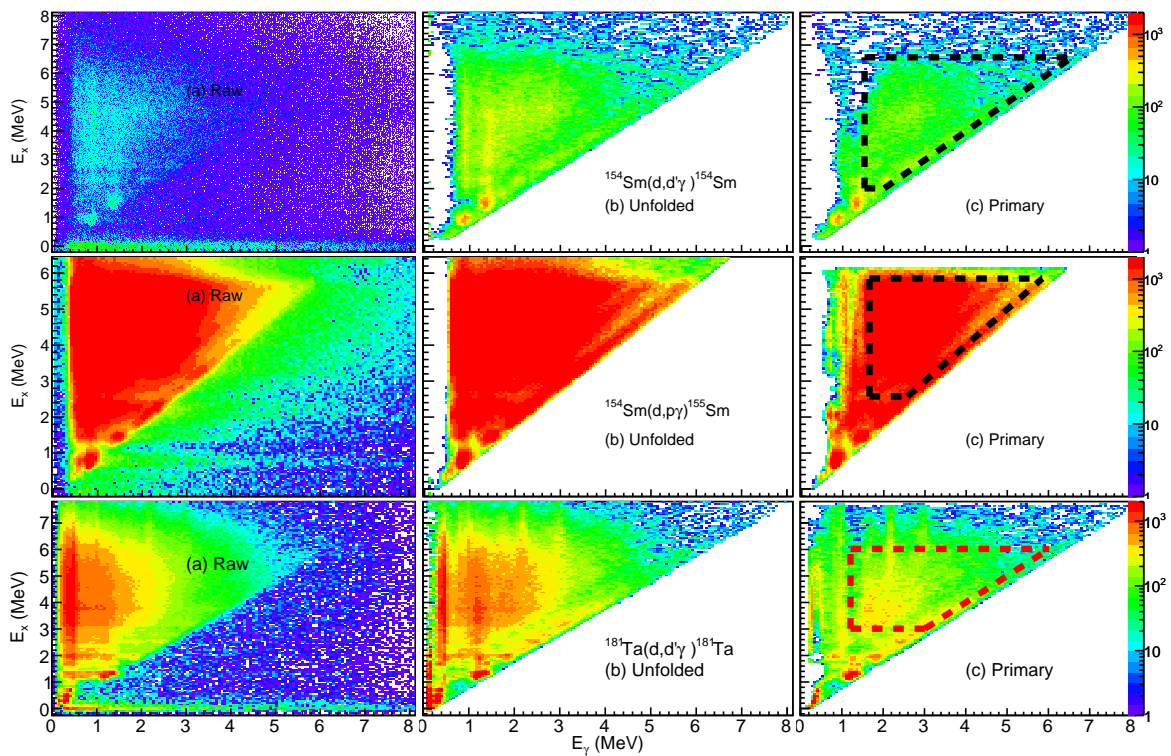


Figure 4.15. The raw, unfolded and first generation (primary) γ -ray matrix of $^{154,155}\text{Sm}$ and ^{181}Ta from this work. The dashed lines indicate the energy region in which the nuclear level density and γ -ray strength function were extracted.

method are shown for $^{154,155}\text{Sm}$ and ^{181}Ta .

4.2.5 Extracting the nuclear level density and the γ -ray strength function

The distribution of the first generation γ -rays can provide a wealth of information on nuclear properties, such as the NLD and the γ SF. The first generation γ matrix, which is given by $P(E_x, E_\gamma)$, gives the γ -decay probability of a γ -ray of energy E_γ decaying from an initial excitation energy E_x and is proportional to the level density $\rho(E_f)$ at the excitation energy $E_f = E_x - E_\gamma$ to which the nucleus decays and to the γ -ray transmission coefficient $\mathcal{T}(E_\gamma)$ at the γ -ray energy E_γ [29]:

$$P(E_x, E_\gamma) \propto \rho(E_x - E_\gamma)\mathcal{T}(E_\gamma), \quad (4.14)$$

where $\mathcal{T}(E_\gamma)$ only depends on the γ -ray energy and neither on the initial nor the final excitation energy, in accordance with the generalized Brink-Axel Hypothesis⁹ [66, 67]. It is assumed in Eq. 4.14 that the γ -decay pattern from any initial excitation energy bin is independent of how the nucleus was excited to this energy bin. That is the γ -decay is independent of whether the bin was populated directly from a nuclear reaction or is populated by decays from higher-lying states prior to γ -emission [43, 147]. The relation in 4.14 holds for decays in the region of high-level density where the nucleus supposedly attains a compound-like system before decaying, even though direct reactions are used. The subsequent decay of a compound state will be statistical since the formation of a compound state is relatively fast $\approx 10^{-18}$ s – 10^{-16} s and is much shorter than the typical lifetime of a state in the quasi-continuum of $\approx 10^{-15}$ s.

The distribution of the first generation γ -rays, which is also proportional to the γ -ray transition probability $\lambda_{i \rightarrow f}$ of the initial state i and the final state f , according to Fermi's golden rule [59] is as follows:

$$\lambda_{i \rightarrow f} = \frac{2\pi}{\hbar} \langle f | \hat{M} | i \rangle^2 \rho(E_x - E_\gamma), \quad (4.15)$$

where $\langle f | \hat{M} | i \rangle$ is the transition matrix element and is related to the γ -ray transmission coefficient, although strongly dependent on the conditions of the initial and final states. According to Eq. 4.14, the first generation matrix can be factorized into two factors $\rho(E_x - E_\gamma)$ and $\mathcal{T}(E_\gamma)$, and to get the exact solution, the experimental first generation matrix $P(E_x, E_\gamma)$ is then compared to the simulated solution $P_{th}(E_x, E_\gamma)$ as follows:

$$P_{th}(E_x, E_\gamma) = \frac{\rho(E_x - E_\gamma)\mathcal{T}(E_\gamma)}{\sum_{E_\gamma=E_\gamma^{min}}^{E_x} \rho(E_x - E_\gamma)\mathcal{T}(E_\gamma)}. \quad (4.16)$$

The experimental first generation matrix $P(E_x, E_\gamma)$ is normalized to unity, that is $\sum_{E_\gamma=E_\gamma^{min}}^{E_x} P(E_x, E_\gamma) = 1$, for every excitation energy bin in the range E_γ^{min} and $E_\gamma^{max} = E$. In order to

⁹The generalized Brink-Axel Hypothesis states that for any collective decay modes, the collective nuclear excitations built on excited states have the same properties as those built on the ground state.

improve the extraction of $\rho(E_x - E_\gamma)$ and $\mathcal{T}(E_\gamma)$, a global χ^2 minimization following Ref. [29] is performed for each iteration:

$$\chi^2 = \frac{1}{N_{free}} \sum_{E_x=E_x^{min}}^{E_x^{max}} \sum_{E_\gamma=E_\gamma^{min}}^{E_\gamma^{max}} \left(\frac{P_{th}(E_x, E_\gamma) - P(E_x, E_\gamma)}{\Delta P(E_x, E_\gamma)} \right)^2, \quad (4.17)$$

where N_{free} are the number of degrees of freedom (related to the total number of entries in $P(E_x, E_\gamma)$, $\rho(E_x - E_\gamma)$ and $\mathcal{T}(E_\gamma)$) and $\Delta P(E_x, E_\gamma)$ is the uncertainty in the experimental first-generation γ -ray matrix. During the iterative χ^2 minimization, the vector elements in $\rho(E_x - E_\gamma)$ and $\mathcal{T}(E_\gamma)$ are treated as free parameters. Boundary conditions (E_x^{min} , E_x^{max} , and E_γ^{min}) are set on the first generation matrix to ensure that the data used are dominated by the transitions from the statistical excitation-energy region, that the statistics is close to the S_n and finally to exclude any possible secondary γ -rays, such as yrast transitions which might have not been left out during first-generation method (see Ref. [29] for more details on boundary conditions). In Fig. 4.16, the merit of the fit between the experimental first generation spectra and simulated spectra for $^{154,155}\text{Sm}$ (that is, the product of the NLD and the γ -ray transmission coefficient) is shown for different excitation energy regions. A similar plot for $^{180,181}\text{Ta}$ is shown

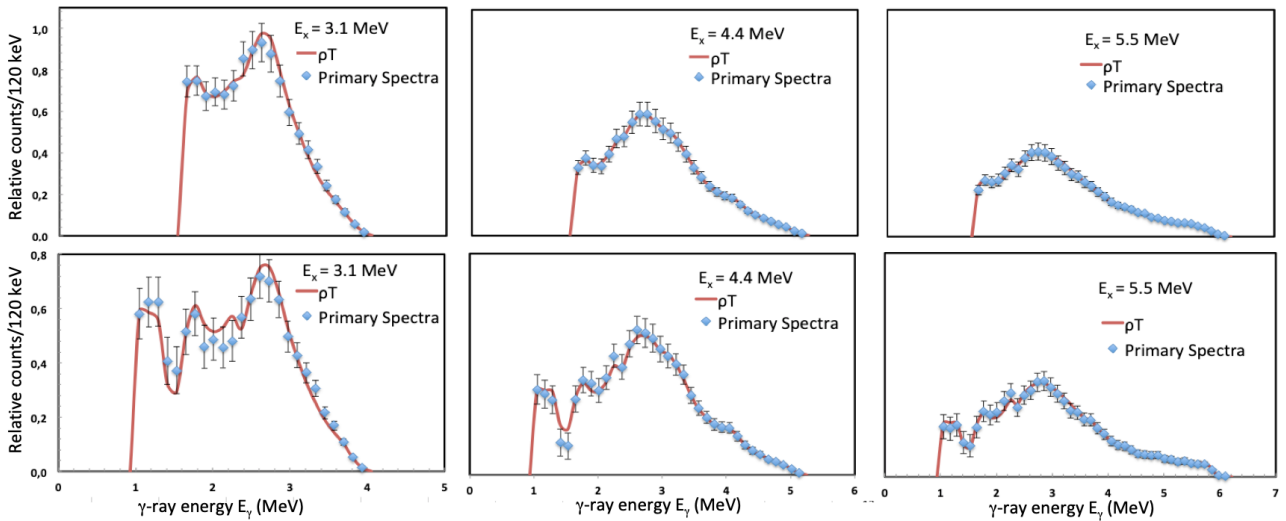


Figure 4.16. The experimental first generation γ -ray spectra (data points with error bars) from $(d,d'\gamma)^{154}\text{Sm}$ (upper panel) and $(d,p\gamma)^{155}\text{Sm}$ (bottom panel) reaction at 15 and 13 MeV beam, respectively, from selected initial excitation energies E_x (indicated in the figure) compared to the product $\rho(E_x - E_\gamma) \times \mathcal{T}(E_\gamma)$ (solid curve) following the global iterative χ^2 minimization of Ref. [29].

in Fig. 6.2 in Appendix A. The errors bars for points shown in Fig. 4.16 reflects the systematic uncertainties associated with the first generation matrices and statistical uncertainties. A satisfactory agreement validates the Brink Hypothesis [66]. Tab. 4.2 shows the regions where the χ^2 fit was performed for the first generation γ -ray matrices. In general, the agreement between the experimental data and the simulated spectra is very good as seen in Fig. 4.16, further confirming the quality of the procedure.

Table 4.2. The regions where the global χ^2 minimization was applied to $^{180,181,182}\text{Ta}$ and for $^{154,155}\text{Sm}$ matrices.

Reaction	E_{beam} (MeV)	E_{γ}^{min} (MeV)	E_x^{min} (MeV)	E_x^{max} (MeV)
$(^3\text{He}, \alpha\gamma)^{180}\text{Ta}$	34	1.73	2.97	6.35
$(\text{d}, \text{t}\gamma)^{180}\text{Ta}$	15	1.21	2.49	5.18
$(\text{d}, \text{d}'\gamma)^{181}\text{Ta}$	15	1.21	3.01	6.02
$(\text{d}, \text{d}'\gamma)^{181}\text{Ta}$	12.5	1.59	2.54	3.84
$(^3\text{He}, ^3\text{He}'\gamma)^{181}\text{Ta}$	34	1.63	2.57	7.38
$(\text{d}, \text{p}\gamma)^{182}\text{Ta}$	12.5	1.54	2.54	5.94
$(\text{d}, \text{d}\gamma)^{154}\text{Sm}$	13&15	1.53	2.01	6.57
$(\text{d}, \text{p}\gamma)^{155}\text{Sm}$	13&15	1.65	2.49	5.85

4.2.5.1 Normalization

At this point, only the functional form of the NLD $\rho(E_x - E_{\gamma})$ and the γ -ray transmission coefficient $\mathcal{T}(E_{\gamma})$ has distinctively been defined in the global iterative procedure. The structures in $\rho(E_x - E_{\gamma})$ and $\mathcal{T}(E_{\gamma})$ will not be altered from this point onward in the analysis. The factorization in Eq. 4.14 leads to infinitely many solutions, which give identical fits to $P(E_x, E_{\gamma})$ through infinite combinations of transformation parameters α , A and B , as follows:

$$\tilde{\rho}(E_x - E_{\gamma}) = A\rho(E_x - E_{\gamma}) \exp[\alpha E_x - E_{\gamma}], \quad (4.18)$$

and

$$\tilde{\mathcal{T}}(E_{\gamma}) = B\mathcal{T}(E_{\gamma}) \exp[\alpha E_{\gamma}]. \quad (4.19)$$

The transformation parameters α , A and B correspond to physical solutions and are deduced from external experimental data to get the exact solution to Eq. 4.14.

4.2.5.2 Nuclear Level density

For the NLD, the slope correction parameter α and the absolute value A in Eq. 4.18 are determined by normalizing $\tilde{\rho}(E_x - E_{\gamma})$ to the level density of known discrete states [143] at low $E_x \lesssim 2$ MeV and interpolated to fit the total NLD $\rho(S_n)$ at high E_x , as shown in Fig. 4.17. The total NLD at the neutron separation energy $\rho(S_n)$ is calculated from the average resonance spacing, D_0 , [58] for s-wave neutrons, as follows [29]:

$$\rho(S_n) = \frac{2\sigma^2}{D_0(J_T + 1) \exp[-(J_T + 1)^2/2\sigma^2] + J_T \exp(-J_T^2/2\sigma^2)}, \quad (4.20)$$

where J_T is the ground-state spin of the target nucleus in (n, γ) or (p, γ) reactions (for the A-1 nucleus). Since no experimental information is available for the spin and parity distributions of the NLD at S_n , we rely on the model dependent formulation of the NLD at the S_n . Four different

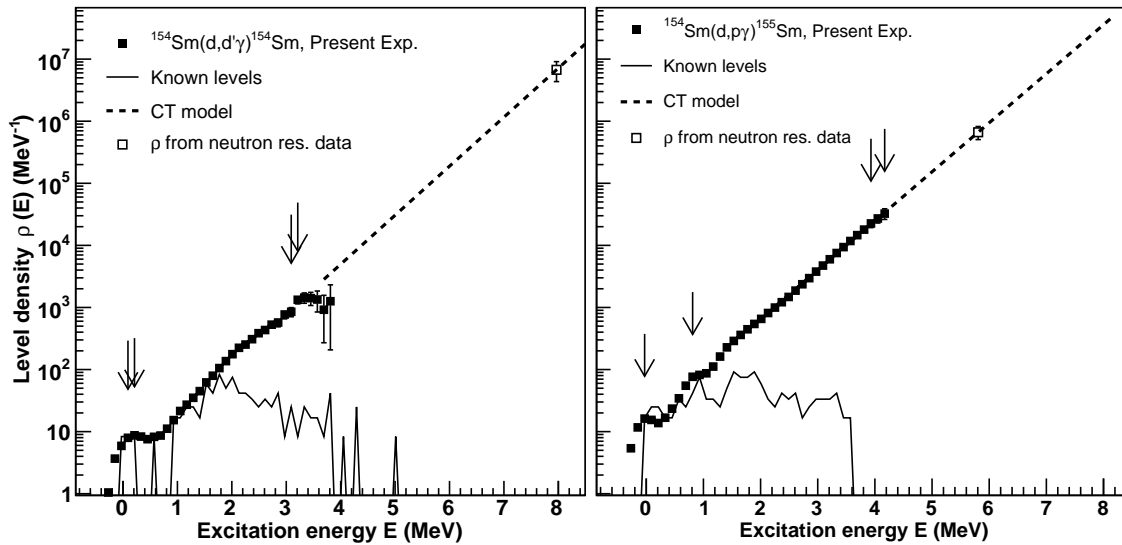


Figure 4.17. The normalized experimental NLDs for $^{154,155}\text{Sm}$. The set of vertical arrows indicate the location at which the χ^2 minimization was performed.

level density models, in particular spin distribution models, were considered for the $^{180,181,182}\text{Ta}$ cases, namely the Back-shifted Fermi-Gas (BSFG) [47, 148], Constant Temperature (CT) model [42], Constant Temperature + Fermi Gas (CT+FG) [40] and Hartree-Fock-Bogoliubov plus combinatorial (HFB+comb.) [53] models. For the $^{154,155}\text{Sm}$ case, three models were used, namely the BSFG model based on the energy- and mass-dependent spin cut-off parameter formulation by von Egidy and Bucurescu (E&B2009) [48] (see Eq. 2.4) and the rigid moment of inertia formula (E&B2006) [47] (see Eq. 2.5), and finally the Constant Temperature (CT) model [42] (see Eq. 2.8) of Gilbert and Cameron. Details on the models mentioned above are found in sec. 2.1. The parameters obtained and used for the normalizations are listed in Tab. 4.3. In Fig. 4.18, the NLD of ^{155}Sm normalized using the different spin distribution models discussed above. The same normalization was performed for the ^{154}Sm and $^{180,181,182}\text{Ta}$ isotopes.

As discussed in chap. 2, the spin distribution at low-excitation energy using Eq. 2.6 was estimated for $^{154,155}\text{Sm}$ and it is shown in Fig. 4.19. Also a range of different spin cut-off parameters as a function of excitation energies for various normalization is shown in Fig. 4.20. The extracted experimental NLD data only reach the highest-excitation energy $E_x < S_n$ and therefore to bridge the gap between the highest-excitation energy point and S_n , an interpolation is made using the CT model [42]. This interpolation can be seen in Fig. 4.17 (or Fig. 6.3 in Appendix A), where a set of arrows indicate the region in which the χ^2 minimization allowing for a reliable fit to the data was performed.

The normalization procedure discussed above is more reliable in the case where the nucleus was populated using the inelastic scattering ($^3\text{He}, ^3\text{He}'\gamma$) and the neutron pick-up reactions ($^3\text{He}, \alpha\gamma$), and ($d, t\gamma$). The transfer or light-ion ($d, p\gamma$) reaction used in the Samarium experiment,

Table 4.3. Parameters used for extraction and normalization of $\rho(E_x)$ and $\mathcal{T}(E_\gamma)$ in $^{154-155}\text{Sm}$ and $^{180-182}\text{Ta}$.

Isotope	J_π	S_n (MeV)	$\sigma(S_n)$	D_0 (eV)	a (MeV ⁻¹)	$E1$ (MeV)	$\rho(S_n)$ (10 ⁶ MeV ⁻¹)	$\rho_{red}(S_n)$ (10 ⁶ MeV ⁻¹)	$\langle\Gamma_\gamma(S_n)\rangle$ (meV)
^{154}Sm	0 ⁺	7.97	6.61±0.66 ^f	3.10±1.25 ^b	18.15	-0.37	7.43±2.80 ^f		83.00±17.44 ^b
^{155}Sm	3/2 ⁻	5.81	6.64±1.58 ^f	112.00±15.00 ^d	17.95	-0.56	0.66±0.16 ^f	0.49±0.12	94.00±7.00 ^d
^{180}Ta	1 ⁺	6.65	4.93±0.49 ^a	0.80±0.24 ^b	17.57	-1.09	10.67±3.50 ^b		62.00±5.77 ^b
^{181}Ta	7/2 ⁺	7.58	4.96±0.50 ^a	1.11±0.11 ^c	17.53	-0.37	14.58±2.80 ^a		51.00±1.58 ^c
^{182}Ta	3 ⁻	6.06	4.88±0.49 ^a	4.18±0.15 ^c	17.44	-1.04	2.02±0.28 ^a		59.00±1.83 ^c

^aCalculated with the back-shifted Fermi gas model [48].

^bEstimated values

^cAverage value from Refs. [58, 149].

^dTaken from Ref. [150].

^fCalculated with the rigid moment of inertia formula of von Egidy and Bucurescu [47].

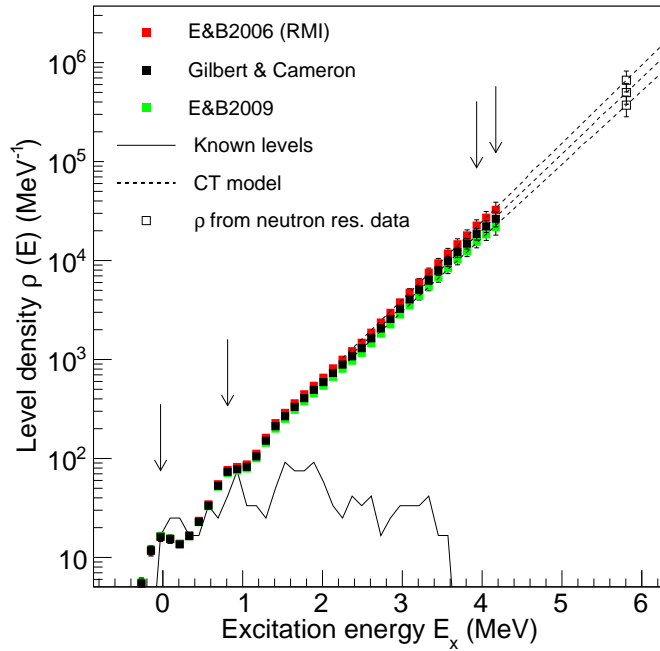


Figure 4.18. The normalized experimental NLDs for ^{155}Sm using different spin distribution models. The set of vertical arrows indicate the location in which χ^2 minimum was performed.

particularly $^{154}\text{Sm}(d,p\gamma)^{155}\text{Sm}$, may not populate all high-spins levels available in the nucleus and this will influence the observed first generation γ -ray spectra $P(E_x, E_\gamma)$. In order to account for the not populated levels, $P(E_x, E_\gamma)$ is fitted by the product of $\rho_{red}(E_x - E_\gamma)\mathcal{T}(E_\gamma)$ as in Eq. 4.14, where $\mathcal{T}(E_\gamma)$ is assumed to be independent of the spin according to the generalized Brink-Axel Hypothesis and $\rho_{red}(E_x - E_\gamma)$ is the reduced NLD extracted by assuming a lower value of $\rho(S_n)$. To estimate a reduced $\rho_{red}(S_n)$, the highest E_x^{spin} is determined where the reliable spin assignment for the (d,p γ) and (d,p) has been made [143]. Now the theoretical spin

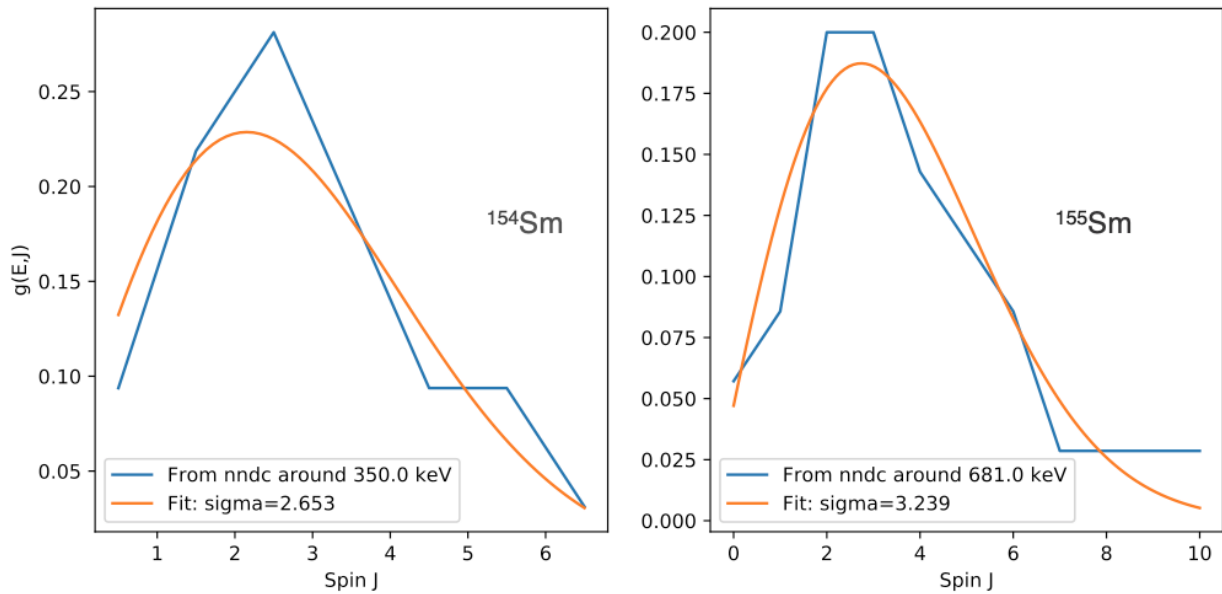


Figure 4.19. The normalized spin distribution at low-excitation energies for $^{154,155}\text{Sm}$.

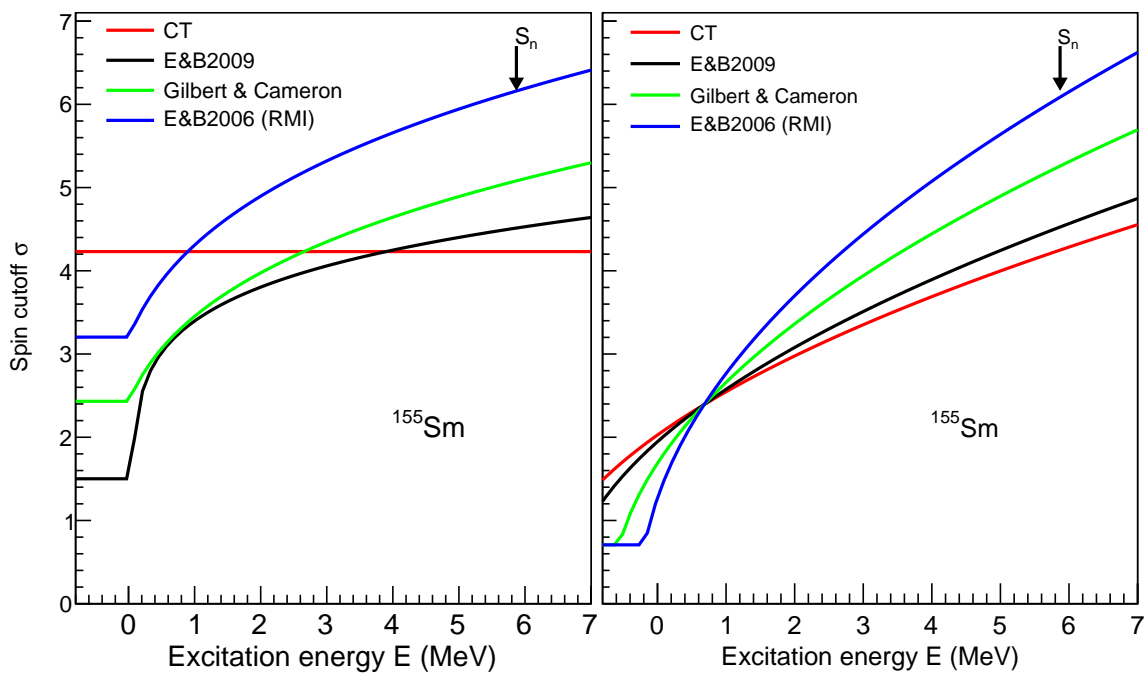


Figure 4.20. The spin cut-off parameter as a function of excitation energy for ^{155}Sm . The CT model assumes a linear dependence of the spin cut-off on excitation energy. Represented in the right panel, are similar spin cut-off parameters models following Eq. 2.7, where a fit is made to reliable spins at known discrete lower-lying levels tabulated in NNDC [143].

distribution $g(E_x^{spin}, J)$ (see Eq. 2.6) is calculated up to to the highest observed spin at E_x^{spin} . The calculated spin distribution for $^{154}\text{Sm}(d,p\gamma)^{155}\text{Sm}$ is shown in Fig. 4.21, with $\sigma(E_x^{spin}=2.0 \text{ MeV})=4.881$. The ratio r between the integral of $g(E_x^{spin}, J)_{populated}$ up to the highest spin J and the total integral of $g(E_x, J)_{total}$ is determined and assuming this ratio holds up to S_n , the

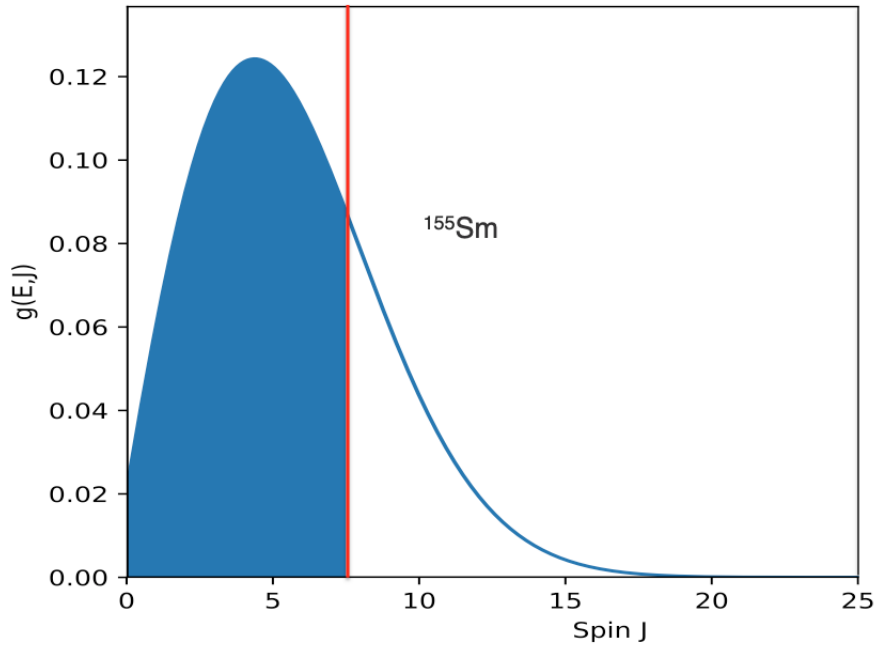


Figure 4.21. The spin distribution at $E_x^{spin}=1.987$ MeV, with $\sigma(E_x^{spin})=4.881$ determined using the spin cut-off of Eq. 2.5, for ^{155}Sm . The red line indicates the highest spin populated $J=15/2$ and the colored blue area shows possible spin population by the (d,p γ) or (d,p) reaction, corresponding to 73.4% of the totals levels being populated.

reduced NLD ρ_{red} is given by [151]:

$$\rho(S_n)_{red} = r \times \rho(S_n)_{tot}. \quad (4.21)$$

At low-excitation energy, a reduced list of discrete states was made by selecting only low-lying energy levels, which were directly populated by the (d,p γ) and (d,p) reaction¹⁰, as tabulated in the National Nuclear Data Center [143].

4.2.5.3 The γ -ray strength function

The slope correction $\exp[\alpha E_\gamma]$ in Eq. 4.19 for the $\mathcal{T}(E_\gamma)$ has already been determined through the normalization of $\rho(E_x - E_\gamma)$, as discussed above. The absolute normalization parameter B of $\mathcal{T}(E_\gamma)$ is determined using the experimental average total radiative width $\langle \Gamma_\gamma \rangle$ of s-wave neutron capture resonances at S_n [96]. Assuming that the statistical decays are dominated by dipole transitions ($l=1$), the $\langle \Gamma_\gamma \rangle$ can be related to the γ -ray transmission coefficient, $\tilde{\mathcal{T}}$, as [96]:

$$\begin{aligned} \langle \Gamma_\gamma(S_n, J_T \pm \frac{1}{2}, \pi_T) \rangle &= \frac{B}{4\pi\rho(S_n, J_T \pm \frac{1}{2}, \pi_T)} \int_0^{S_n} \tilde{\mathcal{T}}(E_\gamma) \times \rho(S_n - E_\gamma) dE_\gamma \\ &\times \sum_{J=-1}^1 g(S_n - E_\gamma, J_T \pm \frac{1}{2} + J), \end{aligned} \quad (4.22)$$

¹⁰Considering that dipole transitions give final spins in the range $\Delta L=-1,0,1$.

where J_T and π_T are the spin and parity of the target nucleus in its ground state in the (n, γ) reactions, and $\rho(S_n - E_\gamma)$ is the experimental NLD. The spin distribution $g(E_\gamma, J)$ is given by Eq. 2.6. The summation and integral run over all final levels with spin that are accessible by $E1$ or $M1$ transitions with energy E_γ .

Due to the uncertainties and possible systematic errors of the Oslo method (as discussed in Ref. [146]) to extract the first generation γ -rays at $E_\gamma \leq E_\gamma^{min}$ and therefore the determination of $\langle \Gamma_\gamma \rangle$, an extrapolation is needed in order to calculate the integral of Eq. 4.22 as $E_\gamma \rightarrow 0$. An exponential function is used to extrapolate the present experimental data E_γ^{exp} which only span the energy region $E_\gamma^{min} \lesssim E_\gamma^{exp} \lesssim S_n$, as $E_\gamma^{min} \rightarrow 0$ and $E_\gamma^{exp} \rightarrow S_n$, see Fig. 4.22. This

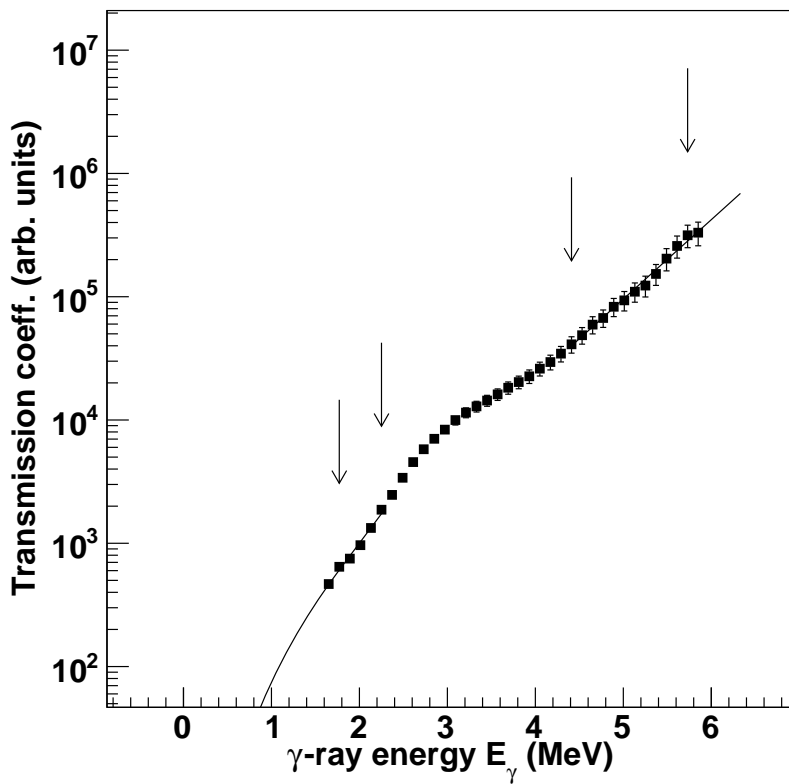


Figure 4.22. The extrapolated γ -ray transmission coefficient of ^{155}Sm . The set of arrows at low and high γ -ray energies E_γ indicate the region where the exponential function has been fitted.

extrapolation contributes not more than 15% to the total radiative width given in Eq. 4.22. The possible errors as a result of poor extrapolation have been pointed out to be of minor importance [96, 146]. The γ -ray transmission coefficient, following Eq. 4.19, can be expressed as [96]:

$$BT(E_\gamma) = B \sum_{XL} \mathcal{T}_{XL}(E_\gamma) \approx B[\mathcal{T}_{E1}(E_\gamma) + \mathcal{T}_{M1}(E_\gamma)], \quad (4.23)$$

for the electromagnetic character X and the multipolarity L , which is assumed to be 1, (*i.e.*

dipole). The total experimental γ SF is then extracted as follows [58]:

$$\begin{aligned} f(E_\gamma) &= f_{E1}(E_\gamma) + f_{M1}(E_\gamma) \\ &= \frac{1}{2\pi E_\gamma^3} BT(E_\gamma). \end{aligned} \quad (4.24)$$

The experimental γ SF for $^{154,155}\text{Sm}$ are shown in Fig. 4.23 (and for $^{180,181,182}\text{Ta}$ in Fig. 6.4 in Appendix A), with and without the spin population correction for ^{155}Sm as outlined in the

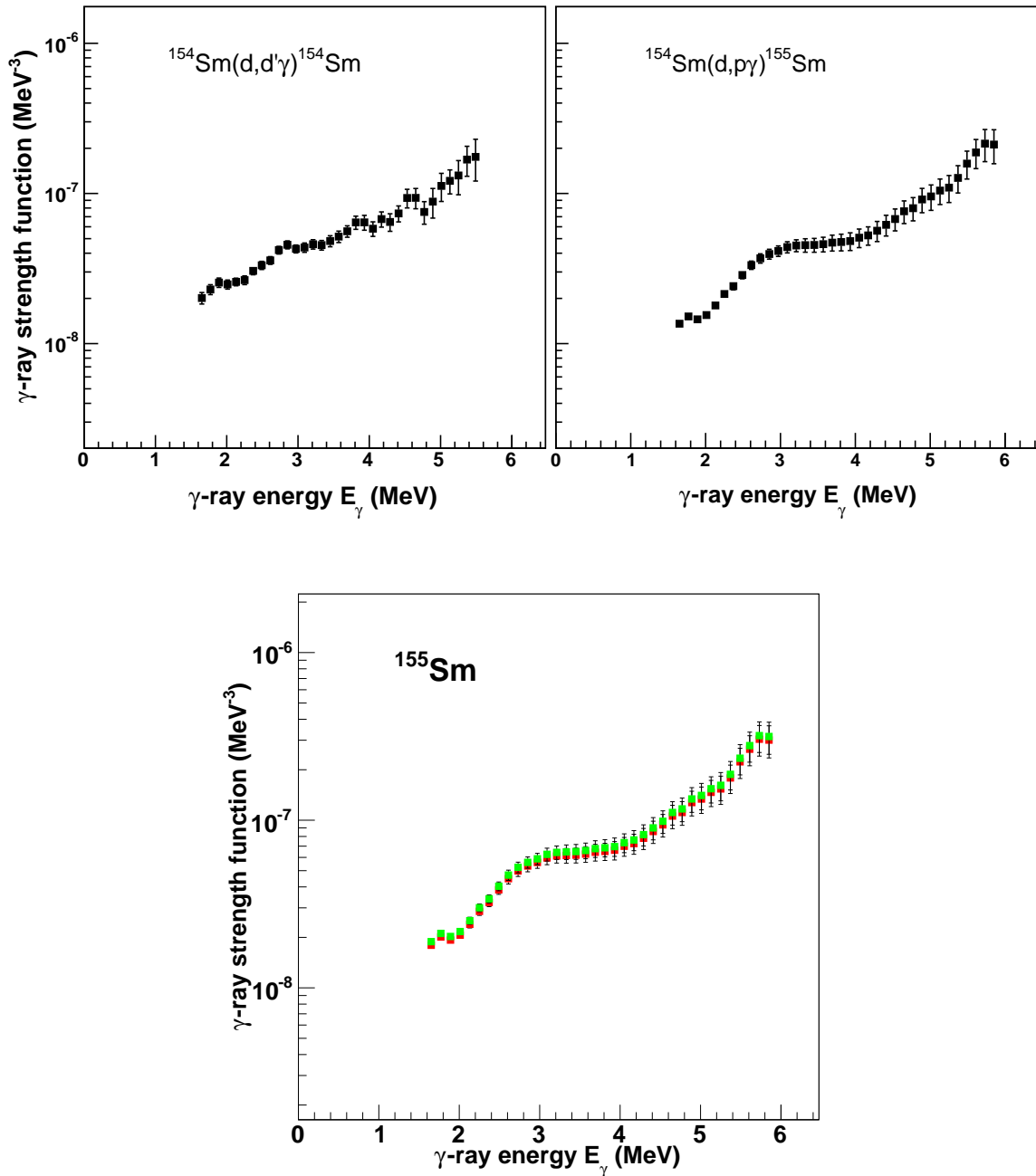


Figure 4.23. The experimental γ SF of $^{154,155}\text{Sm}$ (upper panel). The green data represent the γ SF of ^{155}Sm with spin population correction and the red data points, the γ SF without the spin population correction (lower panel).

previous section. It is observed that both γ SF of ^{155}Sm shown in Fig. 4.23 have a similar slope,

which implies that the effect of the spin population correction can be considered negligible. For the remainder of the analysis the uncorrected γ SF will be used.

4.2.6 Challenges and possible systematic errors in the normalization procedure

The uncertainties obtained using the Oslo method only provide statistical and systematic uncertainties of the unfolding and first generation methods, and do not account for the potential significant contribution of the uncertainties related to measured D_0 and $\langle \Gamma_\gamma(S_n) \rangle$ parameters. By replacing D_0 with $D_0 \pm \Delta D_0$ and $\langle \Gamma_\gamma(S_n) \rangle$ with $\langle \Gamma_\gamma(S_n) \rangle \mp \Delta \langle \Gamma_\gamma(S_n) \rangle$, it is possible to obtain the upper and lower error bands of the NLD and γ SF. ΔD_0 and $\Delta \langle \Gamma_\gamma(S_n) \rangle$ represent uncertainties of the $l=0$ neutron resonance spacing D_0 and the total radiative width $\langle \Gamma_\gamma \rangle$, respectively. In addition, the rigid moment of inertia Θ spin cut-off parameter in Eq. 2.5 is multiplied by reduction factor η at S_n to obtain systematic error bands, where $\eta=0.8, 1.0$ and 1.2 for the lower, mean and upper γ SF. In addition, neither the $l=0$ neutron resonance spacing D_0 nor the average radiative width $\langle \Gamma_\gamma \rangle$ experimental values have been measured for ^{154}Sm and ^{180}Ta , due to unavailability target nuclei for the (n,γ) reactions. Therefore, theoretical values of $\langle \Gamma_\gamma \rangle$ for ^{154}Sm and ^{180}Ta are taken directly from TALYS reaction code, where $\langle \Gamma_\gamma \rangle$ values are estimated using a spline fit function and are given in Tab. 4.3.

In order to estimate the total NLD $\rho(S_n)$, both $\rho(E_x)$ and $\mathcal{T}(E_\gamma)$ of ^{154}Sm and ^{180}Ta are normalized to those of neighboring isotopes $^{153,155}\text{Sm}$ and $^{181,182}\text{Ta}$ on the basis of having similar slopes. It has been shown in Ref. [25, 122, 152] that $\rho(E_x)$ and $\mathcal{T}(E_\gamma)$ of neighboring isotopes have similar slopes independent of the normalization procedure. Using Eq. 4.20, D_0 of ^{154}Sm and ^{180}Ta are calculated from the estimated $\rho(S_n)$, shown in Tab. 4.3 and the respective nuclear level densities are shown in Fig. 4.17 (for ^{180}Ta , see Fig. 6.3 in Appendix A). Furthermore, in the case of ^{154}Sm an exponential function was used to fit the experimental D_0 and $\langle \Gamma_\gamma \rangle$ values of the neighboring even-even isotopes $^{144-148,152}\text{Nd}$, $^{148-152}\text{Sm}$ and $^{154-158}\text{Gd}$, in order to estimate and compare the D_0 and $\langle \Gamma_\gamma \rangle$ of ^{154}Sm to those estimated using the procedure above. Fig. 4.24 shows the estimated value of ^{154}Sm at neutron number 92, which is considered as the range $D_0 = 1.7 - 2.7$ eV (left panel) and $\langle \Gamma_\gamma \rangle = 79 - 168$ meV (right panel). The estimated $\langle \Gamma_\gamma \rangle$ value taken from TALYS lies within the range $\langle \Gamma_\gamma \rangle = 79 - 168$ meV. The D_0 calculated from the estimated $\rho(S_n)$ using Eq. 4.20 lies outside the range $D_0 = 1.7 - 2.7$ eV but gives a reasonable slope of the ^{154}Sm experimental NLD compared to that of the neighboring ^{155}Sm isotope, as shown in Fig. 4.25.

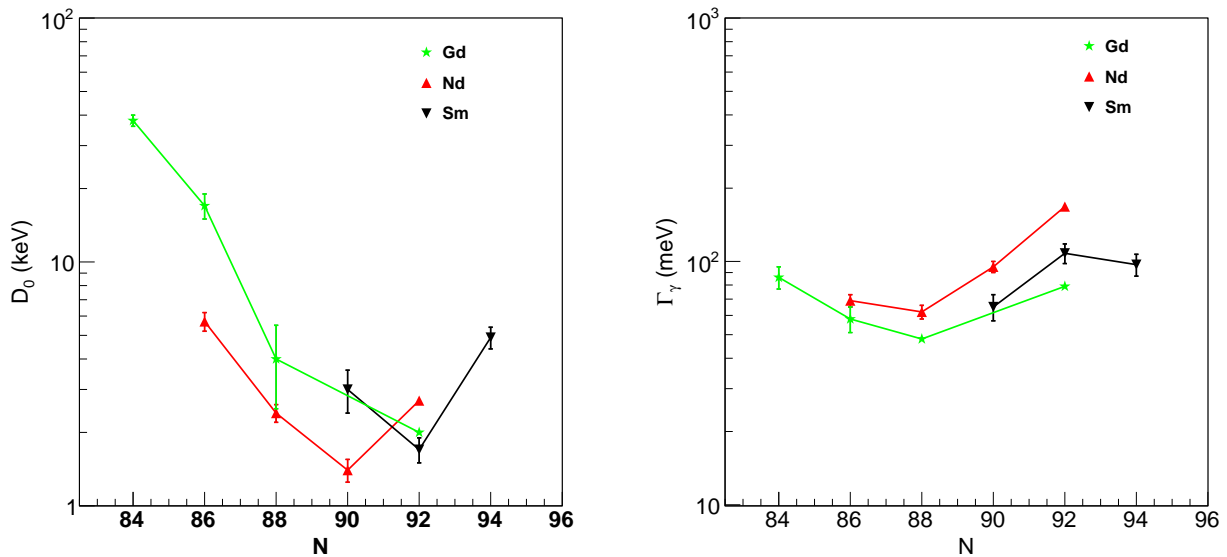


Figure 4.24. The experimental $l=0$ neutron resonance spacing D_0 and the average radiative width $\langle \Gamma_\gamma(S_n) \rangle$ plotted against the neutron number N of even-even $^{144-148,152}\text{Nd}$, $^{148-152}\text{Sm}$ and $^{154-158}\text{Gd}$ isotopes.

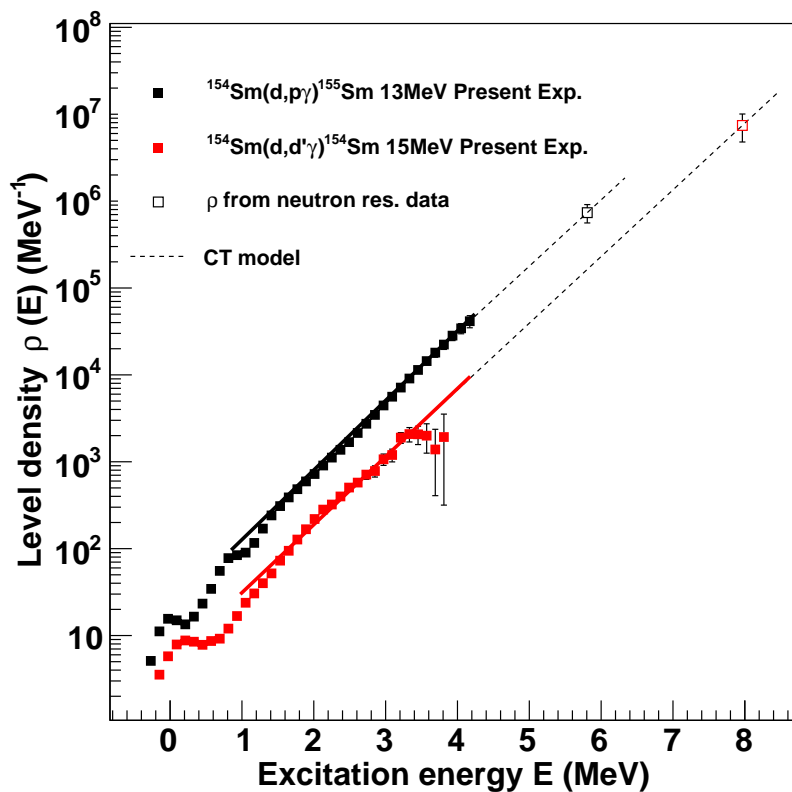


Figure 4.25. The normalized experimental NLDs for $^{154,155}\text{Sm}$. A sudden drop in the ^{154}Sm NLD at high E_x is as a result of low statistics for extracting the primary γ -rays at around E_x^{max} limit shown in Fig 4.15 (a) for ^{154}Sm .

4.3 Resonances and photo-absorption data

The extracted experimental γ SF data are further compared to photo-nuclear $\sigma_{\gamma,abs}$, nuclear resonance fluorescence (NRF) $\sigma_{\gamma,\gamma}$ and average resonance capture (ARC) σ_{ARC} cross-sections. The cross-section σ are transformed to the γ SF using the relation [58]:

$$f(E_\gamma) = \frac{1}{3\pi^2\hbar^2c^2} \frac{\sigma(E_\gamma)}{E_\gamma}. \quad (4.25)$$

In Fig. 4.26, the $^{154,155}\text{Sm}$ experimental γ SFs from this work are compared to the GEDR data from $^{154}\text{Sm}(\gamma,n)$ [153] and $^{154}\text{Sm}(\gamma, n+2n)^{155}\text{Sm}$ [154] photo-nuclear data sets, which indicates a double hump structure. Data from $^{159}\text{Tb}(\gamma,n)$ [155], $^{160}\text{Gd}(\gamma,n)$ [156], $^{156}\text{Gd}(\gamma,xn)$ [157] and $^{149,152,154}\text{Sm}(\gamma,n)$ [153] are shown for completion. The present data is further compared to $E1$ and $M1$ (n,γ) ^{155}Sm data measured in ARC experiments [64] closer to S_n . Several resonances are observed in the γ SF and well known models (*i.e.*, standard (SLO) and generalized (GLO) Lorentzian models [68, 69]) are used to fit the predicted total γ SF to the experimental data. The GLO $f_{gedr1\&2}(E_\gamma)$ was used to fit the $^{154}\text{Sm}(\gamma, n+2n)$ [154] GEDR data above ≈ 12 MeV and $^{154}\text{Sm}(\gamma, n)$ [153] below 12 MeV. At the lower tail of the GEDR, a broad and pronounced resonance is observed in the energy range $\approx 2-4.5$ MeV for the $^{154}\text{Sm}(d,p\gamma)^{155}\text{Sm}$ and was fitted using the SLO $f_{sr}(E_\gamma)$. Although the resonance in $^{154}\text{Sm}(d,d'\gamma)^{154}\text{Sm}$ data at $\approx 2-4.5$ MeV is weak and unclear, it may be fragmented due to some fluctuations and therefore a weak resonance in the form of a SLO was fitted in order to be consistent with trends observed in neighboring isotopes. Around S_n , a gap of no data of about $\approx 2-2.5$ MeV between the present data and the GEDR is observed. Both the $^{154}\text{Sm}(d,d'\gamma)^{154}\text{Sm}$ and $^{154}\text{Sm}(d,p\gamma)^{155}\text{Sm}$ data show an increase in strength towards $S_n=7.97$ MeV and $S_n=5.81$ MeV, respectively, indicating a possible $E1$ pygmy resonance, as can be observed in neighboring rare earth nuclei. The SLO $f_{pyg1\&2}(E_\gamma)$ is used to fit this enhanced strength around S_n , in addition to the excess strength at $E_\gamma=8.5$ MeV. The nature and origin of the resonance at 8.5 MeV is not crucial to this work and therefore was not speculated upon. Although no clear upbend (LEE) is observed at the lower energy $E_\gamma \leq 1.5$ MeV, due to the uncertainties of the Oslo method as $E_\gamma \rightarrow 0$, the possibility of presence of the LEE in $^{154,155}\text{Sm}$ is not ruled out. The total γ SF of $^{154,155}\text{Sm}$ are decomposed as follows: $f_{total}^{154,155}\text{Sm}(E_\gamma) = f_{sr}(E_\gamma) + f_{pyg1}(E_\gamma) + f_{pyg2}(E_\gamma) + f_{gedr1}(E_\gamma) + f_{gedr2}(E_\gamma)$ and the total fit can be seen in Fig. 4.26. The resonance parameters of the $f_{total}(E_\gamma)$ which reproduce the observed experimental data well are given in Tab. 4.4.

The resonances in $^{180,181,182}\text{Ta}$ γ SFs have been presented and discussed in Ref. [36, 37] including the fits but for completion the results are further emphasized in this work. The extracted $^{180,181,182}\text{Ta}$ experimental γ SF are compared with the $^{181}\text{Ta}(\gamma, \gamma)$ [158] from NRF, $^{181}\text{Ta}(\gamma, n)$ [159] and $^{181}\text{Ta}(\gamma, xn)$ [33] photo-nuclear reaction data. In these dissertation, only the updated fits which will later be used for TALYS cross-sections will be highlighted. In addition to the

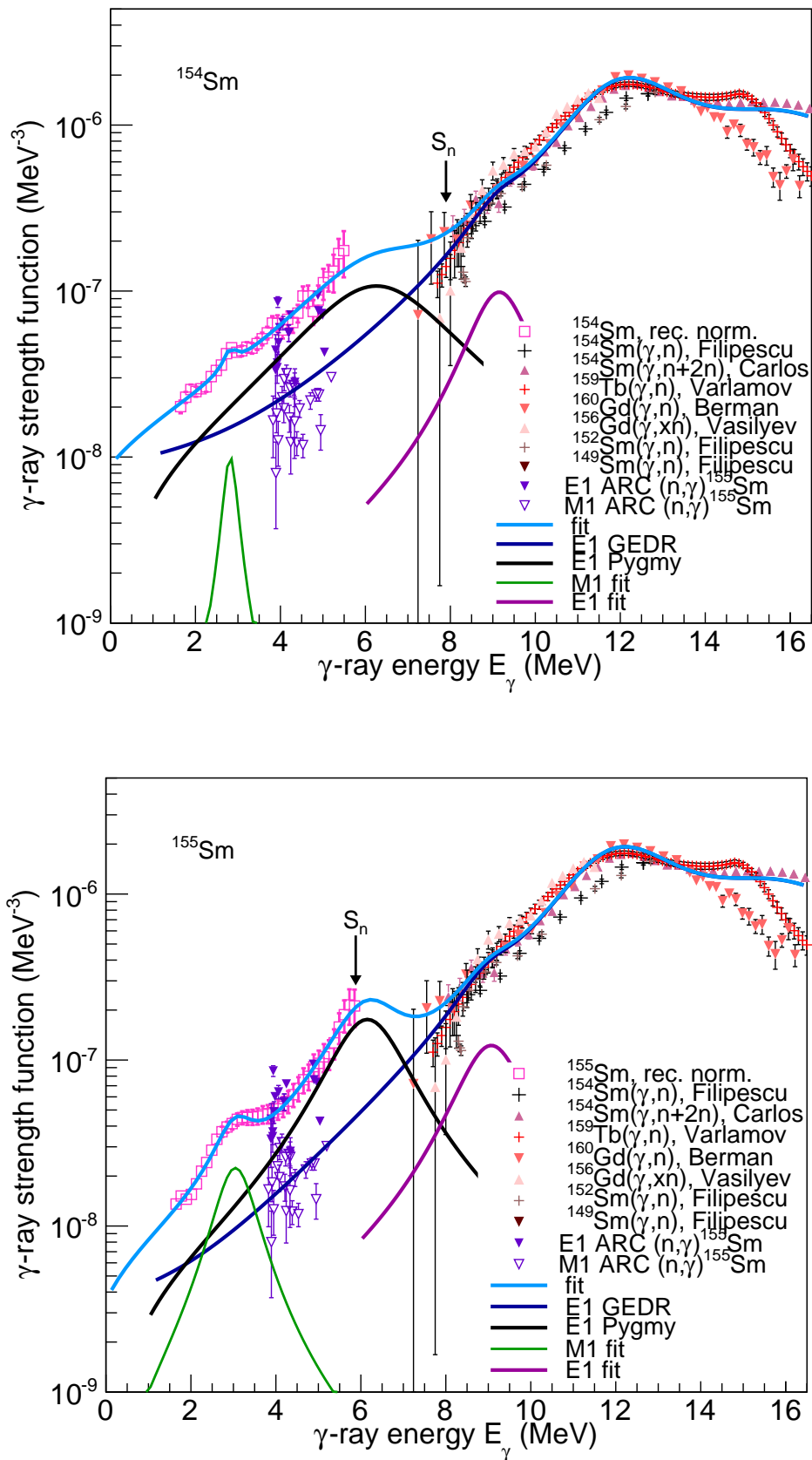


Figure 4.26. The newly extracted experimental γ SFs of $^{154,155}\text{Sm}$ compared to photo-nuclear reaction measurements. The observed resonances in the γ SF are fitted with the SLO and EGLO.

Table 4.4. Resonance parameters used for fitting to experimental γ SF of both $^{154,155}\text{Sm}$, where ω , σ and Γ are the energy centroid, cross-section and width of the resonance.

Isotope	Pygmy 1			Pygmy 2		
	ω_{PDR1} [MeV]	σ_{PDR1} [mb]	Γ_{PDR1} [MeV]	ω_{PDR2} [MeV]	σ_{PDR2} [mb]	Γ_{PDR2} [MeV]
^{154}Sm	6.02(0.4)	10.47(5.1)	2.01(0.5)	8.80(0.3)	12.15(3.5)	1.61(0.8)
^{155}Sm	6.23(0.3)	12.53(5.9)	1.91(0.4)	9.11(0.3)	12.82(3.8)	1.69(0.9)

Giant Dipole Resonance 1 and 2

	ω_{GDR1}	σ_{GDR1}	Γ_{GDR1}	ω_{GDR2}	σ_{GDR2}	Γ_{GDR2}
	[MeV]	[mb]	[MeV]	[MeV]	[mb]	[MeV]
^{154}Sm	12.52(0.07)	249.01(5.8)	3.70(0.3)	16.62(0.07)	5.65(0.5)	146.10(4.9)
^{155}Sm	12.52(0.07)	249.01(5.8)	3.70(0.3)	16.62(0.07)	5.65(0.5)	146.10(4.9)

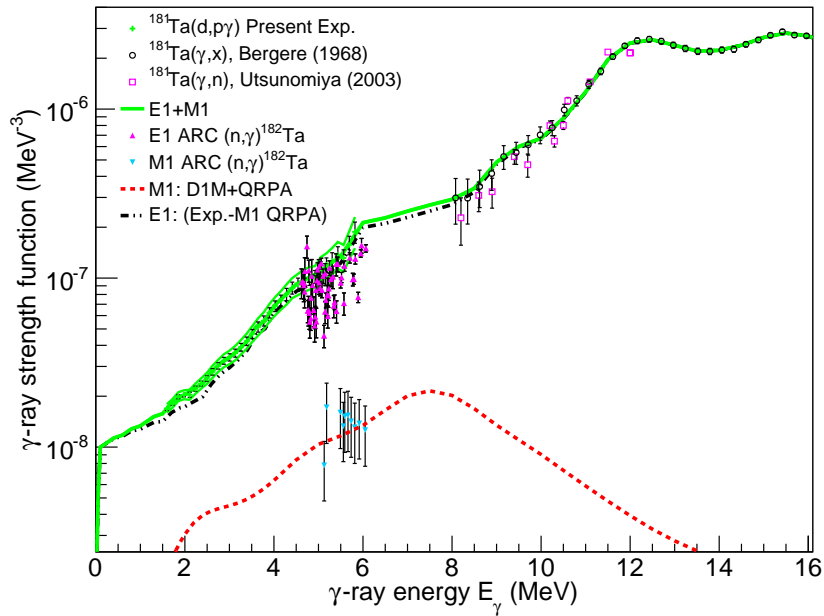


Figure 4.27. The experimental γ SF of ^{182}Ta from the $^{181}\text{Ta}(d,p\gamma)$ reaction in comparison to the $(n,\gamma)^{182}\text{Ta}$ $E1+M1$ ARC data experiments [64], $^{181}\text{Ta}(\gamma,\gamma)$ NRF data [158], $^{181}\text{Ta}(\gamma,n)$ [159] and $^{181}\text{Ta}(\gamma,xn)$ [33] photo-nuclear reaction data. The solid line denote the $E1+M1$ total fit whereas the dotted line are the separate $E1$ and $M1$ fits.

figures presented in Ref. [36, 37], the γ SF is further compared to the $(n,\gamma)^{182}\text{Ta}$ $E1+M1$ data determined in ARC experiments [64] closer to S_n as shown in Fig. 4.27 for ^{182}Ta . The statistical decays are dominated by dipole transitions, that is contributions from $E1$ and $M1$ transitions, and therefore experimental γ SF has to be disentangled. In order to separate the $E1$ and $M1$ γ SF, the D1M-QRPA strength [73] (Quasi-Particle Random Phase Approximation based on the Gogny D1M interaction) is subtracted from the experimental $E1+M1$ γ SF, as shown in Fig. 4.27. The disentangled $E1+M1$ γ SF are denoted by the dotted line. These fit have been

performed for all other reactions involving $^{180,181,182}\text{Ta}$. The $M1$ resonance denoted by the red dotted line in Fig. 4.27 has a width of 2 MeV for all the $^{180,181,182}\text{Ta}$ data sets. The resulting experimental E1 and M1 strengths plus the NLD are used as input in TALYS. The experimental γ SF span the energy region $E_\gamma^{min} \lesssim E_\gamma \lesssim S_n$, and therefore was extrapolated as $E_\gamma \rightarrow 0$, below $E_\gamma \lesssim E_\gamma^{min}$, to reproduce closely the experimental data using an exponential function in TALYS. The procedure worked well as the experimental average radiative width, $\langle \Gamma_\gamma(S_n) \rangle$, could be reproduced within experimental uncertainties.

4.4 The scissors resonance

The integrated scissors resonance strength $B(M1)_{SR}$ are extracted from the $^{154,155}\text{Sm}$ data following the procedure discussed in Subsec. 2.2.3.1. Extraction of the SR in tantalum isotopes is not within the scope of this dissertation and are discussed in Ref. [37]. In order to minimize the background and extract the strength of the SR correctly, contributions from all other resonances are subtracted from the total fit $f_{total}^{154,155}\text{Sm}(E_\gamma)$ above. The SLO used to fit the SR is then integrated using Eq. 2.19 within the SR energy region of about $\approx 2-4$ MeV and the resulting $B_{SR}(M1)$ values are tabulated in Tab. 4.5. The uncertainties related to the extraction

Table 4.5. Resonance parameters used for fitting to scissors resonance, where $B(M1)_{SR}$ is the integrated resonance strength.

Isotope	$\omega_{SR,R}$ [MeV]	$\sigma_{SR,R}$ [mb]	$\Gamma_{SR,R}$ [MeV]	$B_{SR,R}$ [μ_N^2]
^{154}Sm	2.85 (0.2)	0.72 (0.2)	0.95 (0.1)	2.18 (0.9)
^{155}Sm	3.08 (0.3)	0.79 (0.1)	1.03 (0.2)	4.08 (0.6)

of the $B_{SR}(M1)$ are calculated by linearly propagating of Eq. 2.20 as follows:

$$dB_{SR} = \sqrt{\left(\frac{dB_{SR}}{d\omega_{SR}}\right)^2 \Delta\omega_{SR}^2 + \left(\frac{dB_{SR}}{d\sigma_{SR}}\right)^2 \Delta\sigma_{SR}^2 + \left(\frac{dB_{SR}}{d\Gamma_{SR}}\right)^2 \Delta\Gamma_{SR}^2} \quad (4.26)$$

and, the ratio of the strength and calculated errors is given by:

$$\frac{dB_{SR}}{d\omega_{SR}} = \frac{9\hbar c}{32\pi^2} \left(\frac{\sigma_{SR}\Gamma_{SR}}{\omega_{SR}^2} \right) \quad (4.27)$$

$$\frac{dB_{SR}}{d\sigma_{SR}} = \frac{9\hbar c}{32\pi^2} \left(\frac{\Gamma_{SR}}{\omega_{SR}} \right) \quad (4.28)$$

$$\frac{dB_{SR}}{d\Gamma_{SR}} = \frac{9\hbar c}{32\pi^2} \left(\frac{\sigma_{SR}}{\omega_{SR}} \right) \quad (4.29)$$

where $\Delta\omega_{SR}$, $\Delta\sigma_{SR}$ and $\Delta\Gamma_{SR}$ are uncertainties determined by fitting to experimental data. The contribution of the scissors resonance is isolated from the total experimental γ SF as shown in Fig. 4.28 and fitted with the SLO. In case of ^{154}Sm , the fit is undoubtedly unreliable due to

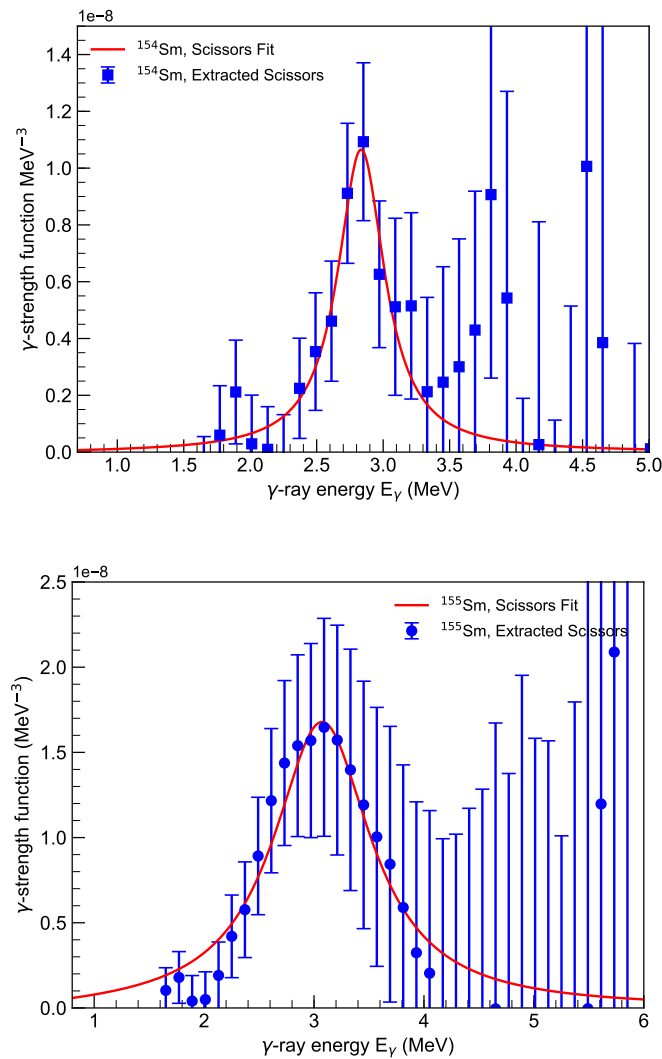


Figure 4.28. The extracted scissors resonance experimental of $^{154,155}\text{Sm}$, fitted with the SLO. The errors here follow directly from the extraction and may not represent the actual errors.

large fluctuations and not enough statistics.

Chapter 5

Discussion of results

“There is nothing like looking, if you want to find something. You certainly usually find something, if you look, but it is not always quite the something you were after.”

— **J.R.R. Tolkien**, *The Hobbit or There and Back Again*

5.1 NLDs and γ SFs of $^{154,155}\text{Sm}$ and the scissors resonance

Nuclear level densities of neighboring samarium isotopes have similar slopes, as shown in Fig. 5.1, and this feature has been observed in all the data sets analyzed with the Oslo Method [160]. The $^{152}\text{Sm}(d,d'\gamma)^{152}\text{Sm}$ experiment [26] was performed using a similar setup with a 13.5 MeV beam energy as the $^{154}\text{Sm}(d,d'\gamma)^{154}\text{Sm}$ reaction of this work. The NLDs of even-even $^{152,154}\text{Sm}$ shown in Fig. 5.1 (left panel) are in very good agreement with each other as expected. In addition, both data sets only reach a maximum E_x of about $\approx 4\text{-}5$ MeV due to low beam energies¹ which populated a limited range of the excitation energy region, and a large gap between the highest experimental data point and $\rho(S_n)$ may introduce some large uncertainties during the extrapolation procedure.

In Fig. 5.1 (right panel) the NLDs of the even-odd $^{151,153}\text{Sm}$ [27], ^{153}Sm [26] and the present ^{155}Sm from different experimental setups and slightly different normalizations are compared. In both the current analysis and that of Ref. [26] the average total radiative width, $\langle I_\gamma \rangle$, and average resonance spacing, D_0 , [150] for s-wave neutrons are taken from the latest Atlas of Neutron Resonances by Mughabghab [150], while that of Ref. [27] uses values tabulated in the RIPL-3 database [58]. In addition, different spin-cut off parameters at S_n and constant temperature parameters T_{ct} were used. The ^{153}Sm NLDs in Fig. 5.1 (right panel) from the

¹The beam energy was optimized for the (d,p) reaction in these experiments.

$^{152}\text{Sm}(d,p\gamma)^{153}\text{Sm}$ and $^{154}\text{Sm}(p,d\gamma)^{153}\text{Sm}$ reactions are in good agreement with each other and show that the statistical decay properties do not depend on the beam energy or the reaction mechanism used to populate the nucleus. Although all the NLDs have similar slopes like in the case of the even-even isotopes, a difference in the absolute values is observed and is attributed to the even-odd shell effects. One would expect to observe a higher NLD in ^{155}Sm compared to the NLD of ^{153}Sm due to the increase in degree of freedom as more neutrons are added and as deformation increases but that is not the case for the even-odd samarium isotopes. Such behavior has also been observed in a series of neodymium isotopes [161, 162] where the lighter, spherical or less deformed isotopes have higher NLDs than the more deformed, heavier isotopes. In order to verify that this phenomenon is not artificial, the microscopic and phenomenological

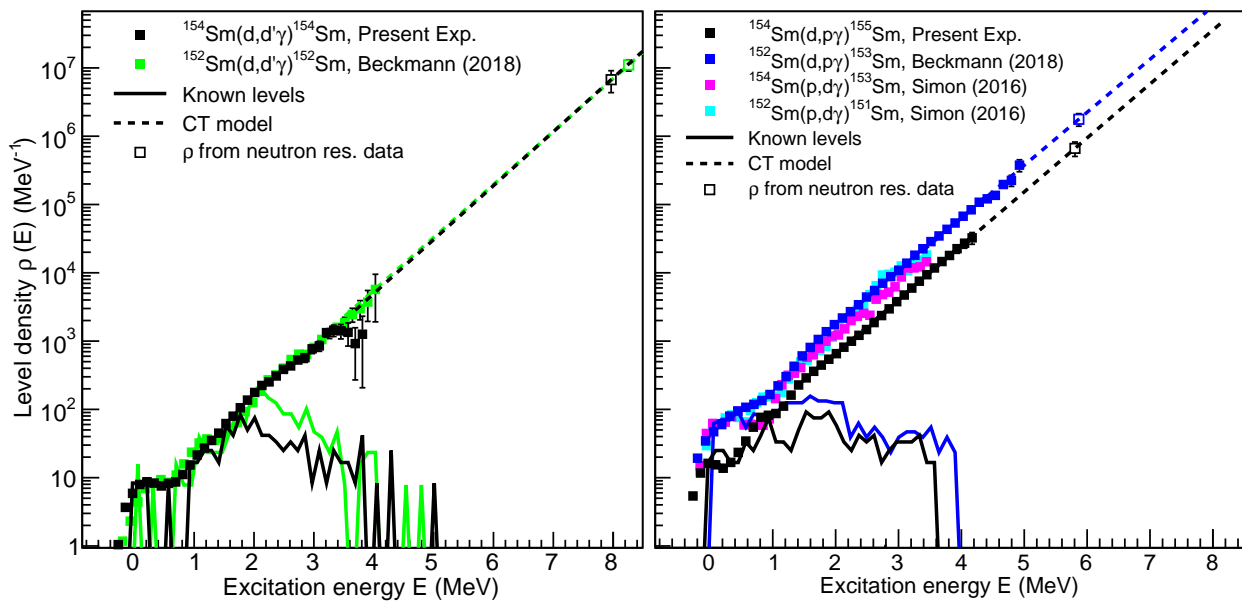


Figure 5.1. The normalized experimental NLDs of $^{154,155}\text{Sm}$ from the present experiment compared to those of $^{152,153}\text{Sm}$ [26], $^{151,153}\text{Sm}$ [27] and $^{147,149}\text{Sm}$ [28]. The solid lines denote the known discrete levels and the dashed lines represent the CT model interpolation between the experimental data (solid squares) and $\rho(S_n)$ (open squares).

theoretical description of the NLDs tabulated in the TALYS reaction code [40, 55], are compared for even-odd $^{153,155}\text{Sm}$. The calculations are corrected for the slope and absolute value by fitting to available data on lower-lying discrete states and to $\rho(S_n)$. The same feature of a lower NLD for ^{155}Sm persists as shown in Fig. 5.2. It is important to note that the calculations have in no way been adjusted or modified on the basis of the present experimental data and that of ^{153}Sm [26]. It is not clear yet what the underlying mechanism is for this feature but clearly it is not artificial and is even theoretically reproducible. The mechanism behind the difference in absolute value between the even-odd samarium isotopes requires further theoretical investigation which is beyond the scope of this work. In Figure 5.3 the NLDs of even-even and even-odd

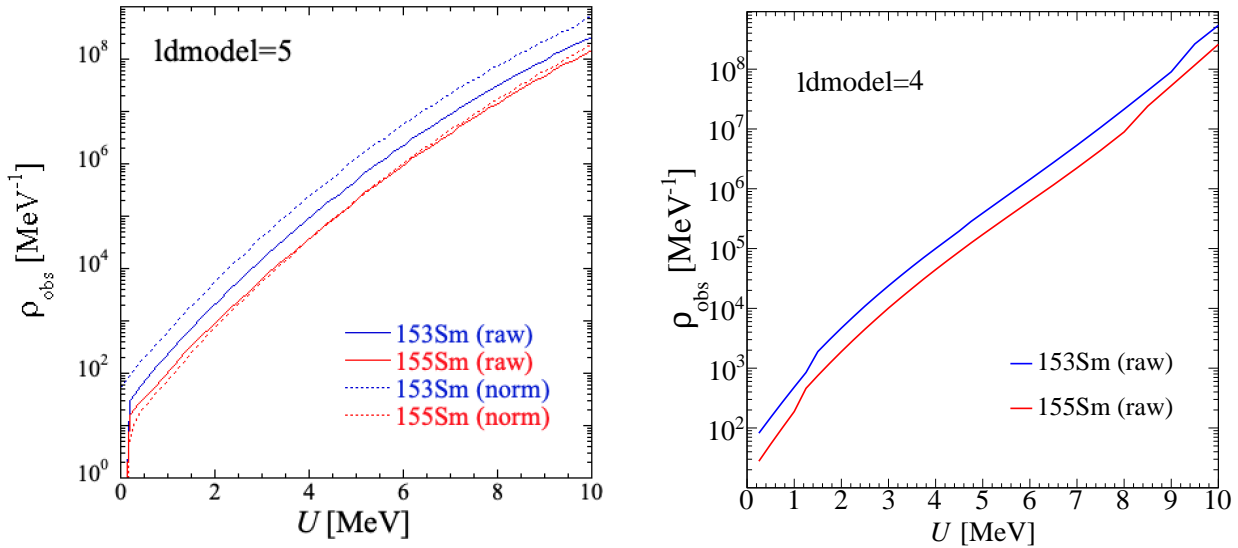


Figure 5.2. The microscopic NLDs from Goriely’s (ldmodel=4) and Hilaire’s combinatorial (ldmodel=5) tables [40, 55] for the even-odd $^{153,155}\text{Sm}$ isotopes. The normalized data represented by the dotted line is corrected for the slope and absolute value but completely independent of the present experimental data and that of ^{153}Sm [26]. Figures from Ref. [163]

samarium isotopes are compared. The even-odd $^{151,153,155}\text{Sm}$ NLDs lie higher than those of even-even isotopes due to one extra unpaired nucleon which increases the degree of freedom for pairing [160].

The γ SFs from the current measurements are compared with existing experimental data on the neighboring isotopes from Refs. [26, 27, 28]. The γ SFs of even-even ^{154}Sm from the present measurement is shown in Fig. 5.4 (left panel) with that of the even-even ^{152}Sm from Ref. [26]. Firstly, it is noted from Fig. 5.4 (left panel) that the γ SF of even-even isotopes have similar slopes and agree well within uncertainties. In addition, the γ SF of ^{152}Sm extends to $E_\gamma \approx 1$ and levels out as $E_\gamma \rightarrow 0$ which could be due to the LEE according to Ref. [26]. Shown in Fig. 5.4 (right panel) are the γ SF of the even-odd deformed ^{155}Sm and compared to those of $^{151,153}\text{Sm}$ of Ref. [27] and ^{153}Sm data of Ref. [26]. The $^{154}\text{Sm}(p,d\gamma)^{153}\text{Sm}$ and $^{152}\text{Sm}(p,d\gamma)^{151}\text{Sm}$ [27, 28] have a steep slope at lower energies in comparison to the $^{153,155}\text{Sm}$ data sets measured at OCL and the differences are particularly due to the experimental approach and normalization. The $(p,d\gamma)^{151,153}\text{Sm}$ [27, 28] experiments were performed at Texas A&M University using Compton suppressed γ -ray detectors which allows for probing the γ -decay strength down to ≈ 500 keV. The OCL type of experiments utilizes collimated NaI detectors and are limited to investigating the γ -ray strength above ≈ 1 MeV due to Compton background. It is crucial to estimate accurately the detector response function at this lower energies in order to perform the Oslo Method as outlined in sec. 4.2, which may be the issue for the clover setup used at Texas A&M University.

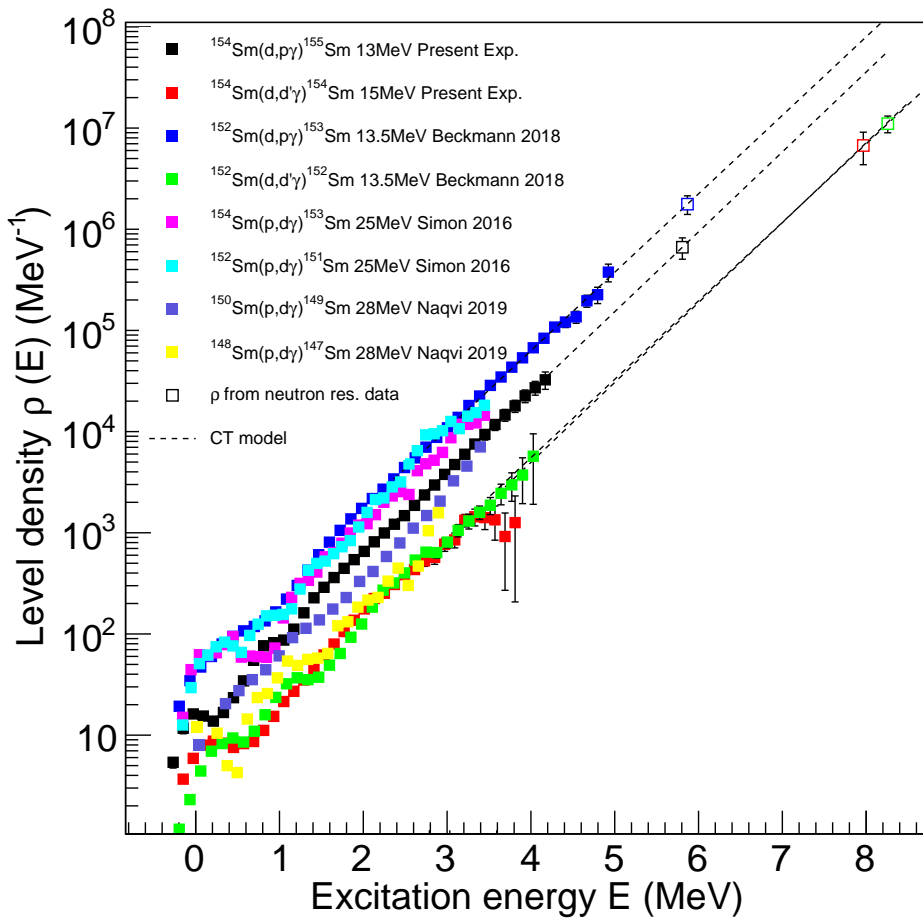


Figure 5.3. The present experimental NLDs of the even-even and even-odd samarium isotopes compared to the $^{151,153}\text{Sm}$ [27], $^{147,149}\text{Sm}$ [28] and $^{152,153}\text{Sm}$ [26].

Furthermore, the $(p,d\gamma)^{151,153}\text{Sm}$ [27, 28] experimental data is compared to the simple modified Lorentzian (SMLO) model and the mean-field-plus-quasiparticle random-phase approximation including the LEE (D1M+QRPA+0lim) calculations [164, 165] in Fig. 5.5. It is clear that the $(^3\text{He},^3\text{He}'\gamma)^{149}\text{Sm}$ [25] experiment performed at the OCL show a reasonable agreement to the calculations at all energies. The $(p,d\gamma)^{151}\text{Sm}$ [27] data shows a great disagreement with the theoretical models for all energies, while the $(p,d\gamma)^{153}\text{Sm}$ [27] data agree well at high energies but deviate especially at the LEE-region. Additionally, a steeper LEE can be seen in Fig. 5.4 for $^{147,149,151,153}\text{Sm}$ data populated through $(p,d\gamma)$ reactions compared to OCL measurements. This discrepancy warrants further investigation of the $^{147,149,151,153}\text{Sm}$ statistical properties, especially the LEE. However, the possibility of the LEE being present can not be ruled out in OCL type experiments due to the limitations of the analytical technique to investigate the γ -decay strength below ≈ 1 MeV, which will be improved with the newly implemented $\text{LaBr}_3:\text{Ce}$ array [138]. Large-scale shell-model calculations [72] showed that the LEE develops and becomes more evident toward the shell closures. The $(^3\text{He},^3\text{He}'\gamma)^{149}\text{Sm}$ and $(^3\text{He},\alpha\gamma)^{148}\text{Sm}$ of Ref. [25] measured at OCL which are only 4 and 5 neutrons away from the closed $N=82$ shell, show no

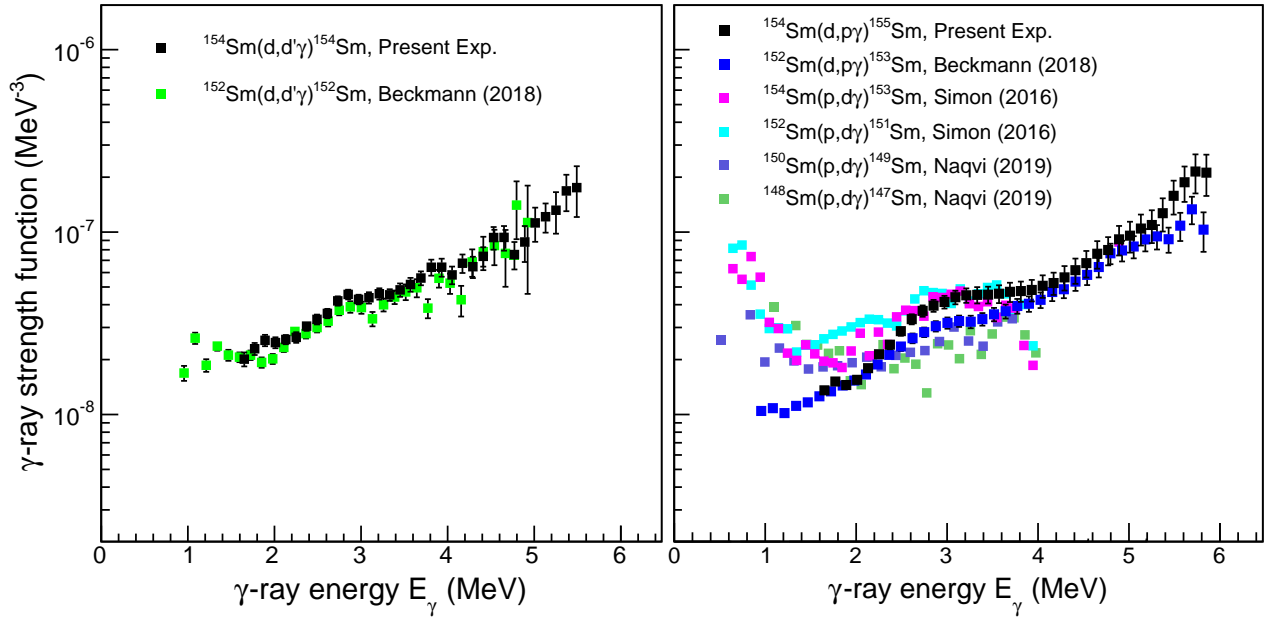


Figure 5.4. The normalized experimental γ SF of even-even $^{152,154}\text{Sm}$ (left panel) and of even-odd $^{147,149,151,153,155}\text{Sm}$ (right panel) isotopes.

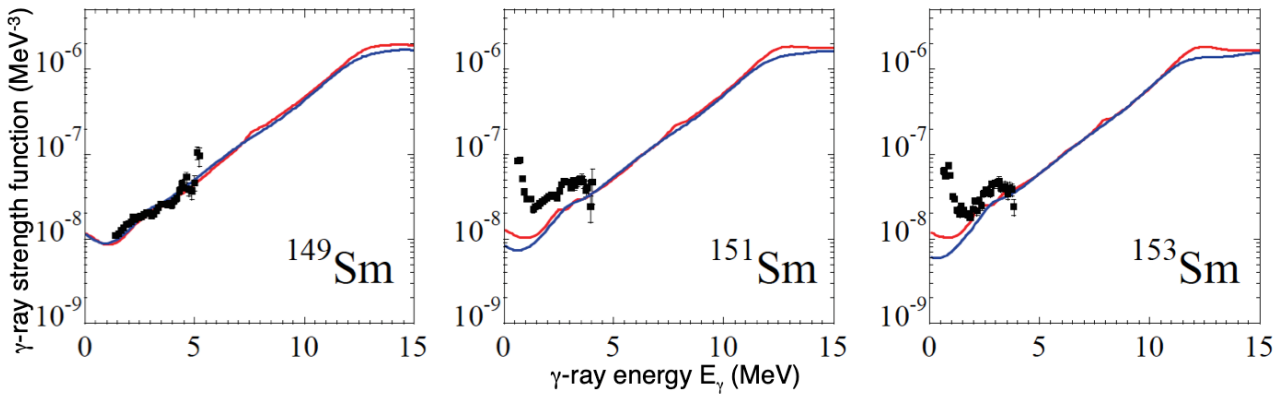


Figure 5.5. The ^{149}Sm [25] and $^{151,153}\text{Sm}$ [27] experimental γ SF compared to the theoretical models, the simple modified Lorentzian (SMLO) (blue lines) and the mean-field-plus-quasiparticle random-phase approximation including the LEE (D1M+QRPA+0lim) (red lines) models [164, 165]. Figure from Ref. [166]

clear LEE in contrast to the $(p,d\gamma)^{147,149,151,153}\text{Sm}$ [27, 28] measured at Texas A&M University. Therefore the discrepancies observed at lower energies require further investigation.

An increase in strength is observed towards the neutron threshold $S_n \approx 5.868$ and 5.807 MeV in $(d,p\gamma)^{153,155}\text{Sm}$ shown in Fig. 5.4 (right panel) and is thought to be the $E1$ PDR. However, it is not possible to determine the electromagnetic nature of the resonance from OCL type experiments and therefore information from other type of experiments such as nuclear resonance fluorescence (NRF) [61] or inelastic proton scattering measurements [80, 81] is crucial. The same

resonance was observed from high-resolution inelastic proton scattering experiments in ^{154}Sm in the energy range of $\approx 5\text{-}7$ MeV [19, 20] and more recently in $^{154}\text{Sm}(\alpha, \alpha')$ [167]. Although the $(d, p\gamma)^{152,154}\text{Sm}$ with $S_n \approx 8.258$ and 7.967 MeV, as shown in Fig. 5.4 (left panel), is limited by statistics and does not reach higher γ -ray energies, the existence of a $E1$ PDR is possibly likely.

A significant and wider enhancement is observed in the γSF of even-odd isotopes as seen in Fig. 5.4 (right panel) at around $E_\gamma \approx 3$ MeV and is regarded to be the $M1$ SR. Visually, there appears to be more scissors resonance strength in the more deformed ^{155}Sm compared to the ^{153}Sm data measured at OCL and ^{151}Sm of Ref. [27] which is consistent with the deformation dependence of the SR. However, for the even-even deformed $^{152,154}\text{Sm}$ the $M1$ SR is either substantially fragmented over a wide energy region or absent as shown in Fig. 5.4 (left panel). In actual fact, it would not be unreasonable to come to the conclusion that no SR is perceivable in both $^{152,154}\text{Sm}$ based on the visual inspection of the γSF . The extracted ^{154}Sm SR shown in Fig. 4.28 exhibits large fluctuations, there are not enough statistics, thereby making the fit not reliable. In Fig. 5.6, the presently extracted $^{154,155}\text{Sm}$ integrated strength of the scissor resonance, $B_{SR}(M1)$, are compared to the values extracted from the $(p, d\gamma)^{149,151,153}\text{Sm}$ [27, 28] data, $(d, d'\gamma)^{152}\text{Sm}$ and $(d, p\gamma)^{153}\text{Sm}$ [26], and NRF measurements on $^{150,152,154}\text{Sm}$ [93]. The present measurements,

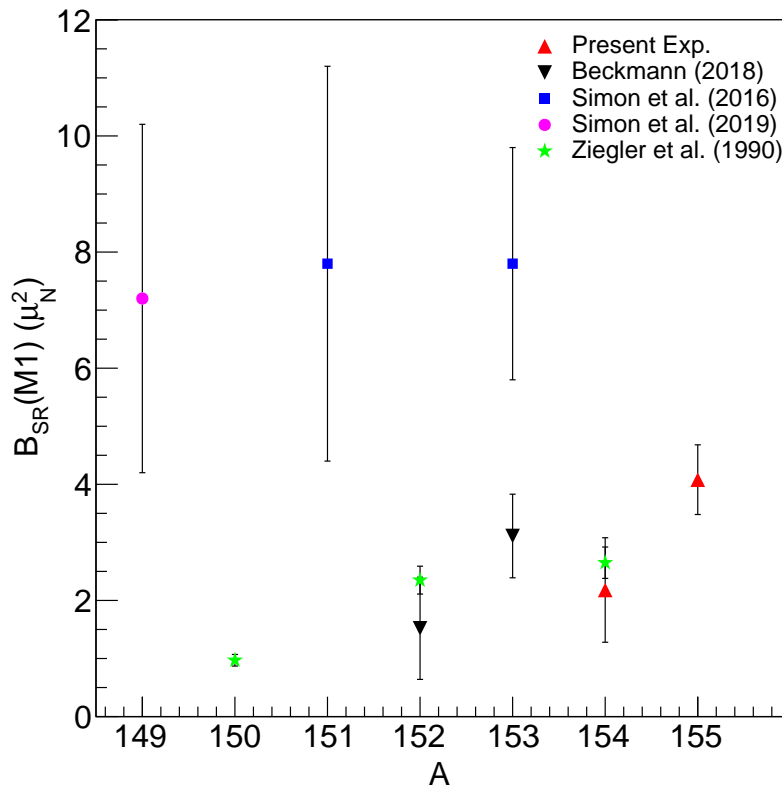


Figure 5.6. The experimental low-lying $M1$ strength, $B_{SR}(M1)$ plotted against the mass number A . The present measurements (red solid triangle) are compared to $^{149,151,153}\text{Sm}$ data from Ref. [27, 28], $^{152,153}\text{Sm}$ of Ref. [26], and $^{150,152,154}\text{Sm}$ from Ref. [93]

NRF [93] and the previous $^{152,153}\text{Sm}$ OCL measurements [26] are relatively consistent and lower

than the $B_{SR}(M1)$ from $(p,d\gamma)^{149,151,153}\text{Sm}$ measurements of Refs. [27, 28]. Even though the $(p,d\gamma)^{149,151,153}\text{Sm}$ measurements of Refs. [27, 28] are extracted over a wider energy range, one would expect this results to agree with NRF and OCL measurements at least within the uncertainties. It was recently shown by Renstrøm *et al.* [102] for dysprosium isotopes, that by extracting the $B_{SR}(M1)$ over the same energy region, data from different types of experiments and theoretical calculations yield similar strength.

The experimental $B_{SR}(M1)$ for samarium isotopes are shown in Table 5.1 as well as the energy ranges, resonance centroids and nuclear ground-state deformations. The SR strengths

Table 5.1. The experimental $B_{SR}(M1)$ for samarium isotopes extracted at given energy ranges. The deformation parameter β_2 is taken from the RIPL-3 database [58] and E_{sc} is the centroid of the scissors resonance.

Nucleus	β_2	Range [MeV]	$B(M1)_{SR}$ [μ_N^2]	E_{sc} [MeV]	Refs.	Extraction technique
^{155}Sm	0.27	2.0 - 4.0	4.08(0.6)	3.08(0.3)	Present Exp.	Oslo Method
^{154}Sm	0.27	2.0 - 4.0	2.18(0.9)	2.85(0.2)	Present Exp.	Oslo Method
^{154}Sm	0.27	2.7 - 3.7	2.65(0.3)	3.20(0.3)	Ziegler <i>et al.</i> (1990) [93]	NRF
^{153}Sm	0.26	0.0 - 5.0	8.00(3.8)	3.00(0.2)	Simon <i>et al.</i> (2016) [27]	Oslo Method
^{153}Sm	0.26	2.0 - 4.0	3.11(0.7)	2.80(0.7)	Beckmann (2018) [26]	Oslo Method
^{152}Sm	0.24	2.0 - 4.0	1.52(0.9)	3.01(0.2)	Beckmann (2018) [26]	Oslo Method
^{152}Sm	0.24	2.7 - 3.7	2.35(0.2)	2.99(0.3)	Ziegler <i>et al.</i> (1990) [93]	NRF
^{151}Sm	0.22	0.0 - 5.0	8.00(3.8)	3.00(0.2)	Simon <i>et al.</i> (2016) [27]	Oslo Method
^{150}Sm	0.21	2.7 - 3.7	0.97(0.1)	3.13(0.3)	Ziegler <i>et al.</i> (1990) [93]	NRF
^{149}Sm	0.18	0.0 - 5.0	7.20(3.0)	3.00(0.3)	Naqvi <i>et al.</i> (2019) [28]	Oslo Method
^{148}Sm	0.18	2.7 - 3.7	0.51(0.1)	3.07(0.3)	Ziegler <i>et al.</i> (1990) [93]	NRF
^{147}Sm	0.14	0.0 - 5.0	9.80(6.9)	3.00(0.2)	Naqvi <i>et al.</i> (2019) [28]	Oslo Method
^{144}Sm	0.08	2.7 - 3.7	0.28(0.0)	3.97(0.4)	Ziegler <i>et al.</i> (1990) [93]	NRF

of $^{147,149,151,153}\text{Sm}$ from Ref. [27, 28] are consistently higher than all the other measurements and at minimum 3.3 times higher than the ^{154}Sm and 1.5 times higher than ^{155}Sm from this work. Recent measurements suggest larger $B_{SR}(M1)$ values for the near spherical $^{147,149}\text{Sm}$ [28], which is rather surprising and warrants further investigation.

As noted in Table 5.1 the scissor resonance remains centralized at the average energy $E_{sc} \approx 3$ MeV as expected. The summed strength of the SR has been observed in previous measurements, and theoretical descriptions, to be correlated to nuclear deformation, in particular it increases proportionally with δ^2 [22]. Furthermore, the experimental $B_{SR}(M1)$ in many cases has proven to be stronger for the deformed even-even than for even-odd nuclei [22, 91]. However the present measurements, as well as others from Table 5.1, contradict the above-stated findings. Firstly, the deformed even-even ^{154}Sm from this work has a relatively small $B_{SR}(M1)$ value compared to the even-odd ^{153}Sm of Ref. [26], as seen in Fig. 5.6 and Table 5.1. Furthermore,

even though both the OCL and NRF measurements agree within uncertainties, there seem to be some even-odd A staggering between the measurements in Fig. 5.6. Measurements with more statistics are needed to make conclusive statements about the results. Both the deformed even-even $^{152,154}\text{Sm}$ have relatively more fragmented (or much narrow) and less strength than the neighboring deformed even-odd $^{153,155}\text{Sm}$, neglecting the $(p,d\gamma)^{149,151,153}\text{Sm}$ measurements of Ref. [27, 28]. The discrepancy in the results may be due to low statistics, that the NLDs and γSF are reaction dependent and excitation-energy dependent, inconsistencies in extracting the γSF , in fitting the resonances or finally extracting the $B_{SR}(M1)$.

To investigate the energy dependence, the primary γ -ray matrix is separated into several excitation energy regions and the γSF is extracted as shown in Fig. 5.7. The extracted γSF

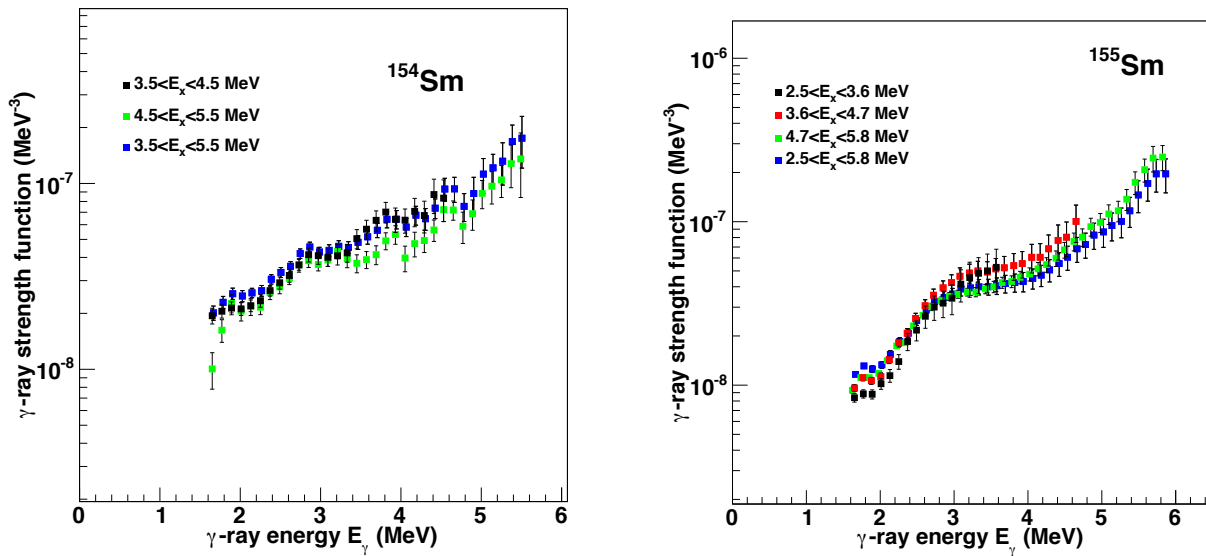


Figure 5.7. The $^{154,155}\text{Sm}$ γSF extracted at several excitation energy regions.

from different excitation energy regions are very similar in shape and agree well within the uncertainties. This is an excellent test for the generalized Brink-Axel hypothesis [66, 67], which states that statistical γ -ray decay from collective features does not depend on excitation-energy. And indeed, such is observed even for the SR, contradicting the controversial claim² of Ref. [168] and also suggesting that the feature is due to collective excitation.

In short, it is not possible to make conclusive statements on the existence and magnitude of the SR for the deformed even-even ^{154}Sm due to low statistics and low beam energies which populated a limited range of the excitation energies (*i.e.*, $E_\gamma \approx 3$ below S_n). It is interesting to note that even though ^{154}Sm is heavily deformed, there seem to be more strength in the less deformed even-odd ^{153}Sm . In addition, one would also expect more strength for the deformed even-even ^{152}Sm but as shown in Fig. 5.4 (left panel) the γSF is quite featureless.

²That the generalized Brink-Axel hypothesis does not hold for the scissors resonance.

In addition, some even-odd A staggering and a more reduced $B_{SR}(M1)$ has been observed for the deformed even-even samarium, gadolinium, and dysprosium isotopes compared to the deformed even-odd neighboring rare-earth nuclei in Kroll *et al.* [106]. This could explain the quenched $B_{SR}(M1)$ in the present ^{154}Sm measurement. Furthermore, the pronounced scissors $M1$ strength from the present ^{155}Sm measurement supplement the observation of Heyde *et al.* [22] (and references therein) in which the scissors mode in the deformed even-odd rare-earth nuclei is largely fragmented due to some escape detection in NRF experiments.

5.2 $^{180,181,182}\text{Ta}$ NLDs and γSFs and $^{180}\text{Ta}^m$ nucleosynthesis

The experimental NLD of ^{181}Ta from two individual reactions at three different beam energies normalized with the CT+FG1 model are shown in Fig. 5.8 and are all in good agreement. As expected the NLDs are independent of how the residual nucleus was populated. The BSGF

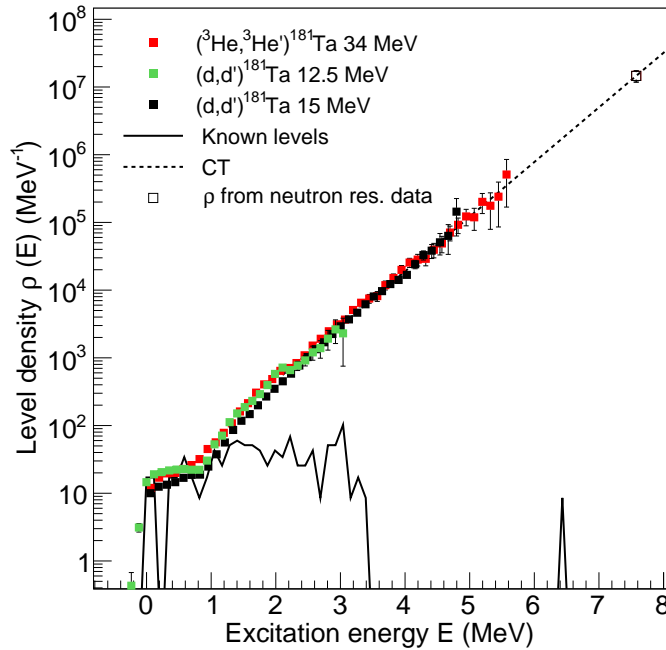


Figure 5.8. The ^{181}Ta NLD populated with the $^{181}\text{Ta}(d,d')$, $^{181}\text{Ta}(d,d')$ and $^{181}\text{Ta}(^3\text{He},^3\text{He}')$ reactions at reaction at 12.5, 15 and 34 MeV beam energies, respectively. The level density deduced from known discrete levels is represented by the solid line and an interpolation between the experimental data and $\rho(S_n)$ (dashed line) is achieved with CT model [42]. Figure taken from Ref. [38].

[47, 148], CT [42], CT+FG [40] and HFB+comb. [53] normalizations previously discussed in sec. 2.1 are used to constrain the $^{180,181,182}\text{Ta}$ total NLDs at the S_n . The range of the results provide upper and lower limits on the uncertainties of $^{180,181,182}\text{Ta}$ NLDs as shown in Fig. 5.9. The solid lines are the level densities calculated by the individual models. The model are normalized to reproduce well the observables such as the known discrete levels (black solid lines) taken from the NNDC database [143] at lower energies, and the total level density $\rho(S_n)$ (open squares) at S_n , which is deduced from experimental average resonance spacing, D_0 , [58] for s-wave neutrons. The solid symbols are the experimental data which are then normalized to these models and are superimposed for comparison. All the models reproduced the D_0 within experimental uncertainties. The different models now reproducing experimental data will later be used as input in TALYS to constrain the upper and lower uncertainties for the neutron capture cross-section calculations. In Fig. 5.10 the newly extracted $^{180,181,182}\text{Ta}$ γSFs are shown together with the previous $^{181}\text{Ta}(\gamma, \gamma)$ [158], $^{181}\text{Ta}(\gamma, n)$ [159] and $^{181}\text{Ta}(\gamma, xn)$ [33]

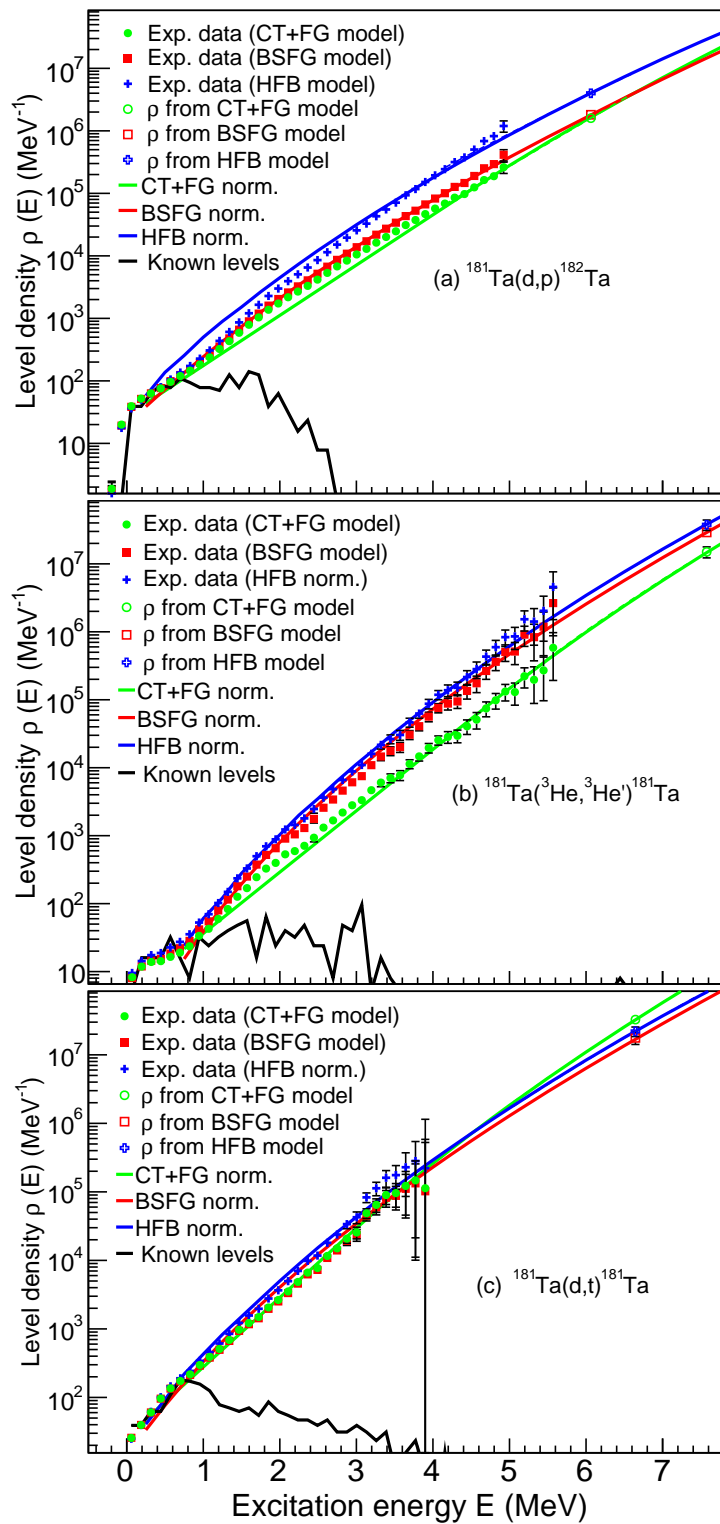


Figure 5.9. The newly extracted experimental NLDs of $^{180,181,182}\text{Ta}$ normalized using the BSFG, CT+FG (1&2) and HFB+comb models. The solid black line denotes the level density of known discrete levels. Figure taken from Ref. [38].

photoreaction cross-sections. The green solid lines represent the upper and lower limits of the uncertainties coming from D_0 and $\langle \Gamma_\gamma(S_n) \rangle$ parameters in addition to the statistical and systematic uncertainties of the unfolding and first generation methods discussed in sec. 4.2.6.

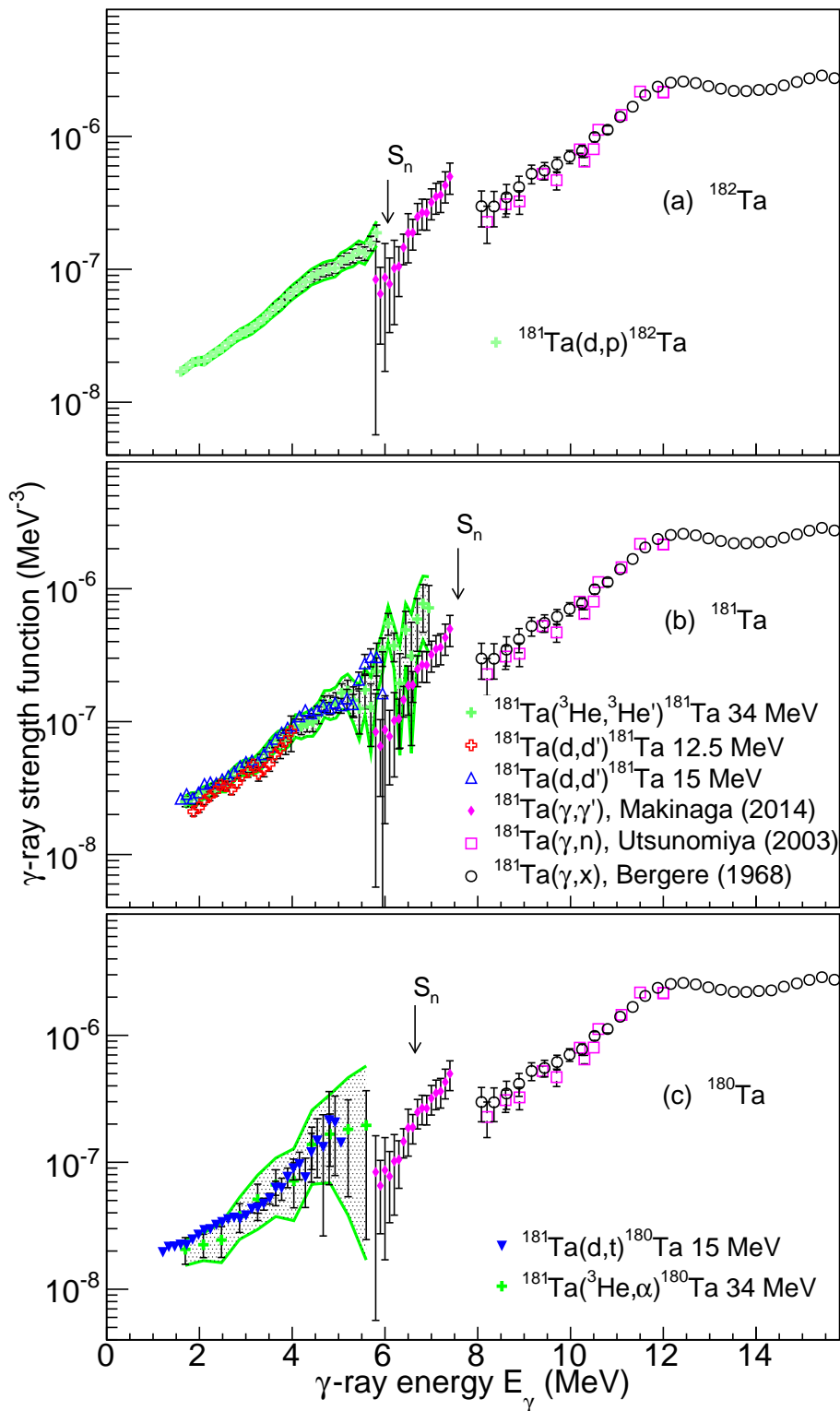


Figure 5.10. The newly extracted experimental γ SFs of $^{180,181,182}\text{Ta}$ compared to $^{181}\text{Ta}(\gamma,n)$ [159], $^{181}\text{Ta}(\gamma,xn)$ [33] photo-nuclear data and $^{181}\text{Ta}(\gamma,\gamma')$ NRF measurements [158].

The $^{179,180,181}\text{Ta}$ experimental NLDs and γ SFs from the current measurements are used as input parameters into the TALYS [40] reaction code to calculate the radiative (n,γ) and the reverse photo-neutron emission (γ,n) reaction cross-sections. Since the experimental γ SF is entered directly into TALYS for calculations of the γ -ray transmission coefficient as discussed in sec.

2.3, the input is modified to have a similar energy grid to that of TALYS for compatibility. As pointed out in Section **2.3**, calculations of cross-sections using the Hauser-Feshbach statistical framework [39] requires nuclear structure properties such as the nuclear masses, deformation parameters, low-lying level schemes, E_x , J^π , NLDs, γ SFs and optical model potentials. The Hofmann-Richert-Tepel-Weidenmüller (HRTW) model [169] for width fluctuation corrections of Equation **2.21** and global neutron optical model potential [40, 170] were applied for the $^{179,180,181}\text{Ta}(n,\gamma)$ calculations in TALYS. The present experimental radiative neutron capture cross-sections are used to extract the astrophysical reaction rates and the Maxwellian-averaged (n,γ) cross-sections (MACS).

The $^{179}\text{Ta}(n,\gamma)^{180}\text{Ta}^m$, $^{179}\text{Ta}(n,\gamma)^{180}\text{Ta}^{gs}$, $^{180}\text{Ta}^m(n,\gamma)^{181}\text{Ta}$, $^{180}\text{Ta}^{gs}(n,\gamma)^{181}\text{Ta}$ and $^{181}\text{Ta}(n,\gamma)^{182}\text{Ta}$ cross-section $\sigma(E_n)$ are calculated as a function of incident neutron energies and shown in Fig. **5.11**. The calculations are performed for incident neutron energies of about $\approx 1 \text{ keV} \leq E_n \leq 5 \text{ MeV}$, but only the neutron energies of $\approx 1 \text{ keV} \leq E_n \leq 1 \text{ MeV}$ relevant for the s - and p -process are considered for this work. The statistical and systematic uncertainties including those of the total s -wave neutron average radiative width and the total average resonance spacing are represented in Fig. **5.11** as the upper and lower bands of the cross-sections. The newly obtained experimental $^{181}\text{Ta}(n,\gamma)^{182}\text{Ta}$ cross-section in Fig. **5.11** (a) based on the CT normalization as well as HFB+comb, CT+FG (1&2) and BSFG models, show excellent agreement with each other and with previous activation [171] and Time-of-Flight (TOF) [172, 173] measurements. The present $^{180}\text{Ta}^m(n,\gamma)$ cross-section are also compared to the experimental $^{180}\text{Ta}^m(n,\gamma)$ cross-section from Ref. [174] and agree well within the error bars, as shown in Fig. **5.11** (b). The $^{179}\text{Ta}(n,\gamma)^{180}\text{Ta}^m$ cross-section, shown in Fig. **5.11** (c), are also in good agreement with predicted [33] $^{180}\text{Ta}^m$ cross-sections determined using the microscopic NLD. The experimental NLDs and γ SFs and the resulting (n,γ) cross-sections from different reaction channels and beam energies, are consistent with each other and show the robustness of the procedure used and that the statistical properties are independent of beam energies and beam type. The excellent agreement between to the present results and direct measurements further validates that the experimental NLD and γ SFs can be used to obtain the (n,γ) cross-section indirectly and has proven to be reliable over different mass regions [49, 175, 176]. In addition, this gives credibility to use this technique to determine (n,γ) cross-section for which no direct measurements are available due to unavailability of target nuclei for nuclear physics experiments [31, 119, 120].

The astrophysical MACS were also calculated for all the $^{179,180,181}\text{Ta}(n,\gamma)$ reactions, at the s - and p -process thermal energies of $kT = 30 \text{ keV}$ ($T = 0.348 \times 10^9\text{K}$) and $kT = 215 \text{ keV}$ ($T = 2.495 \times 10^9\text{K}$), respectively, using the cross-sections from the newly determined NLDs and γ SFs. The MACS were calculated individually for each NLD and γ SF, and combined through the weighted average. The current calculated MACS for the $^{179,180,181}\text{Ta}(n,\gamma)$ are shown in Table **5.2** and show excellent agreement within the errors bars with direct measurements of Refs. [174, 179] and are decreasing with increasing neutron number. It is interesting to note that the

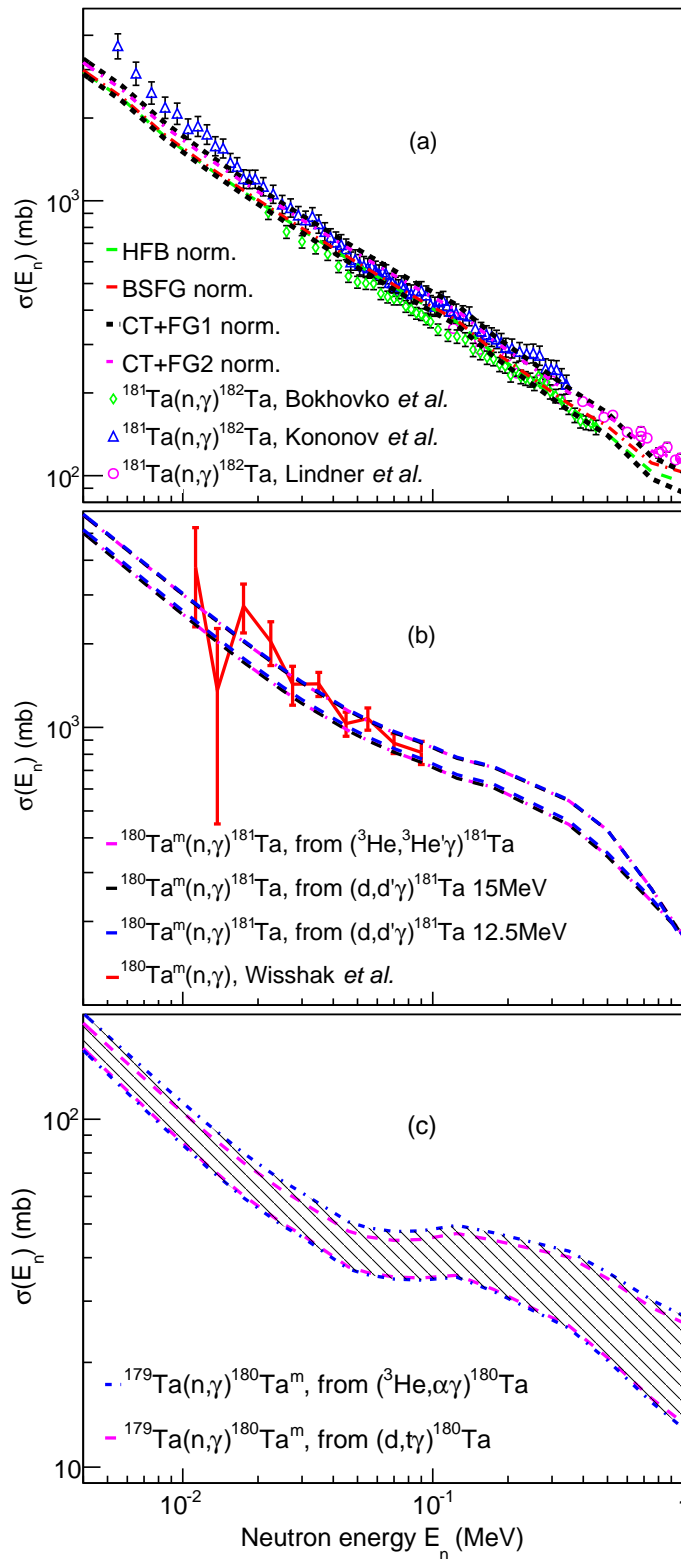


Figure 5.11. The $^{179,180,181}\text{Ta}(n,\gamma)$ cross-sections (bands) extracted from the experimental NLDs and γ SFs in panel (c), (b) and (a) respectively. The $^{181}\text{Ta}(n,\gamma)^{182}\text{Ta}$ cross-sections determined using the BSFG, CT+FG (1&2) and HFB+comb models and their normalizations are compared to previous TOF [172, 173] and activation [171] measurements (a), and the $^{180}\text{Tm}(n,\gamma)$ cross-section to TOF measurements [174] (b). Figure taken from Ref. [177].

Table 5.2. The Maxwellian-averaged (n, γ) cross-sections of $^{179,180,181}\text{Ta}$.

Reaction	$\langle E \rangle$ (keV)	Present Exp. (mb)	Direct Meas. MACS (mb)
$^{179}\text{Ta}(n, \gamma)^{180}\text{Ta}^{tot}$	30	2006.0±497.0	1334.0±422.0 ^a [178]
	215	707.0±233.0	
$^{179}\text{Ta}(n, \gamma)^{180}\text{Ta}^m$	30	56.0±5.0	
	215	34.0±8.0	
$^{179}\text{Ta}(n, \gamma)^{180}\text{Ta}^{gs}$	30	1950.0±492.0	
	215	679.0±226.0	
$^{180}\text{Ta}^m(n, \gamma)^{181}\text{Ta}$	30	1461.0±122.0	1465.0±100.0 [174]
	215	565.0± 48.0	
$^{180}\text{Ta}^{gs}(n, \gamma)^{181}\text{Ta}$	30	1495.0±127.0	
	215	458.0± 46.0	
$^{181}\text{Ta}(n, \gamma)^{182}\text{Ta}$	30	857.0±64.0	815.0±73.0 [179]
	215	258.0±23.0	

^aOnly theoretical estimate available.

$^{179}\text{Ta}(n, \gamma)^{180}\text{Ta}^{tot}$ cross-sections, for which there is no experimental cross-sections or MACS available, are somewhat higher than the theoretical estimate of Ref. [178].

5.3 Nucleosynthesis applications

The newly determined $^{179}\text{Ta}(n, \gamma)^{180}\text{Ta}^{gs,m}$, $^{180}\text{Ta}^{gs,m}(n, \gamma)^{181}\text{Ta}$ and $^{181}\text{Ta}(n, \gamma)^{182}\text{Ta}$ rates from this work are used, in collaboration with theoreticians, as input parameters for the s -process nucleosynthesis calculations of $^{180,181}\text{Ta}$ in Asymptotic Giant Branch (AGB) stars and the p -process synthesis of $^{180}\text{Ta}^m$ in massive stars exploding as Type-II supernovae. Both processes are briefly discussed below to give a partial review of the ^{180}Ta nucleosynthesis in different astrophysical sites. The following two subsections follow closely the discussion in the recently published paper [177].

5.3.1 S-process nucleosynthesis of $^{180}\text{Ta}^m$ and ^{181}Ta

The stellar evolution calculations were performed for the s -process nucleosynthesis of $^{180}\text{Ta}^m$ and ^{181}Ta , which follow the complex production of ^{180}Ta during the thermally pulsing AGB phase. This interval of stellar evolution involves mostly low- to intermediate-mass stars of about 0.6–10 solar masses (M_{\odot}) towards the end of their lives. The STAREVOL code [180, 181] has been

utilized to compute AGB models using an extended s -process reaction network of 411 species and the same input physics as described in Ref. [74]. Of interest to this work, the focus is on a standard $2 M_{\odot}$ $[\text{Fe}/\text{H}] = -0.5^3$ model star known to produce the main s -process elements ranging between $A = 90$ and $A = 204$. When not available experimentally, the cross-sections were calculated within the statistical Hauser-Feshbach model with the TALYS reaction code [40, 55]. The TALYS calculations were also used systematically to deduce from the laboratory (n, γ) cross-sections the stellar rates by allowing for the possible thermalization of low-lying states in the target nuclei. We note that at low temperature, the non-thermalization of the isomeric states of ^{26}Al , ^{85}Kr , ^{115}In , ^{176}Lu and ^{180}Ta is introduced explicitly in the reaction network [3, 182]. Despite some studies predicting the thermalization of the ^{180}Ta ground and isomeric states at a temperature exceeding 25 keV [183, 184], we assume here that both states are not thermalized at the temperatures found in our $2 M_{\odot}$ $[\text{Fe}/\text{H}] = -0.5$ model star. The temperature- and density-dependent β -decay and electron capture rates in stellar conditions were taken from Ref. [185] with the update of Ref. [186]. Most importantly, the factor of about 3 for the uncertainties associated with the $^{179}\text{Hf}(\beta^-)^{179}\text{Ta}$, as well as the 20–30% impact on the $^{179}\text{Ta}(\text{EC})^{179}\text{Hf}$ decay rate are taken into account following the uncertain $\log ft$ transition rates considered in Ref. [186].

The ^{180}Ta nucleosynthesis by the s -process is known to be sensitive to the ^{179}Hf β -decay rate, the ^{179}Ta neutron capture cross-sections and the potential depopulation of the isomeric state by thermal photons via intermediate states to the short-lived ground state. We analyze now the sensitivity of the ^{180}Ta production in our $2 M_{\odot}$ $[\text{Fe}/\text{H}] = -0.5$ model star for the different nuclear and β -decay rates affecting directly the synthesis of $^{180,181}\text{Ta}$. We show in Fig. 5.12 the resulting surface overabundances of elements heavier than Fe at the end of the AGB phase, *i.e.*, after the 29th thermal pulse. While ^{181}Ta is relatively well produced with respect to the overall surface enrichment of s -only nuclei with an overabundance of about 1.7–2 dex, ^{180}Ta is seen to be strongly underabundant by a factor of about 100 in comparison with s -nuclei. As shown in Fig. 5.13, illustrating the profiles of $^{180}\text{Ta}^m$ and ^{181}Ta inside the star, $^{180}\text{Ta}^m$ is not present in the envelope ($M_r \gtrsim 0.67 M_{\odot}$), but its abundance peaks at about 2 dex in a thin layer below the convective envelope. This region lies just below the bottom of the thermal pulse where the temperature is high enough to favour a significant decay of ^{179}Hf into ^{179}Ta followed by a neutron capture, with the neutron stemming from the $^{22}\text{Ne}(\alpha, n)^{25}\text{Mg}$ reaction, hence a production of ^{180}Ta . Note that at a temperature $0.1 T_9$, the $^{179}\text{Hf}(\beta^-)^{179}\text{Ta}$ decay timescale is about 2 Gyr while at $0.3 T_9$, it falls to about 25 yr. However, the neutron captures take place below the thermal pulse where ^{22}Ne has been produced from the previous thermal pulse. Consequently this ^{180}Ta -rich region is not engulfed in the convective pulse, nor by the third dredge-up bringing the ashes of the interpulse and pulse nucleosynthesis up to the surface.

³ $[\text{X}/\text{H}]$ is the star's metallicity which corresponds to the content of elements heavier than hydrogen and helium in a star. Stars with higher (lower) metal content than our Sun have a positive (negative) $[\text{X}/\text{H}]$ value. The metallicity of a star is given in astrophysics unit "dex" (an order of magnitude).

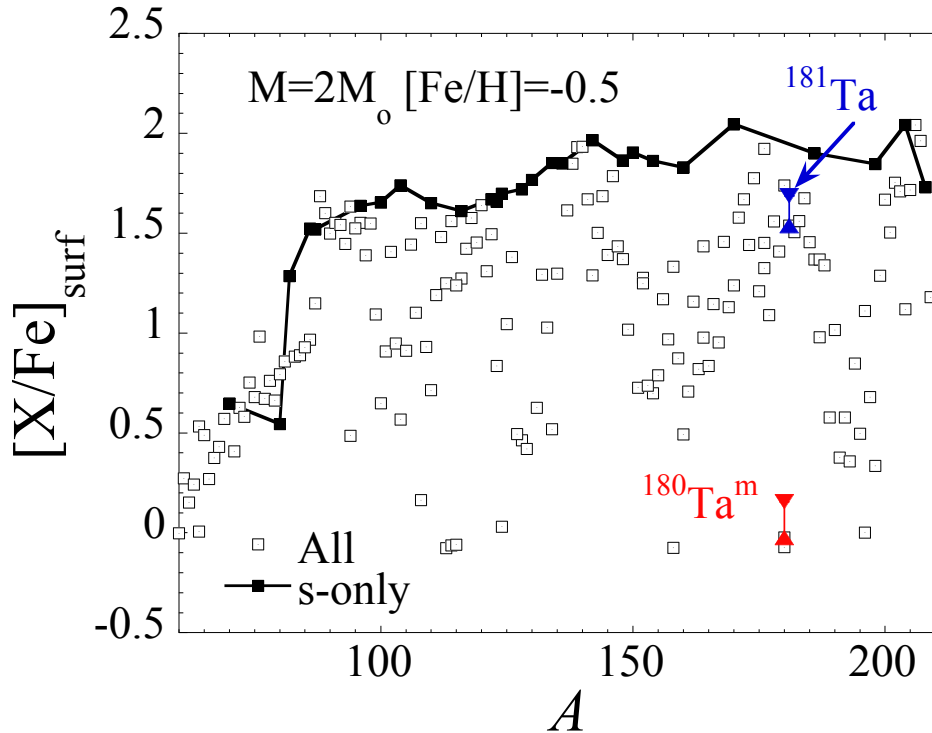


Figure 5.12. Surface overabundances $[X/Fe] = \log_{10}[X/X_{\odot}] - \log_{10}[Fe/Fe_{\odot}]$ as a function of the atomic mass A for all nuclei (open squares) and s -only nuclei (solid squares) at the end of the AGB phase, *i.e.*, after the 29th thermal pulse, of the $2 M_{\odot}$ $[Fe/H] = -0.5$ model star. Highlighted are the $^{180}\text{Ta}^m$ (red triangles) and ^{181}Ta (blue triangles) overabundances and their uncertainties associated with the reaction rates studied in the present work as well as those affecting the $^{179}\text{Hf}(\beta^-)^{179}\text{Ta}$ decay rate (see text for more details). The y-axis is given in logarithmic scale. Figure taken from Ref. [177].

Similar results concerning the absence of ^{180}Ta surface enrichment are found for AGB stars with an initial mass of 1.5 to $3.5 M_{\odot}$. For this reason, contributions of low-mass AGB stars to the ^{180}Ta galactic enrichment can be expected to be relatively negligible.

5.3.2 P-process nucleosynthesis of ^{180}Ta

Now we study the p -process nucleosynthesis on the basis of the Type-II supernova model, as described in [30, 32, 187], *i.e.*, a model for a Z_{\odot} $8 M_{\odot}$ helium star (main sequence mass of about $25 M_{\odot}$) evolved from the beginning of core He burning to the supernova explosion. We consider the 25 layers in the O/Ne-rich zone with explosion temperatures peaking between $1.7\text{--}3.3 T_{\odot}$ responsible for the production of the p -elements. Their total mass is about $0.75 M_{\odot}$. The deepest layer is located at a mass of about $1.94 M_{\odot}$, which is far enough from the mass cut for all the nuclides produced in this region to be ejected during the explosion. All nucleosynthesis calculations have assumed here the absence of neutrinos. Fig. 5.14 shows the overproduction

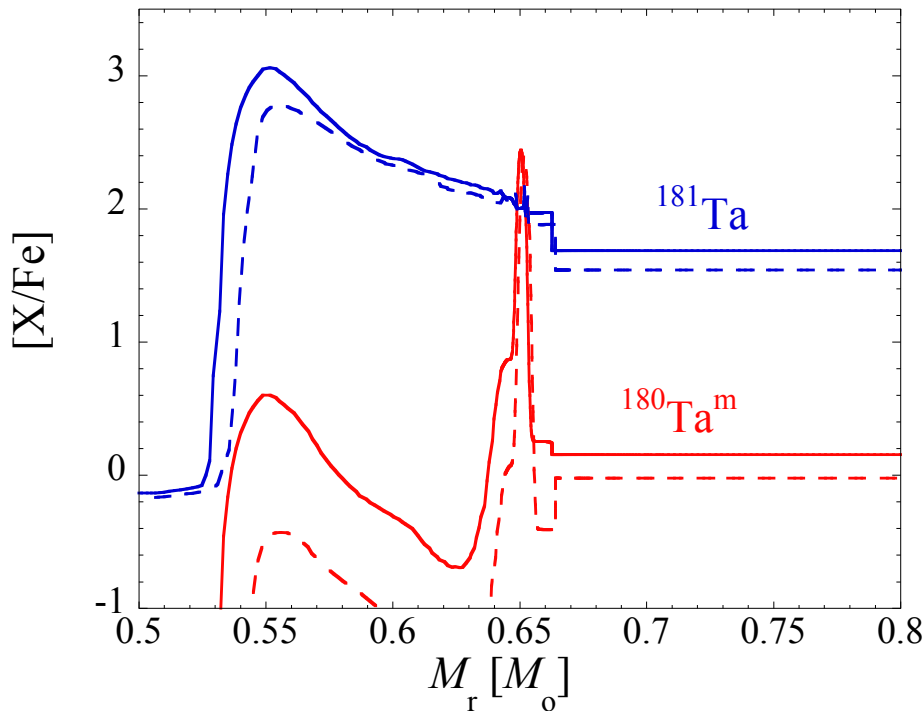


Figure 5.13. Upper (solid line) and lower limits (dashed line) of the $^{180}\text{Ta}^m$ (red lines) and ^{181}Ta (blue lines) overabundances $[X/\text{Fe}]$ inside the star, just below the convective envelope, as a function of the mass coordinate M_r after the 26th thermal pulse of our $2 M_{\odot}$ $[\text{Fe}/\text{H}] = -0.5$ model star. The upper and lower limits are associated with the reaction rates uncertainties from the present work as well as those affecting the $^{179}\text{Hf}(\beta^-)^{179}\text{Ta}$ decay rate (see text for more details). The convective envelope extends above $M_r = 0.665 M_{\odot}$. Figure taken from Ref. [177].

factors $[X/X_{\odot}]$ resulting from the explosive nucleosynthesis in the $0.75 M_{\odot}$ O/Ne-rich layers of the $25 M_{\odot}$ star. The $^{180}\text{Ta}(\gamma, n)^{179}\text{Ta}$ destruction and $^{181}\text{Ta}(\gamma, n)^{180}\text{Ta}$ production rates (estimated from the detailed balance relation) and their associated uncertainties used in the present simulation correspond to the present experimentally constrained values (see Sect. 5.2). Only these rates are modified in the simulation and different combinations considered to estimate their impact on the nucleosynthesis. The resulting uncertainties are seen in Fig. 5.14 to give rise to a rather small error bar on the ^{180}Ta overproduction factor. As shown in Tab. 5.2, the new experimentally constraints essentially affect the $^{179}\text{Ta}(n, \gamma)$ MACS by increasing it by a factor of about 1.5 with respect to the only previously available theoretical estimates (KaDoNiS). Such an increase also impact the reverse $^{180}\text{Ta}(\gamma, n)$ destruction rate leading to a decrease of the $^{180}\text{Ta}^m$ by a factor 1.35 with respect to the yields that would have been obtained with the KaDoNiS rates.

The final ^{180}Ta overproduction is clearly compatible with the p -process enrichment of the other p -nuclei (even neglecting the neutrino effects). Two major effects may still affect the total abundance of ^{180}Ta given in Fig. 5.14. The first one concerns the possible increase of the ^{180}Ta

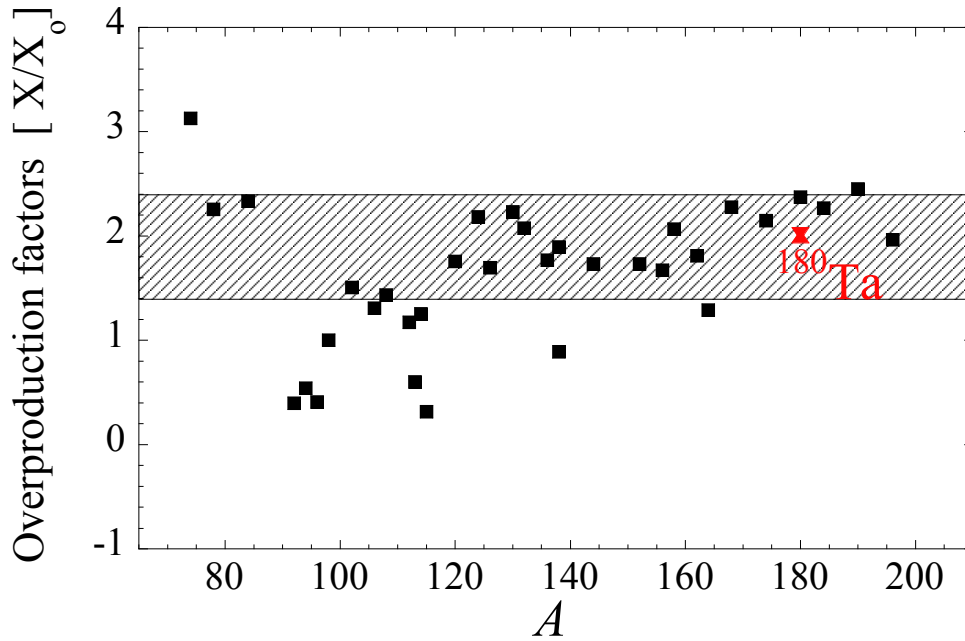


Figure 5.14. P -nuclide overproduction factors $[X/X_{\odot}]$ obtained for the $Z = Z_{\odot}$ $25 M_{\odot}$ model star with TALYS rates for nuclei other than tantalum and the new tantalum production and destruction rates. The ^{180}Ta value corresponds to the total ground state plus isomeric overabundances. The shaded region delineates a factor of 3 around a mean value. For more details see [13, 30]. Figure taken from Ref. [177].

production by neutrino captures [11, 30]. For a total neutrino luminosity $L_{\nu} = 2.3 \times 10^{52}$ ergs s^{-1} , and neutrino temperatures of $T_{\nu_e} = 2.8$ MeV and $T_{\bar{\nu}_e} = T_{\nu_{\mu,\tau}} = 4.0$ MeV [11], we find that the ^{180}Ta abundance is increased by a factor of 1.3, and for a luminosity ten times larger, $L_{\nu} = 2.3 \times 10^{53}$ ergs s^{-1} , by a factor of 4. The charged current capture on ^{180}Hf is found to be the major contributor, while the neutral current on ^{181}Ta leads to half the contribution of the charged current one, as also found in Ref. [11]. Obviously, the impact of this extra production is still subject to all the uncertainties related to the neutrino physics, and in particular to the neutrino luminosity, temperature, oscillation and interaction cross-sections. Note however that the recent measurement of the ^{180}Hf Gamow-Teller strength significantly constrains the $^{180}\text{Hf}(\nu_e, e^{-})$ rate [34].

A second effect arises from the freeze-out of the thermal equilibrium between the isomeric and ground states of ^{180}Ta at temperatures below $\simeq 0.3\text{--}0.4 T_9$ [13, 183, 184]. The ^{180}Ta yields displayed in Fig. 5.14 are obtained under the assumption that ^{180}Ta remains equilibrated until the photoreactions responsible for its production and destruction freeze out. The abundance left over in the isomeric state critically depends on the temperature at which the ground and isomeric states stop thermalizing. For a critical temperature of $0.3\text{--}0.4 T_9$, about 40% of the total ^{180}Ta abundance initially produced during the p -process ends up in the long-lived

isomeric state, and consequently contributes to the galactic enrichment (for more details, see Ref. [13]). The conclusion that ^{180}Ta is essentially produced by the p -process is considered to be robust, and to hold irrespective of the intricacies and uncertainties related to the rates of the main photodisintegrations responsible for its production and destruction, to the thermal equilibration of ^{180}Ta , or to the details of the SNII models, at least in their spherically symmetric one-dimensional approximation.

Chapter 6

Summary and Conclusion

“In literature and in life we ultimately pursue, not conclusions, but beginnings.”

— **Sam Tanenhaus**, *Literature Unbound*

6.1 The scissors resonance in $^{154,155}\text{Sm}$

In conclusion, the rare-earth isotopic chain of samarium provides an excellent opportunity to systematically investigate the evolution of nuclear structure effects from the near spherical ($\beta_2 \approx 0.00$) ^{144}Sm isotope to the well-deformed system ($\beta_2 \approx 0.27$) ^{154}Sm . As the nuclear shape changes, statistical properties such as the nuclear level density (NLD) and γ -strength function (γSF) are expected to be affected. In particular resonance modes, such as the Pygmy Dipole (PDR), Scissors (SR) resonances and the recently discovered Low-Energy Enhancement (LEE) in the rare-earth region may reveal interesting features when their evolution is investigated across several nuclei in an isotopic chain. Most reliable knowledge can be obtained when results from several different experiments are compared.

The NLD and the γSF of the deformed even-even ^{154}Sm and even-odd ^{155}Sm have been measured below the neutron separation energies at the Oslo Cyclotron Laboratory (OCL) using the Oslo Method. The OCL housed a multi-detector scintillator γ -ray array consisting of 24 NaI(Tl) + 6 LaBr₃:Ce (3.5"×8") detectors (later upgraded to 30 LaBr₃:Ce) enclosing the trapezoidal shaped $\Delta E - E$ silicon array for particle detection at the time of the samarium experiments. The statistical properties were extracted simultaneously from the particle- γ coincidences in $^{154}\text{Sm}(\text{d},\text{d}'\gamma)^{154}\text{Sm}$ and $^{154}\text{Sm}(\text{d},\text{p}\gamma)^{155}\text{Sm}$ reactions. This is the first time measurement of NLD and γSF in ^{155}Sm below S_n and below 4.5 MeV in ^{154}Sm . The measured ^{154}Sm covers the energy range of $\approx 1.6 \leq E_\gamma \leq 5.5$ MeV and for $^{155}\text{Sm} \approx 1.6 \leq E_\gamma \leq 5.8$ MeV. The newly extracted NLDs and γSFs have been used to investigate the evolution of nuclear structure effects in $^{154,155}\text{Sm}$

and provide complementary information to the recently measured $^{154}\text{Sm}(p,p')^{154}\text{Sm}$ [19, 20] and $^{154}\text{Sm}(\alpha,\alpha'\gamma)^{154}\text{Sm}$ [167] data on the $E1$ PDR which lie on the low-energy tail of the GDR. The present data confirm a possible PDR presence in ^{155}Sm but its presence is inconclusive for the ^{154}Sm due to the limited energy range.

In addition, the $^{154,155}\text{Sm}$ results further provide a near-complete picture on the evolution of the SR and/or the LEE as the isotopic chain transitions from near spherical ^{144}Sm to very deformed $^{154,155}\text{Sm}$ isotope. A clear and broad enhancement centralized at energies $E_{sc} \approx 3$ MeV is observed in the γSF of ^{155}Sm and is believed to be the $M1$ SR. In contrast, an unclear and hardly-perceivable $M1$ scissors strength in ^{154}Sm γSF is unexpected. The disappearance of the $M1$ scissors strength was observed as well in the γSF of the deformed even-even ^{152}Sm [26]. The absence or fragmentation of the scissors strength for the deformed even-even systems is rather surprising, given that several previous measurements and theory (see Ref. [22] and references therein) assert that the deformed even-even nuclei has pronounced and stronger $M1$ SR compared to neighboring even-odd systems. In both $^{154,155}\text{Sm}$ γSF s there is no indication of the LEE regardless of the limitations of the analytical technique to extract useful information below ≈ 1.6 MeV in this work. In comparing the γSF $^{154,155}\text{Sm}$ results from this work to those of $^{148,149}\text{Sm}$ [25], $^{152,153}\text{Sm}$ [26] and $^{147,149,151,153}\text{Sm}$ [27, 28], a decent agreement is observed between the γSF $^{154,155}\text{Sm}$ and $^{152,153}\text{Sm}$ [26] γSF measured at OCL but there is a significant mismatch with $^{147,149,151,153}\text{Sm}$ [27, 28] data measured at Texas A&M University.

The integrated strength of the scissor resonance, $B_{SR}(M1)$, from this work are in very good agreement with previous OCL data [26] and NRF measurements [93]. However, the $^{154,155}\text{Sm}$ $B_{SR}(M1)$ are 1.5 less than those of the neighboring $^{147,149,151,153}\text{Sm}$ [27, 28] isotopes despite differences in the experimental setups, normalization using recently measured parameters of Ref. [150] and the energy region used to extract the $B_{SR}(M1)$ values. There is therefore reason to believe the results for $^{154,155}\text{Sm}$ are well founded, but the significant differences from Ref. $^{147,149,151,153}\text{Sm}$ [27, 28] merits further investigation.

The quenched/spread $M1$ scissors strength in deformed even-even $^{152,154}\text{Sm}$ could be as a result of low statistics or that the results are reaction dependent which would infer that the compound nuclear assumption is not valid for the Oslo Method. In order to investigate the reaction dependence and improve the statistics, new experiments are desirable. To further explore the vanishing of the strength in deformed even-even samarium isotopes, an experiment already performed at the OCL used a 15 MeV proton beam to study the reactions $^{152,154}\text{Sm}(p,p'\gamma)^{152,154}\text{Sm}$ with the newly commissioned Oslo SCintillator ARray (OSCAR) [138]. The OCL has been equipped with 30 new high-resolution high-efficiency $\text{LaBr}_3:\text{Ce}$ detectors. A different reaction to probing the nuclear structure of $^{152,154}\text{Sm}$ will populate a different spin distribution and the high beam energy will provide a larger excitation energy range up to S_n . Over and above that, the statistical properties for the very neutron rich $^{156-159}\text{Sm}$ will be measured during a planned

experiment [188] to be performed at Argonne National Laboratory. For the very first time, the NLDs and γ SFs will be measured from γ -coincidences with β -decays into $^{156-159}\text{Sm}$ using the beta-Oslo method [120] to investigate the $M1$ SR and the LEE in neutron-rich rare-earth nuclei. In addition, the extracted NLDs and γ SFs will be used as input into nuclear reaction codes such as TALYS to estimate the $^{155-158}\text{Sm}(n,\gamma)$ reaction cross-sections and ultimately place constraints on the reaction rates of astrophysical importance, in particular the r -process.

It is desirable to measure a chain of samarium isotopes at different facilities such as OCL, HI γ S, RCNP and others, and analyze the data sets using different analytical techniques such as the Oslo Method, NRF etc., in order to fully understand the evolution and structure of the resonance features.

6.2 $^{180}\text{Ta}^m$ nucleosynthesis

To sum up, the astrophysical origin of nature's rarest stable isotope ^{180}Ta remained a riddle over the years since many astrophysical processes were thought to produce this neutron-deficient isotope. In particular, the neutrino captures (ν_e, e), scattering reactions ($\nu, \nu'n$) in explosive environments and the s -, r - and p -processes in high-density, high-temperature environments, have all been proposed to explain the synthesis of ^{180}Ta . No consensus exists and it has been proposed that several nucleosynthesis processes, sometimes exclusively, can reproduce the observed abundance of ^{180}Ta in nature. Clearly, many astrophysical processes can theoretically be used to explain the synthesis of ^{180}Ta . However, the significance of each individual process cannot be clearly determined, as a result of the uncertainties on the reaction rates for ^{180}Ta due to the unavailability of experimental data, e.g. the radiative neutron capture rates of ^{179}Ta isotopes or other nuclear ingredients needed to constrain these rates, such as the NLD and γ SF [13]

In this work, the NLDs and γ SFs $^{180,181,182}\text{Ta}$ were obtained experimentally from six independent reactions involving $^{181}\text{Ta}(d,X)^{180,181,182}\text{Ta}$ and $^{181}\text{Ta}(^3\text{He},X)^{180,181}\text{Ta}$ below S_n at the OCL. In order to constraint the systematic uncertainties related to the total NLD at S_n , three different models *i.e.* Back-shifted Fermi-Gas (BSFG), Constant Temperature + Fermi Gas (CT+FG) and Hartree-Fock-Bogoliubov plus combinatorial (HFB+comb.) models were employed in addition to the systematic uncertainties. The $^{180,181,182}\text{Ta}$ NLDs and γ SFs were used as input parameters into the nuclear reactions code TALYS to calculate the $^{179,180,181}\text{Ta}(n,\gamma)$ radiative cross sections. From the latter, the (n,γ) reaction rates and the Maxwellian averaged (n,γ) cross sections (MACS) are obtained. The compatibility of the new measurements with direct measurements supports the approach to use statistical properties *i.e.* NLDs and γ SFs to estimate radiative capture cross sections, reaction rates and MACS. The newly extracted reaction rates are used in s -process calculations in asymptotic giant branch (AGB) stars and p -process simulations

in Type-II supernovae to investigate the nucleosynthesis of ^{180}Ta . The newly constrained reaction rates from this work show that the s -process contribution in low-mass AGB stars to the production of ^{180}Ta galactic enrichment is negligible and that ^{181}Ta is partially produced by AGB stars. The p -process nucleosynthesis of nature's rarest stable isotope ^{180}Ta in Type-II supernovae using new constraints from the current experimental measurements is significant and therefore suggests the p -process to be the fundamental production mechanism of $^{180}\text{Ta}^m$ in the universe. Detailed calculations in additional models stars both for AGBs and SN progenitors will further help in understanding the overall ^{180}Ta enrichment of the galaxy. Two publications based on this work were published [38, 177].

To obtain accurate radiative (n,γ) capture cross sections and to constrain reaction rates for astrophysical processes, future measurements of the statistical properties are essential. In particular, measuring these properties for nuclei important for p -process calculations in Type-II supernova explosions, essential information can be obtained on the synthesis of the under-produced isotopes such as Mo–Ru isotopes, ^{113}In , ^{115}Sn and ^{152}Gd seen in Fig. 5.14. The interesting case of ^{138}La was recently solved [31, 176] using indirect reaction rates extracted from NLD and γSF measurements to show that the p -process is not efficient enough, but that neutrino (ν) captures during the p -process in Type-II supernovae may be responsible for its galactic enrichment [31].

Bibliography

- [1] National Research Council. *Connecting Quarks with the Cosmos: Eleven Science Questions for the New Century*. The National Academies Press, Washington, DC, 2003. ISBN 978-0-309-07406-3. doi: [10.17226/10079](https://doi.org/10.17226/10079).
- [2] H. Schatz. Trends in nuclear astrophysics. *Journal of Physics G: Nuclear and Particle Physics*, 43(6):064001, May 2016. doi: [10.1088/0954-3899/43/6/064001](https://doi.org/10.1088/0954-3899/43/6/064001).
- [3] F. Käppeler, H. Beer, and K. Wisshak. s-process nucleosynthesis-nuclear physics and the classical model. *Reports on Progress in Physics*, 52(8):945–1013, August 1989. doi: [10.1088/0034-4885/52/8/002](https://doi.org/10.1088/0034-4885/52/8/002).
- [4] S. Bisterzo, R. Gallino, F. Käppeler, M. Wiescher, G. Imbriani, O. Straniero, S. Cristallo, J. Görres, and R. J. deBoer. The branchings of the main s-process: their sensitivity to α -induced reactions on ^{13}C and ^{22}Ne and to the uncertainties of the nuclear network. *Monthly Notices of the Royal Astronomical Society*, 449(1):506–527, March 2015. doi: [10.1093/mnras/stv271](https://doi.org/10.1093/mnras/stv271).
- [5] S. Goriely, A. Bauswein, and H. T. Janka. r-process nucleosynthesis in dynamically ejected matter of neutron star mergers. *The Astrophysical Journal*, 738(2):L32, August 2011. doi: [10.1088/2041-8205/738/2/L32](https://doi.org/10.1088/2041-8205/738/2/L32).
- [6] J. de Jesús Mendoza-Temis, M. R. Wu, K. Langanke, G. Martínez-Pinedo, A. Bauswein, and H. T. Janka. Nuclear robustness of the r-process in neutron-star mergers. *Physical Review C*, 92(5), November 2015. doi: [10.1103/physrevc.92.055805](https://doi.org/10.1103/physrevc.92.055805).
- [7] E. Pian, P. D’Avanzo, S. Benetti, M. Branchesi, E. Brocato, S. Campana, et al. Spectroscopic identification of r-process nucleosynthesis in a double neutron-star merger. *Nature*, 551(7678):67–70, October 2017. doi: [10.1038/nature24298](https://doi.org/10.1038/nature24298).
- [8] D. A. Howell C. McCully D. Poznanski D. Kasen J. Barnes M. Zaltzman S. Vasylyev D. Maoz S. Valenti I. Arcavi, G. Hosseinzadeh. Optical emission from a kilonova following a gravitational-wave-detected neutron-star merger. *Nature*, 551(7678):64–66, October 2017. doi: [10.1038/nature24291](https://doi.org/10.1038/nature24291).

- [9] S. E. Woosley, D. H. Hartmann, R. D. Hoffman, and W. C. Haxton. The nu-process. *The Astrophysical Journal*, 356:272, June 1990. doi: [10.1086/168839](https://doi.org/10.1086/168839).
- [10] A. Heger, E. Kolbe, W. C. Haxton, K. Langanke, G. Martínez-Pinedo, and S. E. Woosley. Neutrino nucleosynthesis. *Physics Letters B*, 606(3-4):258–264, January 2005. doi: [10.1016/j.physletb.2004.12.017](https://doi.org/10.1016/j.physletb.2004.12.017).
- [11] A. Sieverding, G. Martínez-Pinedo, L. Huther, K. Langanke, and A. Heger. The ν -process in the light of an improved understanding of supernova neutrino spectra. *The Astrophysical Journal*, 865(2):143, October 2018. doi: [10.3847/1538-4357/aadd48](https://doi.org/10.3847/1538-4357/aadd48).
- [12] A. C. Larsen, A. Spyrou, S. N. Liddick, and M. Guttormsen. Novel techniques for constraining neutron-capture rates relevant for r-process heavy-element nucleosynthesis. *Progress in Particle and Nuclear Physics*, April 2019. doi: [10.1016/j.ppnp.2019.04.002](https://doi.org/10.1016/j.ppnp.2019.04.002).
- [13] M. Arnould and S. Goriely. The p-process of stellar nucleosynthesis: astrophysics and nuclear physics status. *Physics Reports*, 384(1-2):1–84, September 2003. doi: [10.1016/s0370-1573\(03\)00242-4](https://doi.org/10.1016/s0370-1573(03)00242-4).
- [14] T. Rauscher, N. Dauphas, I. Dillmann, C. Fröhlich, Zs. Fülöp, and Gy. Gyürky. Constraining the astrophysical origin of the p-nuclei through nuclear physics and meteoritic data. *Reports on Progress in Physics*, 76(6):066201, May 2013. doi: [10.1088/0034-4885/76/6/066201](https://doi.org/10.1088/0034-4885/76/6/066201).
- [15] M. Arnould, S. Goriely, and K. Takahashi. The r-process of stellar nucleosynthesis: Astrophysics and nuclear physics achievements and mysteries. *Physics Reports*, 450(4-6):97–213, September 2007. doi: [10.1016/j.physrep.2007.06.002](https://doi.org/10.1016/j.physrep.2007.06.002).
- [16] B. R. Mottelson and S. G. Nilsson. Classification of the Nucleonic States in Deformed Nuclei. *Physical Review*, 99(5):1615–1617, September 1955. doi: [10.1103/physrev.99.1615](https://doi.org/10.1103/physrev.99.1615).
- [17] A. Bohr and B. R. MOTTELSON. *Dan. Mat. Fys. Medd*, 27(16), 1953.
- [18] E. Khan N. Paar, D. Vretenar and G. Colò. Exotic modes of excitation in atomic nuclei far from stability. *Reports on Progress in Physics*, 70(5):691–793, April 2007.
- [19] A. Krugmann, D. Martin, P. von Neumann-Cosel, N. Pietralla, and A. Tamii. Investigation of low-energy dipole modes in the heavy deformed nucleus ^{154}Sm via inelastic polarized proton scattering at zero degree. *EPJ Web of Conferences*, 66:02060, 2014. doi: [10.1051/epjconf/20146602060](https://doi.org/10.1051/epjconf/20146602060).
- [20] Andreas Krugmann. *Off-Yrast low-spin structure of deformed nuclei at mass number $A \approx 150$* . PhD thesis, Technische Universität, Darmstadt, June 2014.

- [21] L. Pellegrini. Beam time application iThemba LABS. Technical report, iThemba LABS, 2015.
- [22] K. Heyde, P. von Neumann-Cosel, and A. Richter. Magnetic dipole excitations in nuclei: Elementary modes of nucleonic motion. *Reviews of Modern Physics*, 82(3):2365–2419, September 2010. doi: [10.1103/revmodphys.82.2365](https://doi.org/10.1103/revmodphys.82.2365).
- [23] M. Guttormsen, L. A. Bernstein, A. Bürger, A. Gørgen, F. Gunsing, T. W. Hagen, et al. Observation of Large Scissors Resonance Strength in Actinides. *Physical Review Letters*, 109(16), October 2012. doi: [10.1103/physrevlett.109.162503](https://doi.org/10.1103/physrevlett.109.162503).
- [24] E. B. Balbutsev, I. V. Molodtsova, and P. Schuck. Experimental status of the nuclear spin scissors mode. *Physical Review C*, 97(4), April 2018. doi: [10.1103/physrevc.97.044316](https://doi.org/10.1103/physrevc.97.044316).
- [25] S. Siem, M. Guttormsen, K. Ingeberg, E. Melby, J. Rekestad, A. Schiller, and A. Voinov. Level densities and γ -strength functions in $^{148,149}\text{Sm}$. *Physical Review C*, 65(4), March 2002. doi: [10.1103/physrevc.65.044318](https://doi.org/10.1103/physrevc.65.044318).
- [26] K. S. Beckmann. Dipole Resonances on the Tail of the GDR in Well-Deformed Samarium Isotopes. Master's thesis, University of Oslo, 2018. URL <http://urn.nb.no/URN:NBN:no-68290>.
- [27] A. Simon, M. Guttormsen, A. C. Larsen, C. W. Beausang, P. Humby, J. T. Burke, et al. First observation of low-energy γ -ray enhancement in the rare-earth region. *Physical Review C*, 93(3), March 2016. doi: [10.1103/physrevc.93.034303](https://doi.org/10.1103/physrevc.93.034303).
- [28] F. Naqvi, A. Simon, M. Guttormsen, R. Schwengner, S. Frauendorf, C. S. Reingold, et al. Nuclear level densities and γ -ray strength functions in samarium isotopes. *Physical Review C*, 99(5), May 2019. doi: [10.1103/physrevc.99.054331](https://doi.org/10.1103/physrevc.99.054331).
- [29] A. Schiller, L. Bergholt, M. Guttormsen, E. Melby, J. Rekestad, and S. Siem. Extraction of level density and γ strength function from primary γ spectra. *Nuclear Instruments and Methods in Physics Research Section A: Accelerators, Spectrometers, Detectors and Associated Equipment*, 447(3):498–511, June 2000. doi: [10.1016/s0168-9002\(99\)01187-0](https://doi.org/10.1016/s0168-9002(99)01187-0).
- [30] S. Goriely, M. Arnould, I. Borzov, and M. Rayet. The puzzle of the synthesis of the rare nuclide ^{138}La . *Astronomy & Astrophysics*, 375(2):L35–L38, August 2001. doi: [10.1051/0004-6361:20010956](https://doi.org/10.1051/0004-6361:20010956).
- [31] B. V. Kheswa, M. Wiedeking, F. Giacoppo, S. Goriely, M. Guttormsen, A. C. Larsen, et al. Galactic production of ^{138}La : Impact of $^{138,139}\text{La}$ statistical properties. *Physics Letters B*, 744:268–272, May 2015. doi: [10.1016/j.physletb.2015.03.065](https://doi.org/10.1016/j.physletb.2015.03.065).

- [32] M. Rayet, M. Arnould, M. Hashimoto, N. Prantzos, and K. Nomoto. The p-process in Type II supernovae. *Astronomy & Astrophysics*, 298:517, June 1995. URL <http://adsabs.harvard.edu/abs/1995A26A...298..517R>.
- [33] H. Utsunomiya, H. Akimune, S. Goko, M. Ohta, H. Ueda, T. Yamagata, et al. Cross section measurements of the $^{181}\text{Ta}(\gamma, n)^{180}\text{Ta}$ reaction near neutron threshold and the p-process nucleosynthesis. *Physical Review C*, 67(1), January 2003. doi: [10.1103/physrevc.67.015807](https://doi.org/10.1103/physrevc.67.015807).
- [34] A. Byelikov, T. Adachi, H. Fujita, K. Fujita, Y. Fujita, K. Hatanaka, et al. Gamow-Teller Strength in the Exotic Odd-Odd Nuclei ^{138}La and ^{180}Ta and Its Relevance for Neutrino Nucleosynthesis. *Physical Review Letters*, 98(8), February 2007. doi: [10.1103/physrevlett.98.082501](https://doi.org/10.1103/physrevlett.98.082501).
- [35] H. Beer and R. A. Ward. Neutron-capture nucleosynthesis of nature's rarest stable isotope. *Nature*, 291(5813):308–310, May 1981. doi: [10.1038/291308a0](https://doi.org/10.1038/291308a0).
- [36] K. L. Malatji. Nuclear level densities and gamma-ray strength functions in Ta isotopes and nucleo-synthesis of ^{180}Ta . Master's thesis, University of the Western Cape, 2016. URL <http://hdl.handle.net/11394/5321>.
- [37] C. P. Brits. Search for the scissors resonance in ^{182}Ta . Master's thesis, University of Stellenbosch, 2016. URL <https://scholar.sun.ac.za/handle/10019.1/100282>.
- [38] C. P. Brits, K. L. Malatji, M. Wiedeking, B. V. Kheswa, S. Goriely, F. L. Bello Garrote, et al. Nuclear level densities and γ -ray strength functions of $^{180,181,182}\text{Ta}$. *Physical Review C*, 99(5), May 2019. doi: [10.1103/physrevc.99.054330](https://doi.org/10.1103/physrevc.99.054330).
- [39] W. Hauser and H. Feshbach. The Inelastic Scattering of Neutrons. *Physical Review*, 87(2):366–373, July 1952. doi: [10.1103/physrev.87.366](https://doi.org/10.1103/physrev.87.366).
- [40] A. J. Koning and D. Rochman. Modern Nuclear Data Evaluation with the TALYS Code System. *Nuclear Data Sheets*, 113(12):2841–2934, December 2012. doi: [10.1016/j.nds.2012.11.002](https://doi.org/10.1016/j.nds.2012.11.002).
- [41] H. Bethe. Bremsformel für Elektronen relativistischer Geschwindigkeit. *Zeitschrift für Physik*, 76(5-6):293–299, May 1932. doi: [10.1007/bf01342532](https://doi.org/10.1007/bf01342532).
- [42] A. Gilbert and A. G. W. Cameron. A composite nuclear-level density formula with shell corrections. *Canadian Journal of Physics*, 43(8):1446–1496, August 1965. doi: [10.1139/p65-139](https://doi.org/10.1139/p65-139).
- [43] A. Bohr and B. Mottelson. *Nuclear Structure*, volume 1. New York, 1969.
- [44] C. T. Hibdon. Distribution of the Angular Momenta, Level Spacings, and Neutron Widths of ^{28}Al . *Physical Review*, 114(1):179–194, April 1959. doi: [10.1103/physrev.114.179](https://doi.org/10.1103/physrev.114.179).

- [45] C. T. Hibdon. Nuclear Energy Levels of ^{24}Na in the Region from 630 to 860 keV. *Physical Review*, 124(2):500–514, October 1961. doi: [10.1103/physrev.124.500](https://doi.org/10.1103/physrev.124.500).
- [46] B. Keisch. Yield Ratios of Isomers Produced by Neutron Activation. *Physical Review*, 129(2):769–775, January 1963. doi: [10.1103/physrev.129.769](https://doi.org/10.1103/physrev.129.769).
- [47] T. von Egidy and D. Bucurescu. Erratum: Systematics of nuclear level density parameters [Phys. Rev. C 72, 044311 (2005)]. *Physical Review C*, 73(4), April 2006. doi: [10.1103/physrevc.73.049901](https://doi.org/10.1103/physrevc.73.049901).
- [48] T. von Egidy and D. Bucurescu. Experimental energy-dependent nuclear spin distributions. *Physical Review C*, 80(5), November 2009. doi: [10.1103/physrevc.80.054310](https://doi.org/10.1103/physrevc.80.054310).
- [49] M. Guttormsen, S. Goriely, A. C. Larsen, A. Görge, T. W. Hagen, T. Renstrøm, et al. Quasicontinuum γ decay of $^{91,92}\text{Zr}$: Benchmarking indirect (n,γ) cross section measurements for the s process. *Physical Review C*, 96(2), August 2017. doi: [10.1103/physrevc.96.024313](https://doi.org/10.1103/physrevc.96.024313).
- [50] T. Ericson. A statistical analysis of excited nuclear states. *Nuclear Physics*, 11:481–491, May 1959. doi: [10.1016/0029-5582\(59\)90291-3](https://doi.org/10.1016/0029-5582(59)90291-3).
- [51] A. J. Koning, S. Hilaire, and S. Goriely. Global and local level density models. *Nuclear Physics A*, 810(1-4):13–76, September 2008. doi: [10.1016/j.nuclphysa.2008.06.005](https://doi.org/10.1016/j.nuclphysa.2008.06.005).
- [52] P. Demetriou and S. Goriely. Microscopic nuclear level densities for practical applications. *Nuclear Physics A*, 695(1-4):95–108, December 2001. doi: [10.1016/s0375-9474\(01\)01095-8](https://doi.org/10.1016/s0375-9474(01)01095-8).
- [53] S. Goriely, S. Hilaire, and A. J. Koning. Improved microscopic nuclear level densities within the Hartree-Fock-Bogoliubov plus combinatorial method. *Physical Review C*, 78(6), December 2008. doi: [10.1103/physrevc.78.064307](https://doi.org/10.1103/physrevc.78.064307).
- [54] S. Hilaire and S. Goriely. Global microscopic nuclear level densities within the HFB plus combinatorial method for practical applications. *Nuclear Physics A*, 779:63–81, November 2006. doi: [10.1016/j.nuclphysa.2006.08.014](https://doi.org/10.1016/j.nuclphysa.2006.08.014).
- [55] S. Goriely, S. Hilaire, and A. J. Koning. Improved predictions of nuclear reaction rates with the TALYS reaction code for astrophysical applications. *Astronomy & Astrophysics*, 487(2):767–774, June 2008. doi: [10.1051/0004-6361:20078825](https://doi.org/10.1051/0004-6361:20078825).
- [56] G. A. Bartholomew, E. D. Earle, A. J. Ferguson, J. W. Knowles, and M. A. Lone. Gamma-Ray Strength Functions. In *Advances in Nuclear Physics*, pages 229–324. Springer US, 1973. doi: [10.1007/978-1-4615-9044-6_4](https://doi.org/10.1007/978-1-4615-9044-6_4).
- [57] K.S. Krane. *Introductory Nuclear Physics*. Wiley, 1987. ISBN 9780471805533. URL <https://books.google.co.za/books?id=ConwAAAAMAAJ>.

- [58] R. Capote, M. Herman, P. Obložinský, P. G. Young, S. Goriely, T. Belgia, et al. RIPL – Reference Input Parameter Library for Calculation of Nuclear Reactions and Nuclear Data Evaluations. *Nuclear Data Sheets*, 110(12):3107–3214, December 2009. doi: [10.1016/j.nds.2009.10.004](https://doi.org/10.1016/j.nds.2009.10.004).
- [59] E. Fermi. *Nuclear Physics*. University of Chicago Press, Chicago, 1950.
- [60] J. A. Holmes, S. E. Woosley, W. A. Fowler, and B. A. Zimmerman. Tables of thermonuclear-reaction-rate data for neutron-induced reactions on heavy nuclei. *Atomic Data and Nuclear Data Tables*, 18(4):305–412, October 1976. doi: [10.1016/0092-640x\(76\)90011-5](https://doi.org/10.1016/0092-640x(76)90011-5).
- [61] U. Kneissl, H. H. Pitz, and A. Zilges. Investigation of nuclear structure by resonance fluorescence scattering. *Progress in Particle and Nuclear Physics*, 37:349–433, January 1996. doi: [10.1016/0146-6410\(96\)00055-5](https://doi.org/10.1016/0146-6410(96)00055-5).
- [62] A. M. Hoogenboom. A new method in gamma-ray spectroscopy: A two crystal scintillation spectrometer with improved resolution. *Nuclear Instruments*, 3(2):57–68, August 1958. doi: [10.1016/0369-643x\(58\)90092-6](https://doi.org/10.1016/0369-643x(58)90092-6).
- [63] M. Wiedeking, L. A. Bernstein, M. Krtička, D. L. Bleuel, J. M. Allmond, M. S. Basunia, et al. Low-Energy Enhancement in the Photon Strength of ^{95}Mo . *Physical Review Letters*, 108(16), April 2012. doi: [10.1103/physrevlett.108.162503](https://doi.org/10.1103/physrevlett.108.162503).
- [64] J. Kopecky, S. Goriely, S. Péru, S. Hilaire, and M. Martini. E1 and M1 strength functions from average resonance capture data. *Physical Review C*, 95(5), May 2017. doi: [10.1103/physrevc.95.054317](https://doi.org/10.1103/physrevc.95.054317).
- [65] R. Firestone P. Dimitriou and S. Siem. Summary Report of Consultant’s Meeting on Compilation and Evaluation of Gamma-ray Data, INDC (NDS)-0649. Technical report, IAEA, Vienna, 2013. URL <http://www-nds.iaea.org/publications/indc/indc-nds-0649.pdf>.
- [66] D. M. Brink. Individual particle and collective aspects of the nuclear photoeffect. *Nuclear Physics*, 4:215–220, August 1957. doi: [10.1016/0029-5582\(87\)90021-6](https://doi.org/10.1016/0029-5582(87)90021-6).
- [67] P. Axel. Electric Dipole Ground-State Transition Width Strength Function and 7-Mev Photon Interactions. *Physical Review*, 126(2):671–683, April 1962. doi: [10.1103/physrev.126.671](https://doi.org/10.1103/physrev.126.671).
- [68] J. Kopecky and R.E. Chrien. Observation of the M1 giant resonance by resonance averaging in ^{106}Pd . *Nuclear Physics A*, 468(2):285–300, June 1987. doi: [10.1016/0375-9474\(87\)90518-5](https://doi.org/10.1016/0375-9474(87)90518-5).
- [69] J. Kopecky and M. Uhl. Test of gamma-ray strength functions in nuclear reaction model calculations. *Physical Review C*, 41(5):1941–1955, May 1990. doi: [10.1103/physrevc.41.1941](https://doi.org/10.1103/physrevc.41.1941).

- [70] R. Schwengner, S. Frauendorf, and A. C. Larsen. Low-Energy Enhancement of Magnetic Dipole Radiation. *Physical Review Letters*, 111(23), December 2013. doi: [10.1103/physrevlett.111.232504](https://doi.org/10.1103/physrevlett.111.232504).
- [71] B. A. Brown and A. C. Larsen. Large Low- Energy M1 Strength for $^{56,57}\text{Fe}$ within the Nuclear Shell Model. *Physical Review Letters*, 113(25), December 2014. doi: [10.1103/physrevlett.113.252502](https://doi.org/10.1103/physrevlett.113.252502).
- [72] R. Schwengner, S. Frauendorf, and B. A. Brown. Low-Energy Magnetic Dipole Radiation in Open-Shell Nuclei. *Physical Review Letters*, 118(9), March 2017. doi: [10.1103/physrevlett.118.092502](https://doi.org/10.1103/physrevlett.118.092502).
- [73] S. Goriely, S. Hilaire, S. Péru, M. Martini, I. Deloncle, and F. Lechaftois. Gogny-Hartree-Fock-Bogolyubov plus quasiparticle random-phase approximation predictions of the M1 strength function and its impact on radiative neutron capture cross section. *Physical Review C*, 94(4), October 2016. doi: [10.1103/physrevc.94.044306](https://doi.org/10.1103/physrevc.94.044306).
- [74] S. Goriely and L. Siess. Sensitivity of the s-process nucleosynthesis in agb stars to the overshoot model. *Astronomy and Astrophysics*, 609:A29, 2018. doi: [10.1051/0004-6361/201731427](https://doi.org/10.1051/0004-6361/201731427).
- [75] J Speth and A van der Woude. Giant resonances in nuclei. *Reports on Progress in Physics*, 44(7):719–786, July 1981. doi: [10.1088/0034-4885/44/7/002](https://doi.org/10.1088/0034-4885/44/7/002). URL <https://doi.org/10.1088%2F0034-4885%2F44%2F7%2F002>.
- [76] W. Greiner and J. A. Maruhn. *Nuclear Models*. Springer Berlin Heidelberg, 1996. doi: [10.1007/978-3-642-60970-1](https://doi.org/10.1007/978-3-642-60970-1).
- [77] M. N. Harakeh and A. van der Woude. *Giant Resonances: Fundamental High-Frequency Modes of Nuclear Excitation*. Number Pages 57-58 and 222-224. Oxford University Press, 2001. ISBN 9780198517337.
- [78] D. Savran, T. Aumann, and A. Zilges. Experimental studies of the Pygmy Dipole Resonance. *Progress in Particle and Nuclear Physics*, 70:210–245, May 2013. doi: [10.1016/j.pnpnp.2013.02.003](https://doi.org/10.1016/j.pnpnp.2013.02.003).
- [79] H. K. Toft, A. C. Larsen, A. Bürger, M. Guttormsen, A. Gørgen, H. T. Nyhus, T. Renstrøm, S. Siem, G. M. Tveten, and A. Voinov. Evolution of the pygmy dipole resonance in Sn isotopes. *Physical Review C*, 83(4), April 2011. doi: [10.1103/physrevc.83.044320](https://doi.org/10.1103/physrevc.83.044320).
- [80] R. Neveling, H. Fujita, F. D. Smit, T. Adachi, G. P. A. Berg, E. Z. Buthelezi, et al. High energy-resolution zero-degree facility for light-ion scattering and reactions at iThemba LABS. *Nuclear Instruments and Methods in Physics Research Section A: Accelerators*,

- Spectrometers, Detectors and Associated Equipment*, 654(1):29–39, October 2011. doi: [10.1016/j.nima.2011.06.077](https://doi.org/10.1016/j.nima.2011.06.077).
- [81] A. Tamii, Y. Fujita, H. Matsubara, T. Adachi, J. Carter, M. Dozono, et al. Measurement of high energy resolution inelastic proton scattering at and close to zero degrees. *Nuclear Instruments and Methods in Physics Research Section A: Accelerators, Spectrometers, Detectors and Associated Equipment*, 605(3):326–338, July 2009. doi: [10.1016/j.nima.2009.03.248](https://doi.org/10.1016/j.nima.2009.03.248).
- [82] S. Goriely. Radiative neutron captures by neutron-rich nuclei and the r-process nucleosynthesis. *Physics Letters B*, 436(1-2):10–18, September 1998. doi: [10.1016/s0370-2693\(98\)00907-1](https://doi.org/10.1016/s0370-2693(98)00907-1).
- [83] N. Lo Iudice and F. Palumbo. New Isovector Collective Modes in Deformed Nuclei. *Physical Review Letters*, 41(22):1532–1534, November 1978. doi: [10.1103/physrevlett.41.1532](https://doi.org/10.1103/physrevlett.41.1532).
- [84] D. Bohle, A. Richter, W. Steffen, A. E. L. Dieperink, N. Lo Iudice, F. Palumbo, and O. Scholten. New magnetic dipole excitation mode studied in the heavy deformed nucleus ^{156}Gd by inelastic electron scattering. *Physics Letters B*, 137(1-2):27–31, March 1984. doi: [10.1016/0370-2693\(84\)91099-2](https://doi.org/10.1016/0370-2693(84)91099-2).
- [85] J. W. Rohlfs. *Modern Physics from α to Z*. March 1994.
- [86] F. Iachello. Electron scattering in the interacting boson model. *Nuclear Physics A*, 358: 89–112, April 1981. doi: [10.1016/0375-9474\(81\)90308-0](https://doi.org/10.1016/0375-9474(81)90308-0).
- [87] Y. S. Chen and G. A. Leander. Quasicontinuum properties of M1 spectra in the particle-rotor model. *Physical Review C*, 26(6):2607–2615, December 1982. doi: [10.1103/physrevc.26.2607](https://doi.org/10.1103/physrevc.26.2607).
- [88] A. Richter. Shell model and magnetic dipole modes in deformed nuclei. *Nuclear Physics A*, 507(1):99–128, January 1990. doi: [10.1016/0375-9474\(90\)90571-3](https://doi.org/10.1016/0375-9474(90)90571-3).
- [89] M. Guttormsen, J. Rekstad, A. Henriquez, F. Ingebretsen, and T. F. Thorsteinsen. Nonstatistical Cooling of the Highly Excited ^{161}Dy Nucleus. *Physical Review Letters*, 52(2):102–104, January 1984. doi: [10.1103/physrevlett.52.102](https://doi.org/10.1103/physrevlett.52.102).
- [90] B. Baramsai, F. Bečvář, T. A. Bredeweg, R. C. Haight, M. Jandel, J. Kroll, et al. Scissors Mode of ^{162}Dy Studied from Resonance Neutron Capture. *EPJ Web of Conferences*, 93: 01037, 2015. doi: [10.1051/epjconf/20159301037](https://doi.org/10.1051/epjconf/20159301037).
- [91] N. Pietralla, P. von Brentano, R.-D. Herzberg, U. Kneissl, N. Lo Iudice, H. Maser, H. H. Pitz, and A. Zilges. Systematics of the excitation energy of the 1^+ scissors mode and its empirical dependence on the nuclear deformation parameter. *Physical Review C*, 58(1): 184–190, July 1998. doi: [10.1103/physrevc.58.184](https://doi.org/10.1103/physrevc.58.184).

- [92] I. Bauske, J. M. Arias, P. von Brentano, A. Frank, H. Friedrichs, R. D. Heil, et al. First observation of scissors mode states in an odd-mass nucleus. *Physical Review Letters*, 71(7):975–978, August 1993. doi: [10.1103/physrevlett.71.975](https://doi.org/10.1103/physrevlett.71.975).
- [93] W. Ziegler, C. Rangacharyulu, A. Richter, and C. Spieler. Orbital magnetic dipole strength in $^{148,150,152,154}\text{Sm}$ and nuclear deformation. *Physical Review Letters*, 65(20):2515–2518, November 1990. doi: [10.1103/physrevlett.65.2515](https://doi.org/10.1103/physrevlett.65.2515).
- [94] S. RAMAN, C. W. NESTOR, and P. TIKKANEN. Transition probability from the ground to the first-excited 2^+ state of even-even nuclides. *Atomic Data and Nuclear Data Tables*, 78(1):1–128, May 2001. doi: [10.1006/adnd.2001.0858](https://doi.org/10.1006/adnd.2001.0858).
- [95] A. Richter. Probing the nuclear magnetic dipole response with electrons, photons and hadrons. *Progress in Particle and Nuclear Physics*, 34:261–284, January 1995. doi: [10.1016/0146-6410\(95\)00022-b](https://doi.org/10.1016/0146-6410(95)00022-b).
- [96] A. Voinov, M. Guttormsen, E. Melby, J. Rekstad, A. Schiller, and S. Siem. γ -ray strength function and pygmy resonance in rare earth nuclei. *Physical Review C*, 63(4), March 2001. doi: [10.1103/physrevc.63.044313](https://doi.org/10.1103/physrevc.63.044313).
- [97] E. Melby, M. Guttormsen, J. Rekstad, A. Schiller, S. Siem, and A. Voinov. Thermal and electromagnetic properties of ^{166}Er and ^{167}Er . *Physical Review C*, 63(4), March 2001. doi: [10.1103/physrevc.63.044309](https://doi.org/10.1103/physrevc.63.044309).
- [98] M. Guttormsen, A. Bagheri, R. Chankova, J. Rekstad, S. Siem, A. Schiller, and A. Voinov. Thermal properties and radiative strengths in $^{160,161,162}\text{Dy}$. *Physical Review C*, 68(6), December 2003. doi: [10.1103/physrevc.68.064306](https://doi.org/10.1103/physrevc.68.064306).
- [99] H. T. Nyhus, S. Siem, M. Guttormsen, A. C. Larsen, A. Bürger, N. U. H. Syed, G. M. Tveten, and A. Voinov. Radiative strength functions in $^{163,164}\text{Dy}$. *Physical Review C*, 81(2), February 2010. doi: [10.1103/physrevc.81.024325](https://doi.org/10.1103/physrevc.81.024325).
- [100] T. G. Tornyi, M. Guttormsen, T. K. Eriksen, A. Gørgen, F. Giacoppo, T. W. Hagen, et al. Level density and γ -ray strength function in the odd-odd ^{238}Np nucleus. *Physical Review C*, 89(4), April 2014. doi: [10.1103/physrevc.89.044323](https://doi.org/10.1103/physrevc.89.044323).
- [101] T. A. Laplace, F. Zeiser, M. Guttormsen, A. C. Larsen, D. L. Bleuel, L. A. Bernstein, et al. Statistical properties of ^{243}Pu , and $^{242}\text{Pu}(n,\gamma)$ cross section calculation. *Physical Review C*, 93(1), January 2016. doi: [10.1103/physrevc.93.014323](https://doi.org/10.1103/physrevc.93.014323).
- [102] T. Renstrøm, H. Utsunomiya, H. T. Nyhus, A. C. Larsen, M. Guttormsen, G. M. Tveten, et al. Verification of detailed balance for γ absorption and emission in Dy isotopes. *Physical Review C*, 98(5), November 2018. doi: [10.1103/physrevc.98.054310](https://doi.org/10.1103/physrevc.98.054310).

- [103] M. Guttormsen, L. A. Bernstein, A. Gørgen, B. Jurado, S. Siem, M. Aiche, et al. Scissors resonance in the quasicontinuum of Th, Pa, and U isotopes. *Physical Review C*, 89(1), January 2014. doi: [10.1103/physrevc.89.014302](https://doi.org/10.1103/physrevc.89.014302).
- [104] A. Nord, A. Schiller, T. Eckert, O. Beck, J. Besserer, P. von Brentano, et al. Systematic study of the fragmentation of low-lying dipole strength in odd-A rare earth nuclei investigated in nuclear resonance fluorescence experiments. *Physical Review C*, 54(5):2287–2295, Nov 1996. doi: [10.1103/physrevc.54.2287](https://doi.org/10.1103/physrevc.54.2287).
- [105] J. Enders, N. Huxel, P. von Neumann-Cosel, and A. Richter. Where is the Scissors Mode Strength in Odd-Mass Nuclei? *Physical Review Letters*, 79(11):2010–2013, September 1997. doi: [10.1103/physrevlett.79.2010](https://doi.org/10.1103/physrevlett.79.2010).
- [106] J. Kroll, B. Baramsai, G. E. Mitchell, U. Agvaanluvsan, F. Bečvář, T. A. Bredeweg, et al. Strength of the scissors mode in odd-mass Gd isotopes from the radiative capture of resonance neutrons. *Physical Review C*, 88(3), September 2013. doi: [10.1103/physrevc.88.034317](https://doi.org/10.1103/physrevc.88.034317).
- [107] A. Voinov, E. Algin, U. Agvaanluvsan, T. Belgya, R. Chankova, M. Guttormsen, G. E. Mitchell, J. Rekestad, A. Schiller, and S. Siem. Large Enhancement of Radiative Strength for Soft Transitions in the Quasicontinuum. *Physical Review Letters*, 93(14), Sep 2004. doi: [10.1103/physrevlett.93.142504](https://doi.org/10.1103/physrevlett.93.142504).
- [108] A. C. Larsen, M. Guttormsen, R. Chankova, F. Ingebretsen, T. Lönnroth, S. Messelt, et al. Nuclear level densities and γ -ray strength functions $^{44,45}\text{Sc}$. *Physical Review C*, 76(4), Oct 2007. doi: [10.1103/physrevc.76.044303](https://doi.org/10.1103/physrevc.76.044303).
- [109] A. Bürger, A. C. Larsen, S. Hilaire, M. Guttormsen, S. Harissopulos, M. Kmiecik, et al. Nuclear level density and γ -ray strength function of ^{43}Sc . *Physical Review C*, 85(6), June 2012. doi: [10.1103/physrevc.85.064328](https://doi.org/10.1103/physrevc.85.064328).
- [110] A. C. Larsen, S. Goriely, A. Bürger, M. Guttormsen, A. Gørgen, S. Harissopulos, et al. Primary γ -ray spectra in ^{44}Ti of astrophysical interest. *Physical Review C*, 85(1), Jan 2012. doi: [10.1103/physrevc.85.014320](https://doi.org/10.1103/physrevc.85.014320).
- [111] N. U. H. Syed, A. C. Larsen, A. Bürger, M. Guttormsen, S. Harissopulos, M. Kmiecik, et al. Extraction of thermal and electromagnetic properties in ^{45}Ti . *Physical Review C*, 80(4), October 2009. doi: [10.1103/physrevc.80.044309](https://doi.org/10.1103/physrevc.80.044309).
- [112] M. Guttormsen, A. C. Larsen, A. Bürger, A. Gørgen, S. Harissopulos, M. Kmiecik, et al. Fermi's golden rule applied to the γ decay in the quasicontinuum of ^{46}Ti . *Physical Review C*, 83(1), January 2011. doi: [10.1103/physrevc.83.014312](https://doi.org/10.1103/physrevc.83.014312).

- [113] A. C. Larsen, R. Chankova, M. Guttormsen, F. Ingebretsen, S. Messelt, J. Rekestad, et al. Microcanonical entropies and radiative strength functions of $^{50,51}\text{V}$. *Physical Review C*, 73(6), Jun 2006. doi: [10.1103/physrevc.73.064301](https://doi.org/10.1103/physrevc.73.064301).
- [114] H. Utsunomiya, T. Renstrøm, G. M. Tveten, S. Goriely, S. Katayama, T. Ari-izumi, et al. Photoneutron cross sections for Ni isotopes: Toward understanding (n,γ) cross sections relevant to weak s-process nucleosynthesis. *Physical Review C*, 98(5), Nov 2018. doi: [10.1103/physrevc.98.054619](https://doi.org/10.1103/physrevc.98.054619).
- [115] A. Voinov, S. M. Grimes, C. R. Brune, M. Guttormsen, A. C. Larsen, T. N. Massey, A. Schiller, and S. Siem. γ -strength functions ^{60}Ni from two-step cascades following proton capture. *Physical Review C*, 81(2), February 2010. doi: [10.1103/physrevc.81.024319](https://doi.org/10.1103/physrevc.81.024319).
- [116] L. Crespo Campo, F. L. Bello Garrote, T. K. Eriksen, A. Görgen, M. Guttormsen, K. Hadynska-Klek, et al. Statistical γ -decay properties of ^{64}Ni and deduced (n,γ) cross section of the s-process branch-point nucleus ^{63}Ni . *Physical Review C*, 94(4), October 2016. doi: [10.1103/physrevc.94.044321](https://doi.org/10.1103/physrevc.94.044321).
- [117] L. Crespo Campo, A. C. Larsen, F. L. Bello Garrote, T. K. Eriksen, F. Giacoppo, A. Görgen, et al. Investigating the γ decay of ^{65}Ni from particle- γ coincidence data. *Physical Review C*, 96(1), July 2017. doi: [10.1103/physrevc.96.014312](https://doi.org/10.1103/physrevc.96.014312).
- [118] A. Spyrou, A. C. Larsen, S. N. Liddick, F. Naqvi, B. P. Crider, A. C. Dombos, et al. Neutron-capture rates for explosive nucleosynthesis: the case of $^{68}\text{Ni}(n,\gamma)^{69}\text{Ni}$. *Journal of Physics G: Nuclear and Particle Physics*, 44(4):044002, February 2017. doi: [10.1088/1361-6471/aa5ae7](https://doi.org/10.1088/1361-6471/aa5ae7).
- [119] T. Renstrøm, H. T. Nyhus, H. Utsunomiya, R. Schwengner, S. Goriely, A. C. Larsen, et al. Low-energy enhancement in the γ -ray strength functions of $^{73,74}\text{Ge}$. *Physical Review C*, 93(6), Jun 2016. doi: [10.1103/physrevc.93.064302](https://doi.org/10.1103/physrevc.93.064302).
- [120] A. Spyrou, S. N. Liddick, A. C. Larsen, M. Guttormsen, K. Cooper, A. C. Dombos, et al. Novel technique for Constraining r-Process (n,γ) Reaction Rates. *Physical Review Letters*, 113(23), December 2014. doi: [10.1103/physrevlett.113.232502](https://doi.org/10.1103/physrevlett.113.232502).
- [121] M. Guttormsen, R. Chankova, U. Agvaanluvsan, E. Algin, L. A. Bernstein, F. Ingebretsen, et al. Radiative strength functions in $^{93-98}\text{Mo}$. *Physical Review C*, 71(4), Apr 2005. doi: [10.1103/physrevc.71.044307](https://doi.org/10.1103/physrevc.71.044307).
- [122] A. C. Larsen, I. E. Ruud, A. Bürger, S. Goriely, M. Guttormsen, A. Görgen, et al. Transitional γ strength in Cd isotopes. *Physical Review C*, 87(1), January 2013. doi: [10.1103/physrevc.87.014319](https://doi.org/10.1103/physrevc.87.014319).

- [123] J. E. Midtbø, A. C. Larsen, T. Renstrøm, F. L. Bello Garrote, and E. Lima. Consolidating the concept of low-energy magnetic dipole decay radiation. *Physical Review C*, 98(6), December 2018. doi: [10.1103/physrevc.98.064321](https://doi.org/10.1103/physrevc.98.064321).
- [124] A. C. Larsen, N. Blasi, A. Bracco, F. Camera, T. K. Eriksen, A. Görge, et al. Evidence for the Dipole Nature of the Low-Energy γ Enhancement in ^{56}Fe . *Physical Review Letters*, 111(24), December 2013. doi: [10.1103/physrevlett.111.242504](https://doi.org/10.1103/physrevlett.111.242504).
- [125] A. C. Larsen, M. Guttormsen, N. Blasi, A. Bracco, F. Camera, L. Crespo Campo, et al. Low-energy enhancement and fluctuations of γ -ray strength functions in $^{56,57}\text{Fe}$: test of the Brink-Axel hypothesis. *Journal of Physics G: Nuclear and Particle Physics*, 44(6): 064005, April 2017. doi: [10.1088/1361-6471/aa644a](https://doi.org/10.1088/1361-6471/aa644a).
- [126] M. D. Jones, A. O. Macchiavelli, M. Wiedeking, L. A. Bernstein, H. L. Crawford, C. M. Campbell, et al. Examination of the low-energy enhancement of the γ -ray strength function of ^{56}Fe . *Physical Review C*, 97(2), February 2018. doi: [10.1103/physrevc.97.024327](https://doi.org/10.1103/physrevc.97.024327).
- [127] E. Litvinova and N. Belov. Low-energy limit of the radiative dipole strength in nuclei. *Physical Review C*, 88(3), September 2013. doi: [10.1103/physrevc.88.031302](https://doi.org/10.1103/physrevc.88.031302).
- [128] A. C. Larsen and S. Goriely. Impact of a low-energy enhancement in the γ -ray strength function on the neutron-capture cross section. *Physical Review C*, 82(1), July 2010. doi: [10.1103/physrevc.82.014318](https://doi.org/10.1103/physrevc.82.014318).
- [129] S. Hilaire, Ch. Lagrange, and A. J. Koning. Comparisons between various width fluctuation correction factors for compound nucleus reactions. *Annals of Physics*, 306(2):209–231, August 2003. doi: [10.1016/s0003-4916\(03\)00076-9](https://doi.org/10.1016/s0003-4916(03)00076-9).
- [130] *The homepage of the Oslo Cyclotron Laboratory (OCL)*, 2019. URL <http://www.mn.uio.no/fysikk/english/research/about/infrastructure/OCL/>.
- [131] M. Guttormsen, A. Atac, G. Løvholden, S. Messelt, T. Ramsøy, J. Rekstad, T. F. Thorsteinson, T. S. Tveter, and Z. Zelazny. Statistical Gamma-Decay at Low Angular Momentum. *Physica Scripta*, T32:54–60, January 1990. doi: [10.1088/0031-8949/1990/t32/010](https://doi.org/10.1088/0031-8949/1990/t32/010).
- [132] M. Guttormsen, A. Bürger, T. E. Hansen, and N. Lietaer. The SiRi particle-telescope system. *Nuclear Instruments and Methods in Physics Research Section A: Accelerators, Spectrometers, Detectors and Associated Equipment*, 648(1):168–173, August 2011. doi: [10.1016/j.nima.2011.05.055](https://doi.org/10.1016/j.nima.2011.05.055).
- [133] K. L. Malatji, B. V. Kheswa, M. Wiedeking, F. L. Bello Garrote, C. P. Brits, D. L. Bleuel, et al. Nuclear level densities and γ -ray strength functions of $^{180,181}\text{Ta}$ and neutron capture cross sections. *EPJ Web of Conferences*, 146:01010, 2017. doi: [10.1051/epj-conf/201714601010](https://doi.org/10.1051/epj-conf/201714601010).

- [134] G. M. Tveten. *Developments for studies of the extremes of nuclear matter*. PhD thesis, University of Oslo, 2013. URL <http://urn.nb.no/URN:NBN:no-38977>.
- [135] C. Iliadis. *Nuclear physics of stars*. Physics textbook. Wiley-VCH, Weinheim, 2007. ISBN 9783527406029.
- [136] G. F. Knoll. *Radiation detection and measurement*. John Wiley & Sons, Inc., 3rd ed. edition, 2000. ISBN 9780471073383.
- [137] M. Guttormsen, T. S. Tveter, L. Bergholt, F. Ingebretsen, and J. Rekstad. The unfolding of continuum γ -ray spectra. *Nuclear Instruments and Methods in Physics Research Section A: Accelerators, Spectrometers, Detectors and Associated Equipment*, 374(3):371–376, June 1996. doi: [10.1016/0168-9002\(96\)00197-0](https://doi.org/10.1016/0168-9002(96)00197-0).
- [138] *The projects research page of the Department of Physics at the University of Oslo (UiO)*, 2019. URL <https://www.mn.uio.no/fysikk/english/research/projects/oscar/>.
- [139] A. Schiller, L. Bergholt, M. Guttormsen, E. Melby, S. Messelt, E. A. Olsen, et al. Recent upgrades and performance of the CACTUS detector array. Technical report, Department of Physics, University of Oslo, 1998. URL http://inis.iaea.org/search/search.aspx?orig_q=RN:29032402.
- [140] A. C. Larsen. *Statistical properties in the quasi-continuum of atomic nuclei*. PhD thesis, University of Oslo, 2008. URL <http://urn.nb.no/URN:NBN:no-19731>.
- [141] J. F. Ziegler. Stopping of energetic light ions in elemental matter. *Journal of Applied Physics*, 85(3):1249–1272, February 1999. doi: [10.1063/1.369844](https://doi.org/10.1063/1.369844).
- [142] V. W. Ingeberg. Qkinz Kinematics Calculator, 2018.
- [143] *Data extracted from NuDat database on the National Nuclear Data Center*. Brookhaven National Laboratory, USA, as of September 2018, 2019. URL <https://www.nndc.bnl.gov/nudat2/>.
- [144] M. Guttormsen, T. Ramsøy, and J. Rekstad. The first generation of γ -rays from hot nuclei. *Nuclear Instruments and Methods in Physics Research Section A: Accelerators, Spectrometers, Detectors and Associated Equipment*, 255(3):518–523, April 1987. doi: [10.1016/0168-9002\(87\)91221-6](https://doi.org/10.1016/0168-9002(87)91221-6).
- [145] N. U. H. Syed. *Nuclear structure and statistical decay properties of closed and near closed shell nuclei*. PhD thesis, University of Oslo, 2009. URL <http://urn.nb.no/URN:NBN:no-21833>.

- [146] A. C. Larsen, M. Guttormsen, M. Krtička, E. Běták, A. Bürger, A. Görgen, et al. Analysis of possible systematic errors in the Oslo method. *Physical Review C*, 83(3), March 2011. doi: [10.1103/physrevc.83.034315](https://doi.org/10.1103/physrevc.83.034315).
- [147] L. Henden, L. Bergholt, M. Guttormsen, J. Rekstad, and T. S. Tveter. On the relation between the statistical γ -decay and the level density in ^{162}Dy . *Nuclear Physics A*, 589(2): 249–266, July 1995. doi: [10.1016/0375-9474\(95\)00133-1](https://doi.org/10.1016/0375-9474(95)00133-1).
- [148] T. Von Egidy, H. H. Schmidt, and A. N. Behkami. Nuclear level densities and level spacing distributions: Part II. *Nuclear Physics A*, 481(2):189–206, May 1988. doi: [10.1016/0375-9474\(88\)90491-5](https://doi.org/10.1016/0375-9474(88)90491-5).
- [149] S.F. Mughabghab. *Atlas of Neutron Resonances: Resonance Parameters and Thermal Cross Sections Z = 1–100*. Elsevier, 5th edition, 2006.
- [150] S. F. Mughabghab. Recommended Thermal Cross Sections, Resonance Properties, and Resonance Parameters for $Z = 62–102$. In *Atlas of Neutron Resonances*, pages 89–822. Elsevier, 2018. doi: [10.1016/b978-0-44-463769-7.00015-4](https://doi.org/10.1016/b978-0-44-463769-7.00015-4).
- [151] F. Zeiser. Nuclear structure and dynamics in the quasi-continuum of ^{240}Pu . Master's thesis, University of Oslo, 2016. URL <http://urn.nb.no/URN:NBN:no-53988>.
- [152] H. T. Nyhus, S. Siem, M. Guttormsen, A. C. Larsen, A. Bürger, N. U. H. Syed, H. K. Toft, G. M. Tveten, and A. Voinov. Level density and thermodynamic properties of dysprosium isotopes. *Physical Review C*, 85(1), January 2012. doi: [10.1103/physrevc.85.014323](https://doi.org/10.1103/physrevc.85.014323).
- [153] D. M. Filipescu, I. Gheorghe, H. Utsunomiya, S. Goriely, T. Renstrøm, H. T. Nyhus, et al. Photoneutron cross sections for samarium isotopes: Toward a unified understanding of (γ, n) and (n, γ) reactions in the rare earth region. *Physical Review C*, 90(6), December 2014. doi: [10.1103/physrevc.90.064616](https://doi.org/10.1103/physrevc.90.064616).
- [154] P. Carlos, H. Beil, R. Bergère, A. Leprêtre, A. De Miniac, and A. Veyssière. The giant dipole resonance in the transition region of the samarium isotopes. *Nuclear Physics A*, 225(1):171–188, June 1974. doi: [10.1016/0375-9474\(74\)90373-x](https://doi.org/10.1016/0375-9474(74)90373-x).
- [155] V. V. Varlamov, B. S. Ishkhanov, and V. N. Orlin. New approach to analyzing and evaluating cross sections for partial photoneutron reactions. *Physics of Atomic Nuclei*, 75(11):1339–1349, November 2012. doi: [10.1134/s1063778812110191](https://doi.org/10.1134/s1063778812110191).
- [156] B. L. Berman, M. A. Kelly, R. L. Bramblett, J. T. Caldwell, H. S. Davis, and S. C. Fultz. Giant Resonance in Deformed Nuclei: Photoneutron Cross Sections for ^{153}Eu , ^{160}Gd , ^{165}Ho , and ^{186}W . *Physical Review*, 185(4):1576–1590, September 1969. doi: [10.1103/physrev.185.1576](https://doi.org/10.1103/physrev.185.1576).

- [157] V. A. Semenov O. V. Vasilijev and S. F. Semenko. Giant Dipole Resonance in Transition Region Nuclei with N Approx. 90. *Soviet journal of nuclear physics*, (13):259, 1971.
- [158] A. Makinaga, R. Massarczyk, R. Schwengner, M. Beard, F. Dönau, M. Anders, et al. Dipole strength of ^{181}Ta for the evaluation of the ^{180}Ta stellar neutron capture rate. *Physical Review C*, 90(4), October 2014. doi: [10.1103/physrevc.90.044301](https://doi.org/10.1103/physrevc.90.044301).
- [159] R. Bergère, H. Beil, and A. Veysseyre. Photoneutron cross sections of La, Tb, Ho and Ta. *Nuclear Physics A*, 121(2):463–480, December 1968. doi: [10.1016/0375-9474\(68\)90433-8](https://doi.org/10.1016/0375-9474(68)90433-8).
- [160] L. G. Moretto, A. C. Larsen, F. Giacoppo, M. Guttormsen, and S. Siem. Experimental First Order Pairing Phase Transition in Atomic Nuclei. *Journal of Physics: Conference Series*, 580:012048, February 2015. doi: [10.1088/1742-6596/580/1/012048](https://doi.org/10.1088/1742-6596/580/1/012048).
- [161] K. O. Ay, M. Ozgur, E. Algin, M. Guttormsen, F. L. Bello Garrote, L. Crespo Campo, et al. Nuclear level densities and gamma-ray strength functions of $^{145,149,151}\text{Nd}$ isotopes. *Journal of Physics: Conference Series*, 766:012027, October 2016. doi: [10.1088/1742-6596/766/1/012027](https://doi.org/10.1088/1742-6596/766/1/012027).
- [162] M. Guttormsen. (private communication). 2019.
- [163] S. Goriely. (private communication). 2019.
- [164] S. Goriely, S. Hilaire, S. Péru, and K. Sieja. Gogny-HFB+QRPA dipole strength function and its application to radiative nucleon capture cross section. *Physical Review C*, 98(1), July 2018. doi: [10.1103/physrevc.98.014327](https://doi.org/10.1103/physrevc.98.014327).
- [165] S. Goriely and V. Plujko. Simple empirical E1 and M1 strength functions for practical applications. *Physical Review C*, 99(1), January 2019. doi: [10.1103/physrevc.99.014303](https://doi.org/10.1103/physrevc.99.014303).
- [166] M. Wiedeking. (private communication). 2019.
- [167] L. Pellegrini. (private communication). 2019.
- [168] C. W. Johnson. Systematics of strength function sum rules. *Physics Letters B*, 750:72–75, November 2015. doi: [10.1016/j.physletb.2015.08.054](https://doi.org/10.1016/j.physletb.2015.08.054).
- [169] H. M. Hofmann, J. Richert, J. W. Tepel, and H. A. Weidenmüller. Direct reactions and Hauser-Feshbach theory. *Annals of Physics*, 90(2):403–437, April 1975. doi: [10.1016/0003-4916\(75\)90005-6](https://doi.org/10.1016/0003-4916(75)90005-6).
- [170] A. J. Koning and J. P. Delaroche. Local and global nucleon optical models from 1 keV to 200 MeV. *Nuclear Physics A*, 713(3-4):231–310, January 2003. doi: [10.1016/s0375-9474\(02\)01321-0](https://doi.org/10.1016/s0375-9474(02)01321-0).

- [171] M. Lindner, R. J. Nagle, and J. H. Landrum. Neutron Capture Cross Sections from 0.1 to 3 MeV by Activation Measurements. *Nuclear Science and Engineering*, 59(4):381–394, April 1976. doi: [10.13182/nse76-a26839](https://doi.org/10.13182/nse76-a26839).
- [172] V. N. Kononov, B. D. Jurlov, D. Poletaev, and V. M. Timokhov. *Soviet Journal of Nuclear Physics*, (26):500, 1977.
- [173] M. V. Bokhovko, V. N. Kononov, E. D. Poletaev, N. S. Rabotnov, and V. M. Timokhov. Average Fast Neutron Radiative Capture Cross Sections for Fission Products and for Isotopes of Rare Earth Elements. In *Nuclear Data for Science and Technology*, pages 62–64. Springer Berlin Heidelberg, 1992. doi: [10.1007/978-3-642-58113-7_16](https://doi.org/10.1007/978-3-642-58113-7_16).
- [174] K. Wisshak, F. Voss, C. Arlandini, F. Käppeler, M. Heil, R. Reifarth, M. Krčička, and F. Bečvář. Stellar neutron capture on $^{180}\text{Ta}^m$. I. Cross section measurement between 10 keV and 100 keV. *Physical Review C*, 69(5), May 2004. doi: [10.1103/physrevc.69.055801](https://doi.org/10.1103/physrevc.69.055801).
- [175] A. C. Larsen, M. Guttormsen, R. Schwengner, D. L. Bleuel, S. Goriely, S. Harissopulos, et al. Experimentally constrained $(p,\gamma)^{89}\text{Y}$ and $(n,\gamma)^{89}\text{Y}$ reaction rates relevant to p-process nucleosynthesis. *Physical Review C*, 93(4), April 2016. doi: [10.1103/physrevc.93.045810](https://doi.org/10.1103/physrevc.93.045810).
- [176] B. V. Kheswa, M. Wiedeking, J. A. Brown, A. C. Larsen, S. Goriely, M. Guttormsen, et al. $^{137,138,139}\text{La}(n,\gamma)$ cross sections constrained with statistical decay properties of $^{138,139,140}\text{La}$ nuclei. *Physical Review C*, 95(4), April 2017. doi: [10.1103/physrevc.95.045805](https://doi.org/10.1103/physrevc.95.045805).
- [177] K. L. Malatji, M. Wiedeking, S. Goriely, C. P. Brits, B. V. Kheswa, F. L. Bello Garrote, et al. Re-estimation of ^{180}Ta nucleosynthesis in light of newly constrained reaction rates. *Physics Letters B*, 2019. ISSN 0370-2693. doi: <https://doi.org/10.1016/j.physletb.2019.03.013>.
- [178] T. RAUSCHER and F. K. THIELEMANN. Tables of nuclear cross sections and reaction rates: An addendum to the paper "astrophysical reaction rates from statistical model calculations". *Atomic Data and Nuclear Data Tables*, 79(1):47–64, September 2001. doi: [10.1006/adnd.2001.0863](https://doi.org/10.1006/adnd.2001.0863).
- [179] J. Praena, P. F. Mastinu, M. Pignatari, J. M. Quesada, J. García-López, M. Lozano, N. Dzysiuk, R. Capote, and G. Martín-Hernández. Measurement of the MACS of at $kT=30$ keV as a test of a method for maxwellian neutron spectra generation. *Nuclear Instruments and Methods in Physics Research Section A: Accelerators, Spectrometers, Detectors and Associated Equipment*, 727:1–6, November 2013. doi: [10.1016/j.nima.2013.05.151](https://doi.org/10.1016/j.nima.2013.05.151).
- [180] L. Siess, E. Dufour, and M. Forestini. An internet server for pre-main sequence tracks of low- and intermediate-mass stars. *Astronomy and Astrophysics*, 358(2):593–599, 2000. URL <https://www.scopus.com/inward/record.uri?eid=2-s2.0-0001580266&partnerID=40&md5=20a8f29d48ec0a16d5ff2180d90d162b>.

- [181] L. Siess. Evolution of massive AGB stars. *Astronomy & Astrophysics*, 448(2):717–729, February 2006. doi: [10.1051/0004-6361:20053043](https://doi.org/10.1051/0004-6361:20053043).
- [182] Zs. Nemeth, F. Käppeler, C. Theis, T. Belgya, and S. W. Yates. Nucleosynthesis in the Cd-In-Sn region. *The Astrophysical Journal*, 426:357, May 1994. doi: [10.1086/174071](https://doi.org/10.1086/174071).
- [183] D. Belic, C. Arlandini, J. Besserer, J. de Boer, J. J. Carroll, J. Enders, et al. Photoactivation of $^{180}\text{Ta}^m$ and Its Implications for the Nucleosynthesis of Nature's Rarest Naturally Occurring Isotope. *Physical Review Letters*, 83(25):5242–5245, December 1999. doi: [10.1103/physrevlett.83.5242](https://doi.org/10.1103/physrevlett.83.5242).
- [184] P. Mohr, F. Käppeler, and R. Gallino. Survival of nature's rarest isotope ^{180}Ta under stellar conditions. *Physical Review C*, 75(1), January 2007. doi: [10.1103/physrevc.75.012802](https://doi.org/10.1103/physrevc.75.012802).
- [185] K. Takahashi and K. Yokoi. Beta-decay rates of highly ionized heavy atoms in stellar interiors. *Atomic Data and Nuclear Data Tables*, 36(3):375–409, May 1987. doi: [10.1016/0092-640x\(87\)90010-6](https://doi.org/10.1016/0092-640x(87)90010-6).
- [186] S. Goriely. Uncertainties in the solar system r-abundance distribution. *Astronomy and Astrophysics*, 342(3):881–891, 1999. URL <https://www.scopus.com/inward/record.uri?eid=2-s2.0-0042657251&partnerID=40&md5=eea5e9ac92509dbde35852ebeece1ba>.
- [187] M. A. Hashimoto. Supernova Nucleosynthesis in Massive Stars. *Progress of Theoretical Physics*, 94(5):663–736, November 1995. doi: [10.1143/ptp.94.663](https://doi.org/10.1143/ptp.94.663).
- [188] A. C. Larsen and A. Spyrou. The rare-earth r-process peak: $^{156-159}\text{Sm}(n,\gamma)$ reaction rates constrained with the beta-Oslo method (Proposal 1734). Technical report, Argonne National Laboratory, 2018.

Appendix A

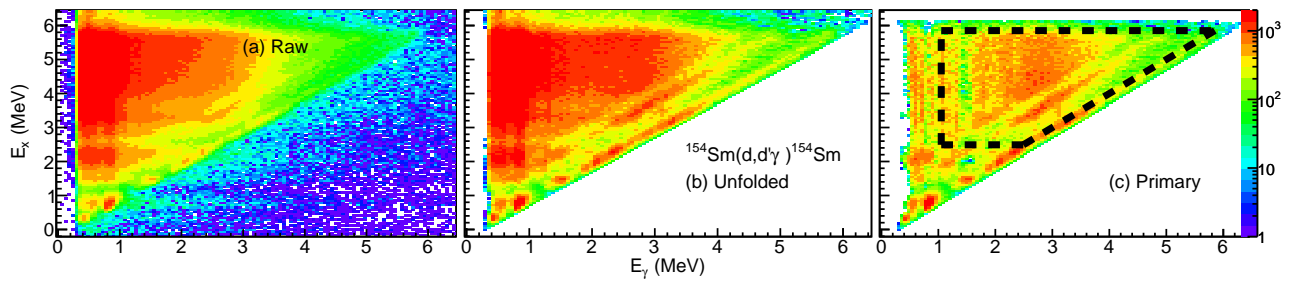


Figure 6.1. The raw γ -ray spectra (a), unfolded γ -ray spectra (b) and first generation (primary) γ -ray (discussed in sec. 4.2.4) spectra of ^{154}Sm extracted from the data collected with the $\text{LaBr}_3:\text{Ce}$ detectors from this work.

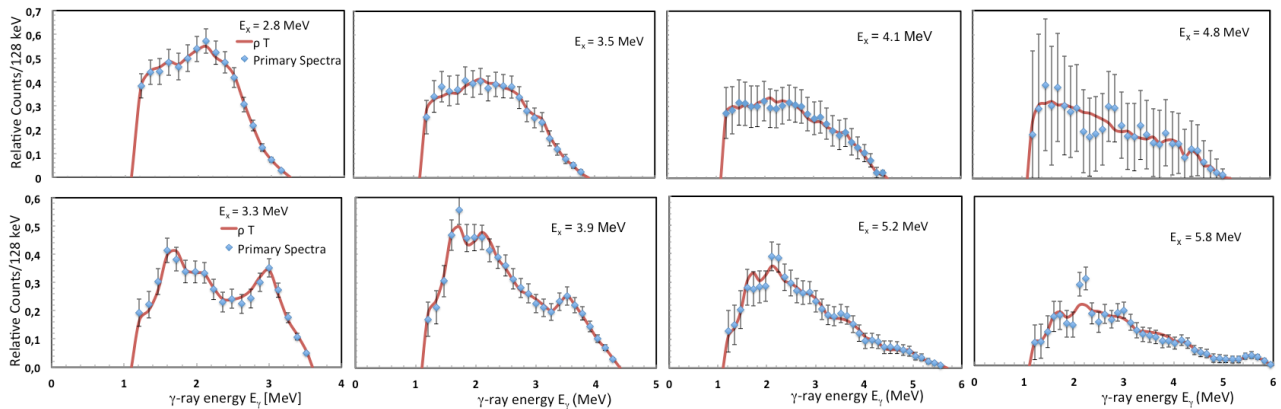


Figure 6.2. The experimental first generation γ -ray spectra (data points with error bars) from $(d,t\gamma)^{180}\text{Ta}$ (upper panel) and $(d,d'\gamma)^{181}\text{Ta}$ (bottom panel) reaction at 15 MeV beam, respectively, from selected initial excitation energies E_x (indicated in the figure) compared to the product $p(E_x - E_\gamma) \times \mathcal{T}(E_\gamma)$ (solid curve) following the global iterative χ^2 minimization of Ref. [29].

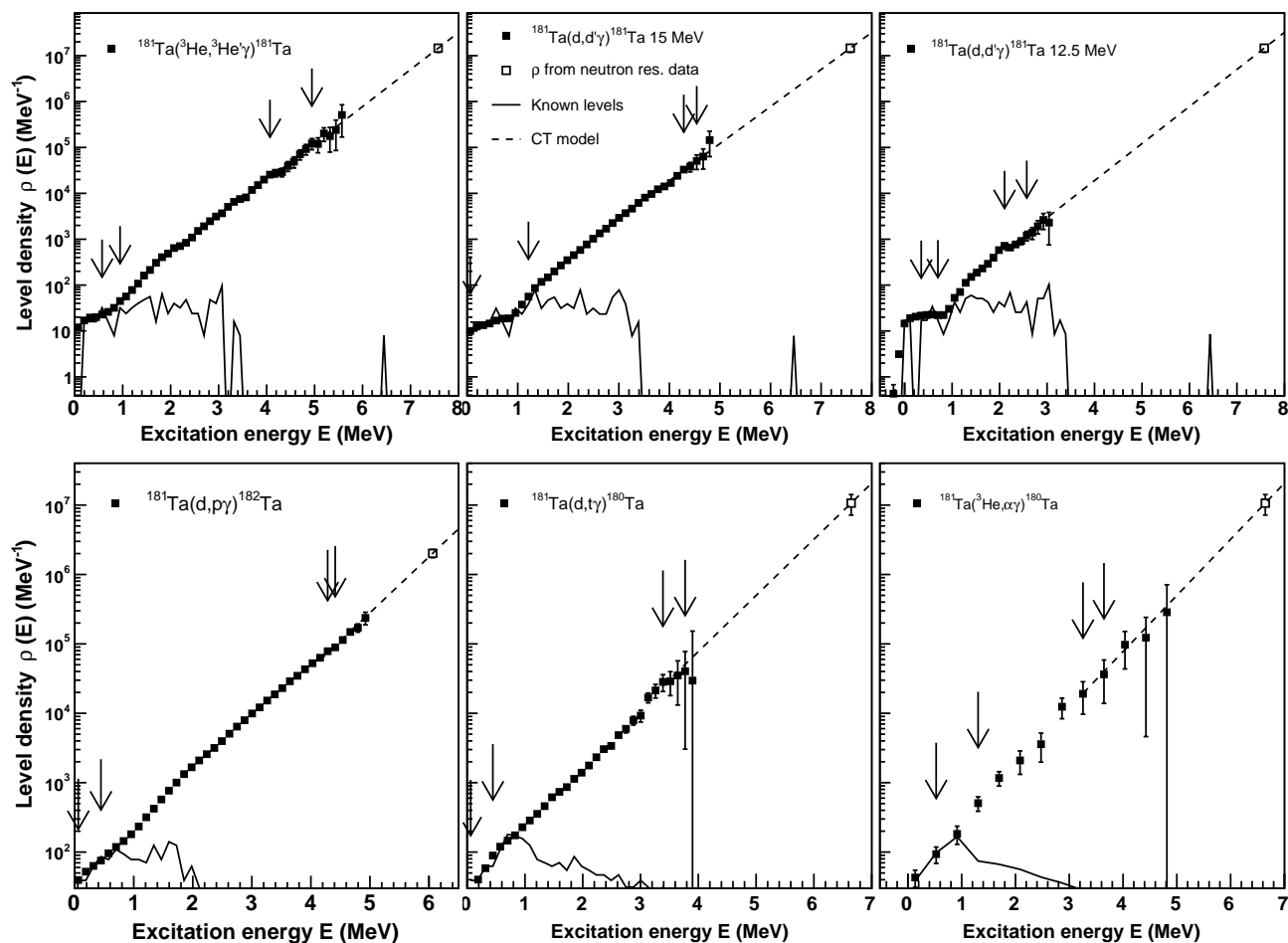


Figure 6.3. The normalized experimental NLDs for $^{180,181,182}\text{Ta}$ isotopes. The set of vertical arrows indicate the location at which the χ^2 minimization was performed. The individual plots have been presented in Refs. [36, 37, 38, 133] but in this thesis, the most recent and final normalization version of the data set is presented.

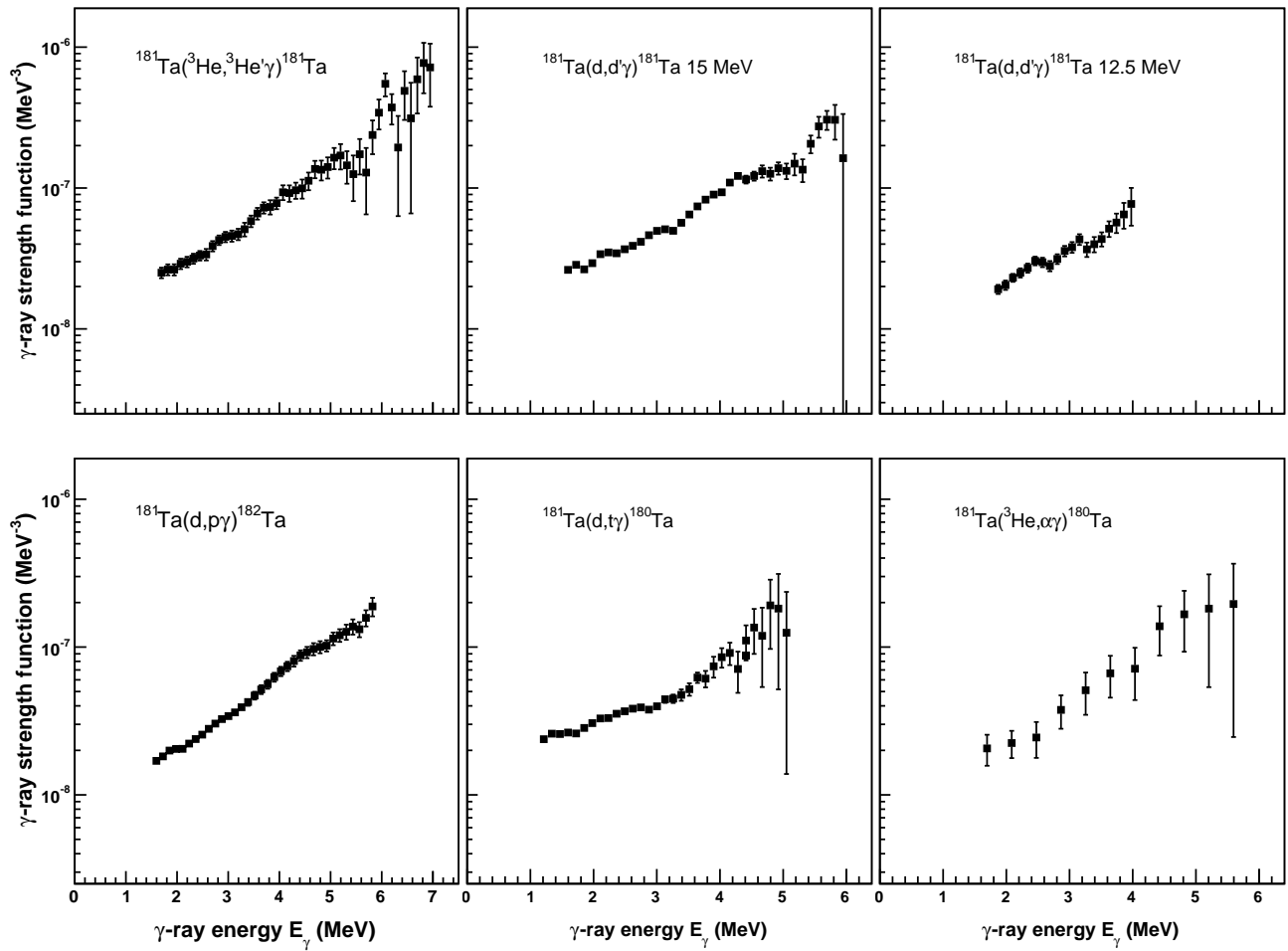


Figure 6.4. The experimental γ SFs of $^{180,181,182}\text{Ta}$. The individual plots have been presented in Refs. [36, 37, 38, 133] but in this thesis, the most recent and final normalization version of the data set is presented.

Sereto sa Kgashane Mamatlepa

Ke nna Kgashane la Mamatlepa.
Ke nna Noko mo Phalaborwa,
waa sealani sa mmamokhuma baa tshekga tjatji le fisa,
mahumo gaMalatji re epa taamane Phalaborwa.
Ke mohlanka wa go epa taamane ka matsogo.
Thaba ya geso ga e namelwe.
Se bone shokwe go falala lehumo lena le benyi.
Bolla noto walla theku bo sele.
Ke sealeng se segolo sa ga mmamohuba waga ngwete,
ke Noko ya le Phalaborwa yeo etxwago sealeng,
ke thete e kgolo ya shaka la moshate,
ba e botxixa bare naa wena thete geo tshaba go fata o tshaba eng?
ya re nna thete ke txhaba nala txa maburu,
ke txhaba go tsimiwa ke Malatji wa Rashiko.
Ke morwa wa Mchethe mohwa mobe le Mmabadimo.
Ageeh noko, noko ya go hlaba ka meetlwa.